THÈSE

Pour obtenir le grade de

DOCTEUR DE L'UNIVERSITÉ GRENOBLE ALPES

École doctorale : PHYS - Physique
Spécialité : Physique Théorique
Unité de recherche : Institut LAUE LANGEVIN

Ordre induit par les fluctuations quantiques dans les aimants frustrés antiferromagnétiques : nouvelles perspectives apportées par la théorie des ondes de spin

Quantum order from disorder in frustrated antiferromagnets: new insights from spin-wave theory

Présentée par :

Romane SCHICK

Direction de thèse :

Mike ZHITOMIRSKY — Directeur de thèse
ingenieur-chercheur, Université Grenoble Alpes

Timothy ZIMAN — Co-directeur de thèse
CNRS

Rapporteurs :

TOMMASO ROSCILDE
Maître de conférences HDR, ENS DE LYON

DMITRY KOVRIZHIN
Professeur des Universités, CY CERGY PARIS UNIVERSITE

Thèse soutenue publiquement le **29 juin 2022**, devant le jury composé de :

TOMMASO ROSCILDE Maître de conférences HDR, ENS DE LYON	Rapporteur
DMITRY KOVRIZHIN Professeur des Universités, CY CERGY PARIS UNIVERSITE	Rapporteur
ANDREAS HONECKER Professeur des Universités, CY CERGY PARIS UNIVERSITE	Président
ELSA LHOTEL Directeur de recherche, CNRS DELEGATION ALPES	Examinatrice
ARNAUD RALKO Maître de conférences HDR, UNIVERSITE GRENOBLE ALPES	Examinateur

Invités :

TIMOTHY ZIMAN
Directeur de recherche, CNRS DELEGATION ALPES

Quantum order by disorder in frustrated antiferromagnets: new insights from spin-wave theory

Romane Schick

Université Grenoble-Alpes
École doctorale de physique
Grenoble, France

Supervisors:

Mike Zhithomirsky
Timothy Ziman

Contents

Abstract

Frustrated spin systems are highly sensitive to fluctuations due to their enlarged classical ground-state manifold. In most cases, fluctuations stabilize one of the classically degenerate ordered ground states through either quantum zero-point motion or entropic selection. This is called order by disorder (OBD). In this thesis I study various instances of the OBD effect in frustrated quantum spin systems with spin-wave theory.

The first part is dedicated to the study of fractional magnetization plateaus in the kagome and pyrochlore antiferromagnets. They are attributed to the stabilization by quantum fluctuations of a given collinear spin state over a field region that exceeds its classical stability point. This is one emblematic manifestation of OBD. I obtain full magnetization curves that exhibit a large fractional plateau for both systems solely within linear spin-wave theory (LSWT). In the case of the kagome lattice, the plateau width fits very well to available numerical data for spins greater than a half. This tends to validate the technique for the pyrochlore case as well, where numerics are much harder to perform due to 3-dimensionality of the lattice. I also derive full analytical expressions for the spin-wave spectra of the canted states.

In the second part of the thesis, I study ground-state selection in the face-centered-cubic Heisenberg antiferromagnet. The classical degeneracy is broken at the harmonic level in spin-wave theory and there is selection of a given state at zero temperature. Surprisingly, at low temperature, thermal population of low-lying magnons results in a different selection. To complement the study, I go to higher order in spin-wave theory and include the effects of magnon-magnon interactions self-consistently. I find that the ground state selected at zero temperature is different from what was found in the harmonic approximation, even at large spin. The failure of LSWT is argued to be due to the large number of accidental gapless modes in the harmonic spin-wave spectrum, reminiscent of the classical ground-state degeneracy. The values for the energies of competing ground states in function of spin compare well to newly available numerical data.

Chapter 1

Introduction

The field of magnetism in condensed matter offers a rich playground to study a plethora of theoretical concepts, which can in some cases be rather general to other areas of physics [1]. One noteworthy feature of this field is the fact that complex and beautiful theoretical objects can actually emerge from simplistic toy models. Another major advantage is that magnetic materials do exist in nature, or at least can be designed and grown in laboratories, such that there is at least hope - if it is not already a reality - that the predicted behaviours are accessible experimentally. In this thesis we focused on one prominent process, namely order by quantum disorder in frustrated antiferromagnets. This introduction aims at providing the notions which are at the basis of the whole remainder of the work here presented.

Condensed matter physics focuses on the study of large (if not infinite) collections of atoms arranged in periodic geometries called lattices. When their outer orbitals are only partially filled with electrons, atoms (or ions) carry a non-zero magnetic moment. If such magnetic ions are present in a compound and interact with each other, the material is said to be magnetic. Throughout this thesis, we focus on the study of *magnetic insulators* only. The behaviour of any physical system is dictated by energy considerations, and all energetics are encapsulated in the Hamiltonian operator $\hat{\mathcal{H}}$. In magnetic insulators, $\hat{\mathcal{H}}$ only depends on the spin degrees of freedom:

$$\hat{\mathcal{H}} = \hat{\mathcal{H}}(\mathbf{S}_1, \mathbf{S}_2, \ldots, \mathbf{S}_N) \ , \tag{1.1}$$

where $\mathbf{S}_i$ is a spin of length S located at position $\mathbf{R}_i$, and N is the total number of sites in the lattice. Such a Hamiltonian is called a *spin Hamiltonian*, and this is our starting point to the theoretical study of magnetic lattices.

A crucial question to the study of a given magnetic system, is the nature of its ground state. Indeed, the behaviour of the system at $T = 0$ and at low temperature is completely determined by its ground state and corresponding excited states. Practically, this means we wish to diagonalize and minimize the Hamiltonian given in Eq. (1.1). In general, this minimization leads to the stabilization of an *ordered state*, within which spins are oriented in a periodic arrangement at $T = 0$. This is called

magnetic *long-range order* (LRO). Note that the periodicity of the magnetic structure is not necessarily commensurate to that of the lattice.

We also are interested in the other eigenstates of the Hamiltonian, which necessarily have a higher energy: the excited states. As the temperature increases, the lowest-lying excited states become energetically accessible, which drives the energetics of the system at low T. Furthermore, as will be explained in more details later on in the context of spin-wave theory, even the energy of the $T = 0$ quantum ground state involves knowledge of its full excitation spectrum. As temperature is increased further, LRO is gradually destroyed by the thermal population of excited states, until the transition temperature at which the material becomes fully paramagnetic. In this PhD work, I studied low-temperature properties only, far below the magnetic transition temperature.

1.1 Heisenberg interaction

The simplest type of magnetic interaction is the isotropic, bilinear Heisenberg exchange interaction[1]. The Heisenberg Hamiltonian is given by:

$$\hat{\mathcal{H}} = \sum_{(i,j)} J_{ij} \mathbf{S}_i \cdot \mathbf{S}_j - \mathbf{H} \cdot \sum_i \mathbf{S}_i \ . \tag{1.2}$$

The first term represents Heisenberg exchange: the sum is made over all inequivalent spin pairs (i, j) of the lattice, and J_{ij} is the quantum mechanical *exchange interaction*. The strength and sign of J_{ij} depends on the specific properties of the material. The second term is called the Zeeman term and accounts for the interaction of spins with an external magnetic field $\mathbf{H}$. Its effect is to reduce the symmetry of the Hamiltonian from $SU(2)$ (global rotational symmetry) to $U(1)$ (rotational symmetry around the field), and to induce a preferential direction for the spins as it is increased. Let us forget the Zeeman term for the moment and only consider the zero field situation.

When J_{ij} is negative, the interaction is called *ferromagnetic* (FM). When J_{ij} is positive, the interaction is called *antiferromagnetic* (AF). The sign of exchange interaction is of major importance to the ground state's structure. Indeed, in materials with dominant ferromagnetic interactions, spins tend to all align in the same direction below the transition temperature. Such materials are called *ferromagnets*. Conversely, in materials with dominant antiferromagnetic interactions, or *antiferromagnets*, neighboring spins tend to be oriented as antiparallel as possible. In its most isotropic form, the exchange coupling J_{ij} only depends on the distance between the two spins[2].

Other kinds of interactions can emerge from the specific environment and electronic structure, and may induce anisotropy. However, Heisenberg exchange is present in all magnetic materials, and apart from very specific cases, it is in general dominant

[1] Here "isotropic" refers to spin space: the strength of exchange interaction is the same for all spin components.

[2] Here, "isotropic" is meant regarding real space: all spatial directions are equivalent.

compared to other types of interactions. It is therefore an appropriate starting point to the study of any magnetic lattice. Throughout this whole PhD thesis, we focus solely on the Heisenberg Hamiltonian of Eq. (1.2). More specifically, we consider *isotropic nearest-neighbor interactions*. Besides being relevant to most magnetic materials, we will see that it gives a great illustration of how already a simplistic model can lead to complex and interesting physics.

As said earlier, determination of the ground state is key to the understanding of a magnetic system. In this quest for the ground state, it is important to distinguish between classical and quantum ground states. Indeed, in most situations they are different, although not necessarily *very* different. Let me illustrate these concepts below, through the simple example of a bipartite lattice with nearest-neighbor Heisenberg interactions. This serves also as a toy demonstration of how LRO arises in magnetic systems.

1.2 Example of bipartite lattices

We consider nearest-neighbor, isotropic exchange interactions on a given lattice:

$$\hat{\mathcal{H}} = J \sum_{\langle i,j \rangle} \mathbf{S}_i \cdot \mathbf{S}_j \ . \tag{1.3}$$

In the above, $\langle . \rangle$ stands for the summation over all pairs of spins which are nearest neighbors to one another in the lattice. There is no external magnetic field, so the Zeeman term in Eq. (1.2) has been removed. We further assume that the lattice is bipartite. This means that it can be decomposed into two Bravais sublattices, in a way that all nearest neighbors of a given site belong to the sublattice opposite to the one of that site. This is for example the case of the square and honeycomb lattices in 2D, or the cubic and body-centered cubic (bcc) lattices in 3D. We wish to determine the ground state of such a system. Let us focus first on the classical situation, where spins are treated as 3 dimensional vectors in real space.

1.2.1 Classical ground state

In Eq. (1.3), the energy associated to a given pair of spins (or *bond*) ij is:

$$E_{ij} = J \mathbf{S}_i \cdot \mathbf{S}_j \ . \tag{1.4}$$

The total energy of the system can then be written from Eq. (1.3) as a sum over nearest-neighbor bond energies:

$$E = \sum_{\langle i,j \rangle} E_{ij} \ . \tag{1.5}$$

Obviously, the sign of J is a decisive parameter in the minimization. We therefore look at the two options separately.

Ferromagnets

When the exchange interaction J is of negative sign, E_{ij} is minimized if the two neighboring spins $\mathbf{S}_i$ and $\mathbf{S}_j$ are aligned to each other in the same direction, see Eq. (1.4). Therefore, the state which minimizes the total Hamiltonian is the ferromagnetic (FM) state, where all spins in the lattice point in the same direction. It is illustrated on the left panel of Fig. (1.1) on the square lattice. Note that in that state, all bond energies E_{ij} are simultaneously minimized with value $E_{ij} = JS^2$ (with negative J). As a result, we have for the classical ground-state energy:

$$E_{\mathrm{FM}}^{\mathrm{cl}} = \frac{Nz}{2} JS^2 \ , \tag{1.6}$$

where N is the total number of spins in the lattice, and z is the coordination number[3]. The FM state has net magnetization $\mathbf{M}_{\mathrm{tot}} = NS\hat{\mathbf{e}}$, where $\hat{\mathbf{e}}$ is a unit vector of arbitrary orientation in spin space.

Antiferromagnets

When the exchange interaction J is of positive sign, the interaction is antiferromagnetic and E_{ij} is minimized if the two neighboring spins are completely antiparallel to each other. In a bipartite lattice, this condition can be fully satisfied on all bonds simultaneously. In the corresponding configuration, all spins of a given sublattice point in the same direction, while all spins of the other sublattice point in the opposite direction. The resulting state is called the Néel state, and is illustrated on the right panel of Fig. (1.1) in the case of the square lattice. We have $E_{ij} = -JS^2$ for all bonds, and for the total ground-state energy:

$$E_{\mathrm{Néel}}^{\mathrm{cl}} = -\frac{Nz}{2} JS^2 \ . \tag{1.7}$$

The Néel state has no net magnetization: $\mathbf{M}_{\mathrm{tot}} = \mathbf{0}$. However, there is still ordering, and the relevant order parameter here becomes the staggered magnetization.

Spontaneous symmetry breaking

On Fig. (1.1), the spins are pointing along the $\pm\hat{\mathbf{e}}_y$ direction for the sake of simplicity, but in both the FM and Néel states, the orientation of the (staggered) magnetization is completely arbitrary. This is a result of the global rotational symmetry SU(2) of the Hamiltonian of Eq. (1.3). Below the transition temperature, the spin structure freezes along one given orientation. Actually, there are several magnetic domains, within which all spins are oriented along the same direction. This is a typical occurrence of spontaneous symmetry breaking (SSB), where the system "picks" one of many degenerate configurations. As a result, the ground state has lower symmetry than the Hamiltonian.

[3] $z = 4$ in the case of the square lattice

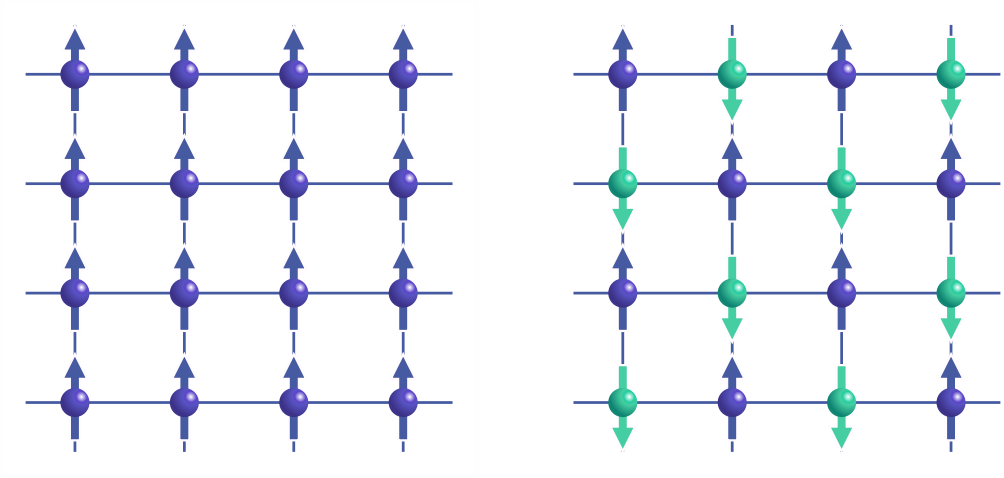

(a) $J < 0$: *FM state* (b) $J > 0$: *Néel state*

Figure 1.1: *Classical ground states of the square lattice with nearest-neighbor Heisenberg exchange interaction* J.

1.2.2 Quantum ground state

Spins are quantum mechanical objects, and in a complete theory they should be treated as such. To that end, one should use quantum spin operators $\hat{S}_i^\alpha$, $\alpha \in \{x, y, z\}$ rather than classical vector components in the Hamiltonian of Eq. (1.3). The dimension d_H of the Hilbert space is determined by all possible sets of local S_i^z projections. Each spin $\mathbf{S}_i$ can have $2S+1$ quantized values for S_i^z, given by $S_i^z \in \{-S, -S+1, \ldots, S-1, S\}$. Then we have $d_H = (2S+1)^N$. We chose the following basis states:

$$|\phi_n\rangle = |m_1, m_2, \ldots, m_N\rangle \ , \tag{1.8}$$

where $n \in \{1, \cdots, d_H\}$ and $m_i = S_i^z$ is the local projection of spin $\mathbf{S}_i$ along the z axis. Any spin state $|\psi\rangle$ can be written as a superposition of the above defined basis states:

$$|\psi\rangle = \sum_{n=1}^{d_H} c_n \, |\phi_n\rangle \ . \tag{1.9}$$

The scalar product of two spins can be written as follows [2]:

$$\mathbf{S}_i \cdot \mathbf{S}_j = \hat{S}_i^x \hat{S}_j^x + \hat{S}_i^y \hat{S}_j^y + \hat{S}_i^z \hat{S}_j^z = \frac{1}{2}\left(\hat{S}_i^+ \hat{S}_j^- + \hat{S}_i^- \hat{S}_j^+\right) + \hat{S}_i^z \hat{S}_j^z \ , \tag{1.10}$$

where we have used the spin-lowering and spin-raising operators $\hat{S}_i^-$ and $\hat{S}_i^+$. They are more convenient than $\hat{S}_i^x$ and $\hat{S}_i^y$, as they allow one to work easily within the basis set by Eq. (1.8). One can rewrite the Hamiltonian of Eq. (1.3) as follows:

$$\hat{\mathcal{H}} = \frac{J}{2} \sum_i \sum_{\boldsymbol{\delta}(i)} \left(S_i^- S_{i+\boldsymbol{\delta}}^+ + S_i^z S_{i+\boldsymbol{\delta}}^z\right) \ , \tag{1.11}$$

where the second sum spans the nearest-neighbor vectors $\boldsymbol{\delta}(i)$ from a given site in position $\mathbf{R}_i$. For the sake of simplicity, I dropped the hats on quantum spin operators. Note that this Hamiltonian remains hermitian due to the summation over all sites and over all nearest neighbors for each site. Indeed, each nearest-neighbor pair is counted twice, which also explains the $1/2$ prefactor.

Ferromagnets

Consider the ferromagnetic case ($J < 0$). Classically, the ground state is given by the FM state, see left panel of Fig. (1.1). With appropriate choice for the quantization axis $\hat{z}$, the FM state corresponds to the state of full saturation, that is:

$$|\psi_{\text{FM}}\rangle = |\phi_{\text{Sat}}\rangle = |S, S, \ldots, S\rangle \ . \tag{1.12}$$

This state is an eigenstate of the quantum Hamiltonian of Eq. (1.11). Indeed, the spin-raising operator $\hat{S}_i^+$ does not act on a fully polarized spin, while the $\hat{S}_i^z$ operator preserves any state written as in Eq. (1.8). The FM state defined in Eq. (1.12) is also the lowest energy eigenstate of the quantum system, and has the same ground-state energy as the classical FM state, see Eq. (1.6). It is therefore the true quantum ground state of the Hamiltonian.

Antiferromagnets

Let us now consider the interaction to be antiferromagnetic ($J > 0$), in which case the Néel state is the classical ground state of the Hamiltonian, see right panel of Fig. (1.1). The quantum mechanical equivalent of the Néel state is written as:

$$|\psi_{\text{Néel}}\rangle = |\phi_{\uparrow\downarrow}\rangle = |S, -S, S, \ldots, -S, S\rangle \ . \tag{1.13}$$

It is easy to see that this is not an eigenstate of the quantum Hamiltonian. Indeed, consider the effect of the operator $S_i^- S_j^+$, where $\mathbf{S}_i$ and $\mathbf{S}_j$ are nearest neighbors. Provided that the spin $\mathbf{S}_i$ has magnetization $m_i = S$ in the chosen Néel state, then necessarily we have $m_j = -S$, and:

$$S_i^- S_{i+\boldsymbol{\delta}}^+ |\phi_{\uparrow\downarrow}\rangle = 2S \cdot |\phi_{ij}\rangle \not\propto |\phi_{\uparrow\downarrow}\rangle \ . \tag{1.14}$$

In the above, $|\phi_{ij}\rangle$ is constructed from the Néel state, by flipping from one unit one pair of antiparallel nearest-neighbor spins i and j:

$$|\phi_{ij}\rangle = |S, -S, S, \ldots, \underset{i}{S-1}, \underset{j}{-S+1}, \ldots, -S, S\rangle \ . \tag{1.15}$$

Therefore, the first term of the Hamiltonian of Eq. (1.11) acts on all $\uparrow\downarrow$ nearest-neighbor spin pairs of the Néel state. It creates a superposition of states $|\phi_{ij}\rangle$ with corresponding local paired spin-flips. The second term of Eq. (1.11) does preserve $|\phi_{\uparrow\downarrow}\rangle$, with associate energy equal to that of the classical Néel state, see Eq. (1.7). Since the Hamiltonian

acts on the Néel state, it is not an eigenstate, and therefore it cannot be the true quantum ground state.

Then what is the true quantum antiferromagnetic ground state? Any other $|\phi_n\rangle$ state written as Eq. (1.8) has a a different set of local magnetizations m_i, and consequently has a higher classical energy. Thus, they can definitely not be the true ground state either. Actually, none of the $|\phi_n\rangle$ states is an eigenstate of the Hamiltonian, except the fully saturated state $|\phi_{\text{Sat}}\rangle$, which has the highest possible energy in the AF case, see Eq. (1.6). Then the true ground state $|\psi_{\text{gs}}\rangle$ can only be a superposition of $|\phi_n\rangle$ states as in Eq. (1.9).

Let us look at this problem through the angle of perturbation theory. The second term in the Hamiltonian of Eq. (1.11) is the unperturbed Hamiltonian $\hat{\mathcal{H}}_0$, and the first term is treated as a perturbation $\hat{V}$:

$$\begin{aligned} \hat{\mathcal{H}} =& \hat{\mathcal{H}}_0 + \hat{V} \ , \\ \hat{\mathcal{H}}_0 = J \sum_{\langle i,j \rangle} S_i^z S_j^z \ , \qquad & \hat{V} = \frac{J}{2} \sum_i \sum_{\boldsymbol{\delta}(i)} S_i^- S_{i+\boldsymbol{\delta}}^+ \ . \end{aligned} \tag{1.16}$$

The eigenstates of $\hat{\mathcal{H}}_0$ are given by Eq. (1.8), the ground state being the Néel state $|\phi_{\uparrow\downarrow}\rangle$ in the AF case, see Eq. (1.13). Then the true quantum ground state is constructed perturbatively from the eigenstates of $\hat{\mathcal{H}}_0$:

$$\begin{aligned} |\psi_{\text{gs}}\rangle =& |\phi_{\uparrow\downarrow}\rangle + |\psi^{(1)}\rangle + |\psi^{(2)}\rangle + \dots \ , \\ |\psi^{(1)}\rangle =& \sum_{n \neq \uparrow\downarrow} \frac{\langle \phi_n | \hat{V} | \phi_{\uparrow\downarrow} \rangle}{E^{\text{cl}}_{\text{Néel}} - E_n} |\phi_n\rangle = \frac{S}{1 - 2zS} \sum_{\langle i,j \rangle} |\phi_{ij}\rangle \ . \end{aligned} \tag{1.17}$$

The first order quantum correction to the antiferromagnetic ground state, mixes the Néel state with states of pairs of nearest-neighbor spin flips $|\phi_{ij}\rangle$, see Eq. (1.15). This gives us the general trend, namely, that *the true quantum ground state can be seen as the Néel state dressed with quantum fluctuations*. The ground-state energy also gets quantum corrections, and is lowered compared to its classical value.

Note that individual local magnetizations m_i are not well-defined anymore in the antiferromagnetic quantum ground state. The quantum fluctuations are shared throughout the whole lattice, as will be developed further when introducing spin-waves. The mean value of on-site staggered magnetization however, can be computed in the dressed quantum ground state. Due to the presence of fluctuations, it gets reduced compared to its classical value S: the quantum antiferromagnet undergoes *spin reduction*.

1.3 Frustrated magnets

In the example of bipartite lattices presented in the previous section, the classical ground state could be easily determined by minimizing all bond energies E_{ij} simultaneously. However, this is not necessarily possible in all models, and this idea is at the origin of the concept of frustration. To illustrate in more details what is commonly meant when talking about frustration, or frustrated magnets, let me use the example of the J_1-J_2 square lattice antiferromagnet (SLAF):

$$\hat{\mathcal{H}} = J_1 \sum_{\langle i,j \rangle} \mathbf{S}_i \cdot \mathbf{S}_j + J_2 \sum_{\langle\langle i,j \rangle\rangle} \mathbf{S}_i \cdot \mathbf{S}_j \ . \tag{1.18}$$

J_2 represents interaction between next-nearest-neighbors (NNN): it acts on the diagonals of the square plaquettes of the lattice. We have $J_1, J_2 \geq 0$ (AF interactions).

$J_2 < J_1/2$: Frustrated bonds

In the model of Eq. (1.18), all pair-wise interactions between spins cannot be minimized simultaneously. Indeed, it is impossible to have *all* nearest-neighbor spins antiparallel to each other (Néel state), and *all* NNN spins antiparallel to each other within the same classical configuration. Whatever the configuration, there will be some spin pairs, of which the energy E_{ij} does not take its minimal possible value, namely $E_{ij}^{\min} = -J_{ij}S^2$. The corresponding bonds are referred to as *frustrated bonds*.

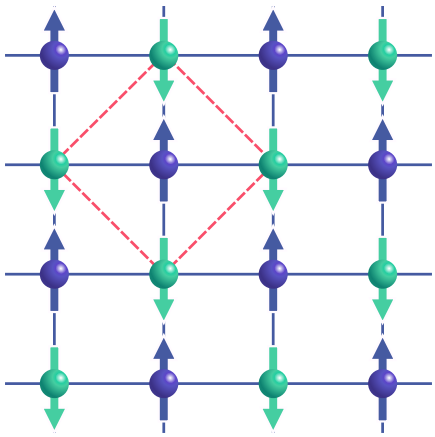

Figure 1.2: *J_1-J_2 SLAF, $J_2 < J_1/2$: Néel state with frustrated bonds.*

Despite the presence of frustrated bonds, the classical ground state might still be uniquely defined. This happens in the J_1-J_2 SLAF, when $J_2 < J_1/2$. In that case, physics is dominated by the nearest-neighbor AF exchange, and the AF Néel state is the classical ground state. It has ordering wave vector $\mathbf{Q}_{\text{Néel}} = (\pi, \pi)$. This state is depicted on Fig. (1.2). The diagonal NNN bonds are frustrated, as is illustrated by the red dotted square. However, this is the state of lowest classical energy, and it is *unique* [4]. Note that in that state the frustrated bonds are *maximally frustrated*, in the sense that E_{ij} takes its maximal possible value, namely $E_{ij}^{\max} = J_{ij}S^2$.

The definitions for a frustrated magnet can vary. Frustration is sometimes referred to simply as the presence of frustrated bonds. This is not however the definition I will use throughout this thesis, even though frustrated bonds are a necessary ingredient to frustration in a magnetic lattice.

[4] Up to global symmetries of the Hamiltonian and lattice.

$J_2 > J_1/2$: Frustrated lattice (weak frustration)

When $J_2 > J_1/2$ in Eq. (1.18) on the SLAF, the NNN AF interaction dominates, and the classical ground state is degenerate: it consists of two interpenetrating Néel sublattices, with *arbitrary relative orientation.* Such a state is shown on the left panel of Fig. (1.3). One sublattice is represented with full arrows, the other sublattice with empty arrows. All NNN bonds are minimized and thus non frustrated, as is indicated by the blue dotted square. The relative angle between the two is also shown in light blue. This angle is a continuous parameter that allows us to navigate in the infinite ground-state manifold.

Such a situation illustrates what is most commonly referred to as *frustration*, or *frustrated lattices.* In the remainder of this thesis, I use this definition of frustration, namely: *a system of which the classical ground state is degenerate beyond the symmetries of the Hamiltonian.* The J_1-J_2 SLAF with $J_2 > J_1/2$ is frustrated following this definition [5].

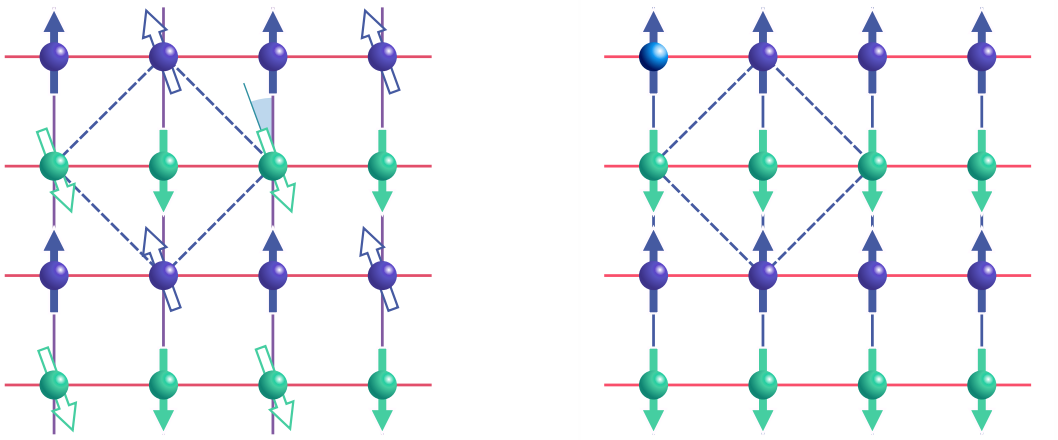

(a) *Arbitrary state.* (b) $\mathbf{Q}_y = (0, \pi)$*: The stripe-y state.*

Figure 1.3: *Classical ground states of the J_1-J_2 SLAF with $J_2 > J_1/2$. Frustrated bonds are highlighted in red.*

However, the ordering wave vectors associated to the classical ground states are only two-fold degenerate. They are indeed given by $\mathbf{Q}_x = (\pi, 0)$ and $\mathbf{Q}_y = (0, \pi)$. In that sense, the system is considered to be only *weakly frustrated.*

Note that among the classical ground-state manifold, two states have a collinear spin structure. They correspond to the situation where the blue angle on the left panel of Fig. (1.3) is equal to either 0 or to π. These states are the two single-$\mathbf{Q}$ states associated to the two ordering wave vectors $\mathbf{Q}_x$ and $\mathbf{Q}_y$. They correspond to ferromagnetic chains stacked antiferromagnetically along the x and y direction, respectively. They are called

[5] Note that the J_1-J_2 SLAF with $J_2 < J_1/2$ is *not frustrated* according to this definition.

stripe states, and one of such states is shown on the right panel of Fig. (1.3). Similar to the Néel state, all frustrated bonds in a stripe state are maximally frustrated. All other states of the classical ground-state manifold, with arbitrary relative angle between the two sublattices, are double-**Q** states: their structure involves contributions from both ordering wave vectors at the same time.

$J_2 = J_1/2$: Frustrated lattice (strong frustration)

At the precise classical phase boundary point $J_2 = J_1/2$, the situation is more complicated. Not only all the aforementioned states (Néel and interpenetrating Néel, including the two stripe states) are degenerate, but the classical degeneracy is even further enlarged. This is related to the fact that in this case, the Hamiltonian of Eq. (1.18) can be rewritten as a sum over square plaquettes p:

$$\hat{\mathcal{H}} = \frac{J_1}{2} \sum_p \left(\mathbf{S}_p^2 - 4S^2 \right) \ , \qquad \mathbf{S}_p = \sum_{i \in p} \mathbf{S}_i \ . \tag{1.19}$$

$\mathbf{S}_p$ is the total spin on plaquette p, that is, the sum of the 4 spins on that plaquette. Then it is easy to see that the classical Hamiltonian of Eq. (1.19) is minimized by imposing the ground state condition that the total spin per plaquette vanishes, for all plaquettes:

$$\mathbf{S}_p = 0 \ .$$

The above condition can be satisfied by infinitely many spin structures, including some lacking LRO.

The possibility to write the Hamiltonian using new spin variables, namely the spins over a given block or plaquette, is often a property of *strongly frustrated magnets*. The fact that frustration is stronger in that situation, is also reflected in the *dimensionality* of the manifold of classically degenerate ordering wave vectors.

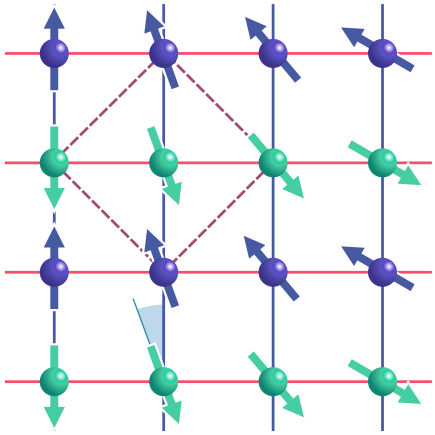

Figure 1.4: *Incommensurate spiral state with* $\mathbf{Q} = (q, \pi)$, q *being the blue angle.*

In the example exposed here, degenerate **Q** vectors form whole lines in reciprocal space given by $\mathbf{Q} = (\pi, q)$ or $\mathbf{Q} = (q, \pi)$, where q can take any real value. These lines connect the discrete ordering wave vectors of the surrounding phases, namely $\mathbf{Q}_{\text{Néel}}$, $\mathbf{Q}_x$ and $\mathbf{Q}_y$. Any state described by one (or a combination of) ordering-wave vector along these lines is a valid classical ground state. Note that in general, single-**Q** states are incommensurate spiral states, as shown on Fig. (1.4). Although the classical ground-state manifold also contained an infinity of states in the previous paragraph, the infinity is somewhat "larger" here at the classical phase boundary.

1.3.1 Geometrical frustration

In the example of the frustrated J_1-J_2 SLAF discussed above, the system is frustrated by explicit competition between different types of exchanges, namely the nearest-neighbor exchange J_1 and NNN exchange J_2. Frustration can, however, also arise solely from the geometry of the lattice, in which case we talk about *geometrical frustration*.

Typically, frustrated geometries are made from triangle-based units, where two nearest neighbors of a given site are also nearest neighbors to each other. Emblematic examples in 2D are the triangular and kagome lattices, which are made of edge-sharing or corner-sharing triangles, respectively. In 3D, the face-centered-cubic (fcc) and pyrochlore lattices are made from edge-sharing and corner-sharing tetrahedra, respectively. Let us mention as well the hyperkagome lattice, made from corner sharing triangles in 3D.

In such lattices, the enlarged classical ground-state degeneracy is already present with only one type of interaction. The simplest example is nearest-neighbor Heisenberg interaction of AF sign. Similar to the case of the J_1-J_2 SLAF with $J_2 = J_1/2$, this is related to the fact that the Hamiltonian can be rewritten as a sum over frustrated blocks, which makes its minimization under-constrained. Note that the triangular lattice is not frustrated per se in zero field, in the sense that there is a unique classical ground state (up to global rotations): the planar 120° structure. It is shown in Fig. (1.5). In that case, frustration is equally shared by all bonds of the lattice, contrary to the Néel and stripe states of the J_1-J_2 SLAF. The triangular lattice AFM becomes frustrated in applied magnetic filed.

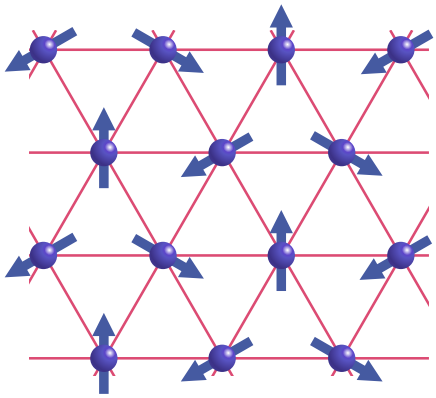

Figure 1.5: *120 ° structure in the triangular antiferromagnet.*

The present PhD work focuses on geometrically frustrated lattices, namely the kagome lattice in 2D, and pyrochlore and fcc lattices in 3D. The nearest-neighbor Heisenberg model is highly frustrated on all these lattices. Details and pictures of the lattices will be given in the dedicated chapters.

1.3.2 Ground states of frustrated magnets

A key feature of frustration, is that one cannot go from a given classical ground state to another through the true symmetries of the Hamiltonian. This is why the classical degeneracy is said to be *accidental*, in the sense that it is an artefact of the classical approximation. This degeneracy must be lifted in a complete theory, such that ultimately, only degeneracies related to the true symmetries of the Hamiltonian should remain. This may be achieved either by the selection of one of the classically degenerate states over the others, or by the stabilization of a new quantum ground state,

which has no simple classical counterpart [6].

Nevertheless, many low energy states still have close-by energies in frustrated magnets, which makes them highly sensitive to small perturbations. This is another key feature of frustration, and actually both aspects (the degeneracy being accidental, and high sensitivity to perturbations) are closely related. For example, small additional anisotropic interactions in the Hamiltonian allow us to explicitly break the spurious symmetry and can lift the degeneracy of the Heisenberg model, already at the classical level. This is what happens a lot in reality, where the specific properties of a given material lead to (at least weak) additional interactions. Indeed, perfectly classically degenerate systems are not entirely realistic.

Even neglecting such additional interactions, frustrated systems remain very sensitive to fluctuations as well. As seen above, the strength of frustration is associated to the size of the ground-state manifold. Then the tendency is that the stronger is the frustration, the stronger become fluctuations as well. In the worst (or best?) case scenario, when fluctuations are very strong, LRO may be completely destroyed in frustrated magnets, even at very low temperatures. Indeed, due to the large classical ground-state degeneracy, the switching of temperature implies that many states are accessible at once, which may lead to a classical spin liquid state [3]. Even at zero temperature, quantum fluctuations can destroy LRO. This is manifested by the aforementioned spin reduction being large enough to overcome the spin length S. This has more chances to happen for low-spin values, especially for the extreme quantum case $S = 1/2$. Then the quantum ground state cannot be described at all from an intuitive classical counterpart like the dressed Néel state discussed above. If no other long-range spin correlations are present, like in valence-bond crystals [4] or spin nematics [5], such states are called quantum spin liquids [6, 7].

However, in most cases, the scenario is much less dramatic, and fluctuations are not strong enough to destroy order. They even have the opposite effect and actually select one - or at least a subset - of the classically degenerate ordered ground states over the others. This surprising effect in which fluctuations induce order goes by the beautiful name of *order by disorder*.

1.3.3 Order by disorder

In the early 80s, a number of seminal works reported the phenomenon where LRO was achieved in frustrated magnetic systems due to inclusion of fluctuations [8–10]. Fluctuations can be of various origins: thermal, quantum, structural. The term "Order by disorder" (OBD) specifically emerged from the paper from Villain et al. [8]. In that paper, the system under study is a classical 2D lattice with competing interactions, and the disorder is of thermal and structural origin. Already before that however, other authors have remarked a possibility that LRO is stabilized by quantum fluctuations in anisotropic ferromagnets [11, 12]. We leave aside structural disorder for now.

[6] Note that this quantum state may or may not retain the symmetries of the Hamiltonian.

Thermal OBD

In the classical picture, the OBD phenomenon stems from thermal fluctuations and the stabilization of a given classical ground state is made from entropic selection [13]. This is shown schematically on Fig. (1.6). Let us say that there is a continuous parameter which allows one to span the classical ground-state manifold in parameter space. This is represented by the white line on Fig. (1.6). Any point on this line in parameter space, is a classical ground state of our frustrated system. Then for each classical ground state, one can evaluate the energy cost of slightly going away from it. If by doing so we leave the ground-state manifold (red arrow on Fig. (1.6)), this energy cost will be non zero [7]. This is typically done by twisting part of the spins away from their classical equilibrium position in the considered ground state. The excitation spectrum so defined, is schematized on the figure as well, regions of smaller energy corresponding to areas of darker blue color. The ground state which has the softest dispersion gains all statistical weight, and becomes the one selected at low temperature. This would correspond to the white dot on Fig. (1.6). Such a scenario is called *thermal order by disorder* [8, 10].

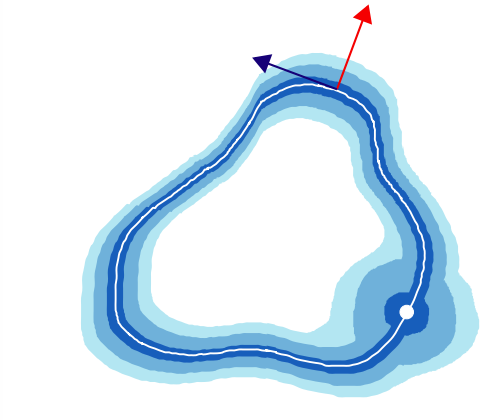

Figure 1.6: *Thermal OBD scheme represented in parameter space.*

Note that in a *quantum* spin system, the relevant excitations become the quantum spin-waves, rather than the aforementioned classical excitations. However, the principle remains the same: states with softest excitations are favored by thermal fluctuations. During my PhD work, I focused solely on the study of quantum spin systems, and therefore will be referring to this last situation when using the terminology *thermal OBD*.

Quantum OBD

At absolute zero temperature, no thermal fluctuations are allowed, and only quantum fluctuations are at play. Competing classical ground states become dressed by quantum fluctuations, as was shown in the previous section in the case of the Néel state. Corresponding energies of the quantum states are reduced compared to the classical ground-state energy. In principle, this quantum energy correction is a state-dependant quantity, which induces an energy difference between competing classical ground states. This determines the ground-state selection, or at least reduces significantly the ground-state manifold. In such a situation, on talks about *quantum order*

[7] Of course, when remaining in the ground-state manifold (blue arrow on Fig. (1.6)), the energy is unchanged at the classical level.

by disorder[8] [9, 11–16]. The quantum correction to a given ordered state is related to the zero-point motion of its elementary excitations, or spin waves, as will be explained in more details later.

General trends for the ground-state selection

Both types of fluctuations (thermal and quantum) have been argued many times to act in favor of collinear or coplanar states over the others [8–10, 17]. This can be illustrated going back to the case of the J_1-J_2 SLAF. Extensive quantum OBD studies have been made on this model [18].

When $J_2 > J_1/2$, the system is weakly frustrated. Let me remind the reader that the classical ground state is made of two interpenetrating Néel sublattices, with arbitrary relative orientation, see left panel of Fig. (1.3). It was quite early on demonstrated, that the true ground state selected by quantum fluctuations is actually one of the two-fold degenerate collinear stripe states, see right panel of Fig. (1.3) [9, 17, 19]. In that case, the quantum OBD phenomenon is quite straightforward.

At the classical phase boundary between the Néel state and the stripe states, namely $J_2 = J_1/2$, determination of the true quantum ground state becomes more complicated. It is expected from the collinearity argument - and from the fact that those are the ground states in surrounding phases - that either the Néel or a stripe state should be selected by quantum fluctuations. However, it was shown that for $S = 1/2$, spin reduction is strong enough to destroy LRO, both in the Néel and stripe phases, when approaching this phase boundary [15, 20]. This is directly related to the system becoming strongly frustrated when $J_2 = J_1/2$. At least the window of parameter space where order is completely destroyed in the ordered phases by quantum fluctuations, one can suspect the true quantum ground state to be a quantum spin liquid [21–23].

OBD can also arise from structural disorder, that is, a material with some concentration of vacancies in the lattice, or with vacant or modified bonds [8, 10]. Let me mention that in that case, the selection is expected to select the *least collinear states*, as opposed to the effect of quantum and thermal fluctuations [10]. One can therefore expect a competition effect between structural OBD and thermal/quantum OBD [24].

In this thesis I focused on the study of ground-state selection by OBD in *quantum* spin systems, the fluctuations being either of quantum or thermal origin. The major analytical tool to study the quantum OBD is spin wave theory, of which the principle is explained below.

[8] Or sometimes: order by quantum disorder.

1.4 Spin-wave theory in a nutshell

The results that will be presented in the following chapters were obtained using Spin-wave theory (SWT) as an analytical tool. The detailed analytical steps of the method are give in appendix A, which will serve as a reference throughout the text. The present section is aimed at introducing the general ideas behind a SWT derivation. Let us say we have a spin Hamiltonian $\hat{\mathcal{H}}$ as in Eq. (1.1). We wish to find the eigenvalues of this quantum Hamiltonian, in order to determine the ground state of the system it describes. In all the projects exposed in this thesis, the spin Hamiltonian only involves isotropic Heisenberg interaction, and interaction with an external field. However, SWT applies in principle to any spin Hamiltonian.

For a few special models, mostly in low dimensions, the quantum ground state is known exactly [25–27]. In general however, exactly solving the eigenvalue problem for such a Hamiltonian is possible analytically only for a very small number of quantum spins. Indeed, we remember that the dimension d_H of the Hilbert space grows exponentially with N, and even faster for large spin values S. Numerically, one can find the exact ground state of larger systems using exact diagonalization. Nevertheless, even with today's most powerful computers, one is still restricted to small system sizes of the order of a few tens of spins, even for small spin values. Although these numerical techniques are exact, they require huge computing power and cannot reproduce the behaviour of the system in the thermodynamic limit. One relies on extrapolation in order to infer the behaviour when $N \to \infty$ from the finite-size results. Furthermore, they do not provide a view on the physical mechanism at play behind the ground-state selection.

SWT is a semiclassical analytical approach in which the quantum Hamiltonian is approximated by a bosonic Hamiltonian that can be solved analytically (or numerically but with light computing power) in the thermodynamic limit. In SWT, one considers quantum states which are not far from a given classical *ordered* ground state, similar to the dressed Néel state discussed above. Quantumness is accounted for as quantum fluctuations (which are presumably small) around this classical ground state: the spin waves. Quantum effects are then manifested as small corrections to the spin orientation, spin length, and ground-state energy of that state. SWT is therefore very suited to the quantum OBD problem. Indeed, in a frustrated system, the true quantum ground state might be one of the classically degenerate ordered states "dressed" by quantum fluctuations. In that case, one can use SWT to compute the quantum corrections of the competing states, in order to determine which state has lowest energy and is ultimately selected.

Working directly with spin operators is complicated. For that reason, the key analytical starting point of a SWT derivation is the Holstein-Primakoff transformation, which is a mapping of the spin operators to bosonic creation and annihilation operators. This allows us to work in second quantization with bosons, which sets a well understood

framework. The Holstein-Primakoff transformation is given by [28]:

$$\begin{aligned} S_i^+ &= S_i^x + iS_i^y = \sqrt{2S - n_i} \cdot a_i \\ S_i^- &= S_i^x - iS_i^y = a_i^\dagger \cdot \sqrt{2S - n_i} \ , \qquad\qquad n_i = a_i^\dagger a_i \ . \\ S_i^z &= S - n_i \end{aligned} \tag{1.20}$$

In the above, a_i and $a_i^\dagger$ are bosonic annihilation and creation operators, respectively, and n_i is the particle number operator. Using this representation, the number n_i of bosonic particles present at a given lattice site i is directly equal to the number of times the spin $\mathbf{S}_i$ in this position is lowered from fully polarized position along the $z-$axis. For that reason, let me refer to these a particles as "local spin-lowerings". The Holstein-Primakoff transformation reproduces exactly the behaviour of original spin operators, meaning that the spin commutation relations are preserved. However, the Hilbert space of bosons is infinite, whereas the number of times a given spin can be lowered is not. The correct, finite size of the spin Hilbert space would be ensured by a constraint on the boson occupation number:

$$n_i \leq 2S \ .$$

This constraint leads to the so-called *kinematic interactions*, which are neglected in the vast majority of spin-wave studies of the literature. Following this tendency, in my work I also did not take this constraint into account, assuming the effects of kinematic interactions to be small.

Exactly evaluating the square roots in S_i^+ and S_i^- cannot be done analytically. For that reason, they are expanded, such that the original spin Hamiltonian of Eq. (1.1) is approximated by a new Hamiltonian in expanded form. We refer to this expanded bosonic Hamiltonian as the spin wave (SW) Hamiltonian $\hat{\mathcal{H}}_{SW}$:

$$\hat{\mathcal{H}}_{SW} = \sum_{n=0}^{\infty} \hat{\mathcal{H}}^{(n)} \ . \tag{1.21}$$

In the above, $\hat{\mathcal{H}}^{(n)}$ contains only products of n bosonic creation or annihilation operators. Terms of increasing orders are proportional to increasing powers of $1/\sqrt{S}$:

$$\hat{\mathcal{H}}^{(n)} \sim S^{2-n/2} \ .$$

The term $\hat{\mathcal{H}}^{(0)}$ is a constant and corresponds to the classical ground-state energy $E_{cl} \sim S^2$. It is the same for all classically degenerate ground states. Provided that the SW expansion is made around a valid classical ground state, the first order term $\hat{\mathcal{H}}^{(1)}$ necessarily vanishes. Indeed, any classical ground state is at least a local minimum of the energy. Linear terms in bosonic operators would indicate an instability of the chosen spin configuration. Higher-order terms of even powers $\hat{\mathcal{H}}^{(2)}$, $\hat{\mathcal{H}}^{(4)}$ and so on, correspond to quantum corrections to the ground-state energy, proportional to increasing orders

of $1/S$. Terms of odd powers $\hat{\mathcal{H}}^{(3)}$, $\hat{\mathcal{H}}^{(5)}$ and so on, correspond to quantum corrections to the original classical spin orientations [9].

No information was given so far, about the classical ground-state spin configuration from which the SW expansion is made. Yet, if we aim at comparing the ground-state energies of different competing states, such information must appear somewhere in our derivations. This is explained in the next subsection.

1.4.1 On the validity of SW expansion

The point of using bosonic operators is to obtain a Hamiltonian of which we know how to find the eigenvalues and eigenstates. In other words, we want to have well-defined energy levels. Firstly, let me stress that this is only possible when linear terms in bosonic operators vanish. Such a condition is ensured by applying the Holstein-Primakoff transformation to *local* spin coordinates for each spin. Those local spin coordinates are defined such that the local z axis of a given spin $\mathbf{S}_i$ coincides with the orientation and direction of this spin in the classical ground state. The square roots in Eq. (1.20) are to be expanded only after this rotation to the local basis is made. This is precisely what is meant by "expanding the Hamiltonian around a classical ground state". Information about the specific spin configuration we started from is then contained in this rotation to the local coordinates.

Secondly, we want to be able to truncate the expanded Hamiltonian of Eq. (1.21) at a given desired order, so as to obtain a problem that can be solved with reasonable effort. For this truncation to be valid, one needs the higher-order terms beyond the truncation order to be vanishingly small. In other words, the expansion of the square roots in the Holstein-Primakoff transformation (see Eq. (1.20)) should be well-behaved. This is guaranteed if the expansion parameter is small, that is, if the following condition is satisfied:

$$\frac{n_i}{2S} \ll 1 \ . \tag{1.22}$$

This criterion is obviously always verified for very large S, which is why SWT is usually efficient in describing the behaviour of systems of large spins. From Eq. (1.22) however, it is clear that the reliability of a spin-wave derivation not only depends on the spin length S, but also on the n_i parameter, that is, the number of local spin-lowerings on a given site. For that reason, if n_i is very large, the SW expansion might be badly behaved, *even for large spins*. Oppositely, if n_i is very small, the SW expansion could be very efficient, *even for small spins*, including $S = 1/2$ [18].

Following the validity criterion set by Eq. (1.22), one wishes to construct the Holstein-Primakoff transformation of Eq. (1.20) in such a way, that the number n_i of elementary local spin-lowerings is small. This has to be true for each lattice site. Within SWT, it is assumed that the ordered state, after being dressed by quantum fluctuations, is not too far from the classical ground-state configuration. Under this assumption, n_i is small *if the z axis coincides with the classical orientation of the spin*

[9] Note that these odd terms vanish in a collinear ground state.

$\mathbf{S}_i$, which is precisely the case when working in the above-mentioned local spin coordinates. Therefore, not only is the transformation to local coordinates necessary for the SW derivation to have a physical meaning, but it also leads in many cases to a simple well-behaved expansion.

The way to compute the corrections associated to $\hat{\mathcal{H}}^{(n)}$ is of increasing complexity with increasing expansion order n. However, it is most common to stop at the harmonic approximation, that is, to neglect terms beyond $\hat{\mathcal{H}}^{(2)}$ in Eq. (1.21). Within this approximation, only the first quantum correction to the ground-state energy is considered. This correction is attributed to the quadratic Hamiltonian $\hat{\mathcal{H}}^{(2)}$ and is of order $1/S$ with respect to the classical ground-state energy. It generally gives good results for large spin values $S \geq 1$. This approximation is often referred to as *linear spin-wave theory*, as the correction is linear in $1/S$. Thus "harmonic" refers to the Hamiltonian, "linear" to the associated energy correction.

1.4.2 Linear spin-wave theory

The linear spin-wave theory (LSWT) consists in truncating the expanded SW Hamiltonian of Eq. (1.21) to second order, that is, throwing out all terms involving products of more than 2 bosonic operators. This gives:

$$\hat{\mathcal{H}}_{LSW} = \hat{\mathcal{H}}^{(0)} + \hat{\mathcal{H}}^{(1)} + \hat{\mathcal{H}}^{(2)} \ .$$

As any classical ground state is a local minimum of the energy, the term linear in bosonic operators $\hat{\mathcal{H}}^{(1)}$ vanishes.

It is more convenient to work in the reciprocal space (or $\mathbf{k}$-space), such that all relevant information is encoded in the first Brillouin zone, which has finite boundaries. For this reason, one applies a discrete Fourier transformation to the bosonic operators a_i, $a_i^\dagger$, and the SW Hamiltonian is expressed as a function of $a_\mathbf{k}$, $a_\mathbf{k}^\dagger$. Then the harmonic contribution to the Hamiltonian is generally written as follows:

$$\hat{\mathcal{H}}^{(2)} = \sum_\mathbf{k} \left\{ A_\mathbf{k} a_\mathbf{k}^\dagger a_\mathbf{k} - \frac{1}{2} B_\mathbf{k} \left(a_\mathbf{k}^\dagger a_{\text{-}\mathbf{k}}^\dagger + a_{\text{-}\mathbf{k}} a_\mathbf{k} \right) \right\} \ . \tag{1.23}$$

The coefficients $A_\mathbf{k}$ and $B_\mathbf{k}$ set the behavior of normal and anomalous terms in quadratic operators, respectively.

If $B_\mathbf{k}$ is non vanishing, the quadratic bosonic Hamiltonian is not diagonal. The $a_\mathbf{k}^\dagger$ spin-waves, made of local spin-lowerings $a_i^\dagger$, are thus not well-behaved excitations, and do not have a definite energy. They interact with their own vacuum, leading to spontaneous creation or annihilation of pairs of spin-flips of opposite momenta. In other words, the basis set by these local excitations is not a good basis to the quadratic Hamiltonian. Consequently, one cannot simply establish the ground state as the vacuum of these spin-lowerings, and the original classical ground state is not a true ground state of the Hamiltonian.

In order to determine the true ground state - up to harmonic approximation - we need to define a proper basis for the quadratic Hamiltonian, in which it is diagonal. New bosonic excitations $\beta_{\mathbf{k}}$, $\beta_{\mathbf{k}}^\dagger$ are thus defined through the canonical Bogolyubov transformation:

$$a_{\mathbf{k}} = u_{\mathbf{k}}\beta_{\mathbf{k}} + v_{\mathbf{k}}\beta_{\text{-}\mathbf{k}}^\dagger \ , \qquad \left[\beta_{\mathbf{k}}, \beta_{\mathbf{k}}^\dagger\right] = 1 \ . \tag{1.24}$$

Those new particles are defined so as to *not* interact with their own vacuum (cancellation of anomalous term). Then the ground state indeed corresponds to the vacuum of such well-behaved particles: the spin-waves (or magnons).

The quadratic Hamiltonian of Eq. (1.23) becomes diagonal in this new basis:

$$\hat{\mathcal{H}}^{(2)} = \sum_{\mathbf{k}} \epsilon_{\mathbf{k}} \left(\beta_{\mathbf{k}}^\dagger \beta_{\mathbf{k}} + \frac{1}{2} \right) + C \ , \tag{1.25}$$

where $\epsilon_{\mathbf{k}}$ is the harmonic spin-wave spectrum, and C is a constant term that is the same for all classically degenerate ground states. The ground state - relative to the classical ground state the expansion was started from - is now redefined as the vacuum of Bogolyubov particles, taking $\beta_{\mathbf{k}}^\dagger \beta_{\mathbf{k}} = 0$. The harmonic quantum correction to the ground-state energy is finally given by:

$$\boxed{\Delta E_q = \frac{1}{2} \sum_{\mathbf{k}} \epsilon_{\mathbf{k}} + C} \ . \tag{1.26}$$

Then the ground state that is selected by quantum fluctuations is the one with lowest zero-point motion of the spin-wave spectrum. It corresponds to the state with "most low-lying" spectrum, which in most cases coincides with the state having softest low-lying excitations. This is the *quantum order-by-disorder* phenomenon.

Take note that the vacuum of $\beta_{\mathbf{k}}^\dagger$ particles does not correspond to the vacuum of $a_{\mathbf{k}}^\dagger$ particles. In other words, we have in principle $n_i > 0$. For that reason, the staggered magnetization in the quantum ground state is lowered by quantum fluctuations: we recover the spin reduction effect discussed earlier.

1.5 Thesis outline

In the first part of this thesis, chapter 2 is devoted to the study of fractional magnetization plateaus in the kagome and pyrochlore antiferromagnets. Only nearest-neighbor Heisenberg interactions are considered. After an introduction to the topic and the method (section 2.1), I give the general form of the spin-wave Hamiltonian which is applicable to both lattices (section 2.2). Then, in sections 2.3 and 2.4 I specifically derive analytical expressions for the harmonic spin-wave spectrum of the kagome and the pyrochlore lattices, respectively. The magnetization curves, which are obtained from these spectra, are also shown. They exhibit the expected fractional magnetization plateaus for both systems. A discussion of the results, as well as a summary of the chapter, are given in section 2.5.

The second part of the thesis focuses on the study of order by disorder in the quantum fcc antiferromagnet. Once again, only nearest-neighbor Heisenberg interactions are considered [10]. Chapter 3 introduces frustration in this system. Then chapters 4 and 5 are dedicated to the results from *linear* spin-wave theory and *interacting* spin-wave theory, respectively.

In chapter 4, section 4.1 presents the ground-state selection operated by quantum fluctuations at zero temperature. The harmonic spin-wave spectra are given for the competing classical states, and corresponding quantum energy corrections are computed. At this harmonic level the AF3 state is selected by quantum OBD at $T = 0$. Then, section 4.2 focuses on the thermal selection due to population of low-lying magnons. The AF1 state is selected by thermal OBD at $T > 0$. The different selections operated by the two types of OBD induce a competition effect between the two, leading to a first-order phase transition at low temperatures. Concluding remarks are given in section 4.3, along with a summary of the chapter.

In chapter 5, section 5.1 is devoted to the inclusion of interactions in the spin-wave derivation. The spectra for the two competing states (AF1 and AF3), are obtained analytically. In section 5.2, the quantum OBD at $T = 0$ is being addressed again, with now inclusions of the effects of interactions. After self-consistent renormalization of the Bogolyubov vacuum, new values for the quantum energies of the two states are obtained. After inclusion of interactions, the AF1 state becomes the ground state selected by quantum fluctuations at $T = 0$ for spin values $S \lesssim 10$. In section 5.3, thermal OBD is looked at. The ground-state selection is unchanged compared to the result without interactions and remains the AF1 state. As a result, no competition between quantum and thermal OBD is found anymore. A discussion about the peculiarities of both spin-wave theory and OBD in that system, as well as a summary of the chapter, are given in section 5.4.

Finally, chapter 6 summarises and concludes all the findings of the thesis.

[10] There is no interaction with an external magnetic field in that case.

Part I

Chapter 2

Fractional magnetization plateaus in the kagome and pyrochlore antiferromagnets

I apply spin-wave theory to the canted states that are surrounding the plateau phase, and restrict to harmonic order. Although diagonalization of the spin-wave Hamiltonian in the kagome and pyrochlore lattices is in principle a 3- and 4-dimensional eigenvalue problem, it can be reduced to a quadratic equation in both systems. This allows us to obtain full analytical expressions for the harmonic spin-wave spectra.

The first quantum correction to the ground-state energies of the canted states is obtained by computing the zero-point motion of the harmonic magnons. The magnetization in each canted state is computed as well, by differentiating the corrected ground-state energy with respect to magnetic field. The extent of the plateau is then determined by intersecting those curves with the expected fractional magnetization, which permits to obtain full magnetization curves for the two systems.

The curves exhibit a clear magnetization plateau, both for the kagome and pyrochlore lattices. The plateau width decreases with spin length, as expected provided that such magnetization plateaus are a quantum feature. The plateau width for the kagome lattice compares well with available numerical data from various techniques, for $S > 1/2$.

2.1 Introduction

The magnetization process of frustrated magnetic insulators offers a striking example of their inclination to challenge the established classical picture of magnetism. At zero magnetic field, spins in an AFM are arranged in such a way that there is no net magnetization. Local magnetic moments interact with an external magnetic field $\mathbf{H}$ via the Zeeman energy:

$$\hat{\mathcal{H}}_Z = -g\mu_B \mathbf{H} \cdot \sum_i \mathbf{S}_i \ , \tag{2.1}$$

where g is the gyromagnetic ratio and μ_B is the Bohr magneton. In the rest of this chapter, I absorb these constants in the magnetic field variable $\mathbf{H}$ to ease reading.

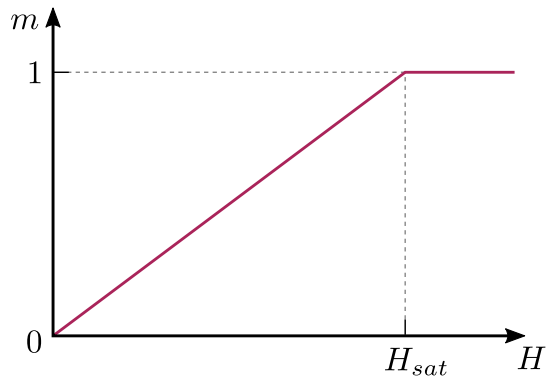

Figure 2.1: *Classical magnetization process of a Heisenberg antiferromagnet*

Classically, spins behave as 3-dimensional vectors and smoothly cant along the field direction as its strength is increased, in order to gain energy through this Zeeman interaction. When only Heisenberg interactions are considered, this leads to a net magnetization $\mathbf{M}$ along the field direction which is linear in magnetic field up to saturation, as depicted in Fig. (2.1). At saturation, all spins are polarized along the field and we have $\mathbf{M}_{sat} = NS\hat{\mathbf{e}}_{z_0}$, where N is the total number of spins in the lattice, S is the size of the magnetic moments, and by convention we took the z_0 axis oriented along the field direction. It is convenient to define the following dimensionless magnetization per site m:

$$m = \frac{M}{M_{sat}} \ , \tag{2.2}$$

such that at saturation we have $m = 1$, see Fig. (2.1).

This simple picture does not hold once the effects of quantum fluctuations are incorporated. Indeed, the curve acquires curvature due to the gradual suppression of quantum fluctuations, already in non frustrated systems [29]. More spectacular features may arise when geometric frustration is at play, due to the large classical ground-state degeneracy. The magnetic field acts as an external handle to trigger competition between many - not necessarily classically stable - states which become available at different field values. As a result, various phase transitions occur along the magnetization process. This leads to the appearance of anomalies in the magnetization curve, like discontinuous slope of the magnetization, or more impressive magnetization jumps or magnetization plateaus, see [30] for example. The latter are the focus of the present chapter.

2.1.1 What are fractional magnetization plateaus?

A fractional magnetization plateau appears as a constant rational value m_p of the magnetization over a finite field interval, as shown in the purple curve of Fig. (2.2). It originates from the stabilization of a given ground state with corresponding magnetization $\langle \hat{S}^z_{tot} \rangle = m_p \cdot NS$, which is gapped to spin excitations over the field range [31].

In Ising systems, plateaus appear in a most intuitive manner. Indeed, consider that the field is applied along the Ising axis and is continuously increased. Then, as soon as the energy gained from the Zeeman term by flipping a spin overcomes the corresponding energy cost from the exchange interaction, it becomes energetically favorable to flip the whole fraction of equivalent spins. Consequently, the magnetization jumps from a constant value to another. In the case where we have further-neighbor interactions, this leads to magnetization plateaus. There is no intermediate phase between successive plateaus, and the magnetization grows in a staircase fashion (see blue curve in Fig. (2.2)). Such Ising plateaus have been observed experimentally on the metallic compound TmB_4, in which magnetic ions lie on a Shastry-Sutherland lattice [32–35]. In another recent work, a plateau at half-saturation was observed in the stacked triangular Ising antiferromagnet $Fe_{1/3}NbS_2$ [36].

Contrary to Ising spins, Heisenberg spins are allowed to cant towards the field to gain energy. Thus, in a simple classical picture, there is in principle no reason for the magnetization not to be smoothly increasing with magnetic field, as shown on Fig. (2.1). Yet magnetization plateaus also appear in Heisenberg spin systems. Both the nature of the plateau states and the mechanisms leading to their appearance are diverse.

In most cases the plateau state corresponds to a collinear spin arrangement along the field direction. The magnetization m_p is then directly related to the fraction of down-pointing spins in the lattice. Such plateaus were predicted for example in the 1D Heisenberg spin-chains with next-nearest-neighbor interactions [37]. More generally, fractional collinear spin arrangements are typically possible in geometrically frustrated lattices [38]. Then m_p is connected to the number of down-pointing spins by frustrated block. A fractional plateau appears if the corresponding state has lowest energy over a finite field range.

The appearance of a collinear plateau may be induced by a purely classical process, such as thermal order by disorder (ObD) [39] or spin-lattice coupling [40]. Plateaus can also originate from the quantum ObD effect, where quantum fluctuations stabilize the collinear structure over a field range that exceeds its classical stability point in field, if any. This phenomenon is fostered by the presence of a larger number of soft modes in the spin wave spectrum for such collinear states, compared to non-collinear ones [10]. This is directly related to quantum fluctuations acting in favor of collinear states in general, as mentioned in the introduction chapter. Contrary to canted states, which spontaneously break the rotational symmetry around the field direction, these collinear states preserve the symmetry of the Hamiltonian. Consequently, they are gapped to

magnetic excitations [14, 31]. Their magnetization m_p thus remains constant over the field range where the gap is finite. In general, the states surrounding the plateau are canted states, in which the magnetization smoothly increases with H, as depicted by the purple curve in Fig. (2.2).

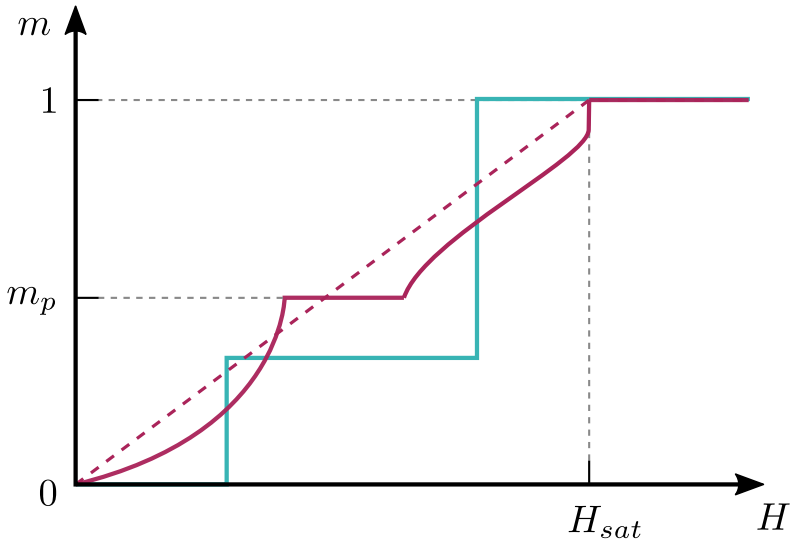

Figure 2.2: *Magnetization processes exhibiting fractional plateaus, for Ising (blue curve) and Heisenberg (dark red curve) systems. The dashed dark red reproduces the classical magnetization curve.*

Collinear plateau states stabilized by quantum ObD are semiclassical, in the sense that they can be viewed as a classical collinear state "dressed" by quantum fluctuations. They were originally studied in the context of the triangular Heisenberg AFM [14]. Later, plateaus were predicted to appear in a variety of frustrated lattices from geometrical arguments [16, 38, 39]. It is such plateaus that we wish to investigate in the present work. Magnetization curves have been extensively studied through a variety of numerical and theoretical techniques [14, 30, 41–48]. In this chapter, we use harmonic spin-wave theory (LSWT) to study the fractional magnetization plateaus appearing at $m = 1/3$ and $m = 1/2$ of saturation value in the 2D kagome and the 3D pyrochlore Heisenberg AFMs, respectively.

We only addressed semiclassical plateaus, but take note that plateau state itself can be of fully quantum nature. For example, quantum plateau states have been proposed int the form of crystals of localized magnons in the frustrated kagome lattice with $S = 1/2$ [43, 44, 49–52]. Such states involve locally resonating spin-flips and have no classical counterpart, which makes them impossible to study by using SWT.

2.1.2 Plateaus in the kagome and pyrochlore antiferromagnets

Both kagome and pyrochlore lattices have a low connectivity due to their corner-sharing structure (of triangles and tetrahedra), which leads to an extensive degeneracy of their classical ground state at all fields below saturation [53–55]. This feature makes them archetypal examples of highly frustrated magnets. There is extensive literature devoted to the investigation of their spin-liquid ground states in zero field [56, 57]. Their structure allows for simple fractional collinear states, which, as stated above, can be stabilized as plateaus.

The kagome Heisenberg AFM with only nearest-neighbor interactions is a well-known example of a 2D frustrated magnet. A plateau at $m = 1/3$ of full saturation is expected to be present for all spin values from order-by-disorder arguments [38]. It was already found numerically in 2001 from exact diagonalization by Hida [42]. In the spin-1/2 case, several other plateaus have been predicted numerically, in particular at $m = 5/9$ and $m = 7/9$ [30, 43, 44, 48, 58, 59]. The $m = 7/9$ plateau in the spin-1/2 case is actually a particular instance of the plateau appearing at $m = 1 - 1/(9S)$, which has been predicted analytically [49]. The state within the plateau is a crystalline arrangement of independent localized magnons, of which the wave function can be exactly constructed [49, 60]. The energy of these localized magnons becomes negative right below the saturation field $H_{\rm sat}$, hence, their condensation in a close-packed structure at $H \lesssim H_{\rm sat}$ leads to a finite magnetization jump from the plateau to full saturation [43, 49–51, 61]. Actually, the $m = 5/9$ and $m = 1/3$ plateaus can also be attributed to such a magnon crystal structure in the spin-1/2 case [30, 44, 52]. Finally, a $m = 1/9$ plateau corresponding to the stabilization of a purely quantum state is also expected for $S = 1/2$ [30].

On the experimental side, difficulties to engineer undistorted compounds with satisfying 2-dimensionality prevent one from obtaining very clear evidence of plateaus. There exists nevertheless an appreciable number of relevant kagome compounds which appear to exhibit the 1/3-plateau [62–67]. Note that the Cd-kapellasite studied in [66] exhibits a very large number of plateaus, which the authors attribute all to magnon crystals sitting on a large 12 sites unit cell.

Another well-known example of geometrical frustration is the nearest-neighbor Heisenberg model on a pyrochlore lattice. Its highly frustrated nature was already recognized by Anderson in 1956 in the case of Ising spins [68]. A fractional plateau at $m = 1/2$ the saturation value is expected to be stabilized by quantum fluctuations around its classical stability field $H/H_{sat} = 1/2$ [38]. It corresponds to the collinear up-up-up-down ($uuud$) structure, where on each tetrahedron of the lattice, 3 spins are aligned to the field, while the fourth one is antiparallel to it, resulting in the fractional half-magnetization. On the one hand, the high dimensionality makes it almost impossible to conduct numerical studies on such a lattice. On the other hand, it presents the advantage of being much more accessible experimentally. Indeed, progresses in the achievable magnetic field intensities made possible the observation of the half-magnetization plateau on several pyrochlore magnets. In particular, many Chromium-

based spinels (ACr_2O_4) have been reported to exhibit a very large 1/2 magnetization plateau [69–78], although the robust plateaus in these compounds is probably stabilized by strong magnetoelastic coupling leading to an effective biquadratic exchange term in the Hamiltonian[40, 71, 79]. Some recent experiments also found magnetization plateau in breathing pyrochlore compounds [80, 81]. Motivated by these experimental and numerical results, we wish to investigate the $m = 1/3$ and $m = 1/2$ plateaus in the kagome and pyrochlore AFMs.

2.1.3 Classical ground-state degeneracy

The Hamiltonian of a nearest-neighbor Heisenberg antiferromagnet (AFM) in a magnetic field is given by:

$$\hat{\mathcal{H}} = J \sum_{\langle i,j \rangle} \mathbf{S}_i \cdot \mathbf{S}_i - \mathbf{H} \cdot \sum_i \mathbf{S}_i \ . \tag{2.3}$$

where $\langle i, j \rangle$ sums over pairs of nearest-neighbors sites i and j, $J > 0$ is the nearest-neighbor exchange interaction and $\mathbf{H} = H\hat{\mathbf{e}}_{z_0}$ is the applied magnetic field. Both the kagome and pyrochlore lattices can be seen as lattices of elementary corner-sharing *frustrated blocks*, each of these blocks being composed of n spins. The elementary block is a triangle ($n = 3$) in the case of the kagome lattice, and a tetrahedron ($n = 4$) in the pyrochlore lattice. The Hamiltonian of Eq. (2.3) can then be rewritten as a sum over these blocks as follows:

$$\hat{\mathcal{H}} = \sum_b \left(J \sum_{(i,j)\in b} \mathbf{S}_i \cdot \mathbf{S}_j - \frac{1}{2} \mathbf{H} \cdot \mathbf{S}_b \right) \ , \tag{2.4}$$

where the b index runs over all triangles (tetrahedra) of the kagome (pyrochlore) lattice, and we defined the local spin variable $\mathbf{S}_b$ as the total spin on a given block:

$$\mathbf{S}_b = \sum_{i\in b} \mathbf{S}_i \ . \tag{2.5}$$

The 1/2 factor in front of the Zeeman term accounts for the fact that each spin in the lattice is shared by two elementary blocks, due to the corner-sharing nature of the two lattices. Classically, spins are treated as vectors of fixed length S in real space, and the following relation holds:

$$\sum_{(i,j)\in b} \mathbf{S}_i \cdot \mathbf{S}_j = \frac{1}{2} \left(\mathbf{S}_b^2 - nS^2 \right) \ . \tag{2.6}$$

Substituting the above relation into Eq. (2.4), and using the fact that the total number of blocks is given by $2N/n$, where N is the total number of lattice sites, one obtains:

$$\mathcal{H}_{\text{cl}} = \frac{J}{2} \sum_b \left(\mathbf{S}_b - \frac{\mathbf{H}}{2J} \right)^2 - NJS^2 - N\frac{H^2}{4nJ} \ . \tag{2.7}$$

Minimizing $\mathcal{H}_{\rm cl}$ with respect to $\mathbf{S}_b$ leads to the following local constraint on each block:

$$\mathbf{S}_b = \frac{\mathbf{H}}{2J} \ . \tag{2.8}$$

This constraint needs to be satisfied simultaneously *on all blocks of the lattice* to minimize the Hamiltonian. Due to the low connectivity of the blocks in the kagome and pyrochlore lattices [55], many different classical spin configurations do meet this requirement. Actually, one can even go from a given classical ground state to the other through completely *local* excitations. As a result, the kagome and pyrochlore antiferromagnets not only are classically degenerate, but exhibit an *extensive classical ground-state degeneracy*, meaning that the classical ground-state manifold grows with lattice size [53, 82, 83]. They are therefore highly frustrated, which explains that they are two canonical examples of quantum spin liquids in zero magnetic field.

Classical ground-state energy and susceptibility

In any classical ground-state configuration, the local constraint of Eq. (2.8) is verified on each frustrated block. Then obviously, increasing the magnetic field induces a progressive canting of the spins towards the field direction - regardless of *how* the constraint is satisfied. The total classical magnetization thus increases linearly with H. Saturation of the magnetization is reached when all spins are aligned ferromagnetically along the field direction, such that $\mathbf{S}_b = nS\hat{\mathbf{e}}_{z_0}$. This implies naturally the following expression for the saturation field $H_{\rm sat}$:

$$H_{\rm sat} = 2nJS \ . \tag{2.9}$$

It is useful to define the normalized field variable h:

$$h = \frac{H}{H_{\rm sat}} \ , \tag{2.10}$$

such that the value for the saturation field is always given by $h_{\rm sat} = 1$, irrespective of the spin length S and the strength of exchange interaction J. The classical ground-state energy $E_{\rm cl}$ as a function of h is then given by substituting Eq. (2.8) in Eq. (2.7):

$$E_{\rm cl} = -NJS^2(1 + nh^2) \ . \tag{2.11}$$

The classical magnetization per site $m_{\rm cl}$ is linear in field and given by:

$$m_{\rm cl} = -\frac{1}{N}\frac{\partial E_{\rm cl}}{\partial H} = hS = \chi_{\rm cl} H \ . \tag{2.12}$$

The slope corresponds to the constant classical susceptibility $\chi_{\rm cl}$:

$$\chi_{\rm cl} = \frac{1}{2nJ} \ . \tag{2.13}$$

Competing states

Already at the level of a single block (triangle or tetrahedron), the constraint of Eq. (2.8) can be verified in many different ways. For example, the classical degeneracy is parametrized by 3 continuous degrees of freedom for a single triangle. Only one of these degrees of freedom is related to the U(1) symmetry of the Hamiltonian around the field direction, such that the two others remain as an accidental degeneracy. This accidental degeneracy is of even larger dimensionality in the case of a tetrahedral block.

Let us now assume that we know the orientations of each spin on one given triangle. In a triangular lattice, this is sufficient to know the spins orientations in the whole lattice. This is due to the fact that a triangular block shares two spins with each of its edge-sharing neighboring blocks. The kagome lattice, however, has lower connectivity due to its corner-sharing nature. Indeed, only one spin is shared between two adjacent blocks. Therefore, even if the spins orientations are known on one given triangle, this does not provide enough information to know what should be the spins orientations in the neighboring triangles. In principle, those spins orientations might be different from one triangle to the next, except of course for the spin that is shared between the two. This is at the origin of the extensive classical ground-state degeneracy discussed above. Note that in the case of the pyrochlore lattice, this degeneracy is even larger as the system is less constrained.

2.1.4 Degeneracy lifting: coplanar states

The spin-wave expansion relies on a classical ground state to expand around. Unfortunately, as we just saw, the classical ground states of the systems we wish to study are far from being uniquely defined. Fortunately, the question of order by disorder in the kagome and pyrochlore antiferromagnets in field has already been addressed before, which gives us guidance in the choice of classical starting points to our spin-wave calculations.

As said in the introduction, quantum fluctuations lift the infinite degeneracy and select a ground state from the zero-point motion of the spin-waves (see Eq. (1.26)). This selection acts in favor of collinear and coplanar spin structures. In such coplanar states, all the spins of the lattice are in the same plane, which also contains the magnetic field $\mathbf{H}$, and they progressively cant towards it as the strength of the field is increased. Since we are studying the quantum spin systems, we limit our study to coplanar spin structures. As a result, only one parameter is needed to give the orientation of a given spin $\mathbf{S}_i$: the canting angle θ_i with respect to the magnetic field direction z_0. It is straightforward to show, from the constraint of Eq. (2.8), that the following relations

hold on each frustrated block in a coplanar classical ground state:

$$\sum_{i\in b} \cos\theta_i = nh \ , \tag{2.14}$$

$$\sum_{i\in b} \sin\theta_i = 0 \ . \tag{2.15}$$

These relations will be useful throughout the whole analytical derivation of the spin-wave spectrum.

Imposing coplanarity restricts a lot the classical ground-state manifold. For example, at the level of one triangular unit, the accidental classical degeneracy gets reduced to only one continuous degree of freedom. Furthermore, in the kagome lattice, all coplanar states are such that the spins orientations in each triangle are the same. There are therefore only 3 different spin orientations throughout the whole lattice. The way these 3 orientations are placed in each triangle may however vary, and consequently the degeneracy remains extensive. Indeed, there are exponentially many such possible coverings [53]. In the pyrochlore lattice, the situation is more complicated. We restrict to the same type of states, in which only 4 different spin orientations are present in the lattice, and each tetrahedron contains one spin of each orientation.

If there is long-range order, the ordering wave-vector $\mathbf{Q}$ defines how adjacent blocks are "rotated", and thus the periodicity of the lattice and size of the magnetic unit cell. The ordered state that has the smallest magnetic unit cell is the $\mathbf{Q} = \mathbf{0}$ state, where adjacent blocks are identical to each other. In this situation, the magnetic unit cell is exactly one block and there are n sublattices, corresponding to the different spin orientations. In both the kagome and pyrochlore lattices, the canting coplanar states that will serve as starting points to the spin-wave derivation will be some sort of Y or V states with $\mathbf{Q} = \mathbf{0}$, as we will see later in more details.

2.1.5 Method

We use linear spin-wave theory (LSWT) to obtain the first quantum correction ΔE_{q} to the ground-state energies of the Y and V states. This correction is attributed to the zero-point motion of the spin-waves, see Eq. (1.26). Following [29], the magnetization curve is obtained for the canted states from the standard expression:

$$M = -\frac{\partial E_{\mathrm{gs}}}{\partial H} \ , \tag{2.16}$$

where $E_{\mathrm{gs}} = E_{\mathrm{cl}} + \Delta E_{\mathrm{q}}$ is the corrected ground-state energy and H is the strength of the external magnetic field. One does not need to go beyond the harmonic level to find the plateau. Indeed, as was done for the triangular lattice in [46], the boundaries of the plateaus are taken as the intersections of the magnetizations of the surrounding Y and V states with the expected fractional value m_p. These states being classical ground states of the Hamiltonian in the corresponding field ranges, their magnon spectra remain real

even in the harmonic approximation. The full magnetization curves are then obtained solely from LSWT for both geometries.

The spin wave spectrum $\epsilon_{\mathbf{k}}$ is required to compute the magnetization from Eqs. (1.26, 2.16). Somewhat counter intuitively, the large degree of frustration of the corner-sharing kagome and pyrochlore lattices actually leads to a simplification of the diagonalization of the LSWT Hamiltonian, compared to the less degenerate edge-sharing triangular lattice. This is due to the presence of full flat zero-energy bands in the harmonic spectra. They are a signature of the extensive degeneracy of the classical ground state mentioned above. These flat bands allow us to reduce the diagonalization to an equation of degree 2. As a result, we obtain *fully analytical expressions* for the two remaining dispersive bands of the harmonic spin-wave spectra of the kagome and pyrochlore AFMs.

2.2 General spin-wave derivation

The spin-wave derivation can be performed in quite a similar manner in the kagome and pyrochlore lattices. Therefore, in this section, I explain this derivation in terms that remain general enough to be suitable for both. This is made possible by the fact that the two lattices share similar geometrical properties. They are constituted of corner-sharing frustrated blocks of n sites [1], and each spin thus has $2(n-1)$ nearest neighbors.

A first property of such lattices is the following: nearest-neighbor bonds are center-symmetric with respect to a given site. Take a given spin $\mathbf{S}_i$ located at position $\mathbf{R}_i$ in either lattice. Then for any of its surrounding nearest-neighbor sites located at position $\mathbf{R}_i + \boldsymbol{\delta}$, there exists another nearest-neighbor site located at position $\mathbf{R}_i - \boldsymbol{\delta}$, as is shown on Fig. (2.3).

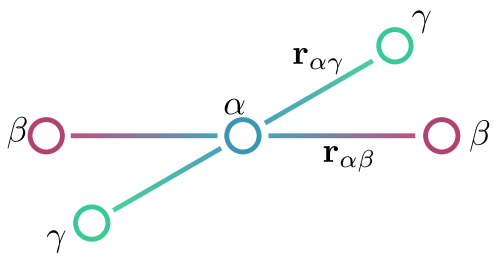

Figure 2.3: *Center-symmetric lattice*

As said previously, we focus on the case $\mathbf{Q} = \mathbf{0}$, such that the magnetic unit cell is exactly one block (triangle or tetrahedron). The spin structure is a periodic repetition of such blocks along the lattice translation vectors, each block having identical spin configuration. The n sites within a block can in principle all have a different orientation. It is then convenient to define n sublattices with n corresponding bosonic modes (one for each site). In the following, the bosonic mode - or equivalently the sublattice - will be identified by the index α, with $\alpha \in \{a, b, c, \dots\}$. Since sublattices and bosonic modes coincide, in the remainder of this chapter I will refer to both indifferently. With this definition, all the spins in a same sublattice have the same orientation. A given spin site is then completely specified by its position $\mathbf{R}$ and its sublattice index α: $\mathbf{S}_i = \mathbf{S}_{\mathbf{R},\alpha}$.

The $\mathbf{Q} = \mathbf{0}$ order implies a further symmetry. Indeed, each spin $\mathbf{S}_{\mathbf{R},\alpha}$ belonging to sublattice α has $(n-1)$ pairs of nearest-neighbor spins from all other $(n-1)$ sublattices $\beta \neq \alpha$. Such pairs are located in opposite symmetric positions with respect to $\mathbf{R}$: $\mathbf{R}+\mathbf{r}_{\alpha\beta}$ and $\mathbf{R}-\mathbf{r}_{\alpha\beta}$. This is schematized on Fig. (2.3). These symmetries allow us to reformulate the Hamiltonian of Eq. (2.3) as follows:

$$\hat{\mathcal{H}} = J \sum_{\mathbf{R}_c} \sum_{\alpha,\beta}^{\neq} \mathbf{S}_{\mathbf{R},\alpha} \cdot \left(\mathbf{S}_{\mathbf{R}+\mathbf{r}_{\alpha\beta},\beta} + \mathbf{S}_{\mathbf{R}-\mathbf{r}_{\alpha\beta},\beta} \right) - H \sum_{\mathbf{R}_c} \sum_{\alpha} S^{z_0}_{\mathbf{R},\alpha} \,, \tag{2.17}$$

where the sum over $\mathbf{R}_c$ spans the positions of the unit cells. The vector $\mathbf{r}_{\alpha\beta}$ is the nearest-neighbor vector that links a spin of sublattice α to one of its nearest neighbors belonging to the sublattice β. We will now show how to obtain a general expression for the LSWT Hamiltonian.

[1] We remind the reader that $n = 3$ and $n = 4$ in the kagome and pyrochlore case, respectively.

2.2.1 Spin-wave matrix in reciprocal space

We use the spin-wave formalism described in appendix A. First, we apply the rotation to local spin coordinates (x, y, z) given by Eq. (A.7) to Eq. (2.17). Then, the Holstein-Primakoff transformation of Eq. (1.20) is applied to the spin operators in this rotated basis. The square root is expanded in the fashion of Eqs. (A.4, A.5). Then one obtains the expression for a given scalar product between two spins. As an example, the expression in terms of bosonic operators is given below for a pair of spins belonging to sublattices a and b, keeping only up to quadratic terms:

$$\begin{aligned}\mathbf{S}_{\mathbf{R},a} \cdot \mathbf{S}_{\mathbf{R}',b} =& S^2 \cos\theta_{ab} + \frac{S\sqrt{2S}}{2} \sin\theta_{ab} \left(b_{\mathbf{R}'} + b^\dagger_{\mathbf{R}'} - a_{\mathbf{R}} - a^\dagger_{\mathbf{R}} \right) \\ &+ \frac{S}{2} \left(\cos\theta_{ab} - 1\right) \left(a_{\mathbf{R}} b_{\mathbf{R}'} + a^\dagger_{\mathbf{R}} b^\dagger_{\mathbf{R}'} \right) \\ &+ \frac{S}{2} \left(\cos\theta_{ab} + 1\right) \left(a_{\mathbf{R}} b^\dagger_{\mathbf{R}'} + a^\dagger_{\mathbf{R}} b_{\mathbf{R}'} \right) \\ &- S \cos\theta_{ab} \left(a^\dagger_{\mathbf{R}} a_{\mathbf{R}} + b^\dagger_{\mathbf{R}'} b_{\mathbf{R}'} \right) \ ,\end{aligned} \tag{2.18}$$

where $\theta_{ab} = \theta_a - \theta_b$ is the opening angle between two spins of sublattices a and b. Similar expressions are obtained for each type of scalar product involving each possible pairs of different sublattices. We also have, for a spin of sublattice a for example:

$$\begin{aligned}S^{z_0}_{\mathbf{R},a} =& S \cos\theta_a - \frac{\sqrt{2S}}{2} \sin\theta_a (a_{\mathbf{R}} + a^\dagger_{\mathbf{R}}) \\ &- \cos\theta_a a^\dagger_{\mathbf{R}} a_{\mathbf{R}} \ .\end{aligned} \tag{2.19}$$

Similar expressions are obtained for any type of sublattice. Substituting these expressions into Eq. (2.17) leads to the expanded form of the LSWT Hamiltonian $\hat{\mathcal{H}}_{\text{LSW}}$:

$$\hat{\mathcal{H}}_{\text{LSW}} = \hat{\mathcal{H}}^{(0)} + \hat{\mathcal{H}}^{(1)} + \hat{\mathcal{H}}^{(2)} \ . \tag{2.20}$$

In both Eq. (2.18) and Eq. (2.19), The first and second terms of first line are of zeroth and first order, respectively, while the remaining lines are of second order. By construction of SWT, $\hat{\mathcal{H}}^{(0)}$ corresponds to the classical ground-state energy. Indeed, from Eqs. (2.18, 2.19), we have:

$$\hat{\mathcal{H}}^{(0)} = J \sum_{\mathbf{R}_c} \sum_{\alpha,\beta}^{\neq} 2S^2 \cos\theta_{\alpha\beta} - HS \sum_{\mathbf{R}_c} \sum_{\alpha} \cos\theta_\alpha \ . \tag{2.21}$$

In any classical ground state, the local constraint of Eq. (2.8) is verified. Substituting the resulting relations of Eqs. (2.14,2.15) in Eq. (2.21), we obtain:

$$\hat{\mathcal{H}}^{(0)} = -NJS^2(1 + nh^2) = E_{\text{cl}} \ , \tag{2.22}$$

where we used the fact that the total number of magnetic unit cells N_c is given by $N_c = N/n$. This expression corresponds to the classical ground-state energy $E_{\rm cl}$ given by Eq. (2.11).

The SW expansion being done about a classical ground state, $\hat{\mathcal{H}}^{(1)}$ naturally vanishes. The first quantum contribution to the ground-state energy comes from the quadratic part of the Hamiltonian $\hat{\mathcal{H}}^{(2)}$. Substituting Eq. (2.18) and Eq. (2.19) into Eq. (2.17), and retaining only the terms that are quadratic in bosonic operators, we obtain $\hat{\mathcal{H}}^{(2)}$. The bosonic operators are Fourier transformed following Eq. (A.10). We remind the reader of the relation:

$$\sum_{\mathbf{R}_c} e^{i\mathbf{k}\cdot\mathbf{R}} = N_c \cdot \delta_{\mathbf{k},\mathbf{0}} \ , \tag{2.23}$$

from which we obtain the phase factors associated to the various quadratic terms of the harmonic spin-wave Hamiltonian in $\mathbf{k}$-space. As there are more than one sublattice, it becomes convenient to express the quadratic Hamiltonian in the matrix form of Eq. (A.11), which we repeat below:

$$\hat{\mathcal{H}}^{(2)} = \frac{1}{2}\sum_{\mathbf{k}} \left(\hat{X}^\dagger_{\mathbf{k}} H_{\mathbf{k}} \hat{X}_{\mathbf{k}} - \mathrm{Tr}[A_{\mathbf{k}}] \right) \ , \tag{2.24}$$

where $\hat{X}^\dagger_{\mathbf{k}}$ is a row vector containing all the Holstein-Primakoff bosonic operators:

$$\hat{X}^\dagger_{\mathbf{k}} = \left(a^\dagger_{\mathbf{k}}, b^\dagger_{\mathbf{k}}, ..., a_{\text{-}\mathbf{k}}, b_{\text{-}\mathbf{k}}, ... \right) \ . \tag{2.25}$$

In Eq. (2.24), $H_{\mathbf{k}}$ is a $(2n) \times (2n)$ matrix with the following block structure:

$$H_{\mathbf{k}} = \begin{pmatrix} A_{\mathbf{k}} & -B_{\mathbf{k}} \\ -B_{\mathbf{k}} & A_{\mathbf{k}} \end{pmatrix} \ . \tag{2.26}$$

$A_{\mathbf{k}}$ and $B_{\mathbf{k}}$ are $n \times n$ matrices, containing the coefficients in front of the diagonal and anomalous terms of the Hamiltonian, respectively. The coefficients of the matrices $A_{\mathbf{k}}$ and $B_{\mathbf{k}}$ are explicitly given by:

$$\begin{aligned} A^{\alpha\alpha}_{\mathbf{k}} &= 2JS \ , & B^{\alpha\alpha}_{\mathbf{k}} &= 0 \ , \\ A^{\alpha\beta}_{\mathbf{k}} &= JS\left(1+\cos\theta_{\alpha\beta}\right)\cos(\mathbf{k}\cdot\mathbf{r}_{\alpha\beta}) \ . & B^{\alpha\beta}_{\mathbf{k}} &= JS\left(1-\cos\theta_{\alpha\beta}\right)\cos(\mathbf{k}\cdot\mathbf{r}_{\alpha\beta}) \ . \end{aligned} \tag{2.27}$$

Then the trace of $A_{\mathbf{k}}$ is given by:

$$\mathrm{Tr}[A_{\mathbf{k}}] = 2nJS = H_{\rm sat} \ . \tag{2.28}$$

Finally, summing the classical ground-state energy of Eq. (2.22) and the harmonic quantum corrections given by Eqs. (2.24 - 2.28), we obtain the full LSW Hamiltonian in momentum space:

$$\hat{\mathcal{H}}_{\rm LSW} = \hat{\mathcal{H}}^{(0)} + \hat{\mathcal{H}}^{(2)} = -NJS(S+1) - NJS^2h^2n + \frac{1}{2}\sum_{\mathbf{k}} \hat{X}^\dagger_{\mathbf{k}} H_{\mathbf{k}} \hat{X}_{\mathbf{k}} \ . \tag{2.29}$$

2.2.2 Diagonalization and spin-wave spectra

The quadratic Hamiltonian of Eq. (2.24) is not diagonal in the basis of the bosonic operators defined in the Holstein-Primakoff transformation. As a consequence, one needs to diagonalize it in order to work with well-behaved quasiparticles, which will propagate on the whole lattice and have a definite energy: the spin-waves. This diagonalization is done through the Bogolyubov transformation, of which the detailed procedure is given in appendix A. After the transformation, the quadratic part of the Hamiltonian has a diagonal form:

$$\frac{1}{2}\sum_{\mathbf{k}} \hat{X}_{\mathbf{k}}^{\dagger} H_{\mathbf{k}} \hat{X}_{\mathbf{k}} = \frac{1}{2}\sum_{\mathbf{k}} \hat{Y}_{\mathbf{k}}^{\dagger} \Omega_{\mathbf{k}} \hat{Y}_{\mathbf{k}} \ , \tag{2.30}$$

where $\Omega_{\mathbf{k}}$ is a diagonal matrix, its elements being the (doubly-degenerate) harmonic spin-wave modes $\epsilon_{i\mathbf{k}}$ ($i \in \{1, .., n\}$). The vectors $\hat{Y}_{\mathbf{k}}^{\dagger}$ and $\hat{Y}_{\mathbf{k}}$ contain the new bosonic operators:

$$\hat{Y}_{\mathbf{k}}^{\dagger} = \left(\beta_{\mathbf{k},1}^{\dagger}, \beta_{\mathbf{k},2}^{\dagger}, ..., \beta_{\text{-}\mathbf{k},1}, \beta_{\text{-}\mathbf{k},2}, ...\right) \ . \tag{2.31}$$

In order to find expressions for the spin-wave modes $\epsilon_{i\mathbf{k}}$, one needs to apply the canonical Bogolyubov transformation. It is used to diagonalize the system under the constraint of preserving bosonic commutation relations for newly defined particles $\beta_{\mathbf{k}}$.

As is shown in appendix A, this $2n \times 2n$ diagonalization procedure can be reduced to a much simpler, $n \times n$ eigenvalue problem:

$$\left|\Delta_{\mathbf{k}}\Sigma_{\mathbf{k}} - \epsilon^2 \mathbb{I}_n\right| = 0 \ , \quad \text{with} \ \begin{cases} \Delta_{\mathbf{k}} = & A_{\mathbf{k}} - B_{\mathbf{k}} \\ \Sigma_{\mathbf{k}} = & A_{\mathbf{k}} + B_{\mathbf{k}} \end{cases} \ . \tag{2.32}$$

This is due to the block structure of $H_{\mathbf{k}}$ (see Eq. (2.26)). The matrix elements of $\Delta_{\mathbf{k}}$ and $\Sigma_{\mathbf{k}}$ are obtained from Eq. (2.27):

$$\begin{aligned} \Delta_{\mathbf{k}}^{\alpha\alpha} &= 2JS \ , & \Sigma_{\mathbf{k}}^{\alpha\alpha} &= 2JS \ , \\ \Delta_{\mathbf{k}}^{\alpha\beta} &= 2JS \cdot \mathcal{C}_{\alpha\beta} t_{\alpha\beta} \ , & \Sigma_{\mathbf{k}}^{\alpha\beta} &= 2JS \cdot \mathcal{C}_{\alpha\beta} \ , \end{aligned} \tag{2.33}$$

where we defined the following notation to ease reading:

$$\begin{aligned} \mathcal{C}_{\alpha\beta} &= \cos(\mathbf{k} \cdot \mathbf{r}_{\alpha\beta}) \ , \\ t_{\alpha\beta} &= \cos\theta_{\alpha\beta} \ . \end{aligned} \tag{2.34}$$

For the sake of completeness, let me as well give the coefficients for the matrix $\Gamma_{\mathbf{k}} = \Delta_{\mathbf{k}}\Sigma_{\mathbf{k}}$:

$$\Gamma_{\mathbf{k}}^{\alpha\alpha} = (2JS)^2 \left(1 + \sum_{\beta\neq\alpha} \mathcal{C}_{\alpha\beta}^2 t_{\alpha\beta}\right) \ , \tag{2.35}$$

$$\Gamma_{\mathbf{k}}^{\alpha\beta} = (2JS)^2 \left(\mathcal{C}_{\alpha\beta}(1 + t_{\alpha\beta}) + \sum_{\gamma\neq\alpha,\beta} \mathcal{C}_{\alpha\gamma}\mathcal{C}_{\gamma\beta} t_{\alpha\gamma}\right) \ . \tag{2.36}$$

Note that this matrix is not symmetric. Note as well the following property obtained from Eqs. (2.14, 2.15):

$$\sum_{\alpha,\beta}^{\neq} t_{\alpha\beta} = \frac{1}{2}\left[(nh)^2 - n\right] \ . \tag{2.37}$$

This will serve in the following analytical derivations.

2.2.3 ground-state energy and magnetization

The quadratic part of the Hamiltonian given by Eq. (2.30) can be written as follows in terms of the harmonic spin-wave modes $\epsilon_{i\mathbf{k}}$:

$$\frac{1}{2}\sum_{\mathbf{k}} \hat{Y}_{\mathbf{k}}^{\dagger}\Omega_{\mathbf{k}}\hat{Y}_{\mathbf{k}} = \sum_{\mathbf{k}}\sum_{i=1}^{n} \epsilon_{i\mathbf{k}}\left(\beta_{\mathbf{k},i}^{\dagger}\beta_{\mathbf{k},i} + \frac{1}{2}\right) \ , \tag{2.38}$$

The ground state of the system corresponding to the vacuum of excitations, we have the following expression for the total ground-state energy:

$$E_{\rm gs} = -NJS(S+1) - NJS^2h^2n + \frac{1}{2}\sum_{\mathbf{k},i}\epsilon_{i\mathbf{k}} = E_{\rm cl} + \Delta E_{\rm q} \ . \tag{2.39}$$

The magnetization per site m is deduced from Eq. (2.39) through Eq. (2.16). Let me write the expression in terms of the dimensionless field $h = H/(2nJS)$:

$$m = hS - \frac{1}{2}\frac{1}{N}\frac{1}{n}\sum_{\mathbf{k},i}\frac{\partial}{\partial h}\left(\frac{\epsilon_{i\mathbf{k}}}{2JS}\right) \ . \tag{2.40}$$

The eigenvalue problem of Eq. (2.32) may now be solved explicitly and independently for the kagome and pyrochlore lattices.

2.3 The kagome lattice

The kagome lattice is a 2D lattice of corner-sharing triangles, such that each lattice site is shared by 2 triangles, one up-pointing and the other down-pointing (see pink and blue triangles on Fig (2.4), respectively). As I said in section 2.1, the nearest-neighbor Heisenberg model on the kagome lattice has an extensive classical ground-state degeneracy. This is related to the fact that the Hamiltonian can be described as a sum over local Hamiltonians on elementary triangular units of $n = 3$ sites, see Eq. (2.4). The classical ground-state constraint given by Eq. (2.8) must be verified on each triangle:

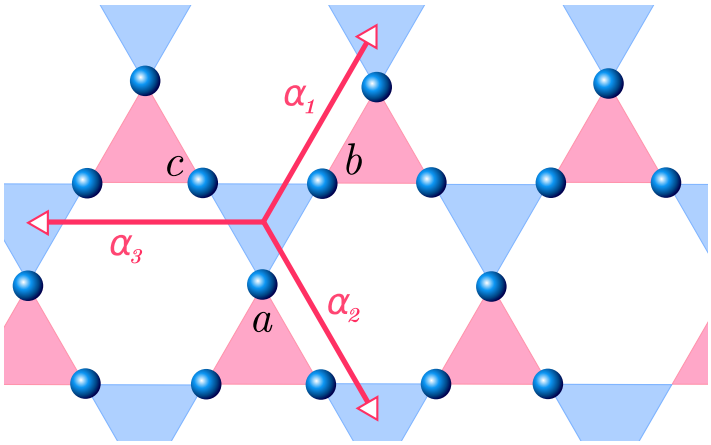

Figure 2.4: *The kagome lattice with a 3-sublattice structure. The elementary unit cell contains a site of each sublattice a, b and c.*

$$\mathbf{S}_{\triangle} = \frac{\mathbf{H}}{2J} \ , \tag{2.41}$$

where $\mathbf{H}$ is the applied magnetic field and $\mathbf{S}_{\triangle}$ is the total spin on a triangle, that is, the sum of the 3 spins of the triangle.

When we restrict to coplanar orderings, the above constraint on a single triangle leaves one accidental continuous degree of freedom. Then for a given set of 3 coplanar vectors $\mathbf{S}_a$, $\mathbf{S}_b$ and $\mathbf{S}_c$ that satisfy Eq. (2.41), classical ground states are constructed by imposing that on each triangle there is one spin of each orientation a, b, c. There are many such coverings - which may exhibit LRO or not - but two are special: the $\mathbf{Q} = \mathbf{0}$ and $\sqrt{3} \times \sqrt{3}$ ordered structures. Their ordering wave-vectors correspond to high symmetry points of the Brillouin zone, namely the $\mathbf{\Gamma}$ and $\mathbf{K}$ points, respectively. They are also the two structures that sustain LRO with the smallest magnetic unit cell size (3 and 9 sites, respectively).

It has been shown previously that among the classically degenerate coplanar configurations, the states favored by quantum fluctuations are the Y and V states for the low-field and high-field regions, respectively [14, 38, 84]. Those states will be described in more details later on. It is important to note however, that those two states do accommodate a collinear spin arrangement, which precisely corresponds to the plateau state. Furthermore, it was found that the $\mathbf{Q} = \mathbf{0}$ order is favored over the $\sqrt{3} \times \sqrt{3}$ [84]. We thus take this as our starting point to the spin wave expansion. The final geometry is shown on Fig. (2.4).

I remind the reader that when $\mathbf{Q} = \mathbf{0}$, each elementary triangle has the exact same spin structure, with spins of a same sublattice placed on the same corner of the plaquette. Then the magnetic unit cell is exactly one triangle of a given kind, let us say for example the down-pointing (blue) triangles on Fig. (2.4). We only need

to define $n = 3$ sublattices a, b, c, all the spins of a given sublattice having the same orientation. To each sublattice is attributed a different bosonic species. The spin-wave Hamiltonian is thus expressed in terms of the 3 corresponding sets of bosonic creation and annihilation operators $a_{\mathbf{k}}^{(\dagger)}, b_{\mathbf{k}}^{(\dagger)}, c_{\mathbf{k}}^{(\dagger)}$. Each unit cell is located in the lattice by a vector $\mathbf{R}_c$ which is a combination of the translation vectors $\boldsymbol{\alpha}_1$ and $\boldsymbol{\alpha}_2$, as given below:

$$\begin{aligned} \mathbf{R}_c =& n_1\boldsymbol{\alpha}_1 + n_2\boldsymbol{\alpha}_2 \ , \qquad n_1, n_2 \in \mathbb{Z} \ , \\ \boldsymbol{\alpha}_1 =& \frac{a}{2}\left(1, \sqrt{3}\right) \ , \\ \boldsymbol{\alpha}_2 =& \frac{a}{2}\left(1, -\sqrt{3}\right) \ , \end{aligned} \tag{2.42}$$

in which a is the characteristic length of the lattice. We also define $\boldsymbol{\alpha}_3 = -(\boldsymbol{\alpha}_2 + \boldsymbol{\alpha}_1)$. Note that this structure can be seen as a triangular superlattice of magnetic cells. A given spin site is completely specified by its position $\mathbf{R}$ and its sublattice index $\alpha \in \{a, b, c\}$: $\mathbf{S}_i = \mathbf{S}_{\mathbf{R},\alpha}$. Each spin $\mathbf{S}_{\mathbf{R},\alpha}$ has four nearest neighbors, two of sublattice β located at positions $\mathbf{R} \pm \mathbf{r}_{\alpha\beta}$, and two of sublattice γ located at positions $\mathbf{R} \pm \mathbf{r}_{\alpha\gamma}$ (with $\alpha \neq \beta \neq \gamma$). The displacement vectors are given by:

$$\begin{aligned} \mathbf{r}_{ab} =& \boldsymbol{\alpha}_1/2 = a/4(1, \sqrt{3}) \ , \\ \mathbf{r}_{bc} =& \boldsymbol{\alpha}_3/2 = a/2(-1, 0) \ , \\ \mathbf{r}_{ca} =& \boldsymbol{\alpha}_2/2 = a/4(1, -\sqrt{3}) \ . \end{aligned} \tag{2.43}$$

They are to be substituted into the general Hamiltonian given in Eq. (2.17).

2.3.1 Spin-wave spectrum of an arbitrary coplanar state

We will now explicitly search for the 3 eigenvalues $\epsilon_{i\mathbf{k}}^2$ of the 3×3 matrix $\Gamma_{\mathbf{k}} = \Sigma_{\mathbf{k}}\Delta_{\mathbf{k}}$ (see Eq. (2.32)), in order to obtain the harmonic spin-wave spectrum. For the sake of simplicity, we define the following:

$$\begin{aligned} \mathcal{C}_1 = \mathcal{C}_{bc} &= \cos\left(\mathbf{k} \cdot \mathbf{r}_{bc}\right) & t_1 = t_{bc} &= \cos\theta_{bc} \\ \mathcal{C}_2 = \mathcal{C}_{ca} &= \cos\left(\mathbf{k} \cdot \mathbf{r}_{ca}\right) \ , & t_2 = t_{ca} &= \cos\theta_{ca} \ . \\ \mathcal{C}_3 = \mathcal{C}_{ab} &= \cos\left(\mathbf{k} \cdot \mathbf{r}_{ab}\right) & t_3 = t_{ab} &= \cos\theta_{ab} \end{aligned} \tag{2.44}$$

From Eq. (2.33), the matrices $\Delta_{\mathbf{k}}$ and $\Sigma_{\mathbf{k}}$ are given by:

$$\Delta_{\mathbf{k}} = 2JS \begin{pmatrix} 1 & \mathcal{C}_3 t_3 & \mathcal{C}_2 t_2 \\ \mathcal{C}_3 t_3 & 1 & \mathcal{C}_1 t_1 \\ \mathcal{C}_2 t_2 & \mathcal{C}_1 t_1 & 1 \end{pmatrix} \ , \qquad \Sigma_{\mathbf{k}} = 2JS \begin{pmatrix} 1 & \mathcal{C}_3 & \mathcal{C}_2 \\ \mathcal{C}_3 & 1 & \mathcal{C}_1 \\ \mathcal{C}_2 & \mathcal{C}_1 & 1 \end{pmatrix} \ . \tag{2.45}$$

To find the eigenvalues, we simply use the characteristic polynomial method. We want to find the roots of the polynomial $p(\lambda)$ defined as:

$$p(\lambda) = \det(\Gamma_{\mathbf{k}} - \lambda \cdot \mathbb{I}_3) \ .$$

Then the root equation is of order 3 in λ:

$$p(\lambda) = -\lambda^3 + b\lambda^2 + c\lambda + d = 0 \ , \tag{2.46}$$

with the following coefficients:

$$\begin{aligned} b =& \Gamma^{aa} + \Gamma^{bb} + \Gamma^{cc} = \mathrm{Tr}(\Gamma_{\mathbf{k}}) \ , \\ c =& \sum_{\alpha,\beta}^{\neq} \left(\Gamma^{\alpha\alpha}\Gamma^{\beta\beta} - \Gamma^{\alpha\beta}\Gamma^{\beta\alpha} \right) \ , \\ d =& \det\left(\Gamma_{\mathbf{k}}\right) \ . \end{aligned} \tag{2.47}$$

First of all, we notice that the determinant of $\Sigma_{\mathbf{k}}$ vanishes. This comes from the fact that the unit cells are closed loops, with $\mathbf{r}_{ab} + \mathbf{r}_{bc} + \mathbf{r}_{ca} = \mathbf{0}$. Indeed, we have $\mathbf{r}_{bc} = -(\mathbf{r}_{ab} + \mathbf{r}_{ca})$, which induces:

$$\mathcal{C}_1 = \mathcal{C}_2\mathcal{C}_3 - \mathcal{S}_2\mathcal{S}_3 \ , \tag{2.48}$$

where $\mathcal{S}_i = \sin(\mathbf{k}\cdot\mathbf{r}_i)$. Using this relation, one easily shows that the determinant of $\Sigma_{\mathbf{k}}$ is given by:

$$\frac{\det\left(\Sigma_{\mathbf{k}}\right)}{(2JS)^3} = 1 + 2\mathcal{C}_1\mathcal{C}_2\mathcal{C}_3 - \mathcal{C}_1^2 - \mathcal{C}_2^2 - \mathcal{C}_3^2 = 0 \ . \tag{2.49}$$

The relation $\det(AB) = \det(A)\det(B)$ implies $\det\left(\Gamma_{\mathbf{k}}\right) = 0$. Since the determinant of a matrix is the product of its eigenvalues, we conclude that at least one of the eigenvalues of our system is equal to 0, which simplifies the diagonalization process further. Indeed, the root equation to solve becomes:

$$p(\lambda) = -\lambda(\lambda^2 - b\lambda + c) = -\lambda.p'(\lambda) = 0 \ , \tag{2.50}$$

of which the 3 roots are $\lambda_{0\mathbf{k}} = 0$ and the two roots $\lambda_{\mathbf{k}}^{\pm}$ of the polynomial $p'(\lambda)$. Note that this property is true *for all values of* $\mathbf{k}$ *and* h, such that there is a completely flat band of zero energy in the harmonic spin-wave spectrum of the kagome Heinseberg AFM in field, at any field value up to saturation. This feature remains true for any $\mathbf{Q} = \mathbf{0}$ coplanar classical ground state. Indeed, it is completely encoded in $\Sigma_{\mathbf{k}}$, which only contains information on the geometry of the lattice but not on the relative orientations of the spins in a triangle. This full band of zero energy is not protected by the Goldstone theorem and is an artefact of the harmonic approximation. It should in principle acquire dispersion, or at least become gapped when one includes higher-order processes. One should understand this as the signature of the extensive classical ground-state degeneracy in the harmonic spin-wave spectrum.

The problem thus reduces to solving the following quadratic equation:

$$p'(\lambda) = \lambda^2 - b\lambda + c = 0 \ , \tag{2.51}$$

of which the determinant is given by:

$$\Delta = b^2 + 4c \ ,$$

where b and c are given in Eq. (2.47). After explicitly substituting the matrix coefficients given in Eqs. (2.35, 2.36), and making use of Eq. (2.49), we obtain, in terms of the $\mathcal{C}_i$ and t_i variables introduced in Eq. (2.44):

$$\frac{\Delta}{(2JS)^4} = 1 + 8\mathcal{C}_1\mathcal{C}_2\mathcal{C}_3\,(1+\chi_{123}) + 4\sum_{i=1}^{3}\mathcal{C}_i^2 t_i(1+t_i) \ , \tag{2.52}$$

where we defined

$$\chi_{123} = t_1 + t_2 + t_3 + t_1t_2 + t_2t_3 + t_3t_1 \ . \tag{2.53}$$

The two roots $\lambda_{\mathbf{k}}^{\pm}$ of Eq. (2.51) are then given by:

$$\frac{\lambda_{\mathbf{k}}^{\pm}}{(2JS)^2} = \frac{1}{2}\left\{3 + 2\sum_{i=1}^{3}\mathcal{C}_i^2 t_i + \pm\sqrt{\Delta/(2JS)^4}\right\} \ . \tag{2.54}$$

The corresponding spin-wave modes are finally:

$$\epsilon_{\mathbf{k}}^{\pm} = \left\{\lambda_{\mathbf{k}}^{\pm}\right\}^{1/2} \ . \tag{2.55}$$

To summarize, the kagome Heisenberg AFM with $\mathbf{Q} = \mathbf{0}$ has 3 spin-wave modes. In the harmonic spin-wave approximation, one of these modes has a completely flat, gapless dispersion $\epsilon_{0\mathbf{k}} = 0$. The two remaining modes $\epsilon_{\mathbf{k}}^{\pm}$ are given by Eqs. (2.52-2.55).

So far, there is no explicit dependency with respect to the magnetic field strength h. The only (implicit) mention of h resides in the fact that we assumed the classical ground-state constraint of Eq. (2.8) to be verified. The expressions derived above are thus in principle applicable to any *coplanar* classical ground state with $\mathbf{Q} = \mathbf{0}$. The explicit dependency with respect to field h of the spectrum of a specific classical ground state is contained in the expressions for the azimutal canting angles θ_α of the spins in that ground state - and consequently, in the t_i variables.

2.3.2 The Y and V states

At $H = 0$, the constraint of Eq. (2.41), required to minimize the Hamiltonian, reduces to the condition that the sum of all spins on a given triangle vanishes ($\mathbf{S}_\triangle = \mathbf{0}$). The coplanar state that satisfies this constraint, is the 120° structure, where each spin of the triangle sustains a 120° opening angle with the two others. When H is finite, the spins cant towards the magnetic field to gain energy, so as to fulfill the constraint of Eq. (2.41), but this canting can be done in several ways. As quantum fluctuations select coplanar states, we assume the spins to lie in the z_0x_0 plane during the whole magnetization process. The classical ground states favoured by quantum fluctuations for the kagome lattice in field are the coplanar Y and V states. These two configurations are shown on Fig. (2.5).

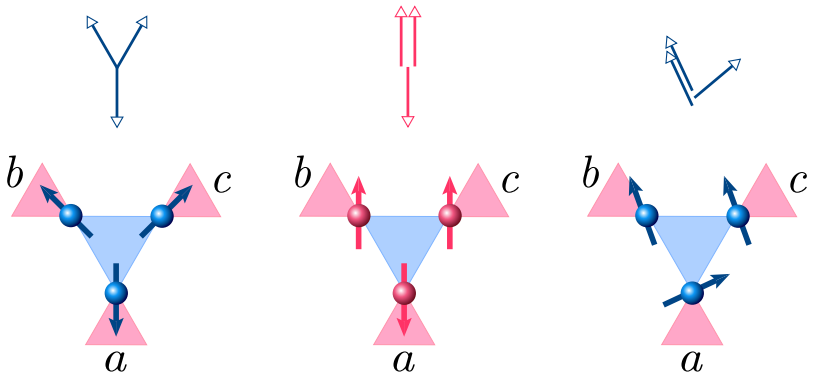

Figure 2.5: *Classical ground-state spin configurations on a plaquette for the kagome Heisenberg AFM in magnetic field. From left to right are shown the low-field Y state, the collinear plateau uud state and the high-field V state.*

The Y state

In the low-field region, the system is in the Y state (left panel on Fig. (2.5)): one spin (say of sublattice a) remains antiparallel to the field, while the two others cant towards the field with a symmetric angle $\pm\theta_Y$. Then the classical constraint of Eq. (2.14) implies:

$$2\cos\theta_Y - 1 = 3h \Rightarrow \cos\theta_Y = \frac{3h+1}{2} \ . \tag{2.56}$$

We have thus:

$$\begin{aligned} \cos\theta_a &= -1 \ , \\ \cos\theta_b = \cos\theta_c &= \cos\theta_Y \ . \end{aligned} \tag{2.57}$$

The constraint of Eq. (2.15) is naturally satisfied from the axial symmetry of the structure with the z_0 axis.

Since we have $\cos\theta_Y \leq 1$, the Y state is only stable for $0 \leq h \leq 1/3$. At the critical field $h = 1/3$, the two spins of sublattice b and c are completely parallel along the field, while the spin of sublattice a is still completely antiparallel: it is the up-up-down (uud) collinear state (middle panel of Fig. (2.5)). This state is of fractional magnetization $m = 1/3$, as $1/3$ of the spins of the lattice is pointing down and $2/3$ is pointing up.

The V state

At higher fields, the antiparallel spin starts canting as well towards the field in order to keep satisfying the constraint of Eq. (2.14). This canting induces a loss of the axial symmetry, such that the other two spins need to compensate in order to satisfy the constraint on the sines (see Eq. (2.15)). This is the V state (right panel of Fig. (2.5)), where one of the spins has a canting angle θ_{V1} (say of sublattice a), while the other

two spins sustain an angle θ_{V2}. This configuration maintains some collinearity, which as we know is favored by quantum fluctuations. We have from Eq. (2.14):

$$2\cos\theta_{V2} + \cos\theta_{V1} = 3h \Rightarrow \cos\theta_{V1} = 3h - 2\cos\theta_{V2} \ . \tag{2.58}$$

From Eq. (2.15):

$$\begin{aligned} \sin\theta_{V1} = 2\sin\theta_{V2} \Rightarrow & \sin^2\theta_{V1} = 4\sin^2\theta_{V2} \\ \Rightarrow & 4\cos^2\theta_{V2} = 3 + \cos^2\theta_{V1} \ . \end{aligned} \tag{2.59}$$

Substituting Eq. (2.58) into Eq. (2.59), one obtains finally:

$$\cos\theta_{V1} = \frac{3h^2 - 1}{2h} \ , \qquad \cos\theta_{V2} = \frac{3h^2 + 1}{4h} \ . \tag{2.60}$$

We have thus:

$$\begin{aligned} \cos\theta_a &= \cos\theta_{V1} \ , \\ \cos\theta_b = \cos\theta_c &= \cos\theta_{V2} \ . \end{aligned} \tag{2.61}$$

The requirement $-1 \leq \cos\theta_{Vi} \leq 1$ makes this configuration physically realisable only for the high-field region $1/3 \leq h \leq 1$. At saturation ($h = h_{\text{sat}} = 1$), all the spins of the lattice are aligned with the field in the fully polarized ferromagnetic (FM) state. Note that at the critical field $h = 1/3$, the V state is in the collinear *uud* configuration.

2.3.3 Specific spin-wave spectra

The Y and V states are our classical starting points to the spin-wave expansion, and the explicit dependency of the spin-wave spectrum given by Eq. (2.54) with respect to magnetic field h will come from the angles given in Eq. (2.56) and Eq. (2.60). We get expressions for the opening angles t_i defined in Eq. (2.44), which are then substituted into Eqs. (2.52-2.55) to obtain analytical expressions for the spectra $\epsilon^{\pm}_{\mathbf{k}}$. First, let us notice the following:

$$t_1t_2 + t_2t_3 + t_3t_1 = \frac{1}{2}\left[(t_1 + t_2 + t_3)^2 - t_1^2 - t_2^2 - t_3^2\right] \ . \tag{2.62}$$

From Eq. (2.37), this can be written as:

$$t_1t_2 + t_2t_3 + t_3t_1 = \frac{1}{2}\left[\frac{1}{4}\left((3h)^2 - 3\right)^2 - t_1^2 - t_2^2 - t_3^2\right] \ . \tag{2.63}$$

Then the expression for χ_{123} given in Eq. (2.53) becomes:

$$\chi_{123} = \frac{1}{8}\left[\left((nh)^2 - 1\right)^2 - 4\left(1 + t_1^2 + t_2^2 + t_3^2\right)\right] \tag{2.64}$$

We can thus rewrite Eq.(2.52) as:

$$\frac{\Delta}{(2JS)^4} = 1 + \mathcal{C}_1\mathcal{C}_2\mathcal{C}_3\left[\left((3h)^2-1\right)^2 - 4\left(t_1^2+t_2^2+t_3^2-1\right)\right] + 4\sum_{i=1}^{3}\mathcal{C}_i^2 t_i(1+t_i)\ . \quad (2.65)$$

Analytical expressions for the non-zero energy modes $\epsilon_{\mathbf{k}}^{\pm}$ of the magnon spectrum are now derived independently for the Y and V states.

The Y state in the low-field region

From Eqs. (2.56 - 2.57), and remembering the definitions of t_i opening angles given in Eq. (2.44), we have:

$$\begin{aligned} t_1 =& (3h+1)^2/2 - 1\ , \\ t_2 =& t_3 = -(3h+1)/2\ . \end{aligned} \quad (2.66)$$

Substituting these expressions into Eq. (2.65), we obtain:

$$\begin{aligned} \frac{\Delta_Y(h)}{(2JS)^4} = 1 &+ 2\mathcal{C}_1\mathcal{C}_2\mathcal{C}_3(3h+1)^2(1-6h) + \mathcal{C}_1^2(3h+1)^2\left[(3h+1)^2-2\right] \\ &+ \left(\mathcal{C}_2^2+\mathcal{C}_3^2\right)(3h+1)(3h-1)\ . \end{aligned} \quad (2.67)$$

We now make use of the following relation, which is directly equivalent to Eq. (2.49):

$$2\mathcal{C}_1\mathcal{C}_2\mathcal{C}_3 = \mathcal{C}_1^2+\mathcal{C}_2^2+\mathcal{C}_3^2-1\ . \quad (2.68)$$

Substituting Eq. (2.68) into Eq. (2.67), we get:

$$\frac{\Delta_Y(h)}{(2JS)^4} = 9h^2\left\{\mathcal{C}_1^2(3h+1)^2 + 2(3h+1)\left[1-\left(\mathcal{C}_2^2+\mathcal{C}_3^2\right)\right]+1\right\} = 9h^2\delta_Y(h)\ . \quad (2.69)$$

The two eigenvalues $\lambda_{Y\mathbf{k}}^{\pm}$ are given by Eq. (2.54):

$$\frac{\lambda_{Y\mathbf{k}}^{\pm}}{(2JS)^2} = \frac{1}{2}\left\{\mathcal{C}_1^2(3h+1)^2 - \left(\mathcal{C}_2^2+\mathcal{C}_3^2\right)(3h+1) + 3 - 2\mathcal{C}_1^2 \pm 3h\sqrt{\delta_Y(h)}\right\}\ .$$

Finally, the two dispersive magnon modes $\epsilon_{Y\mathbf{k}}^{\pm}$ are obtained by taking the square root of $\lambda_{Y\mathbf{k}}^{\pm}$ (relation of Eq. (2.55)):

$$\frac{\epsilon_{Y\mathbf{k}}^{\pm}}{2JS} = \frac{\sqrt{2}}{2}\left\{\mathcal{C}_1^2(3h+1)^2 - \left(\mathcal{C}_2^2+\mathcal{C}_3^2\right)(3h+1) + 3 - 2\mathcal{C}_1^2 \pm 3h\sqrt{\delta_Y(h)}\right\}^{1/2}\ . \quad (2.70)$$

From the above explicit expression of the spin-wave modes, one can finally compute the harmonic ground-state energy correction of Eq. (2.39), and the corrected magnetization of Eq. (2.40). For the sake of completeness, let me now express explicitly the derivative

of $\lambda^{\pm}_{Y\mathbf{k}}$ with h, which is needed to evaluate the expression for the magnetization of Eq. (2.40):

$$\frac{\partial}{\partial h}\left[\frac{\lambda^{\pm}_{Y\mathbf{k}}}{(2JS)^2}\right] = \frac{3}{2}\left\{2\mathcal{C}_1^2(3h+1) - \left(\mathcal{C}_2^2+\mathcal{C}_3^2\right) \pm \frac{f_Y(h)}{\sqrt{\delta_Y(h)}}\right\} \ , \tag{2.71}$$

where I defined the function $f_Y(h)$ as follows:

$$f_Y(h) = \mathcal{C}_1^2(3h+1)(6h+1) - \left(\mathcal{C}_2^2+\mathcal{C}_3^2\right)(9h+2) + 9h + 3 \ . \tag{2.72}$$

The V state in the high-field region

From Eqs. (2.60 - 2.61), we have for the t_i variables in the V state:

$$\begin{aligned} t_1 =& 1 \ , \\ t_2 =& t_3 = (9h^2-5)/4 \ . \end{aligned} \tag{2.73}$$

This has been obtained using the relations between sines given by the classical ground-state constraint of Eq. (2.15):

$$\begin{aligned} \cos\theta_{ca} &= \cos\left(\theta_{V1}+\theta_{V2}\right) \\ &= \cos\theta_{V1}\cos\theta_{V2} - 2\sin^2\theta_{V2} \\ &= \cos\theta_{V2}\left(\cos\theta_{V1} + 2\cos\theta_{V2}\right) - 2 \ . \end{aligned}$$

We now substitute the expressions of Eq. (2.73) into Eq. (2.65). Making use of Eq. (2.68) again, we get:

$$\begin{aligned} \frac{\Delta_V(h)}{(2JS)^4} = \frac{9}{4}\Big[&\mathcal{C}_1^2\left(3h^2+1\right)^2 + 2\left(\mathcal{C}_2^2+\mathcal{C}_3^2\right)\left(3h^2+1\right)\left(3h^2-1\right) \\ &- \left(3h^2-1\right)\left(3h^2+3\right)\Big] = \frac{9}{4}\delta_V(h) \ . \end{aligned} \tag{2.74}$$

From Eq. (2.54) we obtain:

$$\frac{\lambda^{\pm}_{V\mathbf{k}}}{(2JS)^2} = \frac{1}{4}\left\{6 + 4\mathcal{C}_1^2 - 5\left(\mathcal{C}_2^2+\mathcal{C}_3^2\right) + 9h^2\left(\mathcal{C}_2^2+\mathcal{C}_3^2\right) \pm 3\sqrt{\delta_V(h)}\right\} \ . \tag{2.75}$$

The square root of the above expression finally gives the expressions for the two non-zero magnon modes $\epsilon^{\pm}_{V\mathbf{k}}$:

$$\frac{\epsilon^{\pm}_{V\mathbf{k}}}{2JS} = \frac{1}{2}\left\{6 + 4\mathcal{C}_1^2 - 5\left(\mathcal{C}_2^2+\mathcal{C}_3^2\right) + 9h^2\left(\mathcal{C}_2^2+\mathcal{C}_3^2\right) \pm 3\sqrt{\delta_V(h)}\right\}^{1/2} \ . \tag{2.76}$$

The derivative of $\lambda^{\pm}_{V\mathbf{k}}$ with respect to h is given below for completeness:

$$\frac{\partial}{\partial h}\left[\frac{\lambda^{\pm}_{V\mathbf{k}}}{(2JS)^2}\right] = \frac{9h}{2}\left\{\mathcal{C}_2^2+\mathcal{C}_3^2 \pm \frac{\left(3h^2+1\right)\left(\mathcal{C}_1^2-1\right) + 6h^2\left(\mathcal{C}_2^2+\mathcal{C}_3^2\right)}{\sqrt{\delta_V(h)}}\right\} \ . \tag{2.77}$$

2.3.4 Magnetization curve

From the above analytical expressions for the harmonic spin-wave spectrum of the kagome Heisenberg AFM in the Y and V phases, it is now possible to compute the quantum correction ΔE_{q} to the ground-state energy. We define the normalized energy correction per spin Δe_{q} as:

$$\Delta e_{\mathrm{q}} = \frac{\Delta E_{\mathrm{q}}}{NJS} = -1 + \frac{1}{N}\sum_{\mathbf{k},\mathbf{i}} \frac{\epsilon_{i\mathbf{k}}}{2JS} \ , \tag{2.78}$$

where the last equality readily follows from Eq. (2.39). The integral is performed using standard Monte-Carlo integration over the first Brillouin zone of the kagome lattice.

The top panel of Figure 2.6 shows Δe_{q} as a function of the applied magnetic field h. For $h \leq h_c = 1/3$, the classical ground state is the Y state and one uses Eq. (2.70) for the spectrum $\epsilon_{i\mathbf{k}}$, whereas for $h_c \leq h \leq 1$, the system is in the V state and one uses Eq. (2.76). We see a clear cusp in the zero-point energy at the critical field $h_c = 1/3$, which indicates a discontinuity in the first derivative, that is, the magnetization. The quantum corrections are suppressed at saturation field.

From Eq. (2.40), one can now obtain the magnetization curve for the Y and V states. We remind the reader of the relation of Eq. (2.55). The derivative of $\lambda^{\pm}_{\mathbf{k}}$ is given by Eqs. (2.71, 2.72) for the Y state, and Eq. (2.77) for the V state. The integral in Eq. (2.40) is computed using standard Monte Carlo integration over the first Brillouin zone. The resulting magnetization curve is shown on the bottom panel of Fig. (2.6) for $S = 1$. We used $N_{\mathrm{MC}} = 4 \cdot 10^6$ Monte-Carlo points to compute this curve.

The magnetization diverges in the Y and V states in the limit $h \to 1/3$. As a consequence, a big discontinuity in the form of an infinite negative jump is expected from the LSWT calculation. Such a behaviour is obviously nonphysical and demonstrates a failure of LSWT to correctly predict the magnetization close to the classical phase transition between the two states. This failure can however be corrected by a phenomenological argument. Indeed, we know that we expect a magnetization plateau around h_c, which is the result of the stabilization over a wide field range of the *uud* collinear state. Since the collinear phase restores the U(1) symmetry of the Hamiltonian, as opposed to the surrounding canted phases, S^z_{tot} is conserved in the *uud* phase and the magnetization remains of constant value $m = 1/3$. One can therefore simply cut the magnetization curve at $m = 1/3$ to obtain the final magnetization curve [46] (purple line on the bottom panel of Fig. (2.6)).

With this approach, the boundary fields at which the plateau state appears and disappears are determined by the intersection of the analytical curves and $m = 1/3$. The values for the plateau field boundaries as a function of $1/S$ have been reported on Fig. (2.7). As is clearly seen, the plateau width decreases with increasing spin length S, and ultimately vanishes completely in the classical limit $S \to \infty$. Furthermore, the extent of the plateau phase appears to be asymmetrical with respect to the critical field $h = 1/3$. Indeed, the plateau phase extends further to the high field region inside

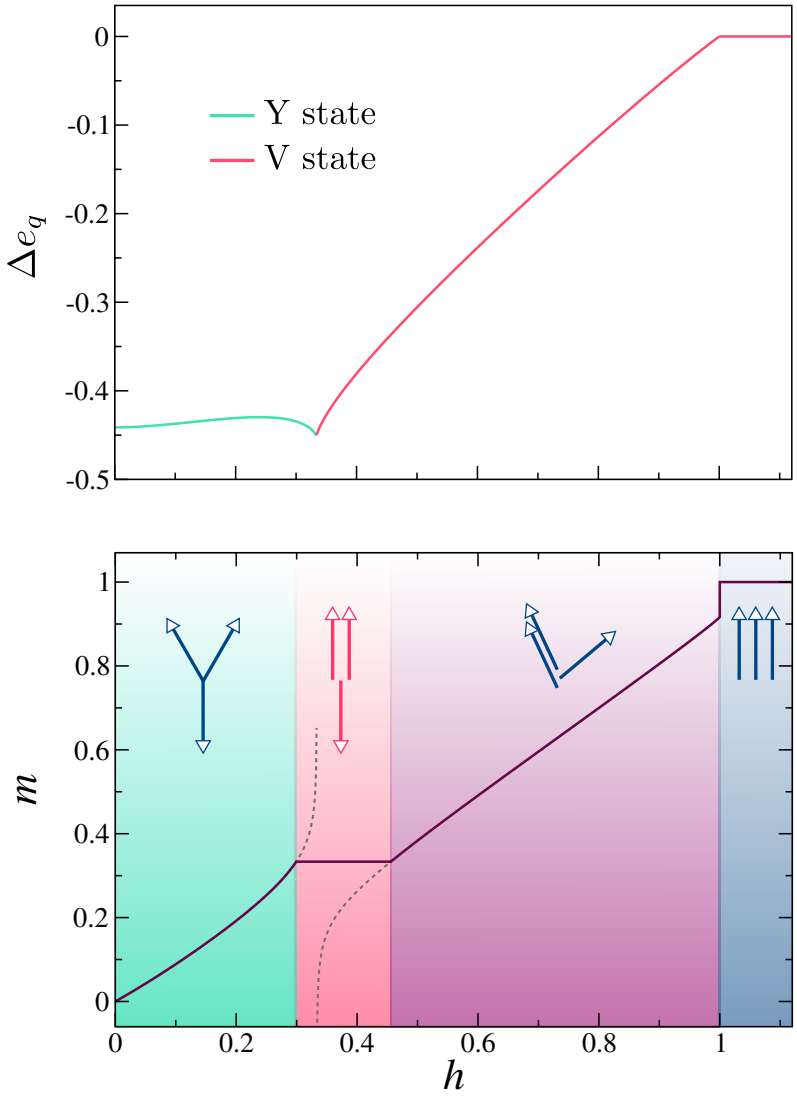

Figure 2.6: *Quantum correction Δe_q to the ground-state energy and magnetization curve of the spin-1 kagome Heisenberg AFM as a function of magnetic field $h = H/H_{sat}$. In the magnetization plot, dashed lines show the magnetization obtained within linear spin-wave theory in the Y and V states. The purple line shows the final magnetization curve. The arrows depict the spin configuration in each phase.*

the V phase, than to the low-field region. Note that there is a clear magnetization jump upon saturation at the end of the magnetization curve. This is directly related to the suppression of quantum fluctuations in the polarized state, which becomes the true quantum ground state when $h \geq 1$. The height δm of this jump is surprisingly close to the value predicted theoretically from the condensation of localized magnons

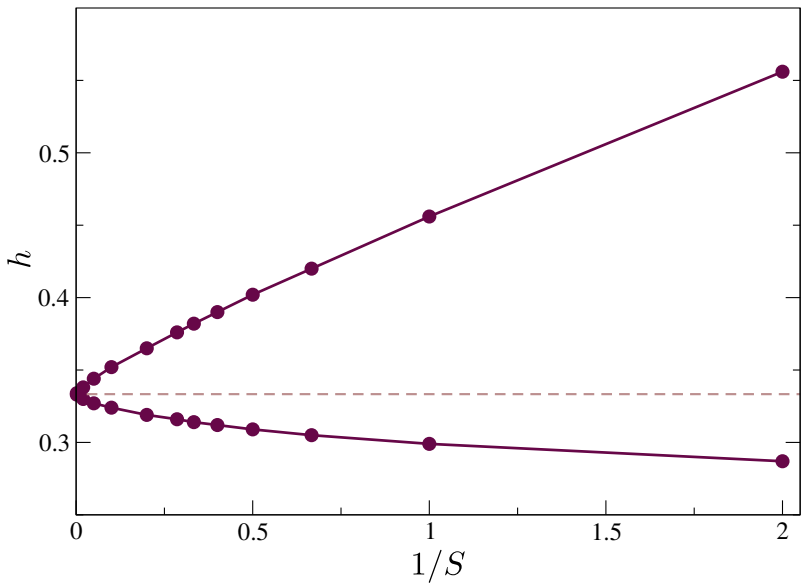

Figure 2.7: *Field boundaries h_{c1} and h_{c2} of the $1/3$-magnetization plateau in the kagome Heisenberg AFM, as a function of inverse spin. The dashed light brown line shows $h_c = 1/3$ as a guide to the eye.*

right below saturation field [49]:

$$\delta m = 1/(9S) \ . \tag{2.79}$$

However, let us not draw any definitive conclusion on whether these two jumps are related or not at the moment. Indeed, the description of a magnon crystal falls beyond the scope of semiclassical SWT.

Note as well that the magnetization curve acquires an upward curvature due to the gradual suppression of spin reduction towards saturation [29]. This is clearly seen on Fig. (2.6), at least in the low-field region. As a result, the magnetic susceptibility at $h \to 0$ is also renormalized by the effect of quantum fluctuations. Within the linear spin-wave approximation, this renormalization appears as a $1/S$ correction to the classical susceptibility $\chi_{\rm cl} = 1/(6J)$. This correction was estimated by fitting the quantum correction to the magnetization towards $h \to 0$, and is given below for the sake of completeness:

$$\chi = \frac{1}{6J}\left(1 - 0.1890(1)/S\right) \ . \tag{2.80}$$

2.4 The pyrochlore lattice

The pyrochlore lattice is a 3D spin lattice of corner-sharing tetrahedra, see Fig. (2.8). Each lattice site has 6 nearest neighbors and is shared between 2 adjacent tetrahedra of opposite orientation (blue and pink tetrahedra on Fig. (2.8)). Due to this corner-sharing nature, the Heisenberg Hamiltonian can be written as a sum over local Hamiltonians on each tetrahedron in the fashion of Eq. (2.4). Classical ground states are thus only constrained by Eq. (2.8) on each tetrahedron:

$$\mathbf{S}_t = \frac{\mathbf{H}}{2J} \ , \tag{2.81}$$

where $\mathbf{H}$ is the applied magnetic field and $\mathbf{S}_t$ is the local spin variable, that is, the sum of the 4 spins of the tetrahedron. So the minimal unit cell must contain at least $n = 4$ sites.

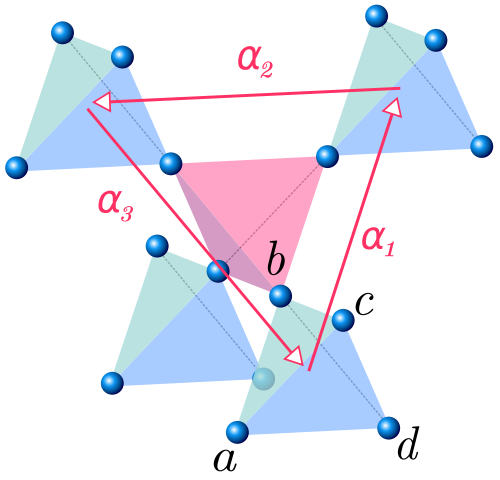

Figure 2.8: *The pyrochlore lattice with a 4-sublattice structure. The elementary unit cell contains a site of each sublattice a, b, c and d.*

Once again, we focus solely on coplanar structures, as being the best candidates for quantum OBD selection. For a given tetrahedron in the pyrochlore lattice, there exists infinitely many possible coplanar arrangements that satisfy the constraint of Eq. (2.81). The ones selected by quantum fluctuations are expected to maximize the collinearity of spins and also to allow for fully collinear configurations. In first approximation, the action of quantum or thermal fluctuations can be described by an effective negative biquadratic term in the Hamiltonian. Penc and collaborators [40] have shown that such a biquadratic interaction stabilizes a Y phase and two different V phases, similarly as in the kagome lattice. Note that in [40], this was done to study the effect of spin-lattice coupling in the stabilization of the 1/2 magnetization plateau. Details about the Y and V phases are given later on. Let me only stress for now that a collinear state can exist in the Y phase and one of the V phases. This collinear phase precisely corresponds to the plateau state.

Even if the spins orientations are known in one tetrahedron, there remains an extensive classical degeneracy related to the locations of these spins in neighboring tetrahedra, similar to the kagome case. Indeed, let us say that we have a set of 4 spin vectors $\mathbf{S}_a$, $\mathbf{S}_b$, $\mathbf{S}_c$ and $\mathbf{S}_d$ that verify Eq. (2.81). Then a classical ground state can be constructed by imposing that all tetrahedra of the lattice contain one spin of each orientation a, b, c and d [2]. This ground-state construction can be done in many ways,

[2]Note that contrary to the kagome lattice, it is also possible to construct ground states in which a different set of four spins is present in different tetrahedra, even with the coplanarity restriction.

and if we have LRO, the relative orientation of adjacent tetrahedra is encoded in the ordering wave-vector $\mathbf{Q}$.

The ordered structure with smallest magnetic unit cell corresponds to $\mathbf{Q} = \mathbf{0}$. In that case, all the blue tetrahedra are identical, meaning that on each of them, spins of same orientations are placed at the same position. The magnetic unit cell then corresponds to one tetrahedron of one kind - say blue tetrahedra on Fig. (2.8) - and contains thus $n = 4$ sites. This means that we can use 4 sublattices to describe our lattice, which correspond to the 4 spin orientations a, b, c and d. To each sublattice is attributed a different bosonic species. The spin-wave Hamiltonian is thus expressed in terms of the 4 corresponding sets of bosonic creation and annihilation operators $a_{\mathbf{k}}^{(\dagger)}, b_{\mathbf{k}}^{(\dagger)}, c_{\mathbf{k}}^{(\dagger)}, d_{\mathbf{k}}^{(\dagger)}$. The position $\mathbf{R}_c$ of a unit cell is given by:

$$\begin{aligned}
\mathbf{R}_c =& n_1\boldsymbol{\alpha}_1 + n_2\boldsymbol{\alpha}_2 + n_3\boldsymbol{\alpha}_3 \ , \qquad n_1, n_2, n_3 \in \mathbb{Z} \ , \\
\boldsymbol{\alpha}_1 =& \frac{a}{2}\,(0,1,1) \ , \qquad (2.82) \\
\boldsymbol{\alpha}_2 =& \frac{a}{2}\,(1,0,1) \ , \\
\boldsymbol{\alpha}_3 =& -\frac{a}{2}\,(1,1,0) \ , \qquad (2.83)
\end{aligned}$$

a being the characteristic length of the lattice. Note that the structure can be seen as an fcc superlattice of tetrahedral magnetic unit cells. A spin $\mathbf{S}_i$ is fully specified by its position $\mathbf{R}$ and its sublattice index $\alpha \in \{a, b, c, d\}$: $\mathbf{S}_i = \mathbf{S}_{\mathbf{R},\alpha}$. A given spin $\mathbf{S}_{\mathbf{R},\alpha}$ has 6 nearest neighbors, two of all other sublattices $\beta \neq \alpha$, located at symmetric positions $\mathbf{R} \pm \mathbf{r}_{\alpha\beta}$. The lattice thus has the center-symmetric property as depicted in Fig. (2.3). This allows us to write the Hamiltonian in the fashion of Eq. (2.17). The displacement vectors $\mathbf{r}_{\alpha\beta}$ between nearest-neighbor spins of different sublattices are given by:

$$\begin{aligned}
\mathbf{r}_{ab} =& \ a/4(0,1,1) \ , \quad \mathbf{r}_{bc} =& \ a/4(1,-1,0) \ , \\
\mathbf{r}_{ac} =& \ a/4(1,0,1) \ , \quad \mathbf{r}_{bd} =& \ a/4(1,0,-1) \ , \\
\mathbf{r}_{ad} =& \ a/4(1,1,0) \ , \quad \mathbf{r}_{cd} =& \ a/4(0,1,-1) \ .
\end{aligned} \qquad (2.84)$$

These vectors are substituted inside the spin-wave matrix $H_{\mathbf{k}}$, of which the coefficients are given by Eqs. (2.26 - 2.27). Then we proceed to the diagonalization of the reduced 4×4 system $\Gamma_{\mathbf{k}}$, of which the coefficients are given by Eqs. (2.35, 2.36).

2.4.1 Spin-wave spectrum of an arbitrary coplanar state

We are looking for the 4 eigenvalues $\lambda_{i\mathbf{k}}$ of the 4×4 matrix $\Gamma_{\mathbf{k}} = \Delta_{\mathbf{k}}\Sigma_{\mathbf{k}}$. Once again, for the sake of simplicity, we define the following:

$$\begin{aligned}
\mathcal{C}_1 &= \mathcal{C}_{ab} = \cos(\mathbf{k}\cdot\mathbf{r}_{ab}) & t_1 &= t_{ab} = \cos\theta_{ab} \\
\mathcal{C}_2 &= \mathcal{C}_{ac} = \cos(\mathbf{k}\cdot\mathbf{r}_{ac}) & t_2 &= t_{ac} = \cos\theta_{ac} \\
\mathcal{C}_3 &= \mathcal{C}_{ad} = \cos(\mathbf{k}\cdot\mathbf{r}_{ad}) \ , & t_3 &= t_{ad} = \cos\theta_{ad} \ . \\
\mathcal{C}_4 &= \mathcal{C}_{bc} = \cos(\mathbf{k}\cdot\mathbf{r}_{bc}) & t_4 &= t_{bc} = \cos\theta_{bc} \\
\mathcal{C}_5 &= \mathcal{C}_{bd} = \cos(\mathbf{k}\cdot\mathbf{r}_{bd}) & t_5 &= t_{bd} = \cos\theta_{bd} \\
\mathcal{C}_6 &= \mathcal{C}_{cd} = \cos(\mathbf{k}\cdot\mathbf{r}_{cd}) & t_6 &= t_{cd} = \cos\theta_{cd}
\end{aligned} \qquad (2.85)$$

These links are represented in Fig. (2.9) as colored numbers. The coefficients of the matrices $\Delta_{\mathbf{k}}$ and $\Sigma_{\mathbf{k}}$ are then given by Eq. (2.33):

$$\Delta_{\mathbf{k}} = 2JS \begin{pmatrix} 1 & \mathcal{C}_1 t_1 & \mathcal{C}_2 t_2 & \mathcal{C}_3 t_3 \\ \mathcal{C}_1 t_1 & 1 & \mathcal{C}_4 t_4 & \mathcal{C}_5 t_5 \\ \mathcal{C}_2 t_2 & \mathcal{C}_4 t_4 & 1 & \mathcal{C}_6 t_6 \\ \mathcal{C}_3 t_3 & \mathcal{C}_5 t_5 & \mathcal{C}_6 t_6 & 1 \end{pmatrix} , \qquad \Sigma_{\mathbf{k}} = 2JS \begin{pmatrix} 1 & \mathcal{C}_1 & \mathcal{C}_2 & \mathcal{C}_3 \\ \mathcal{C}_1 & 1 & \mathcal{C}_4 & \mathcal{C}_5 \\ \mathcal{C}_2 & \mathcal{C}_4 & 1 & \mathcal{C}_6 \\ \mathcal{C}_3 & \mathcal{C}_5 & \mathcal{C}_6 & 1 \end{pmatrix} . \tag{2.86}$$

As was the case for the kagome lattice, one can show that the determinant of $\Sigma_{\mathbf{k}}$ vanishes identically. In the pyrochlore lattice, it is even possible to show that not only one, but actually two of the 4 eigenvalues of $\Sigma_{\mathbf{k}}$ vanish. From the relation $\Gamma_{\mathbf{k}} = \Sigma_{\mathbf{k}} \cdot \Delta_{\mathbf{k}}$, this property directly transfers to $\Gamma_{\mathbf{k}}$. This induces the presence of two full flat, gapless modes of the magnon spectrum, *at any field value*. We stress that the matrix $\Sigma_{\mathbf{k}}$ only involves geometrical terms, and no information on spin orientations or magnetic field, such that this property is a geometrical property of the pyrochlore lattice with $\mathbf{Q} = \mathbf{0}$. Similarly to the kagome lattice, it is a signature of the classical ground-state degeneracy which is here even larger. Let us now proceed to finding the remaining two eigenvalues of $\Gamma_{\mathbf{k}}$. Taking into account the cancellation of two of the roots, the characteristic polynomial $p(\lambda)$ of $\Gamma_{\mathbf{k}}$ is given by:

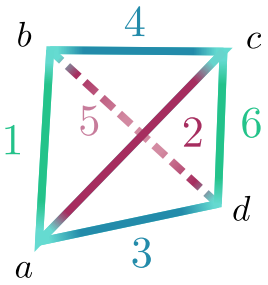

Figure 2.9: *One unit cell (tetrahedron).*

$$\begin{aligned} p(\lambda) =& \det\left(\Gamma_{\mathbf{k}} - \lambda \cdot \mathbb{I}_4\right) \\ =& \lambda^2 \left[\lambda^2 - b\lambda + c\right] = \lambda^2 \cdot p'(\lambda) , \end{aligned} \tag{2.87}$$

where we defined $p'(\lambda) = \lambda^2 - b\lambda + c$, and the b and c coefficients are given by:

$$\begin{aligned} b =& \Gamma^{aa} + \Gamma^{bb} + \Gamma^{cc} + \Gamma^{dd} = \mathrm{Tr}(\Gamma_{\mathbf{k}}) , \\ c =& \sum_{\alpha,\beta}^{\neq} \left(\Gamma^{\alpha\alpha}\Gamma^{\beta\beta} - \Gamma^{\alpha\beta}\Gamma^{\beta\alpha}\right) . \end{aligned} \tag{2.88}$$

The quartic polynomial of Eq. (2.87) has two vanishing roots, as said just above, and two non-vanishing roots which are the solutions of the quadratic equation $p'(\lambda) = 0$. The determinant of this polynomial is given by:

$$\Delta = b^2 - 4c .$$

It is quite cumbersome to derive the analytical expression for Δ in a compact form,

and we give here only the result:

$$\frac{\Delta}{(2JS)^4} = 4\Big\{ \sum_{i=1}^{6} \mathcal{C}_i^2 \left(1+t_i^2\right) - 2 + 2\sum_{\triangle} \mathcal{C}_\triangle \chi_\triangle + 2\left(t_1 t_6 \cdot \zeta_{16} + t_2 t_5 \cdot \zeta_{25} + t_3 t_4 \cdot \zeta_{34}\right) \Big\} \ . \tag{2.89}$$

The $\triangle$ symbol in the sum at the end of the top line, refers to the ensemble of the 4 triangular faces of the tetrahedron $(ijk) \in \{(124),(135),(236),(456)\}$, see Fig. (2.9). For such a triangle (ijk), we defined:

$$\mathcal{C}_\triangle = \mathcal{C}_i \mathcal{C}_j \mathcal{C}_k \ , \tag{2.90}$$

$$\chi_\triangle = \chi_{ijk} = t_i + t_j + t_k + t_i t_j + t_j t_k + t_k t_i \ . \tag{2.91}$$

The ζ_{ij} variables are defined as follows:

$$\zeta_{16} = \mathcal{C}_1 \mathcal{C}_6 \left(\mathcal{C}_2 \mathcal{C}_5 + \mathcal{C}_3 \mathcal{C}_4 - \mathcal{C}_1 \mathcal{C}_6\right) \ , \tag{2.92}$$

and ζ_{25} (resp. ζ_{34}) is obtained by swapping $(2,5)$ indices (resp. $(3,4)$ indices) with $(1,6)$ indices in Eq. (2.92). Note that the pairs $(1,6)$, $(2,5)$ and $(3,4)$ appearing as indices of ζ_{ij} variables correspond to the 3 pairs of opposite bonds in the tetrahedron (opposite in the sense that they have no common site). They are shown as bonds of the same color in Fig. (2.9). The two non-zero roots of Eq. (2.87) have the following form:

$$\frac{\lambda_{\mathbf{k}}^{\pm}}{(2JS)^2} = \frac{1}{2}\left[4 + 2\sum_{i=1}^{6} \mathcal{C}_i^2 t_i \pm \sqrt{\Delta/(2JS)^4}\right] \ . \tag{2.93}$$

The corresponding spin-wave modes are finally given by:

$$\epsilon_{\mathbf{k}}^{\pm} = \left\{\lambda_{\mathbf{k}}^{\pm}\right\}^{1/2} \ . \tag{2.94}$$

The pyrochlore Heisenberg AFM with $\mathbf{Q} = \mathbf{0}$ has 4 spin-wave modes. In the harmonic approximation, two of these modes are dispersionless and of zero energy $\epsilon_{0\mathbf{k}} = 0$. As was the case in the kagome lattice, this is an artefact of the harmonic approximation, and these zero-energy modes are unprotected by the Goldstone theorem. They are related to the extensive classical ground-state degeneracy. The spectra $\epsilon_{\mathbf{k}}^{\pm}$ of the two remaining modes are given by Eqs. (2.89-2.94).

These expressions do not show any explicit dependency with respect to the magnetic field strength h so far. The above derivation is thus applicable to any *coplanar* classical ground state with $\mathbf{Q} = \mathbf{0}$. The explicit dependency with respect to field h will be contained in the azimutal canting angles θ_α of the spins in the classical ground state - and consequently, in the t_i variables defined in Eq. (2.85). Let me give the two relations, which are useful in the upcoming analytical derivation of the spectra:

$$2\mathcal{C}_\triangle = \mathcal{C}_i^2 + \mathcal{C}_j^2 + \mathcal{C}_k^2 - 1 \Rightarrow \sum_{\triangle} \mathcal{C}_\triangle = \sum_i \mathcal{C}_i^2 - 2 \ . \tag{2.95}$$

This first equality is shown in the same way as was Eq. (2.49) in the kagome lattice. Also we have, using the above and from cancellation of the determinant of $\Sigma_{\mathbf{k}}$:

$$\begin{aligned}\det(\Sigma_{\mathbf{k}}) =& 0 = 1 - \sum_i \mathcal{C}_i^2 + 2\sum_{\triangle} \mathcal{C}_{\triangle} - (\zeta_{16} + \zeta_{25} + \zeta_{34}) \\ \Rightarrow& \zeta_{16} + \zeta_{25} + \zeta_{34} = \sum_i \mathcal{C}_i^2 - 3 \ . \end{aligned} \tag{2.96}$$

2.4.2 The Y and V states

As for the kagome lattice, in zero field, the constraint of Eq. (2.8) imposes that the total spin $\mathbf{S}_b$ vanishes on each frustrated block. Unlike in the kagome lattice however, where this could be done uniquely - modulo global rotation - with the 120° structure on a triangular cell, here there remains 2 continuous accidental degrees of freedom. When one restricts to coplanar configurations, this reduces to one continuous degree of freedom. Indeed, any two pairs of antiparallel spins with arbitrary orientations satisfy the constraint of vanishing total spin on a tetrahedron. The continuous degree of freedom is set by the relative angle ϕ between the two orientations. Among all these configurations, only one is fully collinear. It is the collinear up-up-down-down (uudd) state where two spins are pointing in a given direction (say spins of sublattices a and b), and the two others point in the opposite direction (sublattices c and d). It corresponds to the situation $\phi = 0$ or $\phi = \pi$, and is expected to be selected by quantum fluctuations.

When H is increased, the spins progressively cant toward the field to keep satisfying Eq. (2.8). This increases even further the degree of degeneracy, even with the requirement of a coplanar spin configuration. The classical states favored by quantum or thermal fluctuations can in principle be guessed by adding a negative biquadratic exchange term in the Hamiltonian, and solving the classical minimization problem at the scale of one tetrahedron. From [40], the selected configurations are two different V states and a Y state, all being coplanar. Fig. (2.10) shows a representation of these configurations on a tetrahedron. Let me now describe them in more details.

The 22V state

The most intuitive canting configuration is the symmetric 22V state, as it keeps some symmetry of the initial collinear configuration at $H = 0$. Indeed, in the 22V state, spins are paired, and spins inside a given pair have the same orientation. Namely, we chose that the spins a and b cant toward the magnetic field direction z_0 with a given angle θ_{22V}, while the spins c and d cant towards the field with the opposite angle $-\theta_{22V}$. It is shown on the bottom panel of Fig. (2.10). The classical constraint of Eq. (2.14) implies:

$$\cos\theta_{22V} = h \ . \tag{2.97}$$

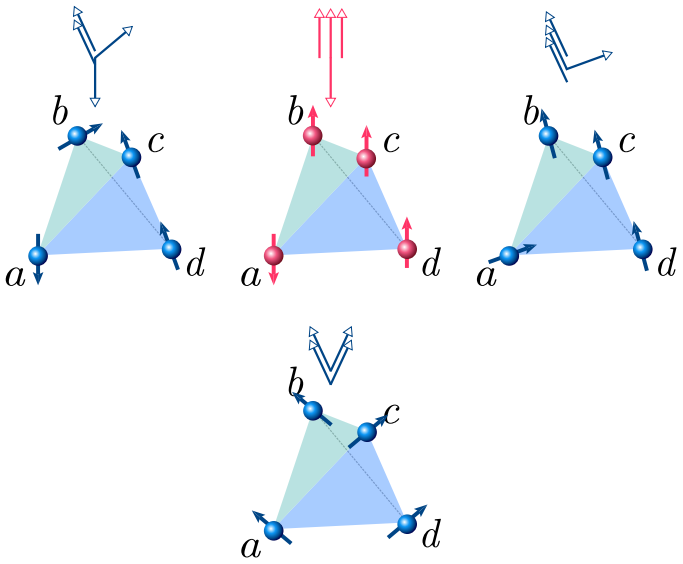

Figure 2.10: *Coplanar ground-state spin configurations of the pyrochlore Heisenberg AFM in field. The top row shows (from left to right) the 211Y, the uuud and the 31V configurations, while bottom row shows the 22V configuration.*

Then we have:

$$\cos\theta_a = \cos\theta_b = \cos\theta_c = \cos\theta_d = \cos\theta_{22V} \ . \tag{2.98}$$

The constraint on the sines (Eq. (2.15)) is verified from the symmetry of this state. The 22V configuration remains a valid classical ground state over the whole magnetization process, that is, for $0 \leq h \leq 1$.

The 211Y state

Another possible coplanar canting configuration in low field is the 211Y state, and is shown on the top left panel of Fig. (2.10). One of the spins (say of sublattice a) remains antiparallel to the field, while two other spins (say sublattices c and d) are paired together and cant towards the field with an angle θ_{Y1}. The last spin (sublattice b) also cants towards the field with an angle $-\theta_{Y2}$. The constraint of Eq. (2.14) on the cosines leads to:

$$2\cos\theta_{Y1} + \cos\theta_{Y2} - 1 = 4h \Rightarrow \cos\theta_{Y2} = 4h + 1 - 2\cos\theta_{Y1} \ . \tag{2.99}$$

Then the constraint on the sines, given by Eq. (2.15), leads to:

$$2\sin\theta_{Y1} = \sin\theta_{Y2} \Rightarrow 4\sin^2\theta_{Y1} = \sin^2\theta_{Y2} \Rightarrow \cos^2\theta_{Y2} = 4\cos^2\theta_{Y1} - 3 \ . \tag{2.100}$$

Squaring Eq. (2.99) and substituting Eq. (2.100), one obtains finally the expression for the two canting angles:

$$\cos\theta_{Y1} = \frac{4h^2 + 2h + 1}{4h + 1} \ , \qquad \cos\theta_{Y2} = \frac{8h^2 + 4h - 1}{4h + 1} \ . \tag{2.101}$$

Then we have explicitly for each sublattice:

$$\begin{aligned} \cos\theta_a &= -1 \ , \\ \cos\theta_b = \cos\theta_c &= \cos\theta_{Y1} \ , \\ \cos\theta_d &= \cos\theta_{Y2} \ . \end{aligned} \tag{2.102}$$

The condition that $-1 \leq \cos\theta_{Yi} \leq 1$ (and choosing by convention $h \geq 0$) implies that this configuration is only a valid classical ground state in the low-field region where $0 \leq h \leq 1/2$. At the critical field $h_c = 1/2$, three of the spins are pointing along the field, while the 4^{th} remains antiparallel to it. This is the collinear up-up-up-down ($uuud$) structure shown on the top middle panel of Fig. (2.10). This collinear configuration has the fractional magnetization $m = 1/2$.

The 31V state

At higher fields $h \geq h_c$, the antiparallel spin starts canting as well along the field in order to keep satisfying the classical constraint of Eq. (2.8). The other three spins need to compensate in order to satisfy the constraint on the sines (see Eq. (2.15)), and are therefore canted as well. The collinearity of the state is maximized if these three spins remain parallel to each other. This is the 31V state, shown on the top right panel of Fig. (2.10). The single spin (say of sublattice a) has a canting angle θ_{3V1}, while the other three spins sustain an angle θ_{3V2}. The constraint on cosines given by Eq. (2.14) imposes:

$$3\cos\theta_{3V2} + \cos\theta_{3V1} = 4h \Rightarrow \cos\theta_{3V1} = 4h - 3\cos\theta_{3V2} \ . \tag{2.103}$$

The constraint on sines (Eq. (2.15)) gives:

$$3\sin\theta_{3V2} = \sin\theta_{3V1} \Rightarrow 9\sin^2\theta_{3V2} = \sin^2\theta_{3V1} \Rightarrow \cos^2\theta_{3V1} = 9\cos^2\theta_{3V2} - 8 \ . \tag{2.104}$$

Substituting this relation into the square of Eq. (2.103) leads to the following canting angles:

$$\cos\theta_{3V1} = \frac{2h^2 - 1}{h} \ , \qquad \cos\theta_{3V2} = \frac{2h^2 + 1}{3h} \ . \tag{2.105}$$

Then we have for each sublattice:

$$\begin{aligned} \cos\theta_a &= \cos\theta_{3V1} \ , \\ \cos\theta_b = \cos\theta_c &= \cos\theta_d = \cos\theta_{3V2} \ . \end{aligned} \tag{2.106}$$

The condition $-1 \leq \cos\theta_{3Vi} \leq 1$ implies that the 3:1V configuration is only valid in the high field region $1/2 \leq h \leq 1$. At saturation ($h = h_{\text{sat}} = 1$), all the spins of the lattice are aligned with the field in the fully polarized FM state. Note that at the lower field boundary $h_c = 1/2$, the 31V state is in the collinear $uuud$ configuration.

Summary

The 22V, 211Y and the 31V states are our classical starting points to the spin-wave expansion. The 211Y and 31V states are classically stable in the low-field and high-field regions, respectively, and become the collinear *uuud* state at their critical field boundary $h_c = 1/2$. This *uuud* state corresponds to the semiclassical plateau state with fractional magnetization $m_p = 1/2$. The 22V state is classically stable at any field value until saturation, and is thus competing with the 211Y and 31V states all along the magnetization process. Note that although the 22V state retains more collinearity than the 211Y and 22V states, it does not permit the fully collinear *uuud* configuration.

2.4.3 Specific spin-wave spectra

Expressions for the opening angles t_i defined in Eq. (2.85) are obtained from the classical canting angles θ_α, see Eqs.(2.97 - 2.106). These t_i variables are then substituted into Eqs. (2.89-2.94), and one obtains analytical expressions for the spectra of the competing states, which explicitly depend on h. For the sake of readability, all functions or variables associated to the the symmetric 22V and asymmetric 31V states will be indicated with the subscripts V_s and V_a, respectively. Functions or variables associated to the 211Y state will go with the subscript Y.

The symmetric 22V state

From Eqs. (2.97, 2.98), we have the following for the opening angles t_i defined in Eq. (2.85):

$$\left.\begin{array}{l} t_1 = t_6 = t_1 t_6 = 1 \ , \\ t_i = t_1 t_i = t_i t_6 = 2h^2 - 1 \ , \\ t_i t_j = (2h^2-1)^2 \ , \end{array}\right\} \text{for } i \in \{2,3,4,5\}. \tag{2.107}$$

Substituting these expressions into Eq. (2.89), we obtain:

$$\begin{aligned} \frac{\Delta_{V_s}(h)}{(2JS)^4} =& 16h^2 \left\{ \left(h^2-1\right) \left[5\left(\Sigma_i \mathcal{C}_i^2 - 2\right) - \left(\mathcal{C}_1^2 + \mathcal{C}_6^2\right) - 2\zeta_{16} \right] + 4\left(\Sigma_i \mathcal{C}_i^2 - 2\right) \right\} \\ =& 16h^2 \cdot \delta_{V_s}(h) \ . \end{aligned} \tag{2.108}$$

Then the two eigenvalues $\lambda^{\pm}_{V_s\mathbf{k}}$ are obtained from Eq. (2.93):

$$\frac{\lambda^{\pm}_{V_s\mathbf{k}}}{(2JS)^2} = 2 + \Sigma_i \mathcal{C}_i^2 + 2\left(h^2-1\right)\left(\mathcal{C}_2^2 + \mathcal{C}_3^2 + \mathcal{C}_4^2 + \mathcal{C}_5^2\right) \pm 2h\sqrt{\delta_{V_s}(h)} \ .$$

Finally, the two non-zero magnon modes $\epsilon^{\pm}_{V_s\mathbf{k}}$ are given by Eq. (2.94):

$$\frac{\epsilon^{\pm}_{V_s\mathbf{k}}}{2JS} = \left\{ 2 + \Sigma_i \mathcal{C}_i^2 + 2\left(h^2-1\right)\left(\mathcal{C}_2^2 + \mathcal{C}_3^2 + \mathcal{C}_4^2 + \mathcal{C}_5^2\right) \pm 2h\sqrt{\delta_{V_s}(h)} \right\}^{1/2} . \tag{2.109}$$

I also give for the sake of completeness the expression for the derivative of $\lambda^{\pm}_{V_s\mathbf{k}}$ with respect to h, as it is useful for computing the magnetization curve from Eq. (2.40):

$$\frac{\partial}{\partial h}\left[\frac{\lambda^{\pm}_{V_s\mathbf{k}}}{(2JS)^2}\right] = 4h\left[\Sigma_i\mathcal{C}_i^2 - \left(\mathcal{C}_1^2+\mathcal{C}_6^2\right)\right] \pm \frac{2f_{V_s}(h)}{\delta_{V_s}(h)} \ , \tag{2.110}$$

where I defined the function $f_{V_s}(h)$ as follows:

$$f_{V_s}(h) = 4\left(\Sigma_i\mathcal{C}_i^2-2\right) + \left(2h^2-1\right)\left[5\left(\Sigma_i\mathcal{C}_i^2-2\right) - \left(\mathcal{C}_1^2+\mathcal{C}_6^2\right) - 2\zeta_{16}\right] \ . \tag{2.111}$$

The asymmetric 31V state in the high-field region

From the expressions for the canting angles of Eqs. (2.105, 2.106), we get the following for t_i variables defined in Eq. (2.85):

$$\left.\begin{array}{l} t_4 = t_5 = t_6 = t_4t_5 = t_4t_6 = t_5t_6 = 1 \ , \\ t_i = t_it_4 = t_it_5 = t_it_6 = \left(8h^2-5\right)/3 \ , \\ t_it_j = \left[\left(8h^2-5\right)/3\right]^2 \ , \end{array}\right\} \text{for } i\in\{1,2,3\}. \tag{2.112}$$

Substituting these into Eq. (2.89), we obtain:

$$\begin{aligned}\frac{\Delta_{V_a}(h)}{(2JS)^4} = \frac{64}{9}\Big\{6\left(1-h^2\right)\left(2h^2+1\right)\Big[\Sigma_i\mathcal{C}_i^2\left(2h^2+1\right) - 6h^2 \\ + 4\left(\mathcal{C}_1^2+\mathcal{C}_2^2+\mathcal{C}_3^2\right)\left(h^2-1\right)\Big]\Big\} = \frac{16}{9}\cdot\delta_{V_a}(h) \ .\end{aligned} \tag{2.113}$$

The two eigenvalues $\lambda^{\pm}_{V_a\mathbf{k}}$ are thus given by Eq. (2.93):

$$\frac{\lambda^{\pm}_{V_a\mathbf{k}}}{(2JS)^2} = \frac{1}{3}\left\{6+3\sum_i\mathcal{C}_i^2 + 8\left(h^2-1\right)\left(\mathcal{C}_1^2+\mathcal{C}_2^2+\mathcal{C}_3^2\right) \pm 4\sqrt{\delta_{V_a}(h)}\right\} \ . \tag{2.114}$$

The two branches of the spin-wave spectrum $\epsilon^{\pm}_{V_a\mathbf{k}}$ are finally obtained from Eq. (2.94):

$$\frac{\epsilon^{\pm}_{V_a\mathbf{k}}}{2JS} = \frac{1}{\sqrt{3}}\left\{6+3\sum_i\mathcal{C}_i^2 + 8\left(h^2-1\right)\left(\mathcal{C}_1^2+\mathcal{C}_2^2+\mathcal{C}_3^2\right) \pm 4\sqrt{\delta_{V_a}(h)}\right\}^{1/2} \ . \tag{2.115}$$

I give as well the derivative of $\lambda^{\pm}_{V_a\mathbf{k}}$ with respect to h:

$$\frac{\partial}{\partial h}\left[\frac{\lambda^{\pm}_{V_a\mathbf{k}}}{(2JS)^2}\right] = \frac{16h}{3}\left\{\mathcal{C}_1^2+\mathcal{C}_2^2+\mathcal{C}_3^2 \pm \frac{f_{V_a}(h)}{\sqrt{\delta_{V_a}(h)}}\right\} \ , \tag{2.116}$$

where $f_{V_a}(h)$ was defined as follows:

$$f_{V_a}(h) = \left(\mathcal{C}_4^2+\mathcal{C}_5^2+\mathcal{C}_6^2\right)\left(1-4h^2\right) + 6h^2\sum_i\mathcal{C}_i^2 - 3\left(1+2h^2\right) \ . \tag{2.117}$$

The 211Y state in the low-field region

In the low-field 211Y state, all calculations are more cumbersome due to the low symmetry of this state. The expressions for opening angles t_i are obtained from Eqs. (2.101, 2.102):

$$\begin{aligned} t_6 &= 1 \ , \\ t_1 = t_1 t_6 &= -\left(8h^2+4h-1\right)/\left(4h+1\right) = -\alpha \ , \\ t_2 = t_3 = t_2 t_6 &= t_3 t_6 = -\left(4h^2+2h+1\right)/\left(4h+1\right) = -\beta \ , \\ t_4 = t_5 = t_4 t_6 &= t_5 t_6 = 4h^2+2h-1 = \gamma \ . \end{aligned} \tag{2.118}$$

Substituting these into Eq. (2.89) leads to very lengthy expression. After developing the terms as a polynomial of h, we obtain:

$$\begin{aligned} \frac{\Delta_Y(h)}{(2JS)^4} =& \frac{16}{(4h+1)^2} \cdot \left\{64h^6 p_6 + 16h^5 p_5 + 4h^4 p_4 + 4h^3 p_3 + h^2 p_2 + h p_1\right\} \\ =& \frac{16}{(4h+1)^2} \cdot \delta_Y(h) \ . \end{aligned} \tag{2.119}$$

where the polynomial coefficients are given by:

$$\begin{aligned} p_1 =& \Sigma_{i=2}^5 \mathcal{C}_i^2 - 2\left[1+\zeta_{16}\right] \ , \\ p_2 =& \Sigma_{i=2}^5 \mathcal{C}_i^2 + 4\left(\mathcal{C}_1^2+\mathcal{C}_6^2\right) + 8 - 10\left[1+\zeta_{16}\right] \ , \\ p_3 =& 4\mathcal{C}_6^2 - 6\left(\mathcal{C}_2^2+\mathcal{C}_3^2\right) + 2\left(\mathcal{C}_4^2+\mathcal{C}_5^2\right) + 4 \ , \\ p_4 =& 12\left(\mathcal{C}_6^2 - 2\mathcal{C}_1^2\right) - 17\left(\mathcal{C}_2^2+\mathcal{C}_3^2\right) + 7\left(\mathcal{C}_4^2+\mathcal{C}_5^2\right) + 16 + 10\left[1+\zeta_{16}\right] \ , \\ p_5 =& 4\left(\mathcal{C}_6^2 - 2\mathcal{C}_1^2\right) - 5\left(\mathcal{C}_2^2+\mathcal{C}_3^2\right) + 7\left(\mathcal{C}_4^2+\mathcal{C}_5^2\right) + 4 + 2\left[1+\zeta_{16}\right] \ , \\ p_6 =& 2\left(\mathcal{C}_4^2+\mathcal{C}_5^2\right) + \mathcal{C}_6^2 - 1 \ . \end{aligned} \tag{2.120}$$

The two non-zero eigenvalues $\lambda_{Y\mathbf{k}}^{\pm}$ are given by Eq. (2.93):

$$\begin{aligned} \frac{\lambda_{Y\mathbf{k}}^{\pm}}{(2JS)^2} =& \left(4h^2+2h-1\right)\left(\Sigma_{i=2}^5 \mathcal{C}_i^2\right) + \mathcal{C}_1^2 + \mathcal{C}_6^2 + 2 \\ & - \frac{8h(h+1)}{4h+1}\left[2h\left(\mathcal{C}_2^2+\mathcal{C}_3^2\right) + \mathcal{C}_1^2\right] \pm \frac{2\sqrt{\delta_Y(h)}}{4h+1} \end{aligned}$$

The magnon modes $\epsilon_{Y\mathbf{k}}^{\pm}$ are then:

$$\begin{aligned} \frac{\epsilon_{Y\mathbf{k}}^{\pm}}{2JS} =& \left\{ \left(4h^2+2h-1\right)\left(\Sigma_{i=2}^5 \mathcal{C}_i^2\right) + \mathcal{C}_1^2 + \mathcal{C}_6^2 + 2 \right. \\ & \left. - \frac{8h(h+1)}{4h+1}\left[2h\left(\mathcal{C}_2^2+\mathcal{C}_3^2\right) + \mathcal{C}_1^2\right] \pm \frac{2\sqrt{\delta_Y(h)}}{4h+1} \right\}^{1/2} \ . \end{aligned} \tag{2.121}$$

Finally, the derivative of $\lambda^{\pm}_{Y\mathbf{k}}$ with respect to h is:

$$\frac{\partial}{\partial h}\left[\frac{\lambda^{\pm}_{Y\mathbf{k}}}{(2JS)^2}\right] = \frac{1}{(4h+1)^2}\Bigg\{8h\Big[\left(16h^2+12h+3\right)\left(\mathcal{C}_4^2+\mathcal{C}_5^2\right) - (2h+1)\left(2\mathcal{C}_1^2+\mathcal{C}_2^2+\mathcal{C}_3^2\right)\Big] + 2\left(\mathcal{C}_2^2+\mathcal{C}_3^2+\mathcal{C}_4^2+\mathcal{C}_5^2-4\mathcal{C}_1^2\right) \pm \frac{f_Y(h)}{\sqrt{\delta_Y(h)}}\Bigg\}\,, \tag{2.122}$$

where $f_Y(h)$ has been defined as:

$$f_Y(h) = 1024h^6q_6 + 192h^5q_5 + 16h^4q_4 + 16h^3q_3 + 12h^2q_2 + 2hq_1 + q_0\ . \tag{2.123}$$

The polynomial coefficients are given below:

$$\begin{aligned}
q_0 =& -2 + \mathcal{C}_2^2+\mathcal{C}_3^2+\mathcal{C}_4^2+\mathcal{C}_5^2-2\zeta_{16}\ ,\\
q_1 =& 2 + 4\left(\mathcal{C}_1^2+\mathcal{C}_6^2\right) - \left(\mathcal{C}_2^2+\mathcal{C}_3^2+\mathcal{C}_4^2+\mathcal{C}_5^2\right) - 6\zeta_{16}\ ,\\
q_2 =& 4 + 4\mathcal{C}_6^2 - 6\left(\mathcal{C}_2^2+\mathcal{C}_3^2\right) + 2\left(\mathcal{C}_4^2+\mathcal{C}_5^2\right)\ ,\\
q_3 =& 30 + 16\mathcal{C}_6^2 - 24\mathcal{C}_1^2 - 23\left(\mathcal{C}_2^2+\mathcal{C}_3^2\right) + 9\left(\mathcal{C}_4^2+\mathcal{C}_5^2\right) + 10\zeta_{16}\ ,\\
q_4 =& 82 + 44\mathcal{C}_6^2 - 88\mathcal{C}_1^2 - 59\left(\mathcal{C}_2^2+\mathcal{C}_3^2\right) + 49\left(\mathcal{C}_4^2+\mathcal{C}_5^2\right) + 30\zeta_{16}\ ,\\
q_5 =& 4 - 8\mathcal{C}_1^2 + 6\mathcal{C}_6^2 - 5\left(\mathcal{C}_2^2+\mathcal{C}_3^2\right) + 11\left(\mathcal{C}_4^2+\mathcal{C}_5^2\right) + 2\zeta_{16}\ ,\\
q_6 =& 2\left(\mathcal{C}_4^2+\mathcal{C}_5^2\right) + \mathcal{C}_6^2 - 1\ .
\end{aligned} \tag{2.124}$$

2.4.4 Magnetization curve

From the above analytical expressions for the harmonic spin-wave spectra in the 22V, 211Y and 31V phases, it is now possible to compute the quantum correction $\Delta E_{\rm q}$ to the ground-state energy of the pyrochlore Heisenberg AFM in field. We remind the reader of the definition of the normalized energy correction per spin $\Delta e_{\rm q}$ given in Eq. (2.78). The integral is performed using standard Monte-Carlo integration over the first Brillouin zone of the pyrochlore lattice.

The top panel of Fig. (2.11) shows $\Delta e_{\rm q}$ as a function of the applied magnetic field h. The 22V state has lowest energy only in the very low-field region. At some field value $h^* \simeq 0.18$, there is a phase transition to the 211Y phase, which remains the ground state until $h = 1/2$. For $1/2 \leq h \leq 1$, the system is in the 31V state. We see a clear cusp in the zero-point energy at the critical field $h = 1/2$, between the 211Y and 31V states, similar to what was seen in the kagome lattice. The quantum corrections are suppressed at saturation field.

The magnetization curve is obtained as for the kagome lattice. We use Eqs. (2.108-2.111) for the 22V state, Eqs. (2.113- 2.117) for the 31V state, and Eqs. (2.119-2.124) for the 211Y state. The integral in Eq. (2.40) is obtained using standard Monte Carlo

integration over the first Brillouin zone. The resulting magnetization curve is shown on the bottom panel of figure 2.11 for $S = 1$. We used $N_{\mathrm{MC}} = 4 \cdot 10^6$ Monte-Carlo points to compute this curve.

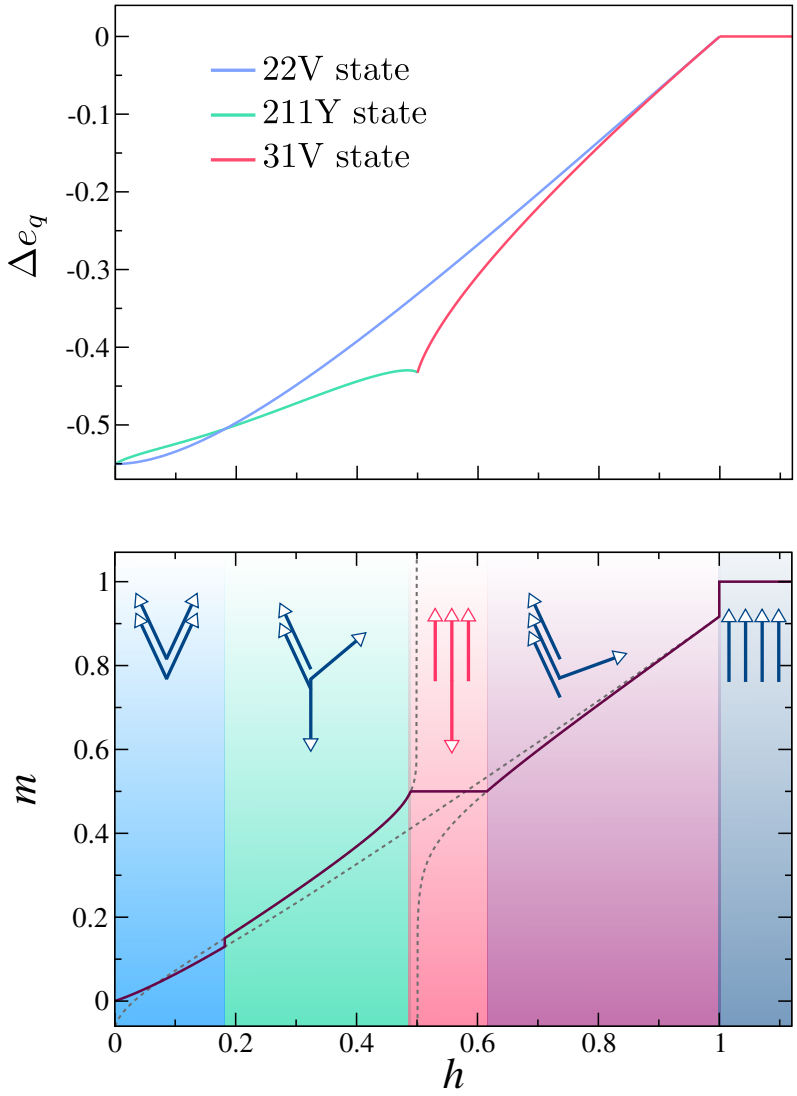

Figure 2.11: *Quantum correction Δe_q to the ground-state energy and magnetization curve of the spin-1 pyrochlore Heisenberg AFM as a function of magnetic field $h = H/H_{sat}$. In the magnetization plot, dashed lines show the magnetization obtained within linear spin-wave theory in the 22V, 211Y and 31V states. The purple line shows the final magnetization curve. The arrows depict the spin configuration in each phase.*

The magnetization diverges in the 211Y and 31V states in the limit $h \to 1/2$, as is seen from the dashed lines on Fig. (2.11). Using the same argument as for the kagome lattice, we intersect those diverging curves with the plateau value $m = 1/2$ to determine

the boundary fields of the plateau phase. Note as well that the transition between the 22V and 211Y states at $h = h^*$, has to be taken into account. This induces a jump of the magnetization, since the slope of the ground-state energy is discontinuous at this phase transition, as is seen from the top panel of Fig. (2.11). The final magnetization curve is shown by the dark purple line. As was the case in the kagome lattice, there is a magnetization jump upon saturation due to quantum fluctuations being suppressed in the polarized phase. Once again, the height of the plateau resembles the height that is predicted theoretically from the condensation of localized magnons [49, 85]:

$$\delta m = 1/(12S) \ . \tag{2.125}$$

The $1/S$ correction to the susceptibility was estimated by fitting the quantum correction to the magnetization towards $h \to 0$:

$$\chi = \frac{1}{8J}\left(1 - 0.526(1)/S\right) \ , \tag{2.126}$$

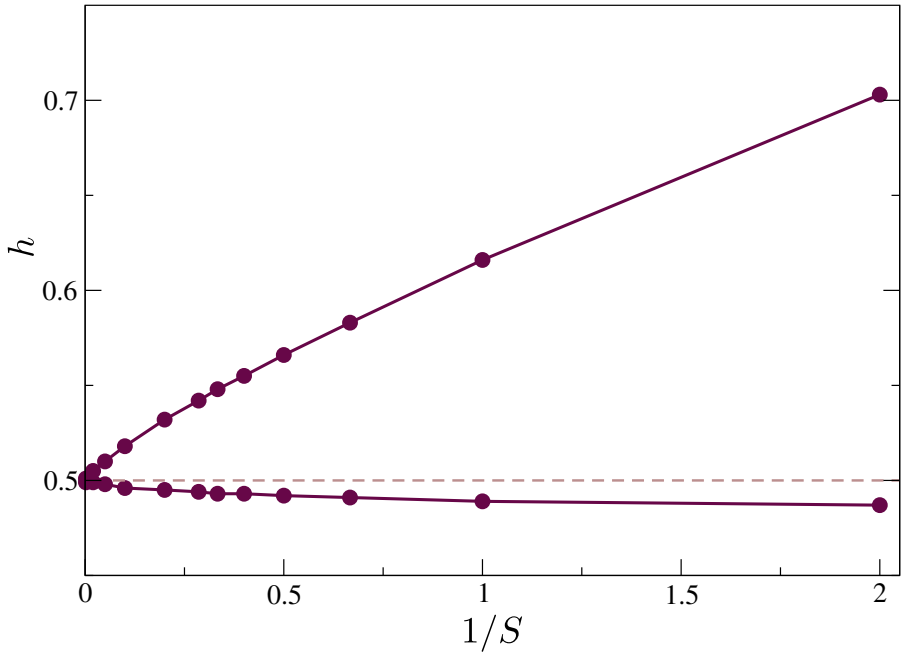

Figure 2.12: *Field boundaries h_{c1} and h_{c2} of the 1/3-magnetization plateau in the pyrochlore Heisenberg AFM, as a function of inverse spin. The dashed light brown line shows $h_c = 1/2$ as a guide to the eye.*

where the classical susceptibility is $\chi_{\rm cl} = 1/(8J)$. The above correction is much larger than the correction obtained for the kagome lattice, see Eq. (2.80). This is related to the fact that the classical ground-state degeneracy of the Heisenberg model on the pyrochlore lattice is larger than on the kagome lattice. Note that for the extreme quantum case $S = 1/2$, Eq. (2.126) even leads to a negative value of the magnetic susceptibility at $H = 0$, which is of course unphysical. This could be interpreted as the signature of a possible disordered state. Indeed, the ground state of the quantum pyrochlore AFM might be a quantum spin liquid state [57, 86]. This result should, however, not be taken too seriously, as no true quantitative conclusion can be reasonably made regarding $S = 1/2$ in such a highly frustrated system from linear spin-wave theory.

The values for the plateau field boundaries as a function of $1/S$ have been reported on Fig. (2.12). Once again, the plateau width decreases with increasing spin length S, and ultimately vanishes completely in the classical limit $S \to \infty$. The asymmetry of the plateau phase with respect to the critical field $h = 1/2$, is even more striking than in the kagome lattice, and the lower field boundary remains rather close to $h = 1/2$, even at $S = 1/2$.

2.5 Discussion and conclusion

In order to evaluate the efficiency of an analytical technique, it is useful to compare its results to other available numerical results. In this aim, Fig. (2.13) shows the

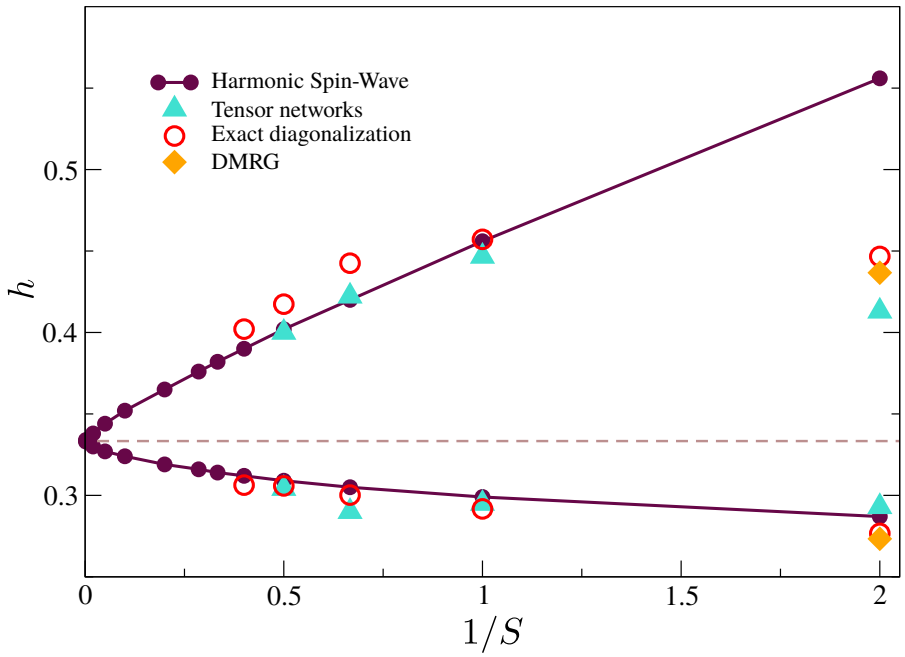

Figure 2.13: *Field boundaries h_{c1} and h_{c2} of the 1/3-magnetization plateau in the kagome Heisenberg AFM, as a function of inverse spin. The purple points with purple curve were obtained in the present work from harmonic spin-wave theory. The blue triangles, red circles and orange diamonds display numerical results obtained by the Tensor Networks (iPEPS) in [58], the exact diagonalization of finite-size clusters in [47, 87], and the DMRG calculations in [30], respectively.*

plateau field boundaries for the kagome lattice, as a function of $1/S$, obtained from various numerical techniques, including the present work. The first observation that we make is that the plateau width decreases with increasing S, until ultimately vanishing completely for the classical limit $S = \infty$. This is because the magnetization plateau is a quantum effect. Indeed, it is stabilized quantum fluctuations, which vanish in the classical limit. In the classical limit, the *uud* state is only stable at $h = 1/3$, and the two field boundaries indeed converge exactly to this value.

The values obtained in my work using LSWT match well the numerical values for $S \geq 1$, especially the tensor networks values. For the extreme quantum case $S = 1/2$, it

seems that LSWT is still efficient in estimating the lower bound of the plateau, but fails to obtain the upper bound, which is largely overestimated. This is not surprising, as it is well established that the plateau state for $S = 1/2$ is a quantum valence-bond crystal of localized magnons with 3 resonating spin-flips on one third of all the hexagons. This state resembles a semiclassical *uud* state on the $\sqrt{3} \times \sqrt{3}$ structure. Because this plateau state is intrinsically quantum, obviously it cannot be well described by SWT. The surrounding compressible phases also probably retain a similar order and cannot be well described by SWT on the semiclassical canted Y and V states. The quantum tunneling required to obtain this resonating state involves 6-th order processes in the case of $S = 1/2$. Higher order processes are involved to obtain the same type of state with larger spins, which makes its stabilization less probable.

The fact that the values obtained in my work fit quite well previous numerical values, is an encouraging perspective for the plateau boundaries found in the case of the pyrochlore lattice as well (at least for $S \geq 1$). In general, such a simple analytical technique to study magnetization plateaus stabilized by quantum fluctuations, is very valuable in the context of 3D systems, where numerical studies are much more limited.

2.5.1 Magnetization singularities at plateau boundaries

Quantum fluctuations are also responsible for the divergence of the the magnetization of the surrounding canted Y and V phases at $h \to h_c$, where $h_c = 1/3$ in the kagome lattice, and $h_c = 1/2$ in the pyrochlore lattice. The quantum correction to the ground-state energy leads to a cusp at h_c, as we see on the top panels of Fig (2.6) and Fig. (2.11) for the kagome and pyrochlore lattices, respectively. When we differentiate the ground-state energy with respect to the field, this cusp intuitively gives rise to an increasing slope of the magnetization toward h_c. The asymptotic behaviour of m close to h_c is related to the extra softness of the zero-energy modes of the collinear phase, compared to its surrounding canted counterparts.

In an AFM, the soft modes in the collinear phase have typically a quadratic dispersion around the zero-energy modes, similar to what is seen in a ferromagnet:

$$\epsilon(\mathbf{k}) \sim \delta k^2 \ , \tag{2.127}$$

where δk is the distance to the zero-energy mode. In the canted phases, the dispersion acquires a linear component around the zero-energy modes, which increases as h goes away from h_c. We have something like:

$$\epsilon(\mathbf{k}) \sim \sqrt{\Delta_h \delta k^2 + \delta k^4} \ , \tag{2.128}$$

where $\Delta_h = |h - h_c|$. One can show that such a dispersion leads to the asymptotic form:

$$\Delta m \sim \Delta_h \ln \Delta_h \ , \tag{2.129}$$

where $\Delta m = m_{\rm cl} - m$. For example, see [29] for the (non-frustrated) square lattice AFM close to saturation field, or for the (frustrated) triangular AFM close to the plateau.

The behavior described by Eq. (2.129) is singular but non divergent, as it retains a finite value at h_c. The derivative of m goes to ∞, such that the magnetization arrives to the plateau with an infinite slope. As the quantum correction given by Eq. (2.129) comes with a factor $1/S$ compared to the classical magnetization $m_{\rm cl} = hS$, the larger is S, the less dramatic is the divergence, which comes back to the fact that the plateau vanishes when $S \to \infty$.

In the case of the kagome lattice, which is highly degenerate, the situation is more complex and the magnetization obtained from the harmonic spectrum actually diverges at h_c. Expanding the analytical expressions for the dispersive bands of the spectrum given by Eq. (2.70) and Eq. (2.76) for the Y and V states, respectively, around the Γ point gives the following expression:

$$\left.\frac{\epsilon^-_{\mathbf{k}}}{2JS}\right|_{\mathbf{k}\to\mathbf{0}} \simeq 2\left\{3\Delta_h\kappa^2_{x/y} + \left(\kappa_x^2 - \kappa_y^2\right)^2\right\}^{1/2} , \tag{2.130}$$

where $\kappa_{x/y} = \kappa_x$ for the Y state, and $\kappa_{x/y} = \kappa_y$ for the V state. It is possible to show from this asymptotic expression of the low-energy modes, that the magnetization obtained by differentiating the ground-state energy diverges as $\ln \Delta_h$ when $\Delta_h \to 0$. This divergent behaviour is a consequence of the remaining lines of zero-energy when $\kappa_x^2 = \kappa_y^2$. Indeed, due to these lines, the dimensionality of the lattice is somehow reduced. This leads to a more singular, divergent behaviour, compared to the typical expected behaviour of a 2D AFM. Specifically, for the Y state, we obtain for the asymptotic behaviour of the magnetization towards h_c:

$$\left.\frac{m}{S}\right|_{\Delta_h\to 0} \sim \frac{1}{3} - \Delta_h + \frac{1}{S}\left(a - b\ln\Delta_h\right) , \tag{2.131}$$

where a and b are constant terms.

It has been argued previously that the width of the plateau $\Delta_p = h_{p2} - h_{p1}$ should vanish as $1/S$ as $S \to \infty$ [46]. This perception is challenged in the present work. Indeed, on Fig. (2.13), it is clearly seen that we have some curvature that persists even for large values of spins. Let me give an explanation for this property. The low-field plateau boundary h_{p1} is obtained by intersecting this diverging magnetization with the value $m_p = 1/3$, which is equivalent to solving the following equation for Δ_{p1}:

$$\Delta_{p1} = \frac{1}{S}\left(a - b\ln\Delta_{p1}\right) = \frac{b}{S}\ln\left(\frac{u}{\Delta_{p1}}\right) , \tag{2.132}$$

where we defined $u = e^{a/b}$. This equation is transcendental, however, in the classical limit $S \to \infty$, it leads to the following behavior of the critical field Δ_{p1}:

$$\lim_{S\to+\infty} \Delta_{p1}(S) \sim \frac{1}{S}\ln S . \tag{2.133}$$

For the pyrochlore lattice, similar arguments can be made, though the expansion of the soft modes around the Γ point is more cumbersome. It is expected however, that the usual critical behaviour at the plateau transition is recovered when the full spin-wave analysis would be made.

2.5.2 Summary of the chapter

Using linear spin-wave theory, I have studied the fractional magnetization plateaus appearing at 1/3 and 1/2 of full saturation in the nearest-neighbor Heisenberg kagome and pyrochlore antiferromagnets, respectively. These plateaus result from the stabilization of an ordered collinear phase by quantum fluctuations over a finite field range, an archetypal example of quantum order by disorder. The spin-wave theory was not applied to the collinear plateau phase, but rather to the surrounding canted phases, which are classically stable in the whole field range, see Fig. (2.5) and Fig. (2.10) for the kagome and pyrochlore lattices, respectively.

Due to the presence of full flat modes of zero energy in the harmonic spectrum in both systems, I was able to derive analytical expressions for the spectra of canted states, see Eq. (2.70) and Eq. (2.76) for the kagome lattice, and Eq. (2.109), Eq. (2.115) and Eq. (2.121) for the pyrochlore lattice. From these spectra, I computed the ground-state energy $E_{\rm gs}$ with first, $1/S$ quantum corrections of the different canted states in the two lattices. The magnetization curves were then derived using the following equation:

$$M = -\frac{\partial E_{\rm gs}}{\partial H} \ . \tag{2.134}$$

The plateau is obtained by intersecting the diverging magnetization curves of the surrounding canted states with the expected $m = 1/3$ (resp. $m = 1/2$) values. The full magnetization curves, as well as ground-state energy correction versus field, are shown on Fig. (2.6) and Fig. (2.11) for the kagome and pyrochlore lattices, respectively.

For $S > 1/2$, the obtained plateau width as a function of spin compares well to available numerical data from other authors in the case of the kagome lattice, see Fig. (2.13). This tends to confirm the efficiency of LSWT in investigating the magnetization curves and semiclassical magnetization plateaus in frustrated quantum antiferromagnets.

Part II

Chapter 3

Frustration in an fcc lattice

The face-centered-cubic (fcc) lattice is one of the cubic close-packed structures, which means that it corresponds to one of the densest ways to arrange spheres in an infinite 3D lattice. Namely, it is made of the stacking of 2D layers of close-packed spheres, where each sphere sits on a vertex of a 2D triangular lattice. Successive 2D layers are stacked in a regular "ABC-ABC" arrangement, where the positions of spheres in different A, B, and C layers do not overlap, see Fig. (3.1). As a 3D lattice, it corresponds to 4 interpenetrating cubic lattices, or to a cubic lattice in which additional sites are inserted at the centers of each face of the cube.

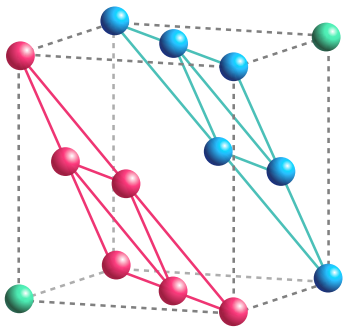

Figure 3.1: *ABC stacking of triangular layers in the fcc close-packed structure. Green, blue and pink spheres belong to A, B and C layers, respectively.*

Close-packing of atoms is at the basis of the solid state of many materials, and for that reason, elements exhibiting an fcc crystal structure are numerous in the periodic table (Ca, Sr, Ni, Cu, Ag, Au, Yb...). Not only is the fcc lattice ubiquitous in nature, but many chemical compounds crystallize in the fcc lattice as well, making it of great experimental interest.

The Heisenberg AFM on an fcc lattice is one of the oldest frustrated spin models [88–93]. It keeps attracting significant interest because of numerous experimental realizations [94–101]. In the following chapters, we will focus on the quantum and thermal order-by-disorder processes at play in the quantum Heisenberg fcc antiferromagnet. The present chapter serves as an introduction to this subject. First, I explain why the fcc Heisenberg antiferromagnet is frustrated, by looking at its classical ground-state degeneracy. Then, I focus on the description of the two collinear states within this classical ground-state manifold. They are best candidates for the ground state selected by quantum and thermal fluctuations. Finally, I give a brief review of the results obtained in previous works addressing the question of OBD in this system.

3.1 Geometrical frustration in the fcc Heisenberg antiferromagnet

We now consider that a spin magnetic moment of length S sits on each site of the fcc lattice. The Hamiltonian for the isotropic nearest-neighbor Heisenberg model is given by Eq. (1.3), which we repeat here:

$$\hat{\mathcal{H}} = J \sum_{\langle i,j \rangle} \mathbf{S}_i \cdot \mathbf{S}_j \ . \tag{3.1}$$

J is the exchange constant and we consider antiferromagnetic interaction, $J > 0$. Each lattice site i in position $\mathbf{R}_i$ has 12 nearest neighbors in positions $\mathbf{R}_i + \boldsymbol{\delta}$. The 12 $\boldsymbol{\delta}$ vectors are given by the set $\pm\mathbf{a}_\mu$, with $\mu \in \{1, \ldots, 6\}$:

$$\begin{aligned} \mathbf{a}_1 &= \frac{a}{2}(0,1,1) \ , & \mathbf{a}_4 &= \mathbf{a}_3 - \mathbf{a}_2 = \frac{a}{2}(0,1,-1) \ , \\ \mathbf{a}_2 &= \frac{a}{2}(1,0,1) \ , & \mathbf{a}_5 &= \mathbf{a}_1 - \mathbf{a}_3 = \frac{a}{2}(-1,0,1) \ , \\ \mathbf{a}_3 &= \frac{a}{2}(1,1,0) \ , & \mathbf{a}_6 &= \mathbf{a}_1 - \mathbf{a}_2 = \frac{a}{2}(-1,1,0) \ , \end{aligned} \tag{3.2}$$

where a is the cubic length of the lattice.

When nearest-neighbor sites of the fcc lattice are connected, one obtains a 3D lattice of edge-sharing tetrahedra, as shown on figure 3.2. As is generally the case for lattices made of tetrahedral units, the fcc lattice is geometrically frustrated. Due to the large coordination number $z = 12$, there is no way to simultaneously minimize the energy associated to each antiferromagnetic bond interaction. That is, it is impossible to make all nearest-neighbor pairs of spins in this lattice antiparallel at the same time, as is done for example in the Néel state for the square or simple cubic lattices. Consequently, any possible spin arrangement on the fcc lattice *must* contain *frustrated bonds*.

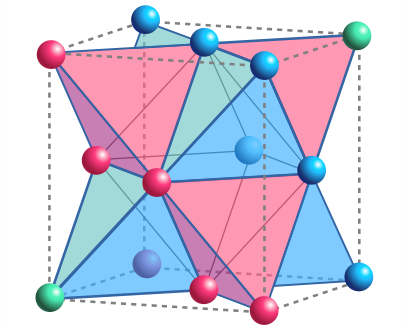

Figure 3.2: *The fcc lattice as edge-sharing tetrahedra.*

There is no intuitive way to determine the classical ordered ground states, that is the periodic spin arrangements which minimizes the Hamiltonian of Eq. (3.1). In order to answer the question of the classical ground state, let us apply a Fourier transformation to the spins in real space $\mathbf{S}_i$:

$$\mathbf{S}_i = \frac{1}{\sqrt{N}} \sum_{\mathbf{q}} \mathbf{S}_\mathbf{q} e^{i\mathbf{q}\cdot\mathbf{R}_i} \ , \tag{3.3}$$

where N is the total number of lattice sites, and the sum is taken over all the $\mathbf{q}$ vectors in the first Brillouin zone of the reciprocal lattice. We make use of the following

relation:

$$\sum_i e^{i\mathbf{q}\cdot\mathbf{R}_i} = N\delta_{\mathbf{q},\mathbf{0}} \ . \tag{3.4}$$

The original Hamiltonian of Eq. (3.1) is written is reciprocal space as:

$$\hat{\mathcal{H}} = \frac{1}{2}\sum_{\mathbf{q}} J_{\mathbf{q}}\mathbf{S}_{\mathbf{q}}\cdot\mathbf{S}_{-\mathbf{q}} \ , \tag{3.5}$$

where $J_{\mathbf{q}}$ is the Fourier transform of the exchange constant. For a given spin arrangement, $\mathbf{S}_{\mathbf{q}}\cdot\mathbf{S}_{-\mathbf{q}}$ can be viewed as the spectral weight of the ordering wave-vector $\mathbf{q}$ in this arrangement. Then it is natural that the Hamiltonian is minimized when the spin structure is ordered with the wave-vector $\mathbf{Q}$ that minimizes $J_{\mathbf{q}}$ (or with combinations of equivalent wave-vectors, then the weights must satisfy the fixed spin length constraint). One therefore needs to minimize $J_{\mathbf{q}}$ in order to determine the ground-state configuration.

In a Bravais lattice and for the nearest-neighbor model given by Eq. (3.1), $J_{\mathbf{q}}$ is expressed as follows:

$$J_{\mathbf{q}} = J\sum_{\boldsymbol{\delta}} e^{-i\mathbf{q}\cdot\boldsymbol{\delta}} \ , \tag{3.6}$$

where the sum is taken over all the nearest-neighbor vectors $\boldsymbol{\delta}$. In the fcc lattice, the 12 nearest-neighbor bond vectors are given by the set of vectors $\pm\mathbf{a}_\mu$, with $\mu \in \{1,\ldots,6\}$, given in Eq. (3.2). Due to the central symmetry of the lattice, contributions to $J_{\mathbf{q}}$ are only real. To lighten the expressions, we define for each spacial component $\alpha \in \{x,y,z\}$:

$$\mathcal{C}_\alpha = \cos\left(q_\alpha a/2\right) \ . \tag{3.7}$$

Eq. (3.6) becomes:

$$J_{\mathbf{q}} = 2J\sum_{i=1}^{6}\cos(\mathbf{q}\cdot\mathbf{a}_i) = 4J\left(\mathcal{C}_x\mathcal{C}_y + \mathcal{C}_y\mathcal{C}_z + \mathcal{C}_z\mathcal{C}_x\right) \ . \tag{3.8}$$

Minima of $J_{\mathbf{q}}$ are found when the following is verified for the 3 components of $\mathbf{Q} = (Q^x, Q^y, Q^z)$:

$$\left.\begin{array}{rcl} Q^\alpha &=& \pm 2\pi/a \\ Q^\beta &=& q \\ Q^\gamma &=& 0 \end{array}\right\} \quad \text{with} \quad \begin{array}{c} q \in [0,1/2] \ , \\ \{\alpha,\beta,\gamma\} \in \{x,y,z\} \ , \alpha\neq\beta\neq\gamma \ . \end{array} \tag{3.9}$$

There is a trivial $6-$fold degeneracy on the choice of two of the components (say α and β), which is related to the cubic symmetry of the fcc lattice and isotropic nature of the Heisenberg interaction. Taking for example $\alpha = x$ and $\beta = y$, one obtains ordering wave vectors of the following form:

$$\mathbf{Q}^{xy} = \frac{2\pi}{a}(1,q,0) \ . \tag{3.10}$$

On top of the trivial 6-fold symmetry, there is an accidental infinite degeneracy encoded in the continuous parameter q. Eq. (3.10) defines a full line of classically degenerate ordering wave vectors in reciprocal space. All such lines are represented in the first Brillouin zone as pink lines on Fig. (3.3). The fcc lattice is therefore another example of a geometrically frustrated lattice. Note that contrary to the pyrochlore and kagome lattices studied in chapter 2, the degeneracy in the fcc lattice is subextensive.

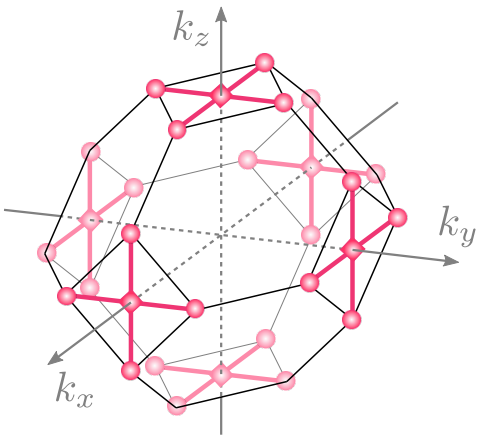

Figure 3.3: *Infinite classical ground-state degeneracy of the fcc Heisenberg antiferromagnet. Pink lines show possible ordering wave vectors associated to the classical ground state.*

This can be understood as follows. In the fcc lattice, one can also write the Hamiltonian in terms of tetrahedral blocks, as for the pyrochlore lattice:

$$\hat{\mathcal{H}} = \frac{J}{4}\sum_t (\mathbf{S}_t)^2 - 2NJS^2 \ , \tag{3.11}$$

where the subscript t refers to the tetrahedral unit, and $\mathbf{S}_t$ is the total spin on a given tetrahedron. This Hamiltonian is minimized when the following constraint is verified for all tetrahedra of the lattice:

$$\mathbf{S}_t = \mathbf{0} \ . \tag{3.12}$$

This is the same constraint as the classical ground-state constraint of the nearest-nieghbour Heisenberg model on the pyrochlore lattice in zero magnetic field, see Eq. (2.81). The degree of degeneracy associated to satisfying this constraint at the level of one tetrahedron is obviously the same for both lattices. The difference resides in the higher connectivity of the fcc lattice compared to the pyrochlore lattice. As a result, once the spins on one tetrahedron are set, the possible configurations that satisfy Eq. (3.12) for the rest of tetrahedra are more constrained and therefore less numerous.

To summarize, at the classical level, any ordering wave vector located on one of the pink lines in Fig. (3.3) sets up a valid ground-state candidate, with degenerate classical ground-state energy $E_{\rm cl}$:

$$E_{\rm cl} = -2NJS^2 \ . \tag{3.13}$$

The mixing of several such ordered structures in any multi-$\mathbf{Q}$ structure is also a valid classical ground state. Different ordering wave vectors along one of the lines are not related to one another by symmetry, and therefore this degeneracy is accidental. It is expected to be lifted, at least partially, when the effects of fluctuations are taken into account through the order-by-disorder phenomenon.

3.2 The AF1 and AF3 structures

In general, multi-$\mathbf{Q}$ states are non coplanar, and it would be unlikely that they are selected by quantum or thermal fluctuations. Let us therefore focus on single-$\mathbf{Q}$ states only. Furthermore, there is no anisotropic term in the Hamiltonian, so the problem remains completely isotropic with respect to cubic symmetry. For that reason, there will be no way to distinguish between equivalent ordering wave-vectors on different symmetry related lines. Let us therefore focus on the line $\mathbf{Q}^{xy}$ defined by Eq. (3.10) from now on. Among the corresponding classically degenerate ordered ground states, 2 allow for collinear spin arrangements and are of particular interest to our study. These two collinear states are called the AF1 and AF3 states, and are briefly introduced in the present section.

The ordering wave vector $\mathbf{Q}$ of an ordered spin configuration contains information about the phase that spin orientation acquires when one moves through real space in the lattice. Namely, for a single-$\mathbf{Q}$ configuration, the orientation of a magnetic moment $\mathbf{S}_i$ in position $\mathbf{R}_i$ is given by the following expression:

$$\mathbf{S}_i = \mathbf{l} e^{i\mathbf{Q}\cdot\mathbf{R}_i} + \mathbf{l}^* e^{-i\mathbf{Q}\cdot\mathbf{R}_i} \ , \tag{3.14}$$

where $\mathbf{l}$ is a complex vector in spin space:

$$\mathbf{l} = (\mathbf{l}_1 - i\mathbf{l}_2)/2 \ . \tag{3.15}$$

Substituting the above into Eq. (3.14) gives:

$$\mathbf{S}_i = \mathbf{l}_1 \cos(\mathbf{Q}\cdot\mathbf{R}_i) + \mathbf{l}_2 \sin(\mathbf{Q}\cdot\mathbf{R}_i) \ . \tag{3.16}$$

It becomes obvious that a single-$\mathbf{Q}$ magnetic structure can only be coplanar. Indeed, all spins given by Eq. (3.16) lie in the plane containing the vectors $\mathbf{l}_1$ and $\mathbf{l}_2$. The spin structure must obey the fixed norm constraint, that is:

$$\|\mathbf{S}_i\| = S \ , \tag{3.17}$$

for any spin site. This generally imposes the following conditions on the two components $\mathbf{l}_1$ and $\mathbf{l}_2$:

$$\mathbf{l}_1 \perp \mathbf{l}_2 \ , \tag{3.18}$$

$$\|\mathbf{l}_1\| = \|\mathbf{l}_2\| = S \ . \tag{3.19}$$

This corresponds in real space to a spiral spin structure, which applies to any ordering wave vector, *commensurate or not*. In such spiral arrangements, a spin in position $\mathbf{R}_i + \boldsymbol{\delta}$ acquires an angular phase $\theta_{\boldsymbol{\delta}}$ with respect to the spin in position $\mathbf{R}_i$, which is directly equal to the quantity $\mathbf{Q}\cdot\boldsymbol{\delta}$. Thus, to any value of q in $\mathbf{Q}^{xy}$ defined by Eq. (3.10), corresponds a spiral state. One obtains the spin structure by substituting the nearest-neighbor vectors defined in Eq. (3.2) into Eq. (3.16), with the convention of Eqs. (3.18, 3.19).

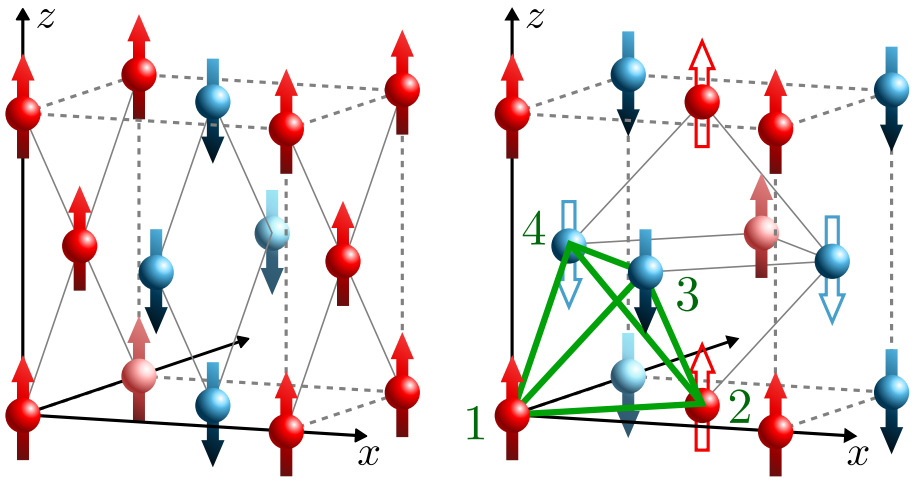

(a) *AF1 state* (b) *AF3 state*

Figure 3.4: *The two collinear states of the classical ground-state manifold in the nearest-neighbor fcc Heisenberg AF.*

When $q = 0$, the spiral structure happens to be collinar. Indeed, the opening angles between neighboring spins is equal to 0 when the two spins are in the same yz plane, and to $\pm\pi$ otherwise. This collinear state is called the AF1 state, and is represented on Fig. (3.4a). It is made of the antiferomagnetic stacking of ferromagnetic yz planes along the x direction.

Another collinear arrangement is possible when $q = 1/2$ in $\mathbf{Q}^{xy}$. Indeed, one can easily verify that for any spin $\mathbf{S}_i$ in position $\mathbf{R}_i$, either $\cos(\mathbf{Q}\cdot\mathbf{R}_i)$ or $\sin(\mathbf{Q}\cdot\mathbf{R}_i)$ vanishes in Eq. (3.16). This implies that the orthogonality condition for $\mathbf{l}_1$ and $\mathbf{l}_2$ given by Eq. (3.18) is not necessary anymore. Actually, their orientation can be completely arbitrary, as long as they preserve the norm S. In particular, one can chose to have $\mathbf{l}_1 = \mathbf{l}_2 = \mathbf{l}_0$, in which case the structure is collinear. Then it is straightforward to show from Eq. (3.16), that the spin structure is given by the following equation:

$$\mathbf{S}_i = \sqrt{2}\mathbf{l}_0 \cos(\mathbf{Q}\cdot\mathbf{R}_i - \pi/4)\ . \tag{3.20}$$

This arrangement is called the AF3 state, and is represented on Fig. (3.4b). Note that on Fig. (3.4), the spins are oriented along the z axis for the sake of a simple visualization, but in principle the orientation axis is arbitrary.

The AF1 and AF3 states become the unique classical ground state in the presence of weak next nearest-neighbor exchange of either FM (AF1) or AFM (AF3) sign. They are therefore natural ground-state candidates for the quantum order-by-disorder selection. Their two ordering wave vectors are explicitly given below:

$$\boxed{\mathbf{Q}_1 = \frac{2\pi}{a}(1,0,0)} \quad \text{and} \quad \boxed{\mathbf{Q}_3 = \frac{2\pi}{a}\left(1,\frac{1}{2},0\right)}\ . \tag{3.21}$$

Both those structures are commensurate, $\mathbf{Q}_1$ and $\mathbf{Q}_3$ being equal to half and a quarter of a reciprocal lattice vector, respectively. Consequently, the magnetic unit cell in the AF1 structure contains 2 sites, and is minimally described using 2 sublattices. Those correspond to the spins of opposite direction, that is the red and blue spins on Fig. (3.4a). The AF3 structure has a twice larger magnetic unit cell and is minimally described using 4 sublattices, as represented by the green tetrahedron on Fig. (3.4b). Note as well that $\mathbf{Q}_1$ and $\mathbf{Q}_3$ (and symmetry-related equivalent points) correspond to high-symmetry points in the first Brillouin zone, namely the X (AF1) and W (AF3) points. The X points are the centers of the square faces of the first Brillouin zone, see pink lozanges on Fig. (3.3). The W points are the vertices of the first Brillouin zone, see pink balls on Fig. (3.3).

3.3 ground-state selection: a literature review

Several authors have intended to determine the ground state selected by quantum and thermal order from disorder processes in the nearest-neighbor fcc AFM [90, 102–106]. From classical Monte-Carlo simulations it is well established that thermal fluctuations act in favor of the AF1 state [104]. Regarding the ground state at $T = 0$ stabilized by quantum fluctuations, the available results diverge. Numerical studies of this system remain scarce, due to the complexity in efficiently simulating 3D lattices.

On the theoretical side, an early work using spin-wave theory (SWT) predicted the stabilization of the AF1 state from quantum fluctuations at $T = 0$ [90]. Unfortunately this result has to be discarded, as the spin-wave spectrum used to describe the AF3 state was incorrect. It was indeed corresponding to the non-collinear state with same ordering wave-vector, rather than the proper collinear AF3 state. A correct version of the spectrum was derived soon after from a Green's functions formalism [107], and later on in the context of spin-wave theory again [93], but no comparison of ground-state energies was made. On the other hand, the conclusions drawn by recent Green's functions method predict the selection of the AF1 state at $T = 0$ by quantum fluctuations, and of the AF3 state from thermal fluctuations [105]. A competition effect and a low-T phase transition is expected for large spin $S \geq 2$.

Chapter 4

Harmonic spin-wave theory

In this chapter we use LSWT to study the ground-state selection operated by quantum fluctuations in the nearest-neighbor Heisenberg fcc antiferromagnet. We first obtain fully analytic expressions for the harmonic spin-wave spectra of competing single-$\mathbf{Q}$ classical ground states. Then for each of these states, we compute numerically the ground-state energy with first quantum correction, from the zero-point motion of their corresponding magnons. By comparison of the ground-state energies, we find that at harmonic order, quantum fluctuations act in favor of the AF3 collinear state. The obtained energy difference between the two collinear states (AF1 and AF3) is shown to be particularly small. The energy of all non-collinear spiral states clearly lies above the energies of AF1 and AF3 states. The spin reduction from quantum fluctuations is also given for the two competing collinear states. Due to the accidental classical ground-state degeneracy of the model, the harmonic spectra contain full lines of zero energy modes, of which the locations in reciprocal space are specified.

We also ask the question about thermal selection in this *quantum* spin system. The free energy as a function of temperature $\Delta F(T)$ is computed from thermal population of the magnons, for AF1 and AF3 states. The AF1 state is found to be selected by thermal fluctuations, as was previously predicted from classical thermal ObD. Due to the smallness of the original energy difference between the two states at $T = 0$, the free energy overcomes it and there is a crossing of the two curves. This is a rare occurrence of competition between quantum and thermal ObD, which leads to a first-order phase transition at low temperatures. The behaviour of the free energy is attributed to the soft modes lying around the numerous accidental zero-energy modes of the harmonic spectra. Exceptionally sharp behaviours for the free energy at low-temperatures are found in both states, with a peculiar fractional exponent in the AF3 state.

4.1 Quantum fluctuations at zero temperature

In this section, we focus on the zero temperature ground-state selection, that is, with only the effects of quantum fluctuations. We compute the first order quantum correction to the ground-state energies of the classically degenerate ground states of the nearest-neighbor fcc AFM. We therefore restrain to the harmonic approximation in spin-wave theory (LSWT), which captures only the free magnon picture. Higher-order processes involving magnon-magnon interactions are neglected.

When only the first quantum correction is considered, the ground-state energy of a state gets corrections of the form of Eq. (1.26). In the case of the fcc lattice specifically, the ground-state energy is given by the following:

$$E_{\text{gs}} = -2NJS(S+1) + \frac{1}{2}\sum_{\mathbf{k}} \epsilon_{\mathbf{k}} \ , \tag{4.1}$$

where $\epsilon_{\mathbf{k}}$ is the harmonic spin wave spectrum, and is in principle different from one classically stable state to another.

The degenerate classical ground states of the nearest-neighbor fcc Heisenberg model have ordering wave vectors given by Eq. (3.10), which we repeat here:

$$\mathbf{Q}^{xy} = \frac{2\pi}{a}(1, q, 0) \ , \tag{4.2}$$

where q is a continuous parameter $q \in [-1/2, 1/2]$. Classically, their degenerate ground-state energy is given by:

$$E_{\text{cl}} = -2NJS^2 \ . \tag{4.3}$$

To compute the ground-state energy given by Eq. (4.1), one needs the magnon spectra $\epsilon_{\mathbf{k}}$ of the degenerate classical ground states. In the next section, I show how to obtain these spectra completely analytically from LSWT, with particular attention on the collinear AF1 and AF3 structures discussed in Sec (3.2).

4.1.1 Harmonic spin-wave spectra of competing states

The nearest-neighbor Heisenberg Hamiltonian, see Eq. (3.1), is explicitly written in terms of spin components as:

$$\hat{\mathcal{H}} = J\sum_{\langle i,j\rangle}\left(S_i^{x_0}S_j^{x_0} + S_i^{y_0}S_j^{y_0} + S_i^{z_0}S_j^{z_0}\right) \ . \tag{4.4}$$

I use the spin wave formalism explained in appendix A to diagonalize this Hamiltonian and obtain the spin wave spectra of the competing classical ground states. First we apply the rotation from the global spin coordinates $(S_i^{x_0}, S_i^{y_0}, S_i^{z_0})$ in Eq. (4.4), to the local spin coordinates (S_i^x, S_i^y, S_i^z), following Eq. (A.7). Then the Holstein-Primakoff transformation is applied to these local coordinates, see Eq. (1.20). After these two

transformations, a scalar product between two spins is written in terms of bosonic operators as follows:

$$\begin{aligned}\mathbf{S}_i \cdot \mathbf{S}_j =& S^2 \cos\theta_{ij} - S\cos\theta_{ij}\left(a_i^\dagger a_i + a_j^\dagger a_j\right) \\ &+\frac{S}{2}\left[\left(\cos\theta_{ij}-1\right)\left(a_i a_j + a_i^\dagger a_j^\dagger\right) + \left(\cos\theta_{ij}+1\right)\left(a_i a_j^\dagger + a_i^\dagger a_j\right)\right] ,\end{aligned} \tag{4.5}$$

where $a_i^\dagger$ and a_i are bosonic creation and annihilation operators. In the above, the first term in S^2 corresponds to the classical scalar product. When any of the classically degenerate configurations is considered, this term naturally leads to the classical ground-state energy of Eq. (4.3). Linear terms in bosonic operators have been left out, as they necessarily vanish when a classically stable configuration is considered. Once the angles θ_{ij} between neighboring spins in the lattice are known, one can substitute Eq. (4.5) in Eq. (4.4) and obtain the harmonic spin-wave Hamiltonian.

In the fcc lattice, the nearest-neighbor Heisenberg Hamiltonian of Eq. (3.1) is written in the following symmetric form with explicit real-space spin positions:

$$\hat{\mathcal{H}} = \frac{J}{2}\sum_{\mathbf{R}}\sum_{\mu=1}^{6}\mathbf{S}_{\mathbf{R}}\cdot\left\{\mathbf{S}_{\mathbf{R}+\mathbf{a}_\mu} + \mathbf{S}_{\mathbf{R}-\mathbf{a}_\mu}\right\} , \tag{4.6}$$

where the nearest-neighbor vectors $\mathbf{a}_\mu$ are given by Eq. (3.2). The summation over $\mathbf{R}$ spans all possible site positions in the lattice, and induces cancellations after the Fourier transformation is applied. The minimal number of bosonic modes which need to be introduced depends on the specific structure and periodicity of the classical ground state we expand around.

The classically degenerate ordering wave vectors $\mathbf{Q}^{xy}$ given by Eq. (4.2) generally describe spiral states when the pitch parameter q is arbitrary. In that case, only one bosonic mode is necessary. In particular, the collinear AF1 state shown on Fig. (3.4a) falls in this category. In the special case where $q = 1/2$, the ordering wave vector can accommodate another collinear ground state, the AF3 state. It is represented on Fig. (3.4b), and requires at least two bosonic modes.

Spiral states

As seen previously, an ordered magnetic structure of ordering wave vector $\mathbf{Q}$ is determined through Eq. (3.14), where $\mathbf{l}$ is a complex vector in spin space. From the classically degenerate ordering wave vectors given in Eq. (4.2), spiral states are obtained from the conventions of Eqs. (3.18, 3.19). The resulting opening angle θ_{ij} sustained between two neighboring spins $\mathbf{S}_i$ and $\mathbf{S}_j$ sitting in positions $\mathbf{R}_i$ and $\mathbf{R}_j$, respectively, is given by:

$$\theta_{ij} = \mathbf{Q}\cdot(\mathbf{R}_j - \mathbf{R}_j) . \tag{4.7}$$

Consequently, all spins in the lattice sustain the same opening angles with their surrounding neighbors. Since only scalar products between pairs of spins are considered

in the Hamiltonian, and since scalar products only involve opening angles and not absolute angles, see Eq. (4.5), it is possible to work in the single-boson picture.

We are only interested into interactions between pairs of nearest-neighbor spins, which in the fcc lattice are separated by the 12 $\pm\mathbf{a}_\mu$ vectors of Eq. (3.2). The scalar products appearing in Eq. (4.6) can thus be written in terms of bosonic operators using Eq. (4.5), where θ_{ij} is replaced by $\mathbf{Q}\cdot\mathbf{a}_\mu$. We now apply a Fourier transform to the bosonic operators using Eq. (A.8), which we repeat here:

$$a_{\mathbf{R}} = \frac{1}{\sqrt{N}}\sum_{\mathbf{k}} a_{\mathbf{k}} e^{i\mathbf{k}\cdot\mathbf{R}} \ , \tag{4.8}$$

where the sum is taken over all the $\mathbf{k}$-vectors of the first Brillouin zone. We substitute this into the scalar product of Eq. (4.5), and the symmetric Hamiltonian of Eq. (4.6) takes the standard single-boson form of Eq. (A.9):

$$\hat{\mathcal{H}} = E_{\text{cl}} + \sum_{\mathbf{k}} \left\{ A_{\mathbf{k}} a^\dagger_{\mathbf{k}} a_{\mathbf{k}} - \frac{1}{2} B_{\mathbf{k}} \left(a^\dagger_{\mathbf{k}} a^\dagger_{\text{-}\mathbf{k}} + a_{\text{-}\mathbf{k}} a_{\mathbf{k}} \right) \right\} \ . \tag{4.9}$$

The coefficients $A_{\mathbf{k}}$ and $B_{\mathbf{k}}$ in front of the normal and anomalous terms, respectively, are given by:

$$\begin{aligned} A_{\mathbf{k}} &= JS \sum_{\mu=1}^{6} \Big[\cos(\mathbf{k}\cdot\mathbf{a}_\mu) \left[1 + \cos(\mathbf{Q}\cdot\mathbf{a}_\mu) \right] - 2\cos(\mathbf{Q}\cdot\mathbf{a}_\mu) \Big] \ , \\ B_{\mathbf{k}} &= JS \sum_{\mu=1}^{6} \Big[\cos(\mathbf{k}\cdot\mathbf{a}_\mu) \left[1 - \cos(\mathbf{Q}\cdot\mathbf{a}_\mu) \right] \Big] \ . \end{aligned} \tag{4.10}$$

Explicitly substituting the $\mathbf{a}_\mu$ vectors of Eq. (3.2) as well as the $\mathbf{Q}^{xy}$ ordering wave vector of Eq. (4.2) leads to:

$$\begin{aligned} A_{\mathbf{k}} &= 2JS \Big\{ \mathcal{C}_y \left[\mathcal{C}_z + \mathcal{C}_x - (\mathcal{C}_x - \mathcal{C}_z)\cos(q\pi) \right] + 2 \Big\} \ , \\ B_{\mathbf{k}} &= 2JS \Big\{ \mathcal{C}_y \left[\mathcal{C}_x + \mathcal{C}_z + (\mathcal{C}_x - \mathcal{C}_z)\cos(q\pi) \right] + 2\mathcal{C}_x\mathcal{C}_z \Big\} \ , \end{aligned} \tag{4.11}$$

where we remind the reader that $\mathcal{C}_\alpha$ is defined in Eq. (3.7). In a single-boson picture as here, there is only one magnon mode in the spectrum, given by:

$$\epsilon_{\mathbf{k}} = \sqrt{A^2_{\mathbf{k}} - B^2_{\mathbf{k}}} \ . \tag{4.12}$$

We have therefore, for any spiral state with associated parameter q in $\mathbf{Q}^{xy}$:

$$\epsilon_{s\mathbf{k}} = 4JS \big[1 + \mathcal{C}_x\mathcal{C}_y + \mathcal{C}_x\mathcal{C}_z + \mathcal{C}_y\mathcal{C}_z \big]^{1/2} \big[1 - \mathcal{C}_x\mathcal{C}_z + \mathcal{C}_y(\mathcal{C}_z - \mathcal{C}_x)\cos(q\pi) \big]^{1/2} \ . \tag{4.13}$$

In particular, when $q = 0$ in Eq. (4.13), one obtains the harmonic spin-wave spectrum of the AF1 collinear state:

$$\epsilon_{1\mathbf{k}} = 4JS\sqrt{\mathcal{S}^2_x(\mathcal{C}_y + \mathcal{C}_z)^2 + \mathcal{S}^2_y\mathcal{S}^2_z} \ , \tag{4.14}$$

where we defined $\mathcal{S}_\alpha$ as:

$$\mathcal{S}_\alpha = \sin(k_\alpha a/2) \ . \tag{4.15}$$

For $q = 1/2$, Eq. (4.13) gives the harmonic spectrum of the noncollinear spiral state with the propagation vector $\mathbf{Q}_3$ given in Eq. (3.21):

$$\epsilon_{3s\mathbf{k}} = 4JS\sqrt{(1-\mathcal{C}_x\mathcal{C}_z)(1+\mathcal{C}_x\mathcal{C}_y+\mathcal{C}_x\mathcal{C}_z+\mathcal{C}_y\mathcal{C}_z)} \ . \tag{4.16}$$

In that state, we have 90° angles between neighboring spins. This expression was taken as the spectrum for the type-3 state in the early work by ter Haar and Lines [90, 91]. This spectrum however does not apply to the collinear AF3 state, which was ignored in this early work.

The collinear AF3 state

The collinear AF3 structure is described by using $\mathbf{Q}_3$ (see Eq. (3.21)) as ordering wave-vector in the modified expression of Eq. (3.20). Contrary to the spiral states, the opening angle between two neighboring spins does not only depend on the $\mathbf{a}_\mu$ vector between them. Then the local environment is not the same for all spins in the lattice, and the spectrum of the collinear AF3 state cannot be described using a single boson species.

There are 4 sublattices in the spin structure, which are represented by the green tetrahedron on Fig. (3.4b). Nevertheless, it is possible to reduce the number of magnon modes to only 2 modes a and b, which simplifies a lot the picture. Indeed, on Fig. (3.4b), sublattices 1 and 3 are symmetry related in the sense that they have the same surrounding nearest-neighbor environment (opening angles). One can therefore attribute the same magnon mode (say a) to all spins of sublattice 1 and 3. The same goes for sublattices 2 and 4, to which we attribute the second magnon mode b. With this construction, sites belonging to the modes a and b are represented as full and empty arrows, respectively, on Fig. (3.4b).

The two magnon modes a and b are independent, and in order to keep track of this information, a spin $\mathbf{S}_i$ in position $\mathbf{R}_i$ is fully specified by its position and family indices, $\mathbf{R}$ and α: $\mathbf{S}_i = \mathbf{S}_{\mathbf{R},\alpha}$, with $\alpha \in \{a, b\}$. The symmetric Hamiltonian of Eq. (4.6) can then be rewritten with the sublattice information as follows:

$$\begin{aligned}\hat{\mathcal{H}} = \frac{J}{2}\sum_{\mathbf{R}}\Bigg[&\sum_{\boldsymbol{\delta}_{\alpha\alpha}}\left\{\mathbf{S}_{\mathbf{R},a}\cdot\mathbf{S}_{\mathbf{R}+\boldsymbol{\delta},a}+\mathbf{S}_{\mathbf{R}',b}\cdot\mathbf{S}_{\mathbf{R}'+\boldsymbol{\delta},b}\right\} \\ &+\sum_{\pm\boldsymbol{\delta}_{ab}}\left\{\mathbf{S}_{\mathbf{R},a}\cdot\mathbf{S}_{\mathbf{R}+\boldsymbol{\delta},b}+\mathbf{S}_{\mathbf{R}',b}\cdot\mathbf{S}_{\mathbf{R}'+\boldsymbol{\delta},a}\right\}\Bigg] \ ,\end{aligned} \tag{4.17}$$

where $\boldsymbol{\delta}_{\alpha\alpha} \in \{\pm\mathbf{a}_2, \pm\mathbf{a}_5\}$ spans lattice vectors connecting nearest-neighbor spins of the same mode, and $\boldsymbol{\delta}_{ab} \in \{\mathbf{a}_1, \text{-}\mathbf{a}_3, \mathbf{a}_4, \text{-}\mathbf{a}_6\}$ spans lattice vectors connecting nearest-neighbor spins of opposite modes. We introduced the notation $\mathbf{R}' = \mathbf{R} + \mathbf{a}_3$ to denote

the exact position of the b site with respect to a given a site in position $\mathbf{R}$. The summation is thus made over only half of the Bravais lattice positions $\mathbf{R}$, namely those occupied by a sites. Note that the structure of the AF3 state can be viewed as alternating layers of a and b sites along the y-axis. Within this viewpoint, the first and second lines of Eq. (4.17) contain intra-layer interactions and inter-layer interactions, respectively.

The steps to get the quadratic Hamiltonian in terms of bosonic operators are the same as for the spiral states, except that one needs to keep track of the two bosonic modes a and b and define accordingly two different sets of operators a_i, b_i. There is another subtelty in the fact that spins of the same mode (a or b) do not necessarily have the same orientation. Indeed, in each a or b layer, spins are arranged antiferromagnetically. Furthermore, nearest-neighbor spins of a same mode (a or b) do exist, which is typically not the case in other systems [1]. For that reason, one needs to carefully keep track of the specific situation in each bond. In the 2 bosons picture, the quadratic part of the Hamiltonian in momentum space is given in the matrix form of Eq. (A.11):

$$\hat{\mathcal{H}}^{(2)} = \frac{1}{2}\sum_{\mathbf{k}} \left(\hat{X}^{\dagger}_{\mathbf{k}} H_{\mathbf{k}} \hat{X}_{\mathbf{k}} - \mathrm{Tr}[A_{\mathbf{k}}] \right) \ , \tag{4.18}$$

where $\hat{X}^{\dagger}_{\mathbf{k}}$ is a row vector containing all the Holstein-Primakoff bosonic operators:

$$\hat{X}^{\dagger}_{\mathbf{k}} = \left(a^{\dagger}_{\mathbf{k}}, b^{\dagger}_{\mathbf{k}}, a_{\text{-}\mathbf{k}}, b_{\text{-}\mathbf{k}} \right) \ . \tag{4.19}$$

In Eq. (4.18), $H_{\mathbf{k}}$ is a 4×4 matrix with the following block structure:

$$H_{\mathbf{k}} = \begin{pmatrix} A_{\mathbf{k}} & -B_{\mathbf{k}} \\ -B^{\dagger}_{\mathbf{k}} & A_{\mathbf{k}} \end{pmatrix} \ , \tag{4.20}$$

where the matrices $A_{\mathbf{k}}$ and $B_{\mathbf{k}}$ are given below:

$$A_{\mathbf{k}} = 4JS \begin{pmatrix} 1 & \gamma_{\mathbf{k}} \\ \gamma^{*}_{\mathbf{k}} & 1 \end{pmatrix} \ , \qquad B_{\mathbf{k}} = 4JS \begin{pmatrix} \mathcal{C}_x\mathcal{C}_z & \gamma^{*}_{\mathbf{k}} \\ \gamma_{\mathbf{k}} & \mathcal{C}_x\mathcal{C}_z \end{pmatrix} \ . \tag{4.21}$$

The phase factor $\gamma_{\mathbf{k}}$ is related to displacements from a given site of a given mode to its nearest neighbors sitting of the opposite mode:

$$\gamma_{\mathbf{k}} = \frac{1}{4}\sum_{\boldsymbol{\delta}_{ab}} e^{-i\mathbf{k}\cdot\boldsymbol{\delta}} = \frac{1}{2}\mathcal{C}_y(\mathcal{C}_x + \mathcal{C}_z) + \frac{i}{2}\mathcal{S}_y(\mathcal{C}_x - \mathcal{C}_z) \ . \tag{4.22}$$

Note that here, contrary to the matrices in the kagome and pyrochlore lattices, the matrix coefficients are complex numbers. The fact that the diagonal terms of the

[1] For example, this was not true in the kagome and pyrochlore lattices studied in chapter 2. Indeed, in those two cases, the number of magnon modes coincides with the number of sublattices, and no two spins of the same sublattice are nearest neighbors to one another.

anomalous $B_{\mathbf{k}}$ matrix do not vanish, is related to the fact that nearest-neighbor sites of the same sublattice do not have the same orientation. The fact that we have complex coefficients is related the lack of inversion symmetry.

The way to perform the Bogolyubov transformation for a matrix Hamiltonian such as in Eqs. (4.18, 4.20) is explained in appendix A. One needs to find the eigenvalues $\epsilon_{\mathbf{k}}$ of the system, but under the constraint that bosonic commutation relations have to be preserved. The obtained expressions for $\epsilon_{\mathbf{k}}$ are precisely the modes of the harmonic spin-wave spectrum.

It is possible to show that the resulting 4-dimensional eigenvalue problem can be reduced to the following 2-dimensional eigenvalue problem for the square of the original eigenvalues:

$$\left|\Delta_{\mathbf{k}}\Sigma_{\mathbf{k}} - \epsilon^2 \mathbb{I}_2\right| = 0 \ . \tag{4.23}$$

$\Delta_{\mathbf{k}}$ and $\Sigma_{\mathbf{k}}$ are 2×2 matrices given by (see Eqs. (A.31, A.32)):

$$\Delta_{\mathbf{k}} = A_{\mathbf{k}} - B_{\mathbf{k}} \ , \tag{4.24}$$

$$\Sigma_{\mathbf{k}} = A_{\mathbf{k}} + B_{\mathbf{k}} \ . \tag{4.25}$$

The positive square roots of the obtained 2 eigenvalues give the SW modes $\epsilon^{\pm}_{\mathbf{k}}$. The final analytical expression is obtained through elementary - though tedious - algebra:

$$\left(\frac{\epsilon^{\pm}_{3\mathbf{k}}}{4JS}\right)^2 = 1 - \mathcal{C}_x^2\mathcal{C}_z^2 \pm \Big\{\mathcal{C}_y^2\left(1-\mathcal{C}_x\mathcal{C}_z\right)^2\left(\mathcal{C}_x+\mathcal{C}_z\right)^2 + \mathcal{S}_y^2\left(\mathcal{C}_x-\mathcal{C}_z\right)^2\left[\mathcal{S}_y^2\left(\mathcal{C}_x+\mathcal{C}_z\right)^2 + \mathcal{S}_x^2\mathcal{S}_z^2\right]\Big\}^{1/2} \ . \tag{4.26}$$

4.1.2 ground-state selection

With analytical expressions for the spectra at hand, it is now very straightforward to compute the vacuum energy of the spin waves in the competing states. Corresponding ground-state energies E_{gs} are obtained from Eq. (4.1). Comparing theses energies allows us to determine which state is favored by quantum fluctuations at the harmonic level. We remember that all classical ground states have the same classical energy E_{cl} given in Eq. (4.3). It is thus sufficient to compare only the quantum corrections ΔE_{q} to E_{gs}:

$$\Delta E_{\text{q}} = E_{\text{gs}} - E_{\text{cl}} = -2JS + \frac{1}{2}\frac{1}{N}\sum_{\mathbf{k}} \epsilon_{\mathbf{k}} \ , \tag{4.27}$$

where the sum is taken over all the $\mathbf{k}$ points of the first Brillouin zone of the reciprocal lattice.

For the spiral states, including the collinear AF1 satte, one substitutes $\epsilon_{s\mathbf{k}}$ from Eq. (4.13) in the above expression. The black curve on Fig. (4.1) shows ΔE_{q} as a function of q. This curve was obtained using $N_{\text{M.C.}} = 10^{10}$ Monte-Carlo points for computing the integral in Eq. (4.27). The AF1 state at $q = 0$ is represented by the

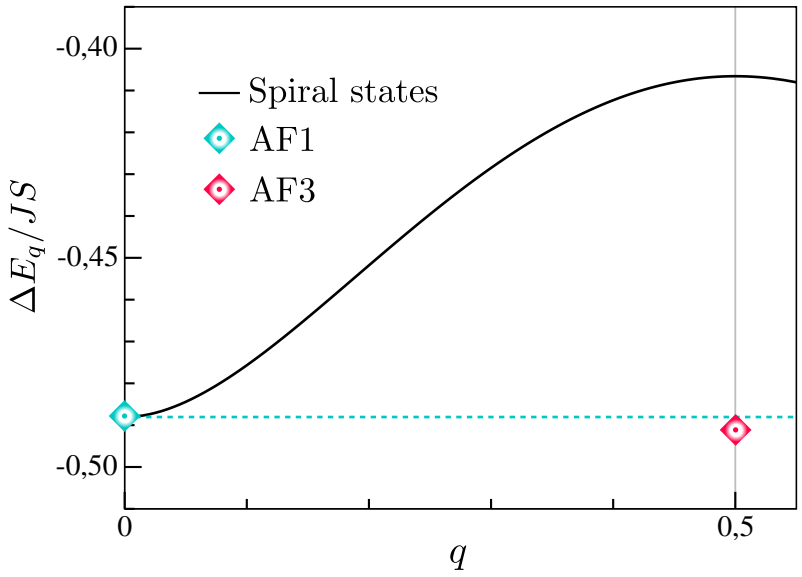

Figure 4.1: *Harmonic quantum correction to the ground-state energy as a function of ordering wave-vector coordinate q.*

blue diamond on Fig. (4.1). Using the spectrum $\epsilon_{1\mathbf{k}}$ of Eq. (4.14), the following value for its ground-state energy is obtained:

$$\boxed{E_1 = E_{\rm cl}\left(1 + \frac{0.4880560(8)}{2S}\right)}, \tag{4.28}$$

where $E_{\rm cl} = -2JS^2$. I used $N_{\rm M.C.} = 10^{12}$ Monte-Carlo points for computing the integral. The first three digits of the $1/S$ correction agree with the result previously obtained by Oguchi [108]. The energy of the spiral states is always above ΔE_1. This is not surprising, as quantum fluctuations favor collinear states. In that regard, the spiral $\mathbf{Q}_3$ state is the "least collinear" spiral state, and consequently has the highest ground-state energy (black curve at $q = 1/2$).

As for the collinear AF3 state, one has to sum up contributions from the two magnon branches, but on a twice smaller Brillouin zone. Using the expressions for $\epsilon^{\pm}_{3\mathbf{k}}$ of Eq. (4.26), we obtain the following ground-state energy:

$$\boxed{E_3 = E_{\rm cl}\left(1 + \frac{0.4911055(4)}{2S}\right)}, \tag{4.29}$$

with again $N_{\rm M.C.} = 10^{12}$ Monte Carlo points over the reduced Brillouin zone. The AF3 state has thus lower energy than the AF1 state, as can be seen on Fig. (4.1) by the red diamond. Therefore, at the harmonic level in spin-wave theory, the collinear AF3

state is selected by quantum fluctuations over the AF1 state. This is surprising, as it was not the state selected by thermal fluctuations. The energy difference between the two states is, however, very tiny:

$$\Delta E_{13} = \frac{E_3 - E_1}{N} \simeq -3.044 \cdot 10^{-3}(JS) \ . \tag{4.30}$$

For the sake of completeness, we give also below the values obtained for the spin reduction ΔS in the two states. Detailed explanations about how to compute can be found in the next chapter, and here we give only the numerical values [2]:

$$\boxed{\Delta S_1 = 0.338777(3)} \ , \quad \boxed{\Delta S_3 = 0.366331(2)} \ . \tag{4.31}$$

The spin reduction is substantial for both states, which tends to demonstrate that quantum fluctuations are strong in the ground state. In agreement with the fluctuation mechanism, the lowest energy state exhibits a larger spin reduction.

4.1.3 Pseudo-Goldstone modes in the dispersion

Although the order-by-disorder phenomenon induces a ground-state selection among classically degenerate states, it preserves the original true symmetries of the problem. Indeed, the global rotational symmetry of the Heisenberg Hamiltonian of Eq. (3.1) remains. When the system orders in a given state (AF1, AF3, or any other), the absolute orientation of spins is completely arbitrary. For example, on Fig. (3.4), I represented the AF1 and AF3 structures with spins oriented along the global z axis, but any other orientation axis would be equivalent by symmetry. This arbitrary selection of an orientation is called spontaneous symmetry breaking.

According to the the Goldstone theorem, spontaneous symmetry breaking of a continuous symmetry must induce the presence of gapless modes in the excitation spectrum, which we call Goldstone modes. In the framework of spin-wave theory, there are two Goldstone modes in the magnon spectrum of an ordered state with ordering wave vector $\mathbf{Q}$. They are associated to the spontaneous breaking of the global rotational symmetry (2 degrees of freedom), and are located at the center Γ of the Brillouin zone and at $\mathbf{k} = \mathbf{Q}$.

The harmonic spin-wave spectra derived for the AF1 and AF3 states contain accidental gapless modes on top of the true Goldstone modes. These are related to the "spontaneous" breaking of the accidental classical degeneracy in the choice of one or the other ordering wave vector among the classically degenerate ones $\mathbf{Q}^{xy}$. They are sometimes called *pseudo-Goldstone modes*, and are an artifact of the harmonic approximation. These pseudo-Goldstone modes are particularly numerous in the fcc lattice. Indeed, in both the AF1 and AF3 configurations, the harmonic spectra contain full lines of zero energy, rather than localized points. These lines are shown on Fig. (4.2).

[2] Those values were also obtained using $N_{\text{M.C.}} = 10^{12}$ Monte-Carlo points over the integration volume.

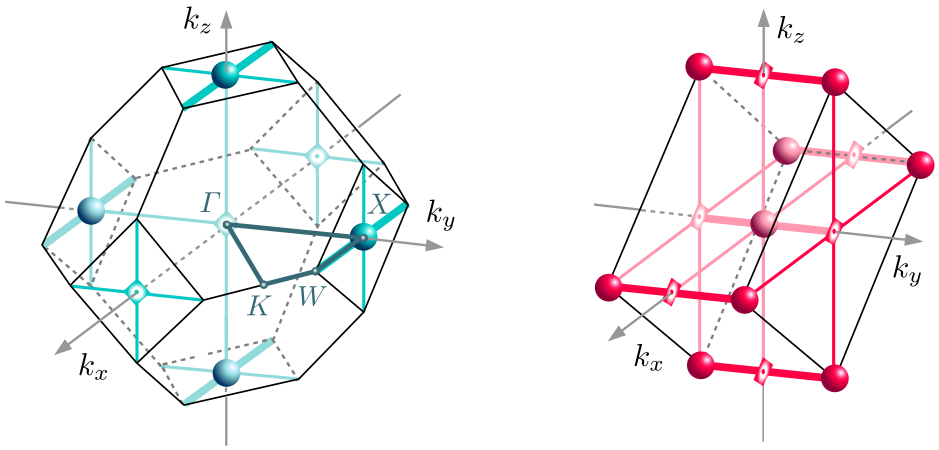

Figure 4.2: *Lines of zero-energy modes of the magnon spectrum of the AF1 (left panel) and AF3 (right panel) states in the harmonic approximation. Thick and thin lines correspond to zero modes along the propagation direction (x for the AF1 state, y for the AF3 state) or orthogonal to it, respectively.*

The blue lines on the left panel of Fig. (4.2) are the lines of gapless modes of the harmonic spectrum of the AF1 state, represented in the first Brillouin zone. From the analytical expression of the spectrum $\epsilon_{1\mathbf{k}}$ given in Eq. (4.14), one can easily identify two types of such lines. Lines along the special k_x direction are displayed as thick blue lines, and correspond to the condition $\mathcal{C}_y = -\mathcal{C}_z = \pm 1$. Explicitly, their equation in $\mathbf{k}$-space is $2\pi(q, \pm 1, 0)$ and $2\pi(q, 0, \pm 1)$, where q is arbitrary. Lines along the other two directions k_y and k_z, are displayed as thin blue lines. They correspond to the condition $\mathcal{S}_x = \mathcal{S}_\alpha = 0$ with $\alpha = z$ (resp. y) for lines along the k_y (resp. k_z) direction. Their explicit equation is $2\pi(n_x, q, n_z)$ for lines along the k_y direction, and $2\pi(n_x, n_y, q)$ for lines along the k_z direction, where $n_\alpha \in \mathbb{Z}$. Crossing points between several lines of zero-energy modes are also of two kinds, and are highlighted as well on Fig. (4.2). Blue diamonds show crossing points between 2 lines, while blue balls show crossing points between 3 lines.

The right panel of Fig. (4.2) shows the gapless modes of the harmonic spectrum of the collinear AF3 state as red lines in the reduced Brillouin zone. From a careful analysis the analytical expression for $\epsilon^{\pm}_{3\mathbf{k}}$, see Eq. (4.26), one can show that the upper branch of the spectrum $\epsilon^{+}_{3\mathbf{k}}$ only has lines of zero-energy modes along the special k_y direction. They obey the condition $\mathcal{S}_x = \mathcal{S}_z = 0$, which translates into the lines $2\pi(n_x, q, n_z)$ in reciprocal space, where $n_x, n_z \in \mathbb{Z}$. The lower branch of the spectrum $\epsilon^{-}_{3\mathbf{k}}$ has much more spurious gapless modes. Similar to the AF1 situation, one can identify two different types of lines of zero energy. Lines along the special k_y direction are the same lines as for the upper branch. They and are displayed as thick red lines on the right panel of Fig. (4.2). Lines along the other 2 directions k_x and k_z are

displayed as thin red lines on Fig. (4.2). They obey either the condition $\mathcal{S}_\alpha = \mathcal{C}_y = 0$ or $\mathcal{S}_\alpha = \mathcal{S}_y = 0$, where $\alpha = z$ (resp. x) for lines along the k_x (resp. k_z) direction. This corresponds to the equation $\pi(q, n_y, 2n_z)$ and $\pi(2n_x, n_y, q)$ for lines along the k_x and k_z directions, respectively. Once again we have $n_\alpha \in \mathbb{Z}$. Crossing points between lines are of two kinds, which are represented as the red balls and red diamonds on Fig. (4.2).

The magnon dispersion in the two collinear states is illustrated in Fig. 4.3 as intensity maps, in the $k_x k_z$ plane with $k_y = 2\pi/a$. The lines of zeo-energy modes are clearly visible as the dark blue regions in the map.

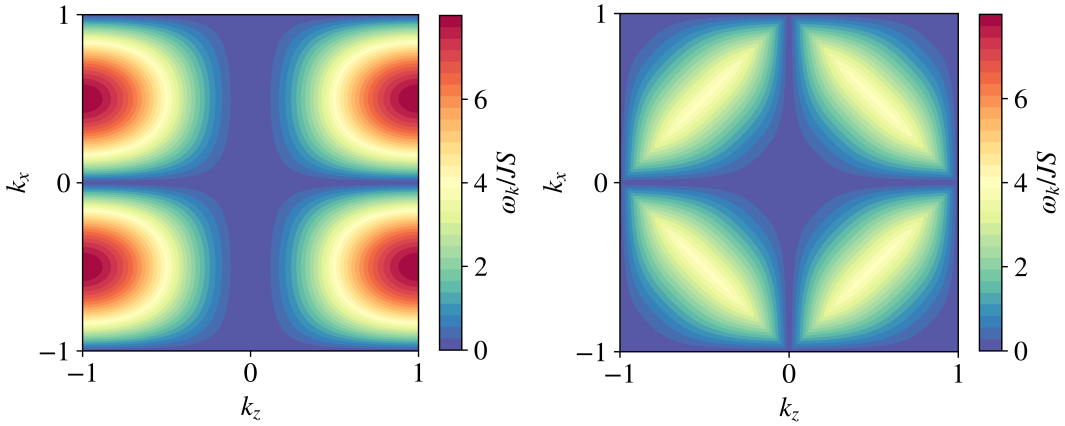

Figure 4.3: *Color intensity map for the magnon dispersion in two collinear antiferromagnetic states with fixed $k_y = 2\pi/a$: $\epsilon_{1\mathbf{k}}$ for the AF1 state (left panel) and $\epsilon^-_{3\mathbf{k}}$ for the AF3 state (right panel).*

4.2 Thermal selection at low temperature

Previous works [104] tend to converge towards an AF1 ordering driven by thermal fluctuations at low temperatures. This result is rather surprising, since thermal and quantum fluctuations are typically believed to lead to the same type of selection process through the order from disorder phenomenon.

For the sake of completeness, and in order to understand the origin of this discrepancy, we will now look at what happens to our system at low temperature. More specifically, we wonder which classical ground state is selected by thermal fluctuations, and whether our result is in agreement with the aforementioned previous studies. The relevant thermodynamic quantity to work with at finite temperature T is the free energy F, which takes into account both the internal energy E of a given state, and its entropy S:

$$F = E - TS \ . \tag{4.32}$$

In first approximation one can neglect the thermal corrections to the internal energy, which consist in a renormalization of the magnons energies. Thus the internal energy E will be considered unchanged from the zero-temperature ground-state energy computed in the previous section. This implies that at a given temperature T, the variation of free energy $\Delta F(T)$ will only come from the entropy part, selecting the ground state with maximal entropy over the others. From bosonic statistical mechanics, we have:

$$\Delta F(T) = k_B T \sum_{\mathbf{k},i} \ln\left(1 - e^{-\epsilon_{i\mathbf{k}}/k_B T}\right) \ , \tag{4.33}$$

where the sum is taken over all the possible $\mathbf{k}$-vectors of the first Brillouin zone, and $\epsilon_{i\mathbf{k}}$ is the energy of a spin wave of wave vector $\mathbf{k}$ (mode i). This additional free energy obviously gives a negative contribution. At sufficiently low temperatures $k_B T \ll JS$, only the lowest-lying magnons contribute significantly. Let us first derive the temperature dependence of $\Delta F(T)$ numerically, in order to determine which classical ground state is favored by thermal fluctuations.

4.2.1 Competition between quantum and thermal fluctuations

The free energy of a given state at a given temperature T is obtained from Eq. (4.33). One substitutes the harmonic spin-wave spectra derived in the previous section for the competing AF1 and AF3 states (see Eq. (4.14) and Eq. (4.26), respectively). The integral is computed using standard Monte-Carlo integration. The obtained value for $\Delta F(T)$ is added to the ground-state energies at zero temperature E_1 and E_3 (see Eq. (4.28) and Eq. (4.29), respectively). Fig. (4.4) shows the free energy $\Delta F = F - E_{\text{cl}}$ for the two competing states AF1 and AF3, as a function of temperature. The $T = 0$ corrections to the ground-state energies are marked by the two diamonds. Then the curves were obtained using a Monte-Carlo integration with $N_{\text{M.C.}} = 10^{10}$ random points to compute $\Delta F(T)$.

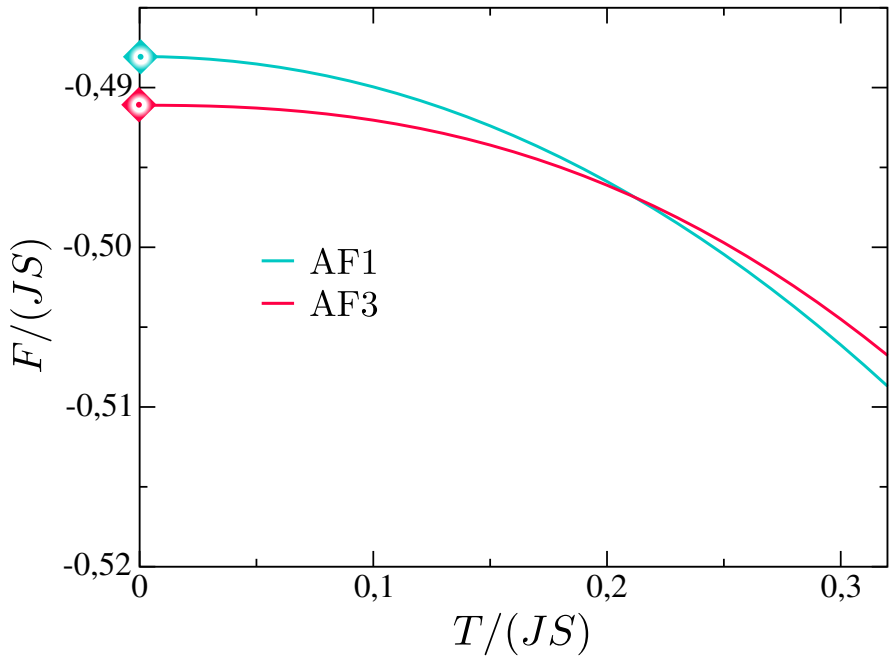

Figure 4.4: *Free energy as a function of temperature of the fcc Heisenberg AFM for AF1 (blue) and AF3 (pink) collinear states. A first-order phase transition occurs at* $T^* \approx 0.21JS$.

It appears clearly from Fig. (4.4) that the AF1 state is favored by thermal fluctuations. Indeed, its free energy $\Delta F_1(T)$ decreases faster with temperature than that of the AF3 state. Due to the tiny ground-state energy difference in favor of the AF3 state at $T = 0$, this behaviour induces a crossing of the two curves at a very low temperature T^* :

$$T^* = 0.212(JS) \ . \tag{4.34}$$

As a result, we predict a first-order phase transition from the zero-temperature ground state AF3 to the low-temperature state AF1. The fact that the AF1 state is favored by thermal fluctuations is in agreement with previous studies on the fcc Heisenberg AFM. The fcc Heisenberg AFM thus presents a unique example of what seems to be a competition effect between quantum and thermal order by disorder at low temperatures.

Of particular interest is also the asymptotic temperature dependence of $\Delta F(T)$ when $T \to 0$. By applying a basic power-law fit to the curves of Fig. (4.4), we find particularly sharp behaviour for both states, compared to the typical $\Delta F(T) \sim -T^4$ behaviour of the unfrustrated AFM:

$$\Delta F_1(T) \sim -T^2 \ , \quad \Delta F_3(T) \sim -T^{7/3} \ . \tag{4.35}$$

The AF3 state has a softer behaviour than the AF1 state, which explains the phase transition. The temperature exponents found above are peculiar, especially for the AF3 state.

In principle, states selected by thermal order by disorder are those exhibiting the softest modes in their magnon spectrum. Indeed, at very low temperatures, it is evident from Eq. (4.33) that only the most low-lying parts of the spectra can give a significant contribution to the free energy. The more low-lying modes are accessible at a given temperature, the larger is the (negative) free energy variation $\Delta F(T)$. This is the standard order-by-disorder statement. The asymptotic form of the softest modes should be directly related to the very low-temperature behaviour of the free energy given in Eq. (4.35). Therefore, in seek for a deeper insight of the low-temperature properties of our system, it is useful to investigate the soft modes of the spectra of the competing states.

In the system of interest here, it is far from obvious to determine which state (AF1 or AF3) has the softest modes. Indeed, soft modes are located around the zero energy modes, which are exceptionally numerous due to the harmonic approximation, as seen in Sec. (4.1.3). The next section is devoted to a careful analysis of the soft modes of harmonic spectra of the AF1 and AF3 states.

4.2.2 Soft modes of the harmonic spectra

The analytical expressions for the harmonic spin-wave spectra can be straightforwardly expanded around different types of zero-energy modes. Below only the main results are given for the AF1 and AF3 states. To further understand the thermal vs. quantum competition we derive analytically the low-temperature asymptotes for $dF(T)$ in the two states.

The AF1 state

We perform a standard Taylor expansion of the analytical expression for the spectrum $\epsilon_{1\mathbf{k}}$ given in Eq. (4.14), around various types of gapless modes. Let us remind the reader that the harmonic spectrum of the AF1 state exhibits gapless modes along full lines in reciprocal space, which can be divided into two categories: lines along the special k_x direction, and lines along the transverse directions k_y and k_z (thick and thin blue lines on the left panel of Fig. (4.2), respectively).

The soft modes lying around the first type of lines is illustrated by expanding Eq. (4.14) around $(q, 0, 2\pi/a)$. One obtains the following, quadratic asymptotic behaviour:

$$\frac{\epsilon_{1\mathbf{k}}}{JS} \approx 2\kappa_\perp^2 \sqrt{1 - \mathcal{C}_x^2 \cos^2(2\varphi)} \ , \tag{4.36}$$

where $\kappa_\perp$ and φ refer to polar coordinates in the plane transverse to the line:

$$\frac{ak_y}{2} = \kappa_y = \kappa_\perp \cos\varphi \ , \tag{4.37}$$

$$\frac{ak_z}{2} - \pi = \kappa_z = \kappa_\perp \sin\varphi \ . \tag{4.38}$$

All lines along the k_x direction (thick blue lines on Fig. (4.2)) have the same type of quadratic soft modes lying around them.

The soft modes lying around the other type of lines are illustrated by expanding Eq. (4.14) around the line $(0, 0, q)$. They have a more complex asymptotic form:

$$\frac{\epsilon_{1\mathbf{k}}}{JS} \approx 4\kappa_\perp \left\{ (1 + \mathcal{C}_z) \left[1 + \mathcal{C}_z \cos(2\varphi) \right] + \kappa_\perp^4 \cdot \cos^2(\varphi) \sin^4(\varphi)/4 \right\}^{1/2} \ . \tag{4.39}$$

Once again, $\kappa_\perp$ refers to the transverse component with respect to the line, and φ is the polar angle. We see that the soft modes described by Eq. (4.39) generally have a linear behaviour in $\kappa_\perp$, which makes them less soft than the quadratic modes of Eq. (4.36). In the transverse planes defined by $(1 + \mathcal{C}_z) = 0$, the modes of Eq. (4.39) acquire a softer, cubic behaviour. Although this may seem like particularly soft modes lie in those planes, this cubic behaviour is actually not surprising. Indeed, the corresponding points along the line are $(0, 0, \pm 2\pi/a)$, which correspond to crossing points between 3 lines (see blue balls on the left panel of Fig. (4.2)). Precisely at these points, in the transverse $k_x k_y$ plane, two lines of zero energy modes are crossing: one line along the special k_x direction, and one line along the other transverse direction k_y. Considering that soft modes lying around these lines have a quadratic and linear behaviour, respectively, the cubic behaviour is naturally expected at their intersection. All lines along the k_y and k_z directions (thin blue lines on Fig. (4.2)) have equivalent soft modes around them.

For the sake of completeness, let me now give the asymptotic behaviour of $\epsilon_{1\mathbf{k}}$ around the crossing points (k_x^0, k_y^0, k_z^0) between several lines. They are divided into two types, namely crossing points between 2 lines and between 3 lines. The first type of crossing points are displayed as blue diamonds on the left panel of Fig. (4.2). They correspond to the crossing between two lines of zero-energy modes of the transverse type (one line along k_y, one line along k_z). The soft modes lying around such points have the following asymptotic behaviour:

$$\frac{\epsilon_{1\mathbf{k}}}{JS} \approx 8 \left\{ \kappa_x^2 + \kappa_y^2 \kappa_z^2 / 4 \right\}^{1/2} \ . \tag{4.40}$$

Here κ_α is defined as follows:

$$\kappa_\alpha = \frac{a}{2}(k_\alpha - k_\alpha^0) \ . \tag{4.41}$$

Such soft modes generally have a linear behaviour in κ_x, except in the $k_y k_z$ plane, where they get a quadratic behaviour. This is naturally explained by the fact that the crossing between the two lines takes place in that plane. Since the soft modes lying

around both lines have a linear asymptotic behaviour, the soft mode becomes quadratic in this plane.

The second type of crossing points are displayed as blue balls on the left panel of Fig. (4.2). They correspond to the crossing between three lines of zero-energy modes: one of the special type along k_x, and two of the transverse type along k_y and k_z. The soft modes around these points have the following asymptotic behaviour:

$$\frac{\epsilon_{1\mathbf{k}}}{JS} \approx 4\left\{\kappa_y^2\kappa_z^2 + \kappa_x^2\left(\kappa_y^4+\kappa_z^4\right)/4\right\}^{1/2} . \tag{4.42}$$

Such soft modes generally have a quadratic behaviour in $\kappa_y\kappa_z$, except in the k_xk_z and k_xk_y planes, where they get a softer, cubic behaviour. This is explained by the fact that in these planes, there is a crossing between a line along the special k_x direction, and a line along a transverse direction (either k_y or k_z). Because the soft modes lying around such lines have a quadratic and linear asymptotic behaviour, respectively, their intersection naturally leads to a cubic behaviour.

To summarize, the softest modes of the harmonic spin-wave spectrum of the AF1 state are located along the lines of pseudo-Goldstone modes along the k_x direction (thick blue lines on the left panel of Fig. (4.2)): $2\pi(q,0,\pm1)$ and $2\pi(q,\pm1,0)$. Consequently, in the very low temperature regime, the behaviour of the free energy $\Delta F(T)$ given by Eq. (4.33) should be dominated by these modes. To confirm this, let us now evaluate the expected temperature dependence of $\Delta F(T)$ associated with such soft modes from the expression of their asymptotic behaviour, see Eq. (4.36). We remember that these modes are quadratic in the transverse $\kappa_\perp$ component:

$$\frac{\epsilon_{1\mathbf{k}}}{JS} \approx A\cdot\kappa_\perp^2 , \tag{4.43}$$

where all the dependency with respect to the longitudinal component κ_x and the angular component around the line φ, is contained in the variable A:

$$A(\kappa_x,\varphi) = 2\sqrt{1-\mathcal{C}_x^2\cos^2(2\varphi)} . \tag{4.44}$$

The sum in Eq. (4.33) is translated into integral form in the thermodynamic limit, and we have, for the free energy associated to such soft modes at very low temperatures:

$$\left.\frac{\Delta F_1(T)}{JS}\right|_{T\to0} \approx T'\frac{1}{v}\int_v \ln\left[1-e^{-A\kappa_\perp^2/T'}\right]d\mathbf{k} . \tag{4.45}$$

v is the volume of the first Brillouin zone of the fcc lattice, and we defined the relative temperature T' as follows:

$$T' = k_BT/JS . \tag{4.46}$$

This can be written in terms of the relevant variables for the line of zero-energy modes, that is, the longitudinal component κ_x, and the polar coordinates $\kappa_\perp$ and φ for the transverse component:

$$\left.\frac{\Delta F_1(T)}{JS}\right|_{T\to0} \sim T'\int_{-\pi}^{\pi}d\kappa_x\int_0^{2\pi}d\varphi\int_0^{\kappa_{\max}}\ln\left[1-e^{-A\kappa_\perp^2/T'}\right]d\left(\kappa_\perp^2\right) . \tag{4.47}$$

The upper limit $\kappa_{\max}$ for the transverse $\kappa_\perp$ component is of the order of π. Its precise value is of no interest here, as only very low-lying modes, close to the gapless line ($\kappa_\perp \to 0$), are contributing significantly. In the above expression, prefactors have been left out, as we are only interested in the temperature dependence. We apply the following change of variable:

$$x = \frac{A \cdot \kappa_\perp^2}{T'} \ , \tag{4.48}$$

and Eq. (4.47) becomes:

$$\left.\frac{\Delta F_1(T)}{JS}\right|_{T\to 0} \sim T'^2 \int\int \frac{d\kappa_x d\varphi}{A(\kappa_x,\varphi)} \int_0^\Lambda \ln\left(1-e^{-x}\right) dx \ . \tag{4.49}$$

We introduced the cutoff parameter Λ, which is of the order of:

$$\Lambda \sim \frac{A\pi^2}{T'} \ . \tag{4.50}$$

As we are interested into very low temperature physics only, we can consider the cutoff Λ to be large. Large x values only contribute marginally to the integral over x in Eq. (4.49). Therefore, it is reasonable to approximate $\Lambda \simeq \infty$, which leads to an integral of finite definite value:

$$\int_0^\Lambda \ln\left(1-e^{-x}\right) dx \approx \int_0^\infty \ln\left(1-e^{-x}\right) dx = -\frac{\pi^2}{6} \ . \tag{4.51}$$

It can be straightforwardly shown that that the integral over κ_x and φ does converge as well in Eq. (4.49), such that we recover the low-temperature T^2 dependence of the free energy of the AF1 state, see Eq. (4.35).

The collinear AF3 state

The analytical expression for the harmonic spin-wave spectrum $\epsilon^\pm_{3\mathbf{k}}$ of the AF3 state is given in Eq. (4.26). It exhibits many lines of gapless modes, both in its lower and upper branches. These lines are divided into two categories: lines along the special k_y direction, which are gapless in both branches of the spectrum, and lines along the transverse directions k_x and k_z, which are gapless only in the lower branch of the spectrum $\epsilon^-_{3\mathbf{k}}$. The two types of lines are shown in reciprocal space as thick and thin red lines on the right panel of Fig. (4.2), respectively. We perform a standard Taylor expansion of Eq. (4.26) around different types of gapless modes. Though quite cumbersome, the expansion is completely standard and we give here only final expressions for the asymptotic forms of the soft modes.

Expanding the upper branch of the spectrum $\epsilon^+_{3\mathbf{k}}$ around the line $(0,q,0)$ gives the following expression for the soft modes lying around such lines along the k_y direction:

$$\frac{\epsilon^+_{3\mathbf{k}}}{JS} \approx 4\kappa_\perp \left\{1+\sqrt{\mathcal{C}_y^2+\mathcal{S}_y^4\cos^2(2\varphi)}\right\}^{1/2} \ . \tag{4.52}$$

Here again, $\kappa_\perp$ and φ are the transverse components to the line, expressed in polar coordinates:

$$\frac{ak_z}{2} = \kappa_z = \kappa_\perp \cos\varphi \ , \tag{4.53}$$

$$\frac{ak_x}{2} = \kappa_x = \kappa_\perp \sin\varphi \ . \tag{4.54}$$

These modes have a linear asymptotic behaviour around the line.

For the lower branch of the spectrum $\epsilon^-_{3\mathbf{k}}$, the soft modes lying around these lines (thick red lines on Fig. (4.2)) have the following asymptotic behaviour:

$$\frac{\epsilon^-_{3\mathbf{k}}}{JS} \approx 4\kappa_\perp \left\{ 1 - \sqrt{\mathcal{C}_y^2 + \mathcal{S}_y^4 \cos^2(2\varphi)} + \kappa_\perp^4 \sin^2(2\varphi)/32 \right\}^{1/2} \ . \tag{4.55}$$

Along the major part of the line, this expression is the same as Eq. (4.52) for the upper branch (up to a sign change) and the soft modes have a linear behaviour in $\kappa_\perp$. Only in specific transverse $k_x k_z$ planes, when $\mathcal{S}_y = 0$, Eq. (4.55) gives a subleading softer cubic behaviour. The corresponding points along the line are displayed as red balls on the right panel of Fig. (4.2), and are crossing points between 3 lines. In the transverse $k_x k_z$ plane, two transverse lines of gapless modes are crossing.

For the other type of soft modes, lying around the transverse gapless lines along k_x and k_z (thin red lines on Fig. (4.2)), I expanded Eq. (4.26) around the line $(0, 0, q)$. I obtain the following asymptotic behaviour:

$$\frac{\epsilon^-_{3\mathbf{k}}}{JS} \approx 2\kappa_\perp \left\{ 2\left(1 - \mathcal{C}_z\right)\left[1 - \mathcal{C}_z \cos(2\varphi)\right] + \kappa_\perp^2 \sin^2(2\varphi)/2 \right\}^{1/2} \ . \tag{4.56}$$

The transverse components to the line are given in polar coordinates by $\kappa_\perp$ and φ. From Eq. (4.56) we conclude that the soft modes lying around the transverse gapless lines generally have a linear behaviour in $\kappa_\perp$, similar to those described by Eq. (4.55). In the transverse planes defined by $(\mathcal{C}_z - 1) = 0$, they acquire a softer, quadratic behaviour. This is explained by the fact that in those planes, 2 lines of gapless modes are crossing: one line along the special k_y direction, and one line along the other transverse direction k_x. Soft modes lying around these lines both have a linear behaviour, such that the quadratic behaviour is naturally expected at their intersection. The associated crossing points are displayed as the red balls on the right panel of Fig. (4.2).

The same line of argument no longer applies for the cubic behaviour of the soft modes in the $k_x k_z$ planes at those crossing points, see Eq. (4.55). Indeed, in those planes, two gapless lines along the transverse components k_x and k_z are crossing. Because such lines generally have a linear behaviour (see Eq. (4.56)), one would expect only a quadratic behaviour at their intersection, rather than a cubic behaviour. Therefore, the situation here differs from what was observed in the AF1 state. Indeed, there seems to be an odd behaviour of the soft modes, which acquire a particularly

soft asymptotic behaviour in the k_xk_z plane at those crossing points. They are therefore expected to play the dominant role in the behaviour of the free energy $\Delta F(T)$ of Eq. (4.33). The asymptotic behaviour of $\epsilon^-_{3\mathbf{k}}$ around these crossing points is given by:

$$\frac{\epsilon^-_{3\mathbf{k}}}{JS} \approx 2\sqrt{2} \cdot \sqrt{\kappa_x^2 + \kappa_z^2} \left\{ \kappa_y^2 + \kappa_x^2 \kappa_z^2 / 4 \right\}^{1/2} , \tag{4.57}$$

where κ_α is defined in Eq. (4.41). This expression is generally quadratic in κ, except in the $\kappa_y = 0$ plane, where it has the soft cubic behaviour. This is in agreement with the study of the soft modes around different types of gapless lines.

For the sake of completeness, let me also give the asymptotic expression for the soft modes lying around the other type of crossing points. These points are displayed as the red diamonds on the right panel of Fig. (4.2), and also correspond to the crossing between 3 lines:

$$\frac{\epsilon^-_{3\mathbf{k}}}{JS} \approx 4 \left\{ \left(\kappa_x^2 + \kappa_z^2\right) - |\kappa_x^2 - \kappa_z^2| \left(1 - \kappa_y^2/2\right) \right\}^{1/2} . \tag{4.58}$$

This expression is rather peculiar. We see that the modes generally have a non-analytic linear behaviour in either κ_x or κ_z. One might interpret this as the fact that the two gapless lines along the transverse k_x and k_z directions do not "see" each other, and thus do not multiply to lead to a quadratic behaviour. On the contrary, in the k_xk_y and k_yk_z planes, the dispersion acquires a softer, quadratic behaviour, which can be explained by the intersection of 2 gapless lines in those planes: one line along the k_y direction, and one line along the other transverse direction. Both have a generally linear behaviour and therefore the dispersion becomes quadratic at their crossing. Let us add, that in those k_xk_y and k_yk_z planes, the expression of $\epsilon^-_{3\mathbf{k}}$ given by Eq. (4.58) is the same as the expression for the other type of points in those planes (see Eq. (4.57)). Indeed, taking either $\kappa_x = 0$ or $\kappa_z = 0$ in Eq. (4.57) and in Eq. (4.58), we obtain the same expression:

$$\frac{\epsilon^-_{3\mathbf{k}}}{JS} \approx 2\sqrt{2} |\kappa_y \kappa_{z/x}| . \tag{4.59}$$

In summary, the softest modes of the harmonic spin-wave spectrum of the AF3 state seem to be located in the lower branch of the spectrum, around the special points equivalent to the Γ point (red balls on the right panel of Fig. (4.2)). Let us now evaluate the expected temperature dependence of $\Delta F(T)$ associated to these soft modes. Their asymptotic expression is given in Eq. (4.57), which I rewrite here in a more convenient manner:

$$\frac{\epsilon^-_{3\mathbf{k}}}{JS} \approx \sqrt{\kappa_\perp^2 \kappa_y^2 + a \kappa_\perp^6} . \tag{4.60}$$

In the above, $\kappa_\perp = \sqrt{\kappa_x^2 + \kappa_z^2}$ and a contains the angular dependence with φ:

$$a(\varphi) = \cos^2\varphi \sin^2\varphi / 4 . \tag{4.61}$$

Note as well that a prefactor $2\sqrt{2}$ has been absorbed, being of no importance here. Substituting Eq. (4.60) in Eq. (4.33), and using again the renormalized temperature T' defined by Eq. (4.46), we obtain for the free energy associated to these soft modes at very low temperatures:

$$\left.\frac{\Delta F_3(T)}{JS}\right|_{T\to 0} \approx T'\frac{1}{v}\int_v \ln\left[1-e^{-\sqrt{\kappa_\perp^2\kappa_y^2+a\kappa_\perp^6}/T'}\right]d\mathbf{k}\ . \tag{4.62}$$

In terms of the relevant variables κ_x, $\kappa_\perp$ and φ, this becomes:

$$\left.\frac{\Delta F_3(T)}{JS}\right|_{T\to 0} \sim T'\int_{-\pi}^{\pi}d\kappa_y\int_0^{2\pi}d\varphi\int_0^{\kappa_{\max}}\ln\left(1-e^{-\sqrt{\kappa_\perp^2\kappa_y^2+a\kappa_\perp^6}/T'}\right)\kappa_\perp d\kappa_\perp\ . \tag{4.63}$$

The upper limit $\kappa_{\max}$ for the transverse $\kappa_\perp$ component is of the order of π. Its precise value is of no interest here, as only very low-lying modes ($\kappa_\perp \to 0$) are contributing significantly. In the above expression, prefactors have been left out, as we are only interested in the temperature dependence. Let us make the following change of variables:

$$x=\kappa_\perp\ ,\quad y^2=\kappa_y\ . \tag{4.64}$$

We have then from Eq. (4.63):

$$\left.\frac{\Delta F_3(T)}{JS}\right|_{T\to 0} \sim T'\int d\varphi\int\int xy\ln\left(1-e^{-\sqrt{x^2y^4+ax^6}/T'}\right)dxdy\ . \tag{4.65}$$

We go to polar coordinates in the xy plane through the following change of variable:

$$x=\rho\cos\theta\ ,\quad y=\rho\sin\theta\ . \tag{4.66}$$

Eq. (4.65) becomes:

$$\left.\frac{\Delta F_3(T)}{JS}\right|_{T\to 0} \sim T'\int d\varphi\int_0^{\rho_{\max}}\int_0^{\frac{\pi}{2}}\rho^3\cos\theta\sin\theta\ln\left(1-e^{-f\rho^3/T'}\right)d\rho d\theta\ , \tag{4.67}$$

where $\rho_{\max}$ is of the order of $\sqrt{\frac{4\pi}{a}}$, and f contains all angular dependence:

$$f(\theta,\varphi)=|\cos\theta|\sqrt{\sin^4\theta+a(\varphi)\cos^4\theta}\ . \tag{4.68}$$

We define finally the following new variable t:

$$t^3=\frac{f\rho^3}{T'}\ , \tag{4.69}$$

such that Eq. (4.67) becomes:

$$\left.\frac{\Delta F_3(T)}{JS}\right|_{T\to 0} \sim T'^{7/3}\int\int g\left(\theta,\varphi\right)d\varphi d\theta\int_0^{\Lambda}t^3\ln\left(1-e^{-t^3}\right)dt\ , \tag{4.70}$$

where the function $g(\theta, \varphi)$ is defined as follows:

$$g(\theta, \varphi) = \frac{\cos\theta \sin\theta}{\left[f(\theta, \varphi)\right]^{4/3}} \ . \tag{4.71}$$

The precise value of the cutoff parameter Λ for the integral in t has no importance. Indeed, as for the AF1 state, one can approximate this integral by the integral up to ∞, provided that the temperature $T' \to 0$. It is possible to show that this leads to a converging, definite value for the intagral:

$$\int_0^{\Lambda} t^3 \ln\left(1 - e^{-t^3}\right) dt \approx \int_0^{\infty} t^3 \ln\left(1 - e^{-t^3}\right) dt = -\frac{1}{4}\Gamma\left(\frac{7}{3}\right)\zeta\left(\frac{7}{3}\right) \ . \tag{4.72}$$

Then only remains the integral over the angular function in the asymptotic expression for the free energy of Eq. (4.70):

$$\left.\frac{\Delta F_3(T)}{JS}\right|_{T\to 0} \sim T'^{7/3} \int\int g(\theta, \varphi)\, d\varphi d\theta \ . \tag{4.73}$$

It can be shown that the angular integral does converge as well, such that from the above expression we recover the low-temperature $T^{7/3}$ dependence of the free energy of the AF1 state, see Eq. (4.35).

4.3 Discussion and conclusion

The low-temperature physics of the fcc Heisenberg AFM gives a valuable insight on the competition that can take place in highly frustrated magnets, between various kinds of OBD processes driven by different fluctuations. The main findings of this study can be summarized in three major points.

First, it appears that *quantum and thermal fluctuations do not necessarily induce the stabilization of the same ordered ground state.* Although collinear spin configurations are favored by fluctuations of both origins, as predicted decades ago [8, 109], there is in principle no guarantee that the *same* collinear state is selected. This can be intuitively understood from the different functions that are involved in the two processes. For the quantum OBD at $T = 0$, the energy of a given state gets first quantum corrections from the zero point motion E_0 of spin-waves, see Eq. (4.1):

$$E_0 = \frac{1}{2} \sum_{\mathbf{k}} \epsilon_{\mathbf{k}} \ , \tag{4.74}$$

where $\epsilon_{\mathbf{k}}$ is the spin-wave spectrum. The state selected by quantum fluctuations is the one that minimizes E_0, which corresponds to the state of smallest average spectrum. In that respect, *magnons of all energies are involved in the quantum OBD.* For the thermal OBD at $T > 0$, the free energy gain $\Delta F(T)$ of a state is given by Eq. (4.33), which goes as:

$$\Delta F(T) = k_B T \sum_{\mathbf{k}} \ln \left(1 - e^{-\epsilon_{\mathbf{k}}/k_B T} \right) \ . \tag{4.75}$$

At low temperatures, minimization of $\Delta F(T)$ acts in favor of states with the "most low-lying" excitations. Therefore, *only low-energy magnons are involved in thermal OBD.* In most cases, the state with lowest-lying modes coincides with the state of smallest average spectrum, and quantum and thermal fluctuations select the same state. This property is, however, not always verified. Indeed, since the two selection mechanisms rely on magnons with different energies, their outcome can also vary. A few other authors have reported a similar competition effect between the two OBD mechanisms [105, 106, 110].

Lowest-lying modes are obviously located in the vicinity of zero-energy modes. In any broken-symmetry state of given ordering wave-vector $\mathbf{Q}$, gapless modes must appear in the the spectrum at positions $\mathbf{k} \in \{\mathbf{0}, \mathbf{Q}\}$ and equivalent points. Those are the true Goldstone modes. As previously stated however, in frustrated magnets the classical ground-state manifold is accidentally enlarged, which induces the presence of additional gapless modes in the harmonic dispersion, the so-called pseudo-Goldstone modes. In principle, each ordered classical ground state has a specific structure for its pseudo-Goldstone modes, as is illustrated on Fig. (4.2) for the AF1 and AF3 states. This takes us to the second point: *the structure of zero energy modes of the spectrum and surrounding soft modes drives the low-T energetics of the quantum spin system.* Indeed, the softness requirement for minimization of the free energy of Eq. (4.75) not

only depends on the softness of the low-lying modes, but also on the *dimensionality* of the zero energy modes around which they lie. This is well illustrated with the AF1 and AF3 states. Because the softest modes of the AF1 state (which have quadratic dispersion in k) exist around whole lines in reciprocal space, they induce a sharper free-energy asymptote when $T \to 0$.

In the fcc Heisenberg AFM studied here, thermal fluctuations are able to overcome the original energy difference between the two states at $T = 0$. This is made possible because this energy difference is particularly tiny, see Eq. (4.30). The third point would be that *the competition between quantum and thermal OBD might lead to a low temperature phase transition when two states are extremely close in energy.* Therefore, in situations where the classical ground-state manifold comprises more than one collinear state, one might need to be cautious when making assumptions on the selection operated by one type of OBD (quantum or thermal), from knowledge of the selection operated by the other.

4.3.1 Summary of the chapter

In this chapter I studied ground-state selection from quantum and thermal fluctuations in the nearest-neighbor fcc Heisenberg antiferromagnet. Using linear spin-wave theory, I derived analytical expressions for the harmonic spin-wave spectra of competing classical ground states, see Eq. (4.13), Eq. (4.14) and Eq. (4.26). The first, $1/S$ quantum correction to the ground-state energy is computed by standard Monte-Carlo integration of the spectra for each state. This correction lifts the classical ground-state degeneracy and the AF3 state is selected at $T = 0$ via the quantum order-by-disorder mechanism, see Fig. (4.1) and Eqs. (4.28 - 4.30).

I also studied the ground-state selection operated by thermal fluctuations at low temperature. Note that we remain in the *quantum* system, such that the relevant quantity to look at is the free energy as a function of temperature $\Delta F(T)$, which corresponds to the thermal population of low-lying magnons. It is computed by Monte-Carlo integration for the two competing collinear ground states (AF1 and AF3). The AF1 state is favored by thermal fluctuations rather than the AF3 state. Therefore, quantum and thermal order by disorder compete in this system at the harmonic level. The tiny ground-state energy difference at $T = 0$ is overcome by the thermal selection. As a result, a first-order phase transition is expected at low temperature from the competition between the two types of order by disorder, see Fig. (4.4) and Eq. (4.34).

The low-temperature behaviour of the free-energy is particularly sharp both for AF1 and AF3 states, compared to the typical T^4 behaviour expected for normal antiferromagnets, see Eq. (4.35). This is explained by the different structure of the pseudo-Goldstone modes and low-lying modes around them, see Fig. (4.2) and Fig. (4.3).

Chapter 5

Effects of magnon-magnon interactions

As said previously, available theoretical results diverge regarding the question of the ground state selected by fluctuations in the fcc Heisenberg antiferromagnet. The linear spin-wave analysis presented in the previous chapter indicates that the AF3 state should be favored by quantum fluctuations at $T = 0$, while the AF1 state is favored by thermal fluctuations at small finite T. In that case the two order-by-disorder mechanisms compete, and one expects a low-T first-order phase transition from one state to the other. Such a situation, where quantum and thermal fluctuations do not lead to the same ground-state selection, has been only rarely seen before. Furthermore, the obtained ground-state energies of the two competing states are remarkably close within the harmonic approximation. This tiny energy difference suggests that the next order in spin wave expansion might change the qualitative result. It is also well known that the degree of frustration is exceptionally high in the vicinity of classical phase boundaries, which makes the $1/S$ expansion of SWT somewhat less reliable in those regions, as fluctuations are believed to be large. All these elements call for a deeper investigation of the problem.

In that perspective, in this chapter I improve the spin-wave theory approach by incorporating the effects of magnon-magnon interactions. First, the spin-wave Hamiltonian with interactions is derived. Quartic terms in bosonic operators are decoupled with the Hartree-Fock method so as to obtain a new effective quadratic Hamiltonian. This effective Hamiltonian now includes mean-field variables that account for interactions. Then, analytical expressions for the spectra and mean-field averages of the competing states are derived, separately for the AF1 and AF3 state.

From these expressions, the ground-state energy with quantum corrections is computed for the two states. This is done both in a perturbative approach, and with a self-consistent renormalization of the spin-waves. Note that the latter corresponds to the $T = 0$ version of Takahashi's modified SWT. By comparison of these energies, it appears that the ground state selected at $T = 0$ by quantum fluctuations is the AF1 state, for most values of spin length. This is at variance with the harmonic result,

which is recovered qualitatively only at a very large spin $S \gtrsim 10$. The self-consistently renormalized spectra acquire quantum gaps along pseudo-Goldstone modes, of which the expression is given, as well as spin-wave velocities.

Then, the thermal OBD is addressed at low-temperature, from thermal population of low-lying magnons. The AF1 state remains the state selected by thermal fluctuations. Conventional T^4 asymptotic behaviour for the free energy $\Delta F(T)$ is recovered at very low temperatures, which is directly related to the self-consistent renormalization of the spectra.

The values of the ground-state energies of the AF1 and AF3 states, obtained via the self-consistent approach, compare well to numerical data. This confirms the efficiency of the method, despite an apparent failure of the perturbative spin-wave expansion in that system.

5.1 Spin-wave theory with interactions: energy corrections and spectra

In harmonic spin-wave theory, the effects of interactions between magnons are neglected. Indeed, expanding the Holstein-Primakoff transformation of spin operators (see Eq. (1.20)) to lowest order only, leads to terms which are at most quadratic in bosonic operators a_i, $a_i^\dagger$. The resulting quadratic Hamiltonian, after Bogolyubov diagonalization, describes a standard single-particle problem (see Eq. (A.41)):

$$\hat{\mathcal{H}}_{\text{LSW}} = E_{\text{g.s.}} + \sum_{\mathbf{k},m} \epsilon_{m\mathbf{k}} \cdot \beta^\dagger_{\mathbf{k},m}\beta_{\mathbf{k},m} \ , \tag{5.1}$$

where $\epsilon_{m\mathbf{k}}$ is the energy of a particle (spin-wave) of momentum $\mathbf{k}$ in mode m. To take into account the effects of interactions, we need to expand the Hostein-Primakoff transformation further (see Eqs. (A.4 - A.5)). In this section, we include in the Hamiltonian the terms describing 2 bosons interactions. The Holstein-Primakoff transformation is given below to relevant order:

$$\begin{aligned} S_i^+ &\approx \sqrt{2S}\left(a_i - \frac{1}{4S}a_i^\dagger a_i a_i\right) \ , \\ S_i^- &\approx \sqrt{2S}\left(a_i^\dagger - \frac{1}{4S}a_i^\dagger a_i^\dagger a_i\right) \ , \\ S_i^z &= S - a_i^\dagger a_i \ . \end{aligned} \tag{5.2}$$

Following the standard spin-wave method described in appendix (A), this transformation is done in the locally rotated frame of classical spins, see Eq. (A.7). The spin operators in the original spin Hamiltonian of Eq. (4.4) are substituted by Eq. (5.2), leading to the bosonic spin-wave Hamiltonian. For the sake of simplicity, we keep all information about the bosonic mode and the position in the lattice encapsulated in the i and j indices for now.

5.1.1 General spin-wave Hamiltonian in real space

Since the two classcial ground states we aim at comparing are collinear spin structures (AF1 and AF3), the scalar products in Eq. (4.4) can be of two kinds: either between parallel spins ($\uparrow\uparrow$) or antiparallel spins ($\uparrow\downarrow$). This allows us to obtain a general expression for the spin-wave Hamiltonian with interactions in real space, and for the resulting quantum corrections to the ground-state energy up to second order in $1/S$. In the local rotated frame (see Eq. (A.7)), the two kinds of scalar products are expressed as:

$$(\mathbf{S}_i \cdot \mathbf{S}_j)^{\uparrow\uparrow} = S_i^z S_j^z + \frac{1}{2}\left(S_i^+ S_j^- + S_i^- S_j^+\right) , \tag{5.3}$$

$$(\mathbf{S}_i \cdot \mathbf{S}_j)^{\uparrow\downarrow} = -S_i^z S_j^z - \frac{1}{2}\left(S_i^+ S_j^+ + S_i^- S_j^-\right) . \tag{5.4}$$

We substitute Eq. (5.2) into Eqs. (5.3-5.4), and we truncate the obtained expressions, keeping only up to quartic terms in bosonic operators. Let us express the associated bond Hamiltonians $\hat{\mathcal{H}}_{ij}$ in the expanded form:

$$\hat{\mathcal{H}}_{ij} = J\mathbf{S}_i \cdot \mathbf{S}_j \approx \varepsilon_{ij}^{\mathrm{cl}} + \mathcal{H}_{ij}^{(2)} + \mathcal{H}_{ij}^{(4)} . \tag{5.5}$$

In the above expression, $\mathcal{H}_{ij}^{(n)}$ corresponds to the n^{th} order in the spin-wave expansion, meaning that it contains only terms involving products of n bosonic operators. The classical energy $\varepsilon_{ij}^{\mathrm{cl}}$ of a given bond is trivially given by:

$$\varepsilon_{ij}^{\mathrm{cl}} = \mathcal{H}_{ij}^{(0)} = \pm JS^2 , \tag{5.6}$$

the positive (resp. negative) sign corresponding to a pair of parallel spins $\uparrow\uparrow$ (resp. antiparallel spins $\uparrow\downarrow$). The quadratic contribution $\mathcal{H}_{ij}^{(2)}$ represents the first quantum correction to the ground-state energy, and is given below for the two types of bonds:

$$\left[\mathcal{H}_{ij}^{(2)}\right]^{\uparrow\uparrow} = JS\left(a_i^\dagger a_j + a_j^\dagger a_i - a_i^\dagger a_i - a_j^\dagger a_j\right) , \tag{5.7}$$

$$\left[\mathcal{H}_{ij}^{(2)}\right]^{\uparrow\downarrow} = JS\left(a_i^\dagger a_i + a_j^\dagger a_j - a_i a_j - a_i^\dagger a_j^\dagger\right) . \tag{5.8}$$

This harmonic contribution captures the free bosons physics, and goes as S^1. It thus generates a $1/S$ correction to the classical ground-state energy (which goes as S^2 as is seen from Eq. (5.6)). The quartic terms in $\mathcal{H}_{ij}^{(4)}$ go as S^0 and account for magnon-magnon interactions. They generate a $1/S^2$ correction to the classical ground-state energy. We explicitly give them below:

$$\left[\mathcal{H}_{ij}^{(4)}\right]^{\uparrow\uparrow} = J\left[a_i^\dagger a_i a_j^\dagger a_j - \frac{1}{4}\left(a_i^\dagger a_j a_i^\dagger a_i + a_j^\dagger a_i a_j^\dagger a_j + a_i^\dagger a_i a_j^\dagger a_i + a_j^\dagger a_j a_i^\dagger a_j\right)\right] , \tag{5.9}$$

$$\left[\mathcal{H}_{ij}^{(4)}\right]^{\uparrow\downarrow} = -J\left[a_i^\dagger a_i a_j^\dagger a_j - \frac{1}{4}\left(a_i^\dagger a_i a_i a_j + a_j^\dagger a_j a_i a_j + a_i^\dagger a_j^\dagger a_j a_j + a_i^\dagger a_j^\dagger a_i^\dagger a_i\right)\right] . \tag{5.10}$$

From Eqs. (5.5-5.10), one can rewrite the original spin Hamiltonian of Eq. (4.4) in its expanded form:

$$\hat{\mathcal{H}} = \sum_{\langle i,j \rangle} \hat{\mathcal{H}}_{ij} \approx E_{\rm cl} + \mathcal{H}^{(2)} + \mathcal{H}^{(4)} \ , \tag{5.11}$$

where the total classical energy $E_{\rm cl}$ is given by Eq. (4.3).

Mean-field decoupling of quartic terms

Evaluating quartic terms as is requires solving tedious 3-dimensional integrals in reciprocal space. It is however possible to simplify this problem by applying a standard Hartree-Fock decoupling to those terms. The assumption behind this approximation is that correlations between fluctuations around the mean fields are small. The following mean-field averages are defined:

$$\begin{aligned} n &= \langle a_i^\dagger a_i \rangle \ , \\ m_{ij} &= \langle a_i^\dagger a_j \rangle \ , \\ \Delta_{ij} &= \langle a_i^\dagger a_j^\dagger \rangle \ . \end{aligned} \tag{5.12}$$

The notation $\langle \cdot \rangle$ stands for the expectation value of a given operator in the ground state considered. Note that the particle number mean field n does not depend on the site position, as we are in a Bravais lattice. Let me show how one decouples a given quartic term, say $a_i^\dagger a_i a_j^\dagger a_j$. One can show that it must involve all possible pair decouplings, which leads to the following:

$$\begin{aligned} a_i^\dagger a_i a_j^\dagger a_j \approx & n\left(a_i^\dagger a_i + a_j^\dagger a_j\right) + m_{ij}\left(a_i^\dagger a_j + a_j^\dagger a_i\right) + \Delta_{ij}\left(a_i a_j + a_i^\dagger a_j^\dagger\right) \\ & - n^2 - m_{ij}^2 - \Delta_{ij}^2 \ . \end{aligned} \tag{5.13}$$

Similar expressions are obtained for all the quartic terms in Eqs. (5.9 - 5.10). The hopping average m_{ij} vanishes for pairs of antiparallel spins ($\uparrow\downarrow$ bonds), while the anomalous average Δ_{ij} vanishes for parallel spins ($\uparrow\uparrow$ bonds).

Effective quadratic Hamiltonian

After the decoupling, $\mathcal{H}_{ij}^{(4)}$ takes an effective quadratic form, such that the bond Hamiltonian is given by:

$$\hat{\mathcal{H}}_{ij} \approx \tilde{\mathcal{H}}_{ij}^{(0)} + \tilde{\mathcal{H}}_{ij}^{(2)} \ , \tag{5.14}$$

where $\tilde{\mathcal{H}}_{ij}^{(n)}$ contains both the original $n^{\rm th}$ order terms of Eq. (5.5), and the additional effective part coming from the decoupling of quartic terms. Below we give the explicit final quadratic form for the two kinds of bond Hamiltonians:

$$\hat{\mathcal{H}}_{ij}^{\uparrow\uparrow} \approx J\Big\{ S^2 - \left(n - m_{ij}\right)^2 - S_{ij}^{\uparrow\uparrow}\left[a_i^\dagger a_i + a_j^\dagger a_j - a_i^\dagger a_j - a_j^\dagger a_i\right] \Big\} \ , \tag{5.15}$$

$$\hat{\mathcal{H}}_{ij}^{\uparrow\downarrow} \approx -J\Big\{ S^2 - \left(n - \Delta_{ij}\right)^2 - S_{ij}^{\uparrow\downarrow}\left[a_i^\dagger a_i + a_j^\dagger a_j - a_i a_j - a_i^\dagger a_j^\dagger\right] \Big\} \ , \tag{5.16}$$

where we defined renormalized spin values:

$$S_{ij}^{\uparrow\uparrow} = S - n + m_{ij} \ , \tag{5.17}$$
$$S_{ij}^{\uparrow\downarrow} = S - n + \Delta_{ij} \ .$$

Substituting Eqs. (5.15-5.16) into Eq. (5.11), one obtains the final quadratic Hamiltonian in the Hartree-Fock approximation:

$$\hat{\mathcal{H}}_{\rm HF} = \tilde{\mathcal{H}}^{(0)} + \tilde{\mathcal{H}}^{(2)} \ , \tag{5.18}$$

where $\tilde{\mathcal{H}}^{(n)}$ is the $n^{\rm th}$ order Hamiltonian including the effective mean-field contribution from interactions:

$$\tilde{\mathcal{H}}^{(n)} = \mathcal{H}^{(n)} + \mathcal{H}_{\rm eff}^{(n)} \ . \tag{5.19}$$

We have for the constant part:

$$\tilde{\mathcal{H}}^{(0)} = E_{\rm cl} + \Delta E^{(0)} \ . \tag{5.20}$$

The classical ground-state energy $E_{\rm cl} = \mathcal{H}^{(0)}$ is degenerate for the two competing states AF1 and AF3. We recover the expression of Eq. (4.3):

$$\frac{E_{\rm cl}}{N} = \frac{JS^2}{N}\left\{\sum_{\langle i,j\rangle}^{\uparrow\uparrow} - \sum_{\langle i,j\rangle}^{\uparrow\downarrow}\right\} = -2JS^2 \sim S^2 \ . \tag{5.21}$$

Indeed, in both configurations, each spin has 4 of its nearest neighbors parallel to it ($\uparrow\uparrow$ bonds), and the 8 remaining are antiparallel ($\uparrow\downarrow$ bonds). The second term $\Delta E^{(0)}$ in Eq. (5.20) is a correction coming from the interactions:

$$\Delta E^{(0)} = J\left[\sum_{\langle i,j\rangle}^{\uparrow\downarrow}(n-\Delta_{ij})^2 - \sum_{\langle i,j\rangle}^{\uparrow\uparrow}(n-m_{ij})^2\right] \sim S^0 \ . \tag{5.22}$$

The quadratic part of Eq. (5.18) is given by:

$$\tilde{\mathcal{H}}^{(2)} = J\sum_{\langle i,j\rangle}^{\uparrow\downarrow} S_{ij}^{\uparrow\downarrow}\left[a_i^\dagger a_i + a_j^\dagger a_j - a_i a_j - a_i^\dagger a_j^\dagger\right] \tag{5.23}$$
$$- J\sum_{\langle i,j\rangle}^{\uparrow\uparrow} S_{ij}^{\uparrow\uparrow}\left[a_i^\dagger a_i + a_j^\dagger a_j - a_i^\dagger a_j - a_j^\dagger a_i\right] \ .$$

General expression for the ground-state energy

Finally, one obtains the ground-state energy with quantum corrections by averaging the Hamiltonian over the ground state. From Eqs. (5.18 - 5.23), we find:

$$E_{\rm gs} \approx \langle\hat{\mathcal{H}}_{\rm HF}\rangle = J\left[\sum_{\langle i,j\rangle}^{\uparrow\uparrow}\left(S_{ij}^{\uparrow\uparrow}\right)^2 - \sum_{\langle i,j\rangle}^{\uparrow\downarrow}\left(S_{ij}^{\uparrow\downarrow}\right)^2\right] \ . \tag{5.24}$$

The quantum corrections to the ground-state energy of a given state are thus expressed as a function of the local mean-field averages n, m_{ij} and Δ_{ij} in that state, see Eq. (5.24) and Eq. (5.17). Fortunately, one does not need to compute independently the values of the mean-field averages m_{ij} and Δ_{ij} for all pairs of nearest-neighbor spins. Indeed, many of those pairs are equivalent, such that we can define a few different categories of pairs. Therefore only a number of mean-field averages equal to the number of categories needs to be computed. This is done differently for the two competing states, as is shown in the next two sections.

5.1.2 The AF1 state

The AF1 state is shown on Fig. (3.4a). I remind the reader that in this state, all spins are equivalent to each other up to a rotation, meaning that a single-boson picture is sufficient to fully describe it within SWT. In that context, all pairs of parallel nearest-neighbor spins are also equivalent, and they should have the same mean-field behaviour. The hopping average m_{ij}, see Eq. (5.12), is thus uniquely defined for all $\uparrow\uparrow$ spin pairs:

$$m_{ij}^{\uparrow\uparrow} = m = \frac{1}{4N} \sum_{\mathbf{R}} \sum_{\boldsymbol{\delta}^{\uparrow\uparrow}} \langle a_{\mathbf{R}}^{\dagger} a_{\mathbf{R}+\boldsymbol{\delta}} \rangle \ . \tag{5.25}$$

We defined $\boldsymbol{\delta}^{\uparrow\uparrow} \in \{\pm\mathbf{a_1}, \pm\mathbf{a_4}\}$, which spans the 4 nearest-neighbor vectors between parallel spins in the AF1 structure. Similarly, the anomalous average Δ_{ij} is uniquely defined for all $\uparrow\downarrow$ bonds:

$$\Delta_{ij}^{\uparrow\downarrow} = \Delta = \frac{1}{8N} \sum_{\mathbf{R}} \sum_{\boldsymbol{\delta}^{\uparrow\downarrow}} \langle a_{\mathbf{R}} a_{\mathbf{R}+\boldsymbol{\delta}} \rangle \ , \tag{5.26}$$

where $\boldsymbol{\delta}^{\uparrow\downarrow} \in \{\pm\mathbf{a_2}, \pm\mathbf{a_3}, \pm\mathbf{a_5}, \pm\mathbf{a_6}\}$ spans the 8 nearest-neighbor vectors between antiparallel spins. The hopping average $m_{ij}^{\uparrow\downarrow}$ for pairs of antiparallel spins, and the anomalous average $\Delta_{ij}^{\uparrow\uparrow}$ for pairs of parallel spins, both vanish. The ground-state energy with quantum corrections is then easily obtained from Eq. (5.24):

$$\frac{E_1}{N} \approx 2J(S - n + m)^2 - 4J(S - n + \Delta)^2 = 2J \left[S_{\uparrow\uparrow}\right]^2 - 4J \left[S_{\uparrow\downarrow}\right]^2 \ . \tag{5.27}$$

The two renormalized spins $S_{\uparrow\uparrow}$ and $S_{\uparrow\downarrow}$ follow from Eq. (5.17):

$$S_{\uparrow\uparrow} = S - n + m \ , \tag{5.28}$$

$$S_{\uparrow\downarrow} = S - n + \Delta \ . \tag{5.29}$$

We apply a Fourier transformation to the bosonic operators in Eqs. (5.25 - 5.26), in order to get expressions for the mean filed averages in reciprocal space:

$$\begin{aligned} n =& \frac{1}{N}\sum_{\mathbf{k}} \langle a^\dagger_{\mathbf{k}} a_{\mathbf{k}}\rangle \ , \\ m =& \frac{1}{4N}\sum_{\mathbf{k}} \langle a^\dagger_{\mathbf{k}} a_{\mathbf{k}}\rangle \sum_{\boldsymbol{\delta}^{\uparrow\uparrow}} e^{i\mathbf{k}\cdot\boldsymbol{\delta}} = \frac{1}{N}\sum_{\mathbf{k}} \langle a^\dagger_{\mathbf{k}} a_{\mathbf{k}}\rangle \, \mathcal{C}_y\mathcal{C}_z \ , \\ \Delta =& \frac{1}{8N}\sum_{\mathbf{k}} \langle a_{\mathbf{k}} a_{\text{-}\mathbf{k}}\rangle \sum_{\boldsymbol{\delta}^{\uparrow\downarrow}} e^{-i\mathbf{k}\cdot\boldsymbol{\delta}} = \frac{1}{2N}\sum_{\mathbf{k}} \langle a_{\mathbf{k}} a_{\text{-}\mathbf{k}}\rangle \, \mathcal{C}_x \left(\mathcal{C}_y + \mathcal{C}_z\right) \ . \end{aligned} \tag{5.30}$$

We remind the reader that the definition of $\mathcal{C}_\alpha$, with $\alpha \in \{x, y, z\}$, given by Eq. (3.7).

One needs to compute the expectation values of the normal and anomalous terms ($\langle a^\dagger_{\mathbf{k}} a_{\mathbf{k}}\rangle$ and $\langle a_{\mathbf{k}} a_{\text{-}\mathbf{k}}\rangle$, respectively) in the ground state, in order to obtain values for n, m and Δ. The ground state is, however, not defined straightforwardly in terms of the $a_{\mathbf{k}}$ particles. Indeed, as in the harmonic case, the Hamiltonian is not diagonal in this basis, and needs to be diagonalized through the Bogolyubov transformation.

Hamiltonian in reciprocal space

The mean-field averages defined in Eqs. (5.25 - 5.26) are substituted into the quadratic part of the Hamiltonian given by Eq. (5.23). After the Fourier transformation, we obtain the quadratic Hamiltonian in reciprocal space, which has the exact same structure as in the harmonic approximation (see Eq. (4.9)):

$$\tilde{\mathcal{H}}^{(2)} = \sum_{\mathbf{k}} \left\{ A_{\mathbf{k}} a^\dagger_{\mathbf{k}} a_{\mathbf{k}} - \frac{1}{2} B_{\mathbf{k}} \left(a^\dagger_{\mathbf{k}} a^\dagger_{\text{-}\mathbf{k}} + a_{\text{-}\mathbf{k}} a_{\mathbf{k}} \right) \right\} \ . \tag{5.31}$$

The coefficients $A_{\mathbf{k}}$ and $B_{\mathbf{k}}$ now include both the harmonic contribution and a contribution coming from interactions with mean fields:

$$A_{\mathbf{k}} = 4J\left(S - n + m\right)\left(1 + \mathcal{C}_y\mathcal{C}_z\right) + 8J\left(\Delta - m\right) = 4JS_{\uparrow\uparrow}(\mathcal{C}_y\mathcal{C}_z - 1) + 8JS_{\uparrow\downarrow} \ , \tag{5.32}$$

$$B_{\mathbf{k}} = 4J\left(S - n + \Delta\right)\mathcal{C}_x(\mathcal{C}_y + \mathcal{C}_z) = 4JS_{\uparrow\downarrow} \cdot \mathcal{C}_x(\mathcal{C}_y + \mathcal{C}_z) \ . \tag{5.33}$$

The quadratic Hamiltonian of Eq. (5.31) has the standard structure for the single-boson picture, see Eq. (A.9). One recovers the harmonic Hamiltonian by ignoring all contributions from mean-field averages in $\tilde{\mathcal{H}}^{(0)}$ (see Eqs. (5.20 - 5.22)) and in $\tilde{\mathcal{H}}^{(2)}$ (see Eqs. (5.31 - 5.33)). Indeed, the expressions of $A_{\mathbf{k}}$ and $B_{\mathbf{k}}$ in the harmonic approximation are recovered when taking $S_{\uparrow\uparrow} = S_{\uparrow\downarrow} = S$ in Eqs. (5.32 - 5.33), or $q = 0$ in Eq. (4.11).

Bogolyubov transformation and spectrum

The quadratic Hamiltonian given in Eqs. (5.31 - 5.33) is diagonalized using the standard Bogolyubov transformation in a single-boson picture. Because it will be useful later,

let me write the transformation explicitly. We define new particles with corresponding bosonic operators $\beta_{\mathbf{k}}$, $\beta^{\dagger}_{\mathbf{k}}$:

$$a_{\mathbf{k}} = u_{\mathbf{k}}\beta_{\mathbf{k}} + v_{\mathbf{k}}\beta^{\dagger}_{\text{-}\mathbf{k}} \ . \tag{5.34}$$

The coefficients $u_{\mathbf{k}}$ and $v_{\mathbf{k}}$ are real. Eq. (5.34) is substituted in Eq. (5.31) in order to get the Hamiltonian in terms of the new operators $\beta_{\mathbf{k}}$. We impose that in this new basis, the anomalous terms must vanish identically, which constrains the coefficients $u_{\mathbf{k}}$ and $v_{\mathbf{k}}$. From bosonic commutation relations (which must be verified both in the old basis and in the new one), we obtain the following:

$$\begin{aligned} v_{\mathbf{k}}^2 =& \frac{1}{2}\left(\frac{A_{\mathbf{k}}}{\epsilon_{1\mathbf{k}}} - 1\right) \ , \\ u_{\mathbf{k}}^2 =& \frac{1}{2}\left(\frac{A_{\mathbf{k}}}{\epsilon_{1\mathbf{k}}} + 1\right) \ , \\ 2u_{\mathbf{k}}v_{\mathbf{k}} =& \frac{B_{\mathbf{k}}}{\epsilon_{1\mathbf{k}}} \ . \end{aligned} \tag{5.35}$$

In the above, $\epsilon_{1\mathbf{k}}$ is the spin-wave spectrum:

$$\epsilon_{1\mathbf{k}} = \sqrt{A_{\mathbf{k}}^2 - B_{\mathbf{k}}^2} \ . \tag{5.36}$$

Although this expression for $\epsilon_{1\mathbf{k}}$ is exactly the same as in the harmonic approximation (see Eq. (4.12)), the coefficients $A_{\mathbf{k}}$ and $B_{\mathbf{k}}$ now involve the different mean fields, see Eqs. (5.32 - 5.33). The spectrum is therefore *renormalized* by interactions.

Diagonal Hamiltonian and zero point motion

After the Bogolyubov transformation, the quadratic part of the Hamiltonian (Eq. (5.31)) has a fully diagonal structure:

$$\tilde{\mathcal{H}}^{(2)} = \sum_{\mathbf{k}} \left[\epsilon_{1\mathbf{k}} \left(\beta^{\dagger}_{\mathbf{k}}\beta_{\mathbf{k}} + \frac{1}{2} \right) - \frac{1}{2}A_{\mathbf{k}} \right] \ . \tag{5.37}$$

The ground state is now naturally defined as the vacuum of $\beta_{\mathbf{k}}$ particles (magnons). The correction to the ground-state energy associated to the quadratic Hamiltonian of Eq. (5.37) is given by:

$$\Delta E^{(2)} = \frac{1}{2}\sum_{\mathbf{k}} (\epsilon_{1\mathbf{k}} - A_{\mathbf{k}}) \ . \tag{5.38}$$

It contains both the harmonic correction in S^1 and a correction in S^0 coming from the interaction with mean fields. The total ground-state energy per site with quantum corrections is given by:

$$\frac{E_{\text{gs}}}{N} \approx \left(E_{\text{cl}} + \Delta E^{(0)} + \Delta E^{(2)} \right) / N \ , \tag{5.39}$$

where E_{cl} and $\Delta E^{(0)}$ are given by Eq. (5.21) and Eq. (5.22), respectively, and $\Delta E^{(2)}$ is given by Eq. (5.38). As is shown below, the correction obtained through Eq. (5.39) is exactly equivalent to the previously obtained expression, see Eq. (5.27).

mean-field averages

We wish to have expressions for the expectation values appearing in the definitions of mean-field averages, see Eq. (5.30). From the explicit Bogolyubov transformation given by Eqs. (5.34), we obtain:

$$\langle a_{\mathbf{k}}^\dagger a_{\mathbf{k}}\rangle = u_{\mathbf{k}}^2 \langle \beta_{\mathbf{k}}^\dagger \beta_{\mathbf{k}}\rangle + u_{\mathbf{k}} v_{\mathbf{k}} \left(\langle \beta_{\mathbf{k}}^\dagger \beta_{\text{-}\mathbf{k}}^\dagger\rangle + \langle \beta_{\text{-}\mathbf{k}} \beta_{\mathbf{k}}\rangle \right) + v_{\mathbf{k}}^2 \langle \beta_{\text{-}\mathbf{k}} \beta_{\text{-}\mathbf{k}}^\dagger\rangle = v_{\mathbf{k}}^2 \ , \tag{5.40}$$

$$\langle a_{\mathbf{k}} a_{\text{-}\mathbf{k}}\rangle = u_{\mathbf{k}}^2 \langle \beta_{\text{-}\mathbf{k}} \beta_{\mathbf{k}}\rangle + u_{\mathbf{k}} v_{\mathbf{k}} \left(\langle \beta_{\mathbf{k}} \beta_{\mathbf{k}}^\dagger\rangle + \langle \beta_{\text{-}\mathbf{k}}^\dagger \beta_{\text{-}\mathbf{k}}\rangle \right) + v_{\mathbf{k}}^2 \langle \beta_{\mathbf{k}}^\dagger \beta_{\text{-}\mathbf{k}}^\dagger\rangle = u_{\mathbf{k}} v_{\mathbf{k}} \ . \tag{5.41}$$

In the above, the last equality for both lines comes from the fact that all expectation values for quadratic terms of $\beta_{\mathbf{k}}$ operators vanish in the Bogolyubov vacuum, except one:

$$\begin{aligned}
\langle 0|\beta_{\mathbf{k}}^\dagger \beta_{\mathbf{k}}|0\rangle &= \langle 0|\beta_{\text{-}\mathbf{k}}^\dagger \beta_{\text{-}\mathbf{k}}|0\rangle = 0 \ , \\
\langle 0|\beta_{\mathbf{k}}^\dagger \beta_{\text{-}\mathbf{k}}^\dagger|0\rangle &= \langle 0|\beta_{\text{-}\mathbf{k}} \beta_{\mathbf{k}}|0\rangle = 0 \ , \\
\langle 0|\beta_{\mathbf{k}} \beta_{\mathbf{k}}^\dagger|0\rangle &= \langle 0|\beta_{\text{-}\mathbf{k}} \beta_{\text{-}\mathbf{k}}^\dagger|0\rangle = 1 \ .
\end{aligned}$$

We substitute Eqs. (5.40 - 5.41) into the expressions for the mean-field averages, see Eq. (5.30). From the explicit coefficients of the Bogolyubov transformation given in Eq. (5.35), we get:

$$\begin{aligned}
n &= \frac{1}{N} \sum_{\mathbf{k}} \frac{A_{\mathbf{k}}}{2\epsilon_{1\mathbf{k}}} - \frac{1}{2} \ , \\
m &= \frac{1}{N} \sum_{\mathbf{k}} \frac{A_{\mathbf{k}}}{2\epsilon_{1\mathbf{k}}} \cdot \mathcal{C}_y \mathcal{C}_z \ , \\
\Delta &= \frac{1}{N} \sum_{\mathbf{k}} \frac{B_{\mathbf{k}}}{4\epsilon_{1\mathbf{k}}} \cdot \mathcal{C}_x (\mathcal{C}_y + \mathcal{C}_z) \ .
\end{aligned} \tag{5.42}$$

Equivalence of two expressions for the ground-state energy

Using Eq. (5.36), we have for the zero-point motion appearing in Eq. (5.38):

$$\frac{1}{2N} \sum_{\mathbf{k}} \epsilon_{1\mathbf{k}} = \frac{1}{2N} \sum_{\mathbf{k}} \frac{A_{\mathbf{k}}^2 - B_{\mathbf{k}}^2}{\epsilon_{1\mathbf{k}}} \ , \tag{5.43}$$

where $A_{\mathbf{k}}$ and $B_{\mathbf{k}}$ are given in Eqs. (5.32 - 5.33). This gives

$$\frac{1}{2N} \sum_{\mathbf{k}} \epsilon_{1\mathbf{k}} = \frac{4J}{N} \sum_{\mathbf{k}} \left\{ \frac{A_{\mathbf{k}} \left[S_{\uparrow\uparrow} (\mathcal{C}_y \mathcal{C}_z - 1) + 2 S_{\uparrow\downarrow} \right]}{2\epsilon_{1\mathbf{k}}} - \frac{B_{\mathbf{k}} \cdot S_{\uparrow\downarrow} \mathcal{C}_x (\mathcal{C}_y + \mathcal{C}_z)}{2\epsilon_{1\mathbf{k}}} \right\} \ .$$

Rearranging terms in the above leads to:

$$\begin{aligned}\frac{1}{2N}\sum_{\mathbf{k}}\epsilon_{1\mathbf{k}} =& 4JS_{\uparrow\uparrow}\left\{\frac{1}{N}\sum_{\mathbf{k}}\frac{A_{\mathbf{k}}}{2\epsilon_{1\mathbf{k}}}\cdot\mathcal{C}_y\mathcal{C}_z-\frac{1}{N}\sum_{\mathbf{k}}\frac{A_{\mathbf{k}}}{2\epsilon_{1\mathbf{k}}}\right\}\\ &+8JS_{\uparrow\downarrow}\left\{\frac{1}{N}\sum_{\mathbf{k}}\frac{A_{\mathbf{k}}}{2\epsilon_{1\mathbf{k}}}-\frac{1}{N}\frac{B_{\mathbf{k}}}{4\epsilon_{1\mathbf{k}}}\cdot\mathcal{C}_x(\mathcal{C}_y+\mathcal{C}_z)\right\}\ .\end{aligned} \tag{5.44}$$

We see that the definitions of the mean-field averages given in Eq. (5.42) appear in the curl brackets. Substituting them in Eq. (5.44), we obtain:

$$\frac{1}{2N}\sum_{\mathbf{k}}\epsilon_{1\mathbf{k}} = 8JS_{\uparrow\downarrow}\left(n-\Delta+1/2\right)-4JS_{\uparrow\uparrow}\left(n-m+1/2\right)\ . \tag{5.45}$$

We also have:

$$\frac{1}{2N}\sum_{\mathbf{k}}A_{\mathbf{k}} = 2JS_{\uparrow\uparrow}\frac{1}{N}\sum_{\mathbf{k}}\left(\mathcal{C}_y\mathcal{C}_z-1\right)+4JS_{\uparrow\downarrow}\frac{1}{N}\sum_{\mathbf{k}} = 4J\cdot S_{\uparrow\downarrow}-2J\cdot S_{\uparrow\uparrow}\ . \tag{5.46}$$

Combining Eq. (5.45) and Eq. (5.46), we obtain the following expression for the correction $\Delta E^{(2)}$ of Eq. (5.38):

$$\frac{\Delta E^{(2)}}{N} = 8JS_{\uparrow\downarrow}(n-\Delta)-4JS_{\uparrow\uparrow}(n-m)\ . \tag{5.47}$$

The correction $\Delta E^{(0)}$ added to the constant part of the Hamiltonian from interactions is given by Eq. (5.22):

$$\frac{\Delta E^{(0)}}{N} = 4J(n-\Delta)^2-2J(n-m)^2\ . \tag{5.48}$$

Finally, we combine Eq. (5.47) and Eq. (5.48) to the classical ground-state energy $E_{\rm cl}=-2NJS^2$, and we obtain the ground-state energy with quantum corrections from Eq. (5.39):

$$\begin{aligned}\frac{E_{\rm gs}}{N} \approx& -2JS^2+4J(n-\Delta)^2-2J(n-m)^2+8JS_{\uparrow\downarrow}(n-\Delta)-4JS_{\uparrow\uparrow}(n-m)\\ =&2J\left[S_{\uparrow\uparrow}\right]^2-4J\left[S_{\uparrow\downarrow}\right]^2\ .\end{aligned} \tag{5.49}$$

We recover the expression of Eq. (5.27).

5.1.3 The AF3 state

The AF3 state is shown on Fig. (3.4b). As was said in subsection 4.1.1, it is more complex than the AF1 state and requires to define at least two different magnon modes, which we refer to as mode a and b. The sites which belong to the mode a (resp. mode b) are illustrated as full arrows (resp. empty arrows) on Fig. (3.4b). The magnetic unit cell is then enlarged and contains two sites of the original Bravais lattice, one site at position $\mathbf{R}$ belonging to mode a, and the other at position $\mathbf{R}+\mathbf{a}_3$ belonging to mode b, where $\mathbf{a}_3$ is given by Eq. (3.2). Such an enlarged unit cell is given by sites 1 and 2 on Fig. (3.4b). The translation vectors used to locate any unit cell become $a/2(1,0,1)$, $a/2(-1,0,1)$ and $a(0,1,0)$.

Within this description, the nearest neighbors of a spin of a given mode do not only belong to the opposite mode, as is the case for simple bipartite structures. Indeed, nearest-neighbor vectors $\boldsymbol{\delta} \in \{\pm\mathbf{a}_2, \pm\mathbf{a}_5\}$ always connect sites located in the same xz plane, and therefore belonging to the same bosonic mode. Consequently, one needs to distinguish between pairs of nearest-neighbor spins belonging to a same mode, or to different modes. Take note that two spins belonging to the same mode do not necessarily have the same orientation. Equivalently, two spins belonging to opposite modes do not necessarily have a different orientation. We need to introduce different mean-field averages for each different type of nearest-neighbor spin pairs. There are 3 such categories of pairs:

- $(\uparrow\downarrow_{ab})$ pairs: antiparallel pairs of spins of opposite magnon modes:
  we define the anomalous mean-field average $\Delta_{ij} = \Delta$ for such pairs.
- $(\uparrow\uparrow_{ab})$ pairs: parallel pairs of spins of opposite magnon modes:
  we define the hopping mean-field average $m_{ij} = m$ for such pairs.
- $(\uparrow\downarrow_{aa})$ and $(\uparrow\downarrow_{bb})$ pairs: antiparallel pairs of spins of same magnon mode:
  we define the anomalous mean-field average $\Delta_{ij} = \Delta_{\alpha\alpha}$ for such pairs.

There are no parallel pairs of nearest-neighbor spins of the same magnon mode, as planes of spins of a given mode have antiferromagnetic arrangement[1]. Each spin $\mathbf{S}_{\mathbf{R},\alpha}$ is paired with four nearest neighbors of each category. The 4 nearest neighbors belonging to the same magnon mode are in positions $\mathbf{R}+\boldsymbol{\delta}_{\alpha\alpha}$, with $\boldsymbol{\delta}_{\alpha\alpha} \in \{\pm\mathbf{a}_2, \pm\mathbf{a}_5\}$. Their orientation is opposite to that of $\mathbf{S}_{\mathbf{R},\alpha}$, forming 4 $(\uparrow\downarrow_{\alpha\alpha})$ pairs. The 8 other nearest neighbors belong to the opposite sublattice and are located in positions $\mathbf{R}\pm\boldsymbol{\delta}_{ab}$, with $\boldsymbol{\delta}_{ab} \in \{\mathbf{a}_1, \mathbf{-a}_3, \mathbf{a}_4, \mathbf{-a}_6\}$. 4 of them are antiparallel to $\mathbf{S}_{\mathbf{R},\alpha}$, forming 4 $(\uparrow\downarrow_{ab})$ pairs. They are located in positions $\mathbf{R}+\boldsymbol{\delta}_{ab}$ or $\mathbf{R}\text{-}\boldsymbol{\delta}_{ab}$ for $\alpha = a$ or $\alpha = b$, respectively. The last 4 nearest neighbor have parallel orientation with $\mathbf{S}_{\mathbf{R},\alpha}$, leading to 4 $(\uparrow\uparrow_{ab})$ pairs. They are located in positions $\mathbf{R}\text{-}\boldsymbol{\delta}_{ab}$ or $\mathbf{R}+\boldsymbol{\delta}_{ab}$ for $\alpha = a$ or $\alpha = b$, respectively. The mean-field

[1] As for the AF1 state, one can show that the hopping average m_{ij} vanishes for $(\uparrow\downarrow)$ pairs, while the anomalous average Δ_{ij} vanishes for $(\uparrow\uparrow)$ pairs.

averages follow then from Eq. (5.12):

$$n = \frac{1}{N}\sum_{\mathbf{R}_c}\left\{\langle a^\dagger_{\mathbf{R}} a_{\mathbf{R}}\rangle + \langle b^\dagger_{\mathbf{R}} b_{\mathbf{R}}\rangle\right\} \ , \tag{5.50}$$

$$m = \frac{1}{4N}\sum_{\mathbf{R}_c}\sum_{\boldsymbol{\delta}_{ab}}\left\{\langle a^\dagger_{\mathbf{R}} b_{\mathbf{R}-\boldsymbol{\delta}}\rangle + \langle b^\dagger_{\mathbf{R}} a_{\mathbf{R}+\boldsymbol{\delta}}\rangle\right\} \ , \tag{5.51}$$

$$\Delta = \frac{1}{4N}\sum_{\mathbf{R}_c}\sum_{\boldsymbol{\delta}_{ab}}\left\{\langle a^\dagger_{\mathbf{R}} b^\dagger_{\mathbf{R}+\boldsymbol{\delta}}\rangle + \langle a_{\mathbf{R}} b_{\mathbf{R}+\boldsymbol{\delta}}\rangle\right\} \ , \tag{5.52}$$

$$\Delta_{\alpha\alpha} = \frac{1}{8N}\sum_{\mathbf{R}_c}\sum_{\boldsymbol{\delta}_{\alpha\alpha}}\left\{\langle a^\dagger_{\mathbf{R}} a^\dagger_{\mathbf{R}+\boldsymbol{\delta}}\rangle + \langle a_{\mathbf{R}} a_{\mathbf{R}+\boldsymbol{\delta}}\rangle + \langle b^\dagger_{\mathbf{R}} b^\dagger_{\mathbf{R}+\boldsymbol{\delta}}\rangle + \langle b_{\mathbf{R}} b_{\mathbf{R}+\boldsymbol{\delta}}\rangle\right\} \ , \tag{5.53}$$

where the sum over $\mathbf{R}_c$ spans the position $\mathbf{R}$ of the extended magnetic unit cell containing two sites of the original Bravais lattice, one of each bosonic mode (a and b).

We obtain from Eq. (5.24) an expression in terms of those mean-field averages for the ground-state energy with quantum corrections:

$$\begin{aligned}\frac{E_3}{N} &\approx 2J(S-n+m)^2 - 2J(S-n+\Delta)^2 - 2J(S-n+\Delta_{\alpha\alpha})^2 \\ &= 2J\left[S_{\uparrow\uparrow}\right]^2 - 2J\left[S_{\uparrow\downarrow}\right]^2 - 2J\left[S^{\alpha\alpha}_{\uparrow\downarrow}\right]^2 \ .\end{aligned} \tag{5.54}$$

It is not straightforward to obtain analytical expressions for the mean fields n, m, Δ and $\Delta_{\alpha\alpha}$ with the same method as for the AF1 state. Indeed, evaluating the expectation values of quadratic operators in $\mathbf{k}$-space, as was done in Eqs. (5.40 - 5.41), requires knowledge of the explicit Bogolyubov transformation. The diagonalization technique for a multiple-bosons representation which is introduced in appendix (A) only allows us to find the spin-wave spectrum, but does not give any information on the coefficients of the change-of-basis matrix. It is nevertheless possible to obtain expressions for the mean-field averages of the AF3 state from another method, as will be explained in a future paragraph. For the time being, let me proceed with the standard spin-wave derivation to determine the renormalized spectrum.

Hamiltonian in reciprocal space

The mean-field averages defined in Eqs. (5.50 - 5.53) are substituted into the quadratic part of the Hamiltonian given by Eq. (5.23). After the Fourier transformation, we obtain the quadratic Hamiltonian in reciprocal space, which has the exact same matrix structure as in the harmonic approximation (see Eq. (4.18)):

$$\hat{\mathcal{H}}^{(2)} = \frac{1}{2}\sum_{\mathbf{k}}\left(\hat{X}^\dagger_{\mathbf{k}} H_{\mathbf{k}} \hat{X}_{\mathbf{k}} - \mathrm{Tr}[A_{\mathbf{k}}]\right) \ , \tag{5.55}$$

where $H_{\mathbf{k}}$ is a 4×4 matrix with the same block structure as in Eq. (4.20):

$$H_{\mathbf{k}} = \begin{pmatrix} A_{\mathbf{k}} & -B_{\mathbf{k}} \\ -B^\dagger_{\mathbf{k}} & A_{\mathbf{k}} \end{pmatrix} \ . \tag{5.56}$$

Note that the sum in Eq. (5.55) is performed over all the $\mathbf{k}$-vectors of the *reduced* Brillouin, which is depicted on the right panel of Fig. (4.2). The matrices $A_{\mathbf{k}}$ and $B_{\mathbf{k}}$ now include both the harmonic contribution and contributions coming from interactions with mean fields. For the sake of compacity, we define the renormalized spin values following Eq. (5.17):

$$\begin{aligned} S_{\uparrow\uparrow} =& S - n + m \ , \\ S_{\uparrow\downarrow} =& S - n + \Delta \ , \\ S^{\alpha\alpha}_{\uparrow\downarrow} =& S - n + \Delta_{\alpha\alpha} \ . \end{aligned} \tag{5.57}$$

It is also useful to define the variable S_0 as follows:

$$S_0 = S_{\uparrow\downarrow} + S^{\alpha\alpha}_{\uparrow\downarrow} - S_{\uparrow\uparrow} = S - n + \Delta + \Delta_{\alpha\alpha} - m \ . \tag{5.58}$$

Then the matrices $A_{\mathbf{k}}$ and $B_{\mathbf{k}}$, of which the diagonal (off-diagonal) elements connect bosonic operators of the same (opposite) mode, are given by:

$$A_{\mathbf{k}} = 4J \begin{pmatrix} S_0 & S_{\uparrow\uparrow} \cdot \gamma_{\mathbf{k}} \\ S_{\uparrow\uparrow} \cdot \gamma^*_{\mathbf{k}} & S_0 \end{pmatrix} \ , \qquad B_{\mathbf{k}} = 4J \begin{pmatrix} S^{\alpha\alpha}_{\uparrow\downarrow} \cdot \mathcal{C}_x\mathcal{C}_z & S_{\uparrow\downarrow} \cdot \gamma^*_{\mathbf{k}} \\ S_{\uparrow\downarrow} \cdot \gamma_{\mathbf{k}} & S^{\alpha\alpha}_{\uparrow\downarrow} \cdot \mathcal{C}_x\mathcal{C}_z \end{pmatrix} \ . \tag{5.59}$$

We remind the reader that $\gamma_{\mathbf{k}}$ is given by Eq. (4.22). The quadratic Hamiltonian of Eq. (5.55) has the standard structure for the multiple-bosons picture, see Eq. (A.11). One recovers the harmonic Hamiltonian of Eqs. (4.18 - 4.22) by ignoring all contributions from mean-field averages in $\tilde{\mathcal{H}}^{(2)}$ (see Eqs. (5.55 - 5.59)).

Bogolyubov transformation and spectrum

The diagonalization process of the quadratic Hamiltonian of Eq. (5.55) is done exactly in the same way as in the harmonic approximation, see section (4.1.1) and see appendix (A) for more details. Although tedious, the calculation is a standard diagonalization of a 2×2 matrix, and I give here only the final result. For the sake of compacity, let me introduce the following functions of $\mathbf{k}$:

$$\begin{aligned} \mu_{\mathbf{k}} &= \mathcal{C}_y^2(\mathcal{C}_x + \mathcal{C}_z)^2 \ , \\ \pi_{\mathbf{k}} &= \mathcal{S}_y^2(\mathcal{C}_x - \mathcal{C}_z)^2 \ , \\ m_{\mathbf{k}} &= S_0 S_{\uparrow\uparrow} - S_{\uparrow\downarrow} S^{\alpha\alpha}_{\uparrow\downarrow} \cdot \mathcal{C}_x\mathcal{C}_z \ , \\ p_{\mathbf{k}} &= S_0 S_{\uparrow\uparrow} + S_{\uparrow\downarrow} S^{\alpha\alpha}_{\uparrow\downarrow} \cdot \mathcal{C}_x\mathcal{C}_z \ . \end{aligned} \tag{5.60}$$

One obtains two branches for the spin-wave spectrum $\epsilon^{\pm}_{3\mathbf{k}}$:

$$\epsilon^{\pm}_{3\mathbf{k}} = 4J \left\{ \mathcal{A}_{\mathbf{k}} \pm \sqrt{\mathcal{D}_{\mathbf{k}}} \right\}^{1/2} \ , \tag{5.61}$$

with

$$\mathcal{A}_{\mathbf{k}} = S_0^2 - \left[S_{\uparrow\downarrow}^{\alpha\alpha} \cdot \mathcal{C}_x \mathcal{C}_z\right]^2 + \frac{1}{4}\left[\left(S_{\uparrow\uparrow}\right)^2 - \left(S_{\uparrow\downarrow}\right)^2\right](\mu_{\mathbf{k}} + \pi_{\mathbf{k}}) \ , \tag{5.62}$$

$$\mathcal{D}_{\mathbf{k}} = \mu_{\mathbf{k}} m_{\mathbf{k}}^2 + \pi_{\mathbf{k}} p_{\mathbf{k}}^2 - \left(S_{\uparrow\downarrow}\right)^2 \left(S_{\uparrow\uparrow}\right)^2 \mu_{\mathbf{k}} \pi_{\mathbf{k}} \ . \tag{5.63}$$

One recovers the harmonic spectrum of Eq. (4.26) by neglecting all mean-field averages, which amounts to take $S_0 = S_{\uparrow\uparrow} = S_{\uparrow\downarrow} = S_{\uparrow\downarrow}^{\alpha\alpha} = S$.

Diagonal Hamiltonian and zero point motion

After diagonalization, we have for $\hat{\mathcal{H}}^{(2)}$ of Eq. (5.55):

$$\tilde{\mathcal{H}}^{(2)} = \sum_{\mathbf{k}} \left[\epsilon_{3\mathbf{k}}^{+}\left(\beta_{\mathbf{k},1}^{\dagger}\beta_{\mathbf{k},1} + \frac{1}{2}\right) + \epsilon_{3\mathbf{k}}^{-}\left(\beta_{\mathbf{k},2}^{\dagger}\beta_{\mathbf{k},2} + \frac{1}{2}\right) - \frac{1}{2}\,\mathrm{Tr}\left[A_{\mathbf{k}}\right]\right] \ . \tag{5.64}$$

The ground state is the Bogolyubov vacuum, such that the corresponding quantum correction to the ground-state energy is given by:

$$\Delta E^{(2)} = \frac{1}{2}\sum_{\mathbf{k}} (\epsilon_{3\mathbf{k}}^{+} + \epsilon_{3\mathbf{k}}^{-} - \Lambda) \ , \tag{5.65}$$

whee we have for Λ:

$$\Lambda = \mathrm{Tr}\left[A_{\mathbf{k}}\right] = 8JS_0 \ . \tag{5.66}$$

Finally, the total ground-state energy per site is obtained from either Eq. (5.39), or Eq. (5.54). Those two forms are equivalent, and both require to evaluate the mean-field averages n, m, Δ and $\Delta_{\alpha\alpha}$.

mean-field averages

Getting analytical expressions for the mean-field averages defined in Eqs. (5.50 - 5.53) is not as straightforward as for the AF1 case (see Eq. (5.42)). Indeed, we did not obtain explicitly the Bogolyubov transformation to get the spectrum in Eq. (5.61). An alternative consists in including an additional term to the original Hamiltonian of Eq. (4.4), in the form of an artificial field H_x that conjugates to a given field x. Then, the mean-field average $\langle x \rangle$ is obtained as follows:

$$\langle x \rangle = \left.\frac{\partial E(H_x)}{\partial H_x}\right|_{H_x \to 0} \ , \tag{5.67}$$

where $E\left(H_x\right)$ is the ground-state energy in the artificial field H_x. As an example, let me illustrate this method with the particle number mean field n.

Remembering the definition of n given by Eq. (5.50), we add to the original Hamiltonian an interaction term with a corresponding conjugate field H_n:

$$\hat{\mathcal{H}}(h_n) = \hat{\mathcal{H}}_{\mathrm{HF}} + H_n \sum_{\mathbf{R}} \left(a_{\mathbf{R}}^{\dagger} a_{\mathbf{R}} + b_{\mathbf{R}'}^{\dagger} b_{\mathbf{R}'}\right) \ . \tag{5.68}$$

Once again, $\mathbf{R}' = \mathbf{R} + \mathbf{a}_3$ is the position of the b site in the magnetic unit cell of position $\mathbf{R}$. After applying a Fourier transform to the bosonic operators in the above, on obtains the following, including all relevant terms:

$$\hat{\mathcal{H}}(H_n) = \hat{\mathcal{H}}_{\rm HF} + \frac{H_n}{2}\sum_{\mathbf{k}}\left(a^\dagger_{\mathbf{k}}a_{\mathbf{k}} + b^\dagger_{\mathbf{k}}b_{\mathbf{k}} + a_{\text{-}\mathbf{k}}a^\dagger_{\text{-}\mathbf{k}} + b_{\text{-}\mathbf{k}}b^\dagger_{\text{-}\mathbf{k}} - 1\right) \ . \tag{5.69}$$

It is easily seen that the field term above only couples to the diagonal elements of the quadratic Hamiltonian. We have therefore:

$$\tilde{\mathcal{H}}^{(2)}(H_n) = \frac{1}{2}\sum_{\mathbf{k}}\left[\hat{X}^\dagger_{\mathbf{k}}H_{\mathbf{k}}(H_n)\hat{X}_{\mathbf{k}} - \Lambda(H_n)\right] \ , \tag{5.70}$$

where $H_{\mathbf{k}}(H_n)$ is straightforwardly given by:

$$H_{\mathbf{k}}(H_n) = H_{\mathbf{k}} + H_n\mathbb{I}_4 \ . \tag{5.71}$$

In the above, $H_{\mathbf{k}}$ is the spin wave matrix without the conjugate field and is given by Eqs. (5.56 - 5.59). We have naturally for the constant Λ:

$$\Lambda(H_n) = \mathrm{Tr}[A_{\mathbf{k}}(H_n)] = 8JS_0 + 2H_n \ . \tag{5.72}$$

Note that the constant part of the spin-wave Hamiltonian in real space remains unchanged:

$$\tilde{\mathcal{H}}^{(0)}(H_n) = \tilde{\mathcal{H}}^{(0)} \ . \tag{5.73}$$

We have therefore, for the ground-state energy:

$$\frac{E_3(H_n)}{N} = \frac{E_{\rm cl} + \Delta E^{(0)}}{N} - 2JS_0 - \frac{H_n}{2} + \frac{1}{2N}\sum_{\mathbf{k},\pm}\epsilon^{\pm}_{3\mathbf{k}}(H_n) \ . \tag{5.74}$$

This leads to the following expression for the mean-field average n:

$$n = \frac{1}{N}\left.\frac{\partial E_3(H_n)}{\partial H_n}\right|_{H_n\to 0} = -\frac{1}{2} + \frac{1}{2N}\sum_{\mathbf{k},\pm}\left.\frac{\partial\epsilon^{\pm}_{3\mathbf{k}}(H_n)}{\partial H_n}\right|_{H_n\to 0} \ . \tag{5.75}$$

We need an expression for the spin-wave spectrum in the artificial field $\epsilon^{\pm}_{3\mathbf{k}}(H_n)$. To this end we have to do the Bogolyubov diagonalization of the quadratic Hamiltonian in field given in Eq. (5.70). Fortunately however, it is not necessary to go through the whole diagonalization procedure again. Indeed, from Eq. (5.71) it is clear that in order to include the effects of H_n in the Hamiltonian, one only needs to do the following transformation in the spin-wave matrix $H_{\mathbf{k}}$ given in Eqs. (5.56 - 5.59):

$$S_0 \Rightarrow S_0(h_n) = S_0 + h_n \ , \quad \text{with} \quad h_n = \frac{H_n}{4J} \ . \tag{5.76}$$

Therefore, the diagonalization procedure is exactly the same, and the final expression for the spectrum retains the same form as in no field, given by Eqs. (5.60 - 5.63). The only modification is the one given by the above transformation on $S_0(h_n)$. Explicitly, we have for the spectrum in field:

$$\epsilon^{\pm}_{3\mathbf{k}}(h_n) = 4J\left\{\mathcal{A}_{\mathbf{k}}(h_n) \pm \sqrt{\mathcal{D}_{\mathbf{k}}(h_n)}\right\} \ , \tag{5.77}$$

with following expressions for $\mathcal{A}_{\mathbf{k}}(h_n)$ and $\mathcal{D}_{\mathbf{k}}(h_n)$:

$$\begin{aligned}\mathcal{A}_{\mathbf{k}}(h_n) =& \mathcal{A}_{\mathbf{k}} + 2h_n S_0 + h_n^2 \ , \\ \mathcal{D}_{\mathbf{k}}(h_n) =& \mathcal{D}_{\mathbf{k}} + 2h_n S_{\uparrow\uparrow}\left(\mu_{\mathbf{k}} m_{\mathbf{k}} + \pi_{\mathbf{k}} p_{\mathbf{k}}\right) + h_n^2 \left(S_{\uparrow\uparrow}\right)^2 \left(\mu_{\mathbf{k}} + \pi_{\mathbf{k}}\right) \ .\end{aligned} \tag{5.78}$$

The functions in no field $\mathcal{A}_{\mathbf{k}}$ and $\mathcal{D}_{\mathbf{k}}$ in no field are given in Eqs. (5.62 - 5.63), and $\mu_{\mathbf{k}}$ and $\pi_{\mathbf{k}}$ in Eq. (5.60). From Eqs. (5.76 - 5.78), we have:

$$\begin{aligned}\frac{\partial \epsilon^{\pm}_{3\mathbf{k}}(H_n)}{\partial H_n} &= \frac{1}{4J}\frac{\partial \epsilon^{\pm}_{3\mathbf{k}}(h_n)}{\partial h_n} \\ &= \frac{2J}{\epsilon^{\pm}_{3\mathbf{k}}(h_n)}\left\{2\left(S_0 + h_n\right) \pm \frac{S_{\uparrow\uparrow}\left[\mu_{\mathbf{k}} m_{\mathbf{k}} + \pi_{\mathbf{k}} p_{\mathbf{k}} + h_n S_{\uparrow\uparrow}\left(\mu_{\mathbf{k}} + \pi_{\mathbf{k}}\right)\right]}{\sqrt{\mathcal{D}_{\mathbf{k}}(h_n)}}\right\} \ .\end{aligned}$$

The final expression for n is then derived from Eq. (5.75):

$$n = \frac{1}{N}\sum_{\mathbf{k},\pm}\left\{\frac{J}{\epsilon^{\pm}_{3\mathbf{k}}}\left[2S_0 \pm \frac{S_{\uparrow\uparrow}}{\sqrt{\mathcal{D}_{\mathbf{k}}}}\left(\mu_{\mathbf{k}} m_{\mathbf{k}} + \pi_{\mathbf{k}} p_{\mathbf{k}}\right)\right]\right\} - \frac{1}{2} \ . \tag{5.79}$$

In the above, $\epsilon^{\pm}_{3\mathbf{k}}$ is the spectrum in no artificial field, and one should refer to Eqs. (5.60 - 5.63) for all the functions of $\mathbf{k}$. This expression is to be integrated over the reduced Brillouin zone in order to obtain a value for n.

The same method is applied for the 3 remaining mean-field averages m, Δ and $\Delta_{\alpha\alpha}$. Those mean fields couple to $S_{\uparrow\uparrow}$, $S_{\uparrow\downarrow}$ and $S^{\alpha\alpha}_{\uparrow\downarrow}$, respectively. The spectra in the corresponding conjugate fields H_m, $H_{\Delta 1}$ and $H_{\Delta 2}$ are then given by substituting the following transformations to Eqs. (5.60 - 5.63):

$$\begin{aligned}\text{For } m\text{:} \quad & S_{\uparrow\uparrow} \Rightarrow S_{\uparrow\uparrow}(h_m) = S_{\uparrow\uparrow} + h_m \ , \\ \text{For } \Delta\text{:} \quad & S_{\uparrow\downarrow} \Rightarrow S_{\uparrow\downarrow}(h_{\Delta 1}) = S_{\uparrow\downarrow} - h_{\Delta 1} \ , \qquad \text{with } h_x = \frac{H_x}{4J} \\ \text{For } \Delta_{\alpha\alpha}\text{:} \quad & S^{\alpha\alpha}_{\uparrow\downarrow} \Rightarrow S^{\alpha\alpha}_{\uparrow\downarrow}(h_{\Delta 2}) = S^{\alpha\alpha}_{\uparrow\downarrow} - h_{\Delta 2} \ .\end{aligned} \tag{5.80}$$

For the sake of lightness, I give here only the final expressions for those three remaining mean fields. Let me first define the following function:

$$\chi^{\pm}_{\mathbf{k}} = \mu_{\mathbf{k}} m_{\mathbf{k}} \pm \pi_{\mathbf{k}} p_{\mathbf{k}} \ . \tag{5.81}$$

The mean-field averages in the AF3 state are then given by the following integral expressions:

$$
\begin{aligned}
n &= \frac{J}{N}\sum_{\mathbf{k},\pm}\left\{\frac{2S_0 \pm \left[S_{\uparrow\uparrow}\cdot\chi^{+}_{\mathbf{k}}\right]/\sqrt{\mathcal{D}_{\mathbf{k}}}}{\epsilon^{\pm}_{3\mathbf{k}}}\right\} - \frac{1}{2}\,, \\
m &= \frac{J}{N}\sum_{\mathbf{k},\pm}\left\{\frac{S_{\uparrow\uparrow}(\mu_{\mathbf{k}}+\pi_{\mathbf{k}})/2 \pm \left[S_0\cdot\chi^{+}_{\mathbf{k}} - S_{\uparrow\uparrow}\left(S_{\uparrow\downarrow}\right)^2\mu_{\mathbf{k}}\pi_{\mathbf{k}}\right]/\sqrt{\mathcal{D}_{\mathbf{k}}}}{\epsilon^{\pm}_{3\mathbf{k}}}\right\}\,, \qquad (5.82) \\
\Delta &= \frac{J}{N}\sum_{\mathbf{k},\pm}\left\{\frac{S_{\uparrow\downarrow}(\mu_{\mathbf{k}}+\pi_{\mathbf{k}})/2 \pm \left[S^{aa}_{\uparrow\downarrow}\cdot\mathcal{C}_x\mathcal{C}_z\chi^{-}_{\mathbf{k}} + \left(S_{\uparrow\uparrow}\right)^2 S_{\uparrow\downarrow}\cdot\mu_{\mathbf{k}}\pi_{\mathbf{k}}\right]/\sqrt{\mathcal{D}_{\mathbf{k}}}}{\epsilon^{\pm}_{3\mathbf{k}}}\right\}\,, \\
\Delta_{aa} &= \frac{J}{N}\sum_{\mathbf{k},\pm}\left\{\frac{2S^{aa}_{\uparrow\downarrow}\cdot\mathcal{C}_x\mathcal{C}_z \pm \left[S_{\uparrow\downarrow}\cdot\chi^{-}_{\mathbf{k}}\right]/\sqrt{\mathcal{D}_{\mathbf{k}}}}{\epsilon^{\pm}_{3\mathbf{k}}}\right\}\cdot\mathcal{C}_x\mathcal{C}_z\,.
\end{aligned}
$$

5.2 ground-state selection at zero temperature

We now have everything at hand to compute the ground-state energies of the AF1 and AF3 states, including quantum corrections up to second order in the $1/S$ spin-wave expansion. The two ground-state energies E_1 and E_3 are expressed in a most compact manner from the various mean-field averages of each state, see Eq. (5.27) and Eq. (5.54). Expressions for these mean-field averages are given by Eq. (5.42) for the AF1 state, and by Eq. (5.82) for the AF3 state.

It is key to notice, that the determination of these various mean-field averages is a self-consistent problem. Indeed, for the AF1 case, getting n, m and Δ involves the evaluation of integrals of functions of $A_{\mathbf{k}}$, $B_{\mathbf{k}}$ and $\epsilon_{1\mathbf{k}}$, see Eq. (5.42) . Yet those 3 functions do depend on n, m and Δ themselves, see Eqs. (5.32 - 5.33) and Eq. (5.36). One shall then compute n, m and Δ self-consistently. The same goes for the AF3 state, where expressions to obtain the mean-field averages n, m, Δ and $\Delta_{\alpha\alpha}$ involve functions containing these mean fields, see Eq. (5.82). As a first step, one can compute the mean-field averages in the harmonic approximation.

5.2.1 Perturbative approach

In the harmonic spin wave approximation, interactions between magnons are neglected and therefore the mean fields do not appear in the spin-wave Hamiltonian. This implies that we have $S_{\uparrow\uparrow} = S_{\uparrow\downarrow} = S$ for the AF1 state, and $S_{\uparrow\uparrow} = S_{\uparrow\downarrow} = S^{\alpha\alpha}_{\uparrow\downarrow} = S$ for the AF3 state.

The AF1 state

We use the harmonic functions $A^{(0)}_{\mathbf{k}}$, $B^{(0)}_{\mathbf{k}}$, and corresponding harmonic spectrum $\epsilon^{(0)}_{1\mathbf{k}}$, to compute the values of the mean fields in the harmonic approximation. We have:

$$\begin{aligned} A^{(0)}_{\mathbf{k}} =& 4JS(1+\mathcal{C}_y\mathcal{C}_z) \ , \\ B^{(0)}_{\mathbf{k}} =& 4JS\cdot\mathcal{C}_x(\mathcal{C}_y+\mathcal{C}_z) \ , \\ \epsilon^{(0)}_{1\mathbf{k}} =& 4JS\sqrt{\mathcal{S}_x^2(\mathcal{C}_y+\mathcal{C}_z)^2+\mathcal{S}_y^2\mathcal{S}_z^2} \ . \end{aligned} \tag{5.83}$$

Those are substituted into the integrals on the right hand-side of Eq. (5.42). It is obvious to notice that within this first approximation, the mean-field averages do not depend on the spin value. The integrals are evaluated numerically using standard Monte-Carlo integration on the cubic Brillouin zone (first and second Brillouin zone), and we obtain:

$$\begin{aligned} n^{(0)} =& 0.338777(3) \ , \\ m^{(0)} =& 0.109938(2) \ , \\ \Delta^{(0)} =& 0.285365(2) \ . \end{aligned} \tag{5.84}$$

We used $N_{\text{M.C.}} = 10^{12}$ random points in the integration volume. Note that the particle number average $n^{(0)}$ is indeed the same as was found in the previous chapter for the spin reduction ΔS_1, see Eq. (4.31). From the above values, one easily obtains the ground-state energy of the AF1 state with quantum corrections for any spin value, see Eq. (5.27). Let me rewrite this expression in a form that explicitly shows the quantum corrections to the classical energy in powers of $1/(2S)$:

$$E_1 = E_{\text{cl}} \left[1 + \frac{4\,(2\Delta - m - n)}{(2S)} - \frac{4\left[(n-m)^2 - 2(n-\Delta)^2\right]}{(2S)^2} \right] . \tag{5.85}$$

Substituting the mean-field values of Eq. (5.84) into Eq. (5.85) leads to the following:

$$E_1 = E_{\text{cl}} \left[1 + \frac{0.488060}{(2S)} - \frac{0.186646}{(2S)^2} \right] . \tag{5.86}$$

As a first quantum correction, we recover the value obtained from LSWT in the previous chapter, see Eq. (4.28).

The AF3 state

To obtain first values of n, m, Δ and $\Delta_{\alpha\alpha}$ in the harmonic approximation - that is, within the harmonic Bogolyubov vacuum - we impose $S_{\uparrow\uparrow} = S_{\uparrow\downarrow} = S^{\alpha\alpha}_{\uparrow\downarrow} = S$ in all the functions appearing in the right hand-side of Eq. (5.82). Note that this means in particular, that we are using the harmonic spin-wave spectrum given by Eq. (4.26). The integrals are computed numerically using standard Monte-Carlo integration with $N_{\text{M.C.}} = 10^{12}$ random Monte-Carlo points in the integration volume. We obtain:

$$\begin{aligned} n^{(0)} &= 0.366331(2) \ , \\ m^{(0)} &= 0.0283547(6) \ , \\ \Delta^{(0)} &= 0.2232140(6) \ , \\ \Delta^{(0)}_{\alpha\alpha} &= 0.294248(2) \ . \end{aligned} \tag{5.87}$$

The particle number average $n^{(0)}$ corresponds to the harmonic spin reduction ΔS_3 given in the previous chapter, see Eq. (4.31). The ground-state energy is found from Eq. (5.88), which I rewrite below with explicit quantum corrections in powers of $1/(2S)$:

$$E_3 = E_{\text{cl}} \left[1 + \frac{4\,(\Delta + \Delta_{\alpha\alpha} - m - n)}{(2S)} - \frac{4\left[(n-m)^2 - (n-\Delta)^2 - (n-\Delta_{\alpha\alpha})^2\right]}{(2S)^2} \right] . \tag{5.88}$$

We substitute the values of the mean field of Eq. (5.87) into Eq. (5.88), and get the following:

$$E_3 = E_{\text{cl}} \left[1 + \frac{0.491104}{(2S)} - \frac{0.354197}{(2S)^2} \right] . \tag{5.89}$$

The first quantum correction in $1/(2S)$ found within LSWT, see Eq. (4.29), is recovered here.

ground-state selection

In Eqs. (5.86, 5.89), the first quantum correction in $1/(2S)$ comes from the non-interacting magnons: we recover Eqs. (4.28, 4.29) of the previous chapter. This harmonic correction has a positive sign, meaning that it lowers the ground-state energy. Indeed, the classical ground-state energy $E_{\rm cl}$ is negative, see Eq. (5.21). Within this harmonic approximation, the AF3 state has lower ground-state energy than the AF1 state for all spin values, see dashed lines on Fig. (5.1). The second correction in $1/(2S)^2$ comes from the two-bosons interactions. Contrary to the harmonic correction, it is of negative sign, and it thus increases the ground-state energy. In that sense, one could say that the effect of interactions somehow compensates partly the large energy lowering operated by the harmonic correction. It is striking that this energy correction remains of the same order of magnitude as the harmonic correction, especially in the AF3 state. This indicates a strong effect of interactions between magnons, and a possible instability of the SWT perturbative treatment, especially for small spin values [20]. Fig. (5.1) shows the correction to the ground-state energy of the two states as a function of inverse spin. It appears that with the effects of magnon-magnon interactions, the

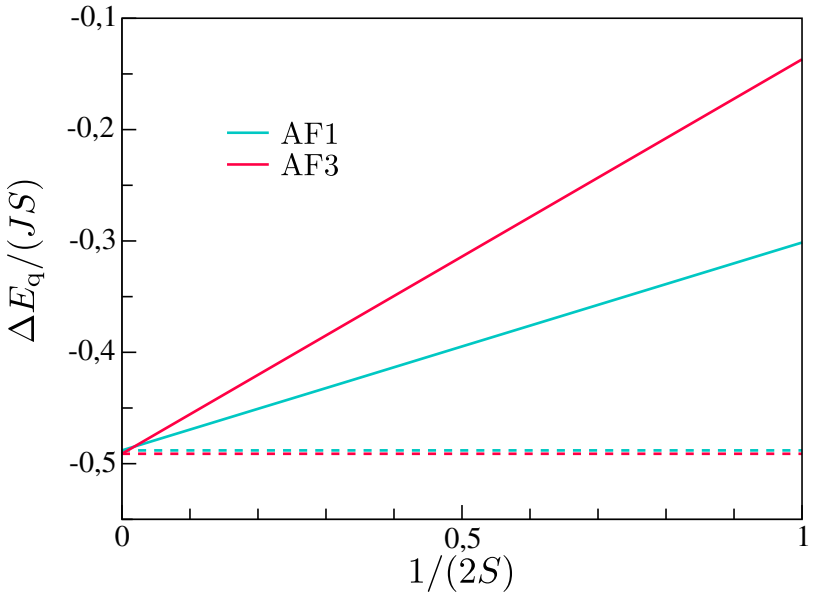

Figure 5.1: *Quantum correction to the ground-state energy of the AF1 and AF3 states as a function of inverse spin* $1/(2S)$. *Dashed lines correspond to the harmonic spin-wave result, which is spin-independent. Full lines show the energy correction including the effect of interactions, up to second order in* $1/S$.

ground-state selection operated by quantum fluctuations is completely altered. Indeed, the AF1 state has lower energy than the AF3 state *for all physically relevant values of*

spin. The harmonic result, within which the AF3 state is favored, is recovered only for a very large spin value. From Eq. (5.86) and Eq. (5.89), the energy difference between the two states, with quantum correction up to second order in $1/S$, is given by:

$$\Delta E_{13} = \frac{E_3 - E_1}{N} = \left\{ -3.044 \cdot 10^{-3} + \frac{0.167551}{(2S)} \right\} \cdot (JS) \ . \tag{5.90}$$

One can easily verify, that ΔE_{13} remains positive for values of spin up to:

$$S^* \simeq 27.5 \ . \tag{5.91}$$

From Eq. (5.90), it is clear that for all reasonable values of spin, the second order contribution to ΔE_{13} is orders of magnitude larger than that of the first order[2]. This is well seen on Fig. (5.1). It thus largely overcomes the tiny energy difference between the two states in the harmonic approximation, reversing the ground-state selection process.

This is particularly true for small spin values. As an example, from Eq. (5.90) we have for the extreme quantum case $S = 1/2$:

$$\Delta E_{13}(1/2) = 0.164508(JS) \sim 10^{-1}(JS) \ . \tag{5.92}$$

This is 2 orders of magnitude larger than the energy difference in the harmonic approximation, which is of the order of $10^{-3}(JS)$ for all spins, see Eq. (4.30). In any perturbative treatment, higher order contributions are expected to be vanishingly small compared to low order terms. The fact that it is not the case here indicates a possible instability of the spin-wave expansion. This could lead to think that it is not suited to describe this problem. The determination of the mean-field averages is, however, a self-consistent problem, and shall therefore be treated as such.

5.2.2 Self-consistent renormalization

We now expose the results obtained from the self-consistent evaluation of the mean-field averages. The values obtained in the harmonic approximation (see Eq. (5.84) and Eq. (5.87) for the Af1 and AF3 states, respectively) serve as a first step to the self consistent loop. They are substituted into the right hand-side of Eq. (5.42) and Eq. (5.82) to compute a new value for the mean-field averages, which can be substituted again, and so on, until convergence of the values. Note that through this self-consistent process, the spin-wave spectrum gets *renormalized* as well by the interactions with the mean fields. This method is formally equivalent to Takahashi's modified spin-wave theory with $T = 0$ [111]. The ground-state energy of the two states is finally given again by Eq. (5.27) and Eq. (5.54).

Treating this problem self-consistently ensures that the particles defined via the Bogolyubov transformation are "well-behaved", that is, that they do not interact with

[2]This is probably an effect of chance though, as the two contributions have the same order of magnitude of $10^{-1}(JS)$ for the to states, see Eqs. (5.86, 5.89)

their own vacuum [20]. Contrary to the mean-field averages obtained in the previous section within the harmonic approximation, the values obtained with the self-consistent treatment are now spin-dependant. The numerically obtained values can be found in appendix B for all spin lengths considered in this work. The ground-state energy correction $\Delta E_q = E_{\text{g.s.}} - E_{\text{cl}}$ of the AF1 and AF3 states is shown as a function of inverse spin on Fig. (5.2). These corrections have been computed using Eq. (5.27) and Eq. (5.54). For all physically relevant values of spin, the AF1 state has lower energy

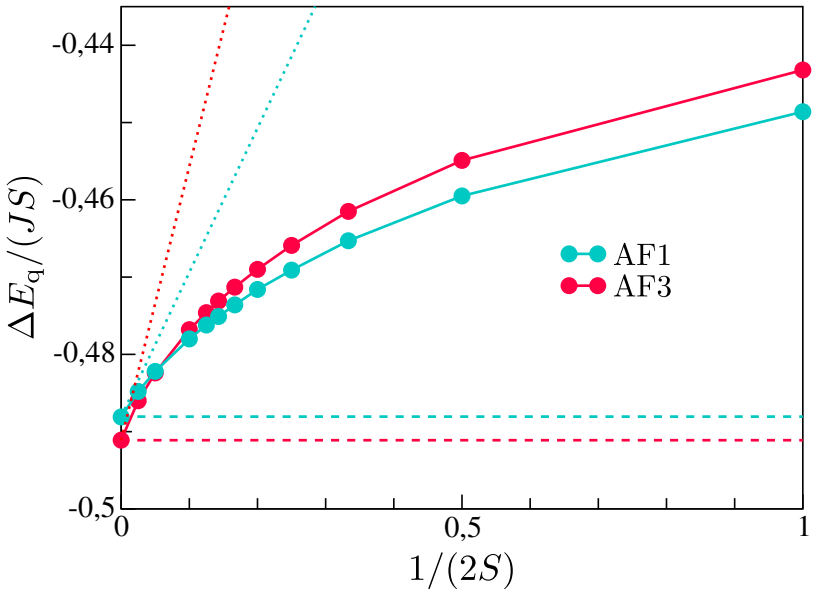

Figure 5.2: *Quantum correction to the ground-state energy of the AF1 and AF3 states as a function of inverse spin* $1/(2S)$. *Dashed lines show the harmonic spin-wave result. Full lines with circles show the energy correction with self-consistent inclusion of the effect of interactions. For comparison, the dotted lines show the perturbative result without self-consistency.*

than the AF3 state, and is thus selected by quantum fluctuations. The self-consistent calculation induces a strong renormalization of the energies, compared to the simple perturbative calculation obtained from harmonic mean-field averages in the previous subsection (see dotted lines on Fig. (5.2) for comparison). As a consequence, the spin value S^* at which the harmonic result is qualitatively recovered is smaller than that of Eq. (5.91). We have indeed, within the self-consistent inclusion of interactions:

$$S^* \simeq 10 \ . \tag{5.93}$$

The energy difference between the two competing states is also much reduced, compared to the results obtained without self-consistency. For the extreme case $S = 1/2$, we have:

$$\Delta E_{13}^{\text{s.c.}}(1/2) = 5.561 \cdot 10^{-3}(JS) \ , \tag{5.94}$$

which is 2 orders of magnitude smaller than in Eq. (5.92). We recover the same order of magnitude as what was found in the non-interacting harmonic spin wave theory, see Eq. (4.30), which is still particularly small.

We are facing a rare situation, where the harmonic spin wave approximation fails to predict the correct ordered ground-state selection from quantum order-by-disorder process, *up to any physically relevant spin value*. The harmonic spin wave results are recovered qualitatively only at very large spin. We attribute this failure of the harmonic approximation to the numerous accidental zero energy modes of the harmonic spin-wave spectra, see Fig. (4.2). For that reason, the integrals involved in the calculation of the mean-field averages are overestimated when computed in the harmonic approximation. Indeed, they all contain the spectrum in the denominator (see Eq. (5.42) and Eq. (5.82) for the AF1 and AF3 states, respectively). After inclusion of the interactions and self-consistent renormalization, and only the true Goldstone modes remain. The spectra for $S = 1/2$ and $S = 5/2$ are displayed on Fig. (5.3) along high symmetry directions of the Brillouin zone[3]. The harmonic spectra (dashed lines) are completely flat along the pseudo-Goldstone modes, while the renormalized spectra (full lines) acquire a dispersion and/or quantum gaps. We used the values of the mean-field averages obtained after convergence of the self-consistent loop to obtain the renormalized spectra, see Eqs. (5.32 - 5.33) and Eq. (5.36) for the AF1 state, and Eqs. (5.60 - 5.63) for the AF3 state. We now give explicit analytical expressions for these gaps and for the spin-wave velocities near the Goldstone modes. As will be seen in the next chapter, determination of the quantum gaps, as well as the spin-wave velocities in the vicinity of Goldstone modes, is key to the understanding of the low-temperature problem.

AF1 state

The line nodes of the harmonic spin-wave spectrum of AF1 state can be separated into two kinds: lines along the propagation direction k_x and lines along the orthogonal directions k_y and k_z. They are shown with thick and thin blue lines, respectively, on the left panel of Fig. (4.2). Lines along k_x are explicitly $2\pi(q, 0, \pm 1)$ and $2\pi(q, \pm 1, 0)$. The section XW in Fig. (5.3) belongs to this category. It is straightforward to show from Eqs. (5.32-5.33) and Eq. (5.36), that the interacting spectrum $\epsilon_{1\mathbf{k}}$ acquires a constant gap Δ_1 along those lines:

$$\boxed{\Delta_1 = 8J(\Delta - m)}\,, \tag{5.95}$$

making the corresponding pseudo-Goldstone modes dispersionless. These lines being fully gapped is coherent with the absence of true Goldstone modes along them. Furthermore, we have $\Delta_1 \sim S^0$, which is coherent with the expectation from Rau et al. for "type II" pseudo-Goldstone modes, that is, pseudo- Golstone modes with a quadratic dispersion in the transverse component [112]. We remind the reader that the dispersion of the harmonic spectrum around such lines is indeed quadratic in $\kappa_\perp$, see Eq. (4.36).

[3]The high symmetry points are shown on the left panel of Fig. (4.2)

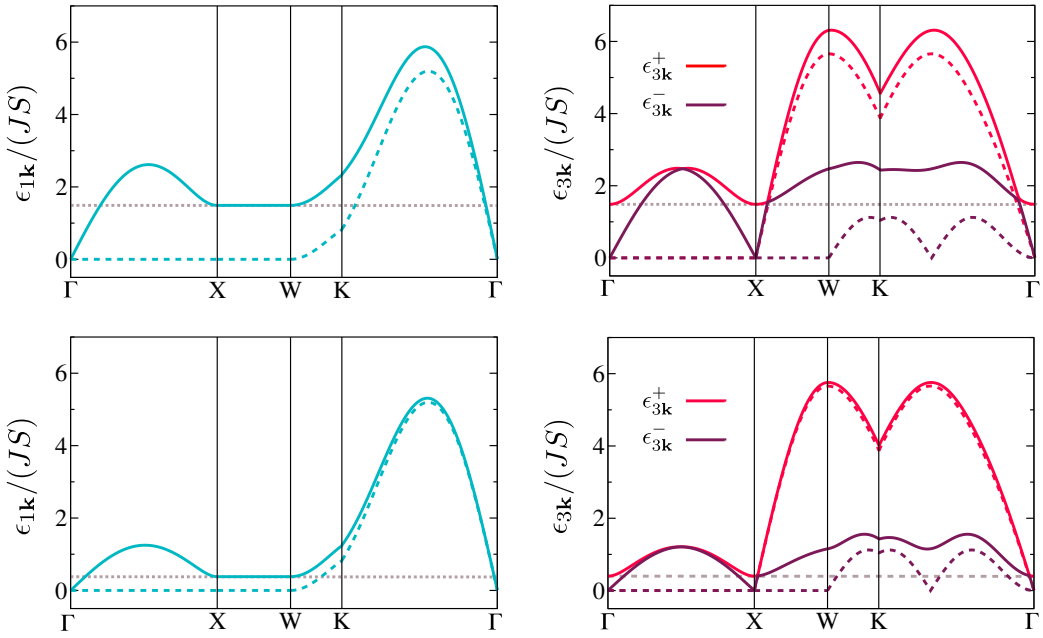

Figure 5.3: *Spin-wave dispersions along high symmetry directions for the AF1 (left panels) and AF3 (right panels) states, with $S = 1/2$ (top panels) and $S = 5/2$ (bottom panels). Continuous lines correspond to the renormalized spectrum with interactions, while dashed lines show the harmonic spectrum. Dotted grey lines show the quantum gaps.*

The quantum gaps can be readily obtained for various spin lengths, from Eq. (5.95) and from the mean-field averages values given in appendix B.

Lines along transverse k_y and k_z directions on the other hand, do contain true Goldstone modes. On Fig. (5.3), the section ΓX belongs to one of such lines. The spectrum acquires dispersion all along the lines once magnon-magnon interactions are included. It vanishes exclusively at $\mathbf{k} = \mathbf{\Gamma}$ and $\mathbf{k} = \mathbf{Q}_1$ (or equivalent points), see blue diamonds on the left panel of Fig. (4.2). At intersection with a line along k_x (see blue balls on Fig. (4.2)), it is gapped with Δ_1 given by Eq. (5.95). Note that the maximal gap opening along such lines is such that $\Delta \sim \sqrt{S}$. This is also in agreement with the estimation from ref. [112] for "type I" pseudo-Goldstone modes, that is, pseudo-Goldstone modes with a linear dispersion around them, see Eq. (4.39).

The renormalized spectrum acquires a linear dispersion in the vicinity of the zero-energy modes. Lowest-order analytical expansion of of $\epsilon_{1\mathbf{k}}$ around $\mathbf{k} = \mathbf{\Gamma}$ (or equivalently around $\mathbf{k} = \mathbf{Q}_1$), gives the following asymptotic behavior:

$$\epsilon_{1\mathbf{k}} \approx \left\{ k_x^2 c_{1\parallel}^2 + \left(k_y^2 + k_z^2\right) c_{1\perp}^2 \right\}^{1/2} , \tag{5.96}$$

where the longitudinal and transverse spin-wave velocities $c_{1\parallel}$ and $c_{1\perp}$ are given by:

$$c_{1\parallel}^2 = (4J)^2 \cdot (S_{\uparrow\downarrow})^2 \tag{5.97}$$
$$c_{1\perp}^2 = (4J)^2 \cdot \frac{1}{2} S_{\uparrow\downarrow}(\Delta - m) \ .$$

We remind the reader that $S_{\uparrow\downarrow}$ is given by Eq. (5.29).

AF3 state

In a similar manner as for the AF1 state, the line nodes of the harmonic spin-wave spectrum of AF3 state are separated into two kinds: lines along the propagation direction k_y and lines along the orthogonal directions k_x and k_z (thick and thin red lines on the right panel of Fig. (4.2), respectively).

The first type of lined along k_y are explicitly given by $(0, q, 0)$, $2\pi(0, q, \pm 1)$ and $2\pi(\pm 1, q, 0)$. The section ΓX on Fig. (5.3) belongs to this category. Both branches of the harmonic spectrum vanish along these lines. The renormalized spectrum $\epsilon_{3\mathbf{k}}^{\pm}$ given by Eqs. (5.60 - 5.63)) acquires dispersion along these lines, for both branches. The only remaining zero-energy modes are the true Goldstone modes corresponding to $\mathbf{k} = \mathbf{\Gamma}$ and $\mathbf{k} = \mathbf{Q}_3$ on the lower branch $\epsilon_{3\mathbf{k}}^{-}$. The quantum gap resides also at true Goldstone modes, but on the upper branch $\epsilon_{3\mathbf{k}}^{+}$. It is given by:

$$\boxed{\Delta_3 = 8J\sqrt{(\Delta_{\alpha\alpha} - m)(\Delta - m)}} \ , \tag{5.98}$$

and is of similar magnitude as the quantum gap Δ_1 of the AF1 state (see Eq. (5.95)). The relation to the type of soft modes, as is done in ref. [112], is less clear here than in the AF1 state. Indeed, the harmonic spectrum remains asymptotically linear all along those lines for the upper branch, see Eq. (4.52): it is a type I pseudo-Goldstone mode. In that situation, one expects the quantum gap to be of the order of $\Delta \sim \sqrt{S}$. Possibly, the $\Delta \sim S^0$ gap here is rather related to the particularly soft cubic behaviour of the lower branch at Goldstone modes, see Eq. (4.55). Note that away from the true Goldstone modes, the maximal gaps for $\epsilon_{3\mathbf{k}}^{\pm}$, above the pseudo-Goldstone lines, is of order $\Delta \sim \sqrt{S}$. This is in accordance with the expectation for a type-I pseudo-Goldstone mode. The quantum gaps can be readily obtained for various spin lengths, from Eq. (5.98) and from the mean-field averages values given in appendix B.

Only the lower branch of the harmonic spectrum $\epsilon_{3\mathbf{k}}^{-}$ vanishes along the other type of lines along k_x and k_z. One of such lines is appears as section XW on Fig. (5.3). The spectrum also acquires dispersion all along these lines, and vanishes exclusively at true Goldstone modes, where $\epsilon_{3\mathbf{k}}^{+}$ acquires the gap Δ_3 given by Eq. (5.98). Away from these points, the spectrum is gapped with $\Delta \sim S^1$, which is expected for pseudo-Goldstone modes of this kind, having a linear asymptotic behaviour, see Eq. (4.56).

As is the case for the AF1 state, the spectrum of the AF3 state gets a linear asymptotic dispersion in the vicinity of the true Goldstone modes after renormalization:

$$\epsilon_{3\mathbf{k}}^{-} \approx \left\{ k_y^2 c_{3\parallel}^2 + \left(k_x^2 + k_z^2\right) c_{3\perp}^2 \right\}^{1/2} \ . \tag{5.99}$$

Note that this is the exact same expression as for the AF1 state, see Eq. (5.96). The longitudinal and transverse spin-wave velocities $c_{3\parallel}$ and $c_{3\perp}$ are given by:

$$c_{3\parallel}^2 = (4J)^2 \cdot \frac{1}{2}\left(\frac{S_{\uparrow\downarrow} + S_{\uparrow\downarrow}^{\alpha\alpha}}{2}\right)(\Delta - m) \ , \tag{5.100}$$
$$c_{3\perp}^2 = (4J)^2 \cdot \frac{1}{4}\left(\frac{S_{\uparrow\downarrow} + S_{\uparrow\downarrow}^{\alpha\alpha}}{2}\right)\left[2S_{\uparrow\downarrow}^{\alpha\alpha} + (\Delta - m)\right] \ ,$$

where $S_{\uparrow\downarrow}$ and $S_{\uparrow\downarrow}^{\alpha\alpha}$ are given by Eq. (5.57). The longitudinal velocity $c_{\parallel}^2$ compares very well with the transverse velocity $c_{\perp}^2$ in the AF1 case (see 5.97).

The quantum gaps Δ_1 and Δ_3 given by Eq. (5.95) and Eq. (5.98), respectively, represent a $1/S$ correction to the spectrum from the interactions. Indeed, we have:

$$\epsilon_{1\mathbf{k}}, \epsilon_{3\mathbf{k}}^{\pm} \sim S^1 \ ,$$
$$\Delta_1, \Delta_3 \sim S^0 \ .$$

Therefore, as the spin increases, effects of magnon-magnon interactions on the spectrum become lighter. Ultimately the harmonic spectrum is recovered in the extreme classical

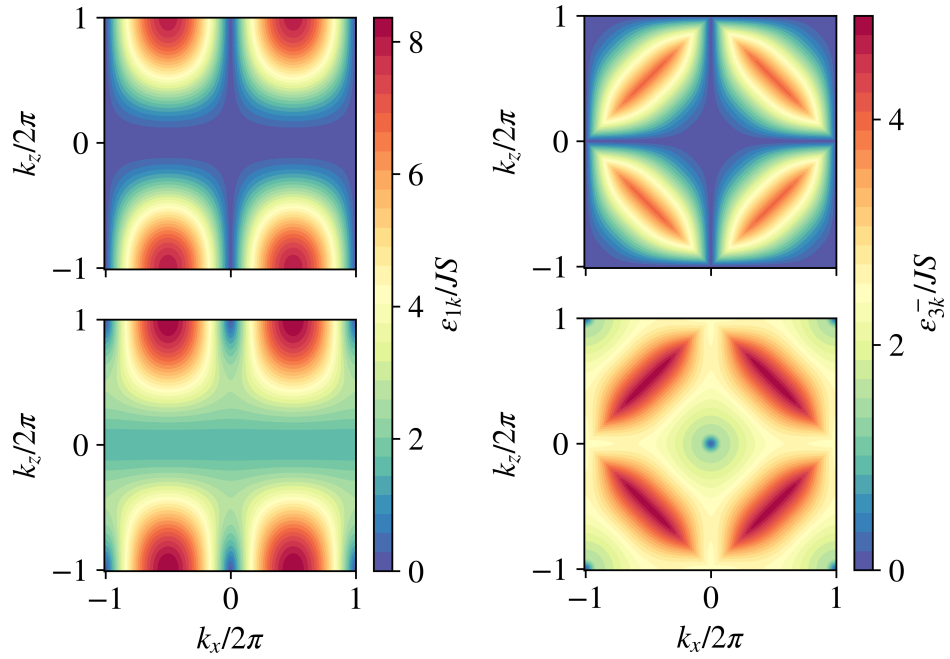

Figure 5.4: *Spin-wave dispersions in the xz plane $k_y = 2\pi$, for the AF1 (left panels) and AF3(right panels) states, with $S = 1/2$. Top panels display the harmonic spin-wave result, where the spectra exhibits accidental lines of zero-energy modes. Bottom panels show the spectra with quantum corrections coming from magnon-magnon interactions, computed in a self-consistent manner.*

case, when $S \to \infty$. This is illustrated on Fig. (5.3), where the top and bottom panels show the spectra for $S = 1/2$ and $S = 5/2$, respectively. The quantum gaps are identified by dotted black lines and clearly decrease with increasing spin. Nevertheless, even if corrections to the harmonic spectra become almost negligible near high-energy modes for the $S = 5/2$ case, they remain important along pseudo-Goldstone modes. To illustrate better the importance of quantum corrections coming from interactions on the spin-wave spectra, Fig. (5.4) displays intensity maps of the harmonic (top panels) and corrected (bottom panels) spectra for $S = 1/2$. The accidental line nodes are clearly visible on the harmonic spectra, and are completely lifted after renormalization.

Please be aware that the energy colorbar does not have the same values for the two different states, and is adapted to the maximum value of the spectrum after self-consistent renormalization.

5.3 Low-temperature behaviour

We have seen in the previous chapter, that within the harmonic spin-wave approximation, a competition effect between quantum and thermal order by disorder occurs in the nearest-neighbor fcc AFM. Indeed, the ground-state selection from quantum fluctuations at $T = 0$ acts in favor of the AF3 state, whereas the thermal selection acts in favor of the AF1 state, see Fig. (4.4). This originates from the different nature of the two selection processes: the quantum selection at $T = 0$ is governed by the zero-point motion of the spin-waves, see Eq. (4.27), while at low temperature, only the softest modes of the spectrum contribute to the free energy, see Eq. (4.33).

The many accidental pseudo-Goldstone modes which are present in the harmonic spectra affect both these processes in a different manner. On the one hand, the zero point motion of spin waves is underestimated in the harmonic approximation. This induces an overestimation of the negative quantum energy correction to the ground-state energies. In particular, this results in the AF3 state being favored, although the energy difference with the AF1 state is very small, see Eq. (4.30). One might speculate, that this is related to the particularly large number of accidental gapless modes in the spectrum of the AF3 state. On the other hand, the presence of the line nodes causes an overestimation of the decrease speed of the free-energy. Indeed, main contributions to ΔF come from quadratic soft modes lying along whole lines in the harmonic spectrum for the AF1 state, which induces an abnormally sharp $\Delta F \sim -T^2$ behaviour. In the AF3 state, major contributions come from quadratic soft modes with cubic subleading behaviour around special points in the spectrum. This leads to a peculiar fractional exponent $\Delta F \sim -T^{7/3}$. From this analysis, the AF1 state is favored by thermal fluctuations at low temperatures in the quantum spin system, and can be considered as having "the softest spectrum". A first-order phase transition at $T^* \simeq 0.2(JS)$ is predicted.

After inclusion of magnon-magnon interactions, the $T = 0$ ground-state selection is reversed for most values of spin, and the AF1 state is favored. The harmonic result with selection of the AF3 state is recovered only at very large spin $S^* \approx 10$, see Fig. (5.2). Despite this different selection, the energy difference between the two competing states remains of the same order of magnitude as in the harmonic approximation, that is, of the order of $10^{-3}(JS)$. Furthermore, there is in principle no reason to believe that thermal fluctuations operate the same ground-state selection as in the harmonic approximation. Indeed, the asymptotic behaviour of soft modes in the spectra dictate the temperature power law of the free energy. After renormalization of the spectrum by the interactions, accidental line nodes acquire a gap, and only remain the true Goldstone modes. The behaviour of the free energy is then modified, and at very low temperatures only the soft modes lying around Goldstone modes play a role. The asymptotic behaviour of these soft modes is linear in both states, see Eq. (5.96) and Eq. (5.99) for the AF1 and AF3 states, respectively. Explicitly, it is given by the

following common expression:

$$\epsilon_{\mathbf{k}} \approx \left\{ k_{\parallel}^2 c_{\parallel}^2 + k_{\perp}^2 c_{\perp}^2 \right\}^{1/2} \quad . \tag{5.101}$$

In the above, $k_{\parallel}$ is the special direction in $\mathbf{k}$-space (that is, k_x for the AF1 state and k_y for the AF3 state), and $k_{\perp}$ contains the two remaining transverse coordinates: $k_{\perp}^2 = k_y^2 + k_z^2$ for the AF1 state, and $k_{\perp}^2 = k_z^2 + k_x^2$ for the AF3 state. One can show (see appendix (?) for details), that such low-energy modes as in Eq. (5.101) induce the following contribution to the free energy of Eq. (4.33) at low temperatures:

$$\Delta F(T) \approx -(T')^4 \cdot \frac{a^3 \pi^2}{180} \frac{(JS)^3}{c_{\parallel} c_{\perp}^2} \ , \tag{5.102}$$

where T' is the normalized temperature defined in Eq. (4.46). This result is valid for both the AF1 and AF3 states. The typical T^4 behaviour of the free energy of unfrustrated $3D$ spin systems is recovered, due to the renormalization of the spin wave spectrum operated by interactions.

From Eq. (5.102), the decrease speed of the free energy is completely determined by the spin wave velocities of the renormalized spin-wave spectra. The transverse velocity $c_{\perp}$ contributes twice more than the longitudinal velocity $c_{\parallel}$, as it is associated to two directions instead of one. The state with smallest product $c_{\parallel} c_{\perp}^2$ decreases therefore faster in energy, and is favored by thermal fluctuations. Expressions for the velocities were computed in the previous section and are given by Eq. (5.97) and Eq. (5.100) for the AF1 and AF3 state, respectively. For the AF1 state, we have:

$$c_{1\perp} \sim \sqrt{S(\Delta - m)} \ll c_{1\parallel} \sim S \ . \tag{5.103}$$

The tendency is opposite for the AF3 state, for which we have:

$$c_{3\parallel} \sim \sqrt{S(\Delta - m)} \ll c_{3\perp} \sim S \ . \tag{5.104}$$

The AF1 state is therefore favored by thermal fluctuations at very low temperatures, which does not challenge the result found in the harmonic approximation. This analysis applies in principle to any spin value. Note that when temperatures are increased above the quantum gaps, the harmonic behaviour should be more or less recovered. There is therefore no reason to expect a situation where the AF3 state would be favored by thermal fluctuations. As a consequence, a competition effect between thermal and quantum order by disorder, as was found in the harmonic approximation, is only realisable when the AF3 state is favored by quantum fluctuations at $T = 0$, that is, for unphysically large values of spin $S \geq 10$.

For the sake of completeness, we compute the low-temperature free energy of the two competing states after self-consistent renormalization of the spectrum. We use Eq. (4.33), in which we substitute for the spectra Eqs. (5.32, 5.33, 5.36) for the AF1 state, and Eqs. (5.60 - 5.63) for the AF3 state. As the self consistent mean fields are

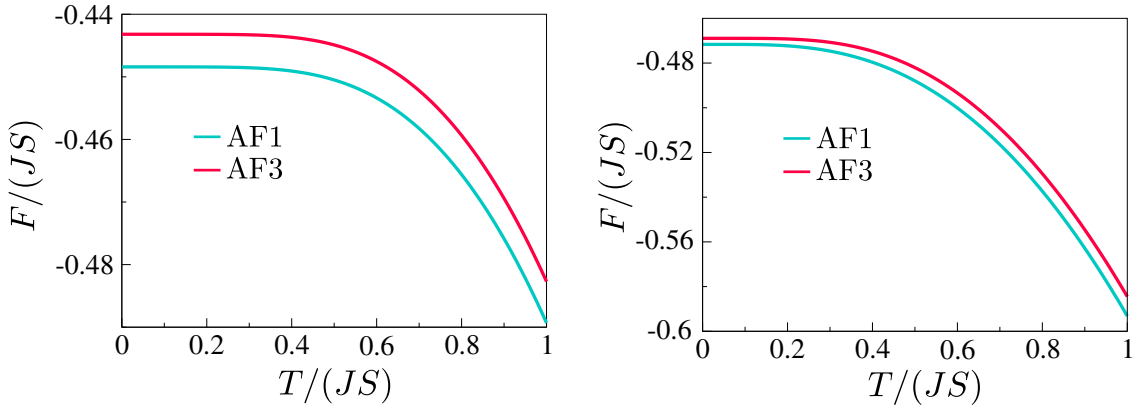

Figure 5.5: *Free energy as a function of temperature in the AF1 and AF3 states, for* $S = 1/2$ *(left panel) and* $S = 5/2$ *(right panel).*

obtained independently for different spin values, $\Delta F(T)$ has to be computed as well independently. On Fig. (5.5) we show the ground-state energy versus temperature for both states, in the $S = 1/2$ and $S = 5/2$ cases. There is no phase transition in both cases, as the AF1 state appears to remain the state selected by thermal fluctuations.

Note that the behaviours of the various spin-wave velocities can be directly related to the presence of a pseudo-Goldstone mode - and if so, to its type - along the transverse and longitudinal directions. Indeed, in the AF1 state, there is no pseudo-Goldstone mode in the longitudinal direction k_x. As a result, the spectrum is expected to behave as S^1, and so does the spin-wave velocity, see Eq. (5.103) and section ΓK on the left panel of Fig. (5.3). Along the transverse directions k_y and k_z, however, there is a pseudo-Goldstone mode of type I. After inclusion of the interactions, it is gapped as $\Delta \sim \sqrt{S}$, and the transverse spin-wave velocity has similar behaviour, see Eq. (5.103) and section ΓX on the left panel of Fig. (5.3).

Regarding the AF3 state, there is a pseudo-Goldstone mode of type I along the longitudinal direction k_y. It becomes therefore gapped with $\Delta \sim \sqrt{S}$, and the longitudinal spin-wave velocity has similar behaviour, see Eq. (5.104) and section ΓX on the right panel of Fig. (5.3). The situation along transverse directions k_x and k_z is slightly more complex. Although there is a type I pseudo- Goldstone mode as well in the lower-branch of the spectrum, there is none in the upper branch, which therefore retains a S^1 behaviour before and after inclusion of the interactions. There appears to be a crossing of the two modes, see section XW on the right panel of Fig. (5.3). This results in the transverse spin-wave velocity having both a linear component in S^1, and a subleading $\sqrt{S}$ component, see Eq. (5.100).

5.4 Discussion and conclusion

In order to check the validity of the obtained results, we compare them to available numerical data. ground-state energies for the AF1 and AF3 states were computed by Johannes Richter and collaborators, using the coupled-cluster method (CCM), a variational real-space numerical technique [113]. Fig. (5.6) shows the ground-state energy of the two competing states as a function of inverse spin, with both the results from self-consistent SWT and the extrapolation of the CCM data. The results obtained

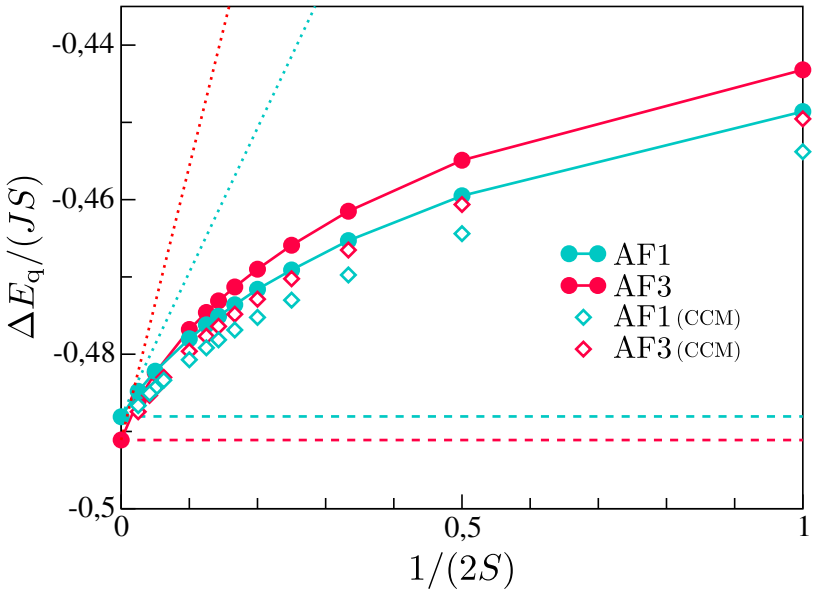

Figure 5.6: *Quantum correction to the ground-state energy of the AF1 and AF3 states as a function of inverse spin. Full circles show the data obtained with spin-wave theory, including interactions self-consistently. Open diamonds show the numerical data obtained from the CCM method. Dashed lines and dotted lines show the perturbative spin-wave results at harmonic order and second order in* $1/S$*, respectively.*

in the present work appear to fit relatively well to the numerical values, *even for spin-*1/2. At the qualitative level at least, the results are equivalent regarding quantum OBD: the AF1 state is selected by quantum fluctuations, up to a large spin value $S^* \approx 10$. Note as well that the energies obtained from the perturbative SWT up to second order in $1/S$ are completely off the numerical values.

From Fig. (5.6), it seems fair to state that LSWT is not efficient in determining the ground state selected by quantum fluctuations in the fcc Heisenberg antiferromagnet [4]. Furthermore, including the effects of magnon-magnon interactions in a perturbative,

[4] at least for reasonable spin lengths

$1/S$ manner does not appear to give satisfying values for the quantum ground-state energies. The self-consistent inclusion of interactions however, apparently provides good results. Anyhow, at the qualitative level, whether included perturbatively or self-consistently, interactions have a determining role in the ground-state selection, and select a ground state different from the one selected in the harmonic approximation, *for any physically relevant value of spin.*

5.4.1 Subtleties of spin-wave theory in the fcc Heisenberg antiferromagnet

Several aspects contribute to the complexity of the quantum OBD mechanism in this system. Let me expose the most essential points, which I believe are applicable to a more general discussion on SWT.

i) *The difference between the ground-state energies of the two competing states is extremely small at the harmonic level.* It is indeed of the order of $10^{-3}(JS)$, see Eq. (4.30). This is a very important point. For another example of such nearby harmonic energies, see [84]. In such cases, one needs a very precise estimate of the energy to be sure about the ultimate ground-state selection. Indeed, the possibility has to be considered, that higher orders terms in SWT can be of comparable magnitude as this tiny harmonic energy difference. And if so, they could alter the qualitative result - which state has lowest energy. This is precisely what is shown to happen in the present chapter. Therefore, in such situations where two states remain very close in energy at the harmonic level, one should take the results obtained by LSWT with a grain of salt. This gives an interesting illustration of the following statement: *LSWT might fail to give good qualitative results for the ground-state selection, even for large spin values.*

ii) *The perturbative expansion about the harmonic Bogolyubov vacuum is not particularly well-behaved.* Indeed, in the perturbative expansion, the second order correction to the ground-state energy is of same order of magnitude as the first order correction, namely $10^{-1}(JS)$, see Eq. (5.86) and Eq. (5.89). Although these second order corrections come with a $1/S$ coefficient, they remain substantial compared to the first corrections up to large spin values, see Fig. (5.1). A similar situation takes place for example in the frustrated J_1-J_2 square lattice AFM discussed in the introduction, where the perturbative SWT expansion fails to give reliable results [15, 20, 114]. Note that the perturbative approach here might however not be badly-behaved *per se*. If we consider the expansion parameter to be $\langle n \rangle / (2S)$, then the expansion is expected to be efficient only *if* this parameter is small. When $\langle n \rangle$ is taken over the harmonic Bogolyubov vacuum, it is quite substantial for both states, see Eq. (4.31). Therefore, the perturbative expansion has no reason in principle to be efficient for small spin values, which is the common statement about SWT. The "smallness criterion" is somehow not met. Nevertheless, in non-frustrated, or weakly frustrated magnets, the pertur-

bative approach to SWT gives very good results, *even for rather small values of spins* like $S = 1$ or even sometimes $S = 1/2$. This may be attributed to the fact that $\langle n \rangle$ has a smaller value in the harmonic Bogolyubov vacuum in such systems. There seems however to be an additional smallness coming into play. The expansion indeed often has vanishingly small coefficients in front of increasing orders of the expansion parameter, *even if it is taken to be* $\langle n \rangle / (2S)$ [115]. This is most probably related to the harmonic Bogolyubov vacuum being already a good approximation to the real quantum ground state. This takes us to the third point.

iii) *Interactions are large in the harmonic Bogolyubov vacuum.* Actually, this statement is equivalent to the previous one, they are two sides of the same coin. Another way to see this, is that the effective contributions to the harmonic part of the Hamiltonian, coming from interactions, are not negligible in the Bogolyubov vacuum, although they come with a $1/S$ factor, see Eqs. (5.15 - 5.16). Therefore, treating these interactions perturbatively is not so efficient, because the perturbation is of same order of magnitude as the unperturbed Hamiltonian. What makes interactions be so large in this system? This takes us to the next point.

iv) *The effects of interactions become stronger in highly frustrated systems.* Indeed, the accidental classical ground-state degeneracy leads to corresponding accidental gapless modes in the harmonic spectrum: the pseudo Goldstone modes. As we saw earlier, in the AF1 and AF3 states, these pseudo Goldstone modes are quite numerous, see Fig. (4.2). This directly relates to the large classical ground-state degeneracy in this system, see Fig. (3.3). As a result, the mean-field averages calculated in the harmonic Bogolyubov vacuum are overestimated. This is particularly true for the spin reduction, see again Eq. (4.31). This is not surprising, as they involve integrals of functions where the harmonic spectrum is in the denominator, see Eq. (5.42) for the AF1 state and Eq. (5.82) for the AF3 state. Interactions then become strong in the harmonic Bogolyubov vacuum.

5.4.2 The self-consistent method

On the bright side, *the strength of SWT appears to be well restored by treating interactions self-consistently.* Within this method, the Bogolyubov particles are being renormalized, as well as the corresponding Bogolyubov vacuum. Interactions are included self-consistently, which means that contributions from all orders in $1/S$ are taken into account. One can therefore not speak about a perturbative expansion anymore, and cannot attribute a specific $1/S$ order to a given contribution. The consequences of this technique are the following:

i) The so defined Bogolyubov vacuum is necessarily closer to the real quantum ground state, as higher orders in the expansion of the Holstein-Primakoff square root are included. So we are closer to the exact transformation.

ii) Within the self-consistently renormalized Bogolyubov transformation, excited states do not interact with their own vacuum: the particles are better-behaved.

iii) The pseudo-Goldstone modes are lifted and only the true Goldstone modes remain in the spectrum. Pseudo-Goldstone modes acquire quantum gaps, of which the height is related to the type of pseudo-Goldstone mode.

iv) As a consequence of the latter point, mean-field averages are believed to be better determined, avoiding the many zeroes in the denominator. Note that new values for the spin reduction, obtained after convergence of the self-consistent loop, are much reduced compared to the harmonic approximation, see Fig. (5.7). This is particularly true at small spin. This means that the true quantum ground state is somewhat closer to the classical ordered state than could be thought from the harmonic results. In other words, fluctuations are not that huge. It also means, that the expansion of the square root in the Holstein-Primakoff transformation is more relevant.

Note as well that the self-consistent loops converge quite fast in this system, within only a few steps, which is enjoyable. Let me however insist that this technique only applies to collinear states, which restricts quite a lot the possibilities for applications.

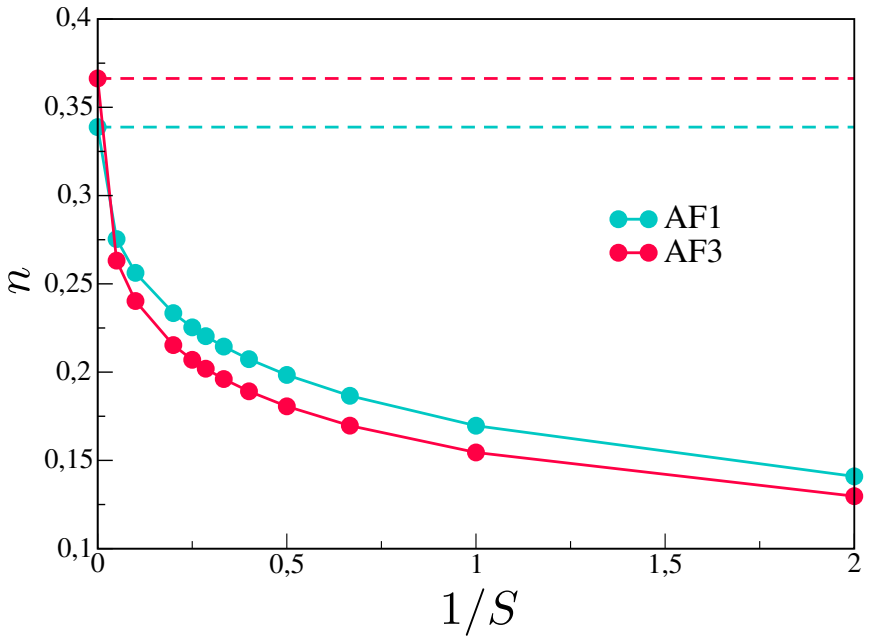

Figure 5.7: *Spin reduction versus inverse spin for the AF1 and AF3 states, after self-consistent renormalization of the vacuum. Similar figures are shown in appendix B for other mean-field averages.*

5.4.3 Summary of the chapter

In this chapter, I considered the effects of magnon-magnon interactions in the ground state selected from quantum and thermal fluctuations in the nearest-neighbor fcc Heisenberg antiferromagnet. In that aim, I went to higher order in spin-wave theory and included quartic terms in bosonic Holstein-Primakoff operators. Note that I focused only on the two collinear classical ground states, the AF1 and AF3 states. For that reason, cubic terms in the expanded spin-wave Hamiltonian do not need to be considered. The quartic terms were decoupled in the Hartree-Fock fashion, and we obtained an effective quadratic Hamiltonian which depends on pairwise magnon averages (mean fields), see Eq. (5.12) and Eq. (5.23). Consequently, the ground-state energy with quantum corrections depends on the mean-field averages as well for the two states, see Eq. (5.27) and Eq. (5.54) for the AF1 and AF3 states, respectively.

The spectrum, including the effects of magnon-magnon interactions, was derived analytically, see Eqs. (5.32 - 5.33) and Eq. (5.36) for the AF1 state, and Eqs. (5.60 - 5.63) for the AF3 state. Expressions for the mean-field averages were obtained as well, see Eq. (5.42) and Eq. (5.82) for the AF1 and AF3 states, respectively. Evaluation of these expressions is a self-consistent problem, equivalent to Takahashi's modified spin-wave theory at $T = 0$.

I computed the ground-state energies with quantum corrections for the two states. Note that the energy now depends on spin value, contrary to the harmonic case. The mean-field averages were computed self-consistently using standard Monte-Carlo integration, with a rather fast convergence of the self-consistent loop involving at most 15 steps. The ground-state energy was obtained using the values for the mean-field averages after convergence.

It appears that the AF1 state has lower energy than the AF3 state, for all physically relevant spin values ($S \lesssim 10$), see Fig. (5.2). The quantum order by disorder therefore gives a different qualitative selection from the linear spin-wave approximation, even at large spins, which indicates a failure of the perturbative approach in this system.

This failure is attributed to the large number of pseudo-Goldstone modes in the harmonic spectrum, which induce an overestimation of the strength of quantum fluctuations. After self-consistent renormalization, the spectra acquire gaps and only remain the true Goldstone modes predicted by the Goldstone theorem, see Fig. (5.3) and Eq. (5.95) and Eq. (5.98).

As a result, the normal T^4 behaviour of the free-energy at very low temperatures is recovered in the two states, see Eq. (5.102). The AF1 state remains favored by thermal fluctuations, due to a different magnitude of the transverse and longitudinal spin-wave velocities in the two states, see Eqs. (5.103 - 5.104). There is thus no competition between quantum and thermal order by disorder once the effects of magnon-magnon interactions are included, see Fig. (5.5).

Chapter 6

Conclusions

In conclusion, during my PhD I have studied the order-by-disorder mechanism in various geometrically frustrated quantum spin lattices with nearest-neighbor antiferromagnetic Heisenberg interaction.

6.1 Magnetization plateaus

I first studied fractional magnetization plateaus in the kagome and pyrochlore antiferromagnets, two emblematic examples of highly frustrated spin systems. Both systems are known to exhibit fractional magnetization plateaus at $m = 1/3$ and $m = 1/2$ of full saturation, respectively. The spin arrangement within the plateaus correspond to collinear ordered states, in which a fractional part of the spins are pointing opposite to the field direction, while the rest is pointing along it. The plateaus appear due to the stabilization of such collinear phases over a finite field range that extends beyond their classical stability point. In the present work we study such stabilization by the quantum order-by-disorder mechanism at $T = 0$. Full magnetization curves are obtained within the framework of linear spin-wave theory (LSWT).

The collinear plateau phase is surrounded by compressible phases, which correspond to canted states. Using LSWT, I derived full analytical expressions for the harmonic magnon spectra of these canted states in field. This is made possible by the presence of full flat, gapless energy bands in the spectra at the harmonic level, reminiscent of the extensive classical ground-state degeneracy [1]. The ground-state energies of these states are then computed with first quantum correction in $1/S$, from the zero-point motion of the spin-waves. Finally, I get corresponding magnetization, by differentiation of these ground-state energies with respect to the magnetic field.

Applying spin-wave theory directly to the study of the plateau phase itself would require going beyond the linear approximation. Indeed, the collinear state is classically stable only at one field value. Therefore, LSWT would break down if applied to this state anywhere outside that field point. Fortunately, knowledge of the magnetization

[1] One band for the kagome lattice, two bands for the pyrochlore lattice.

curves in the canted phases surrounding the plateau phase, already gives useful information. The extent of the plateau is obtained by intersecting these curves with the fractional magnetization value expected in the plateau phase, namely $m = 1/3$ and $m = 1/2$ of full saturation for the kagome and pyrochlore lattices, respectively. The argument behind this method, is that the U(1) symmetry of the Hamiltonian is restored in the collinear plateau state, rendering it gapped to spin excitations. As a result, S^z_{tot} is conserved within that phase and the classical, fractional value of the magnetization is retained. With this technique, the magnetization curves of both the kagome and the pyrochlore antiferromagnets exhibit the fractional magnetization plateau. Its width decreases with increasing spin.

In the case of the kagome lattice, the values obtained for the plateau field boundaries as a function of inverse spin, match pretty well with available numerical data from exact diagonalization and tensor networks calculations for $S \geq 1$. This gives the encouraging hope that the method used in the present work is efficient in determining the extent of a plateau phase associated to quantum OBD mechanism. The fact that the values do not match numerical results for $S = 1/2$ is not surprising, as the plateau state is known to be of a different, fully quantum nature in that case.

The magnetization of the canted states is shown to exhibit a logarithmic divergence towards the critical field h_m at which they cease to be classically stable. Note that it is also the unique field value at which the collinear plateau state becomes classically stable. This divergence is explained by the extra softening of one of the non-flat magnon branches upon arrival to that state. Indeed, additional lines of zero energy modes appear in the spectrum due to semi local gapless excitations arising in the collinear states, and that do not exist in the canted states. The width of the plateau is also shown to vanish as $(1/S)\ln S$ at the classical limit $S \to \infty$.

6.2 Fcc antiferromagnet: ground-state selection

In the second part of the thesis, I studied ground-state selection by quantum and thermal fluctuations in the quantum nearest-neighbor fcc Heisenberg antiferromagnet. This frustrated spin system has been known for decades, yet no systematic spin-wave analysis was done so far. The classical ground-state degeneracy, despite being sub-extensive, remains substantial. Indeed, the degeneracy of ordering wave vectors consists of full lines in reciprocal space, connecting high-symmetry points of the Brillouin zone. Two collinear spin states are allowed within this classical ground-state manifold: the AF1 and the AF3 state. Note that they become the true ground states of the system when next-nearest-neighbor exchange J_2 of negative or positive sign, respectively, is included. Consequently, those two states are the best ground-state candidates for quantum or thermal OBD. I used spin-wave theory to study the effects of fluctuations.

6.2.1 Linear spin wave theory

Firstly, I applied LSWT to this problem. I derived full analytical expressions for the harmonic spectra of all competing, single-$\mathbf{Q}$ states. Then, the first quantum correction to the ground-state energy is computed from the zero-point motion of the spin-waves, for all competing states. The classical ground-state degeneracy is lifted by these quantum corrections. All non-collinear states are found to have higher energy than the aforementioned collinear AF1 and AF3 states, as expected from quantum fluctuations. The AF3 state is found to be the state of lowest energy. The energy difference to the next state, namely the AF1 state, is extremely tiny, which challenges the robustness of that finding. The spin reduction is quite large in both states, with a value of approximately $\Delta S \simeq 0.3$.

I then computed the free energy as a function of temperature $\Delta F(T)$ for the AF1 and and AF3 states. In a quantum spin system, this corresponds to the thermal population of low-lying magnons, which is straightforward to compute once we have full knowledge of the spectra. It is found that the AF1 state is favored by thermal fluctuations, meaning that its free energy decreases faster with temperature compared to that of the AF3 state. The different ground-state selection operated by quantum fluctuations on one side, and thermal fluctuations of the other side, is seen as a rare competition effect between the two. Due to its smallness, the original ground-state energy difference between the two states at $T = 0$ is ultimately overcome by thermal fluctuations and one expects a phase transition between the two states at low temperature $T \simeq 0.21(JS)$.

In both states, the free energy has a particularly sharp behaviour in temperature, namely $\Delta F(T) \sim -T^2$ for the AF1 state, and $\Delta F(T) \sim -T^{7/3}$ in the AF3 state. This is directly attributed to the extremely soft modes lying around some of the many pseudo-Goldstone modes in the harmonic spectra. In that regard, not only the softness of the modes has to be considered, but also their dimensionality. For example, the T^2 behaviour of the free energy in the AF1 state is related to the presence of quadratic soft modes along whole lines of zero energy modes in reciprocal space.

6.2.2 Interacting spin wave theory

The smallness of the ground-state energy difference between the AF1 and AF3 states at the harmonic level, calls for an investigation of the effects of magnon-magnon interactions. Indeed, although such effects are typically thought to be small compared to the harmonic corrections, they might be sufficiently large to overcome that tiny energy difference, and therefore change qualitatively the ground-state selection. Moreover, the spin reduction being substantial also adds further motivation to that study. The efficiency of LSWT is not expected to be at its best when quantum fluctuations are large, and should be questioned when applied to classical phase boundaries in general.

Therefore, I went to higher orders in the spin-wave theory so as to include effects of magnon-magnon interactions in the picture. I stopped at the quartic order in the

bosonic Hamiltonian. The quartic terms are decoupled in a Hartree-Fock sense, which leads to an effective quadratic Hamiltonian to be added to the harmonic one. Higher-order scattering processes are neglected. The new quadratic Hamiltonian now includes contributions from the interactions, in the form of pair-wise mean-field averages. Determination of the corresponding quantum corrections to the ground-state energy becomes a self-consistent problem. Indeed, the Bogolyubov transformation is redefined so as to recover a diagonal form of the quadratic Hamiltonian. Simultaneously, this new definition changes our approximate quantum ground state - the Bogolyubov vacuum. Within this new quantum ground state, pair-wise mean-field averages are different, and so is the strength of interactions between Bogolyubov magnons. Therefore, the Bogolyubov transformation has to be corrected again. This process is repeated until convergence of the values of the mean-field averages. The final Bogolyubov vacuum is considered to be our best approximation to the true quantum ground state. Note that this self-consistent renormalization corresponds to the inclusion of a certain family of diagrams, up to virtually infinite order. Note as well, that this method is equivalent to the modified spin-wave theory of Takahashi, at $T = 0$.

I performed the self-consistent calculation for the AF1 and AF3 states. After convergence of the values for mean-field averages, the quantum correction to the ground-state energy is easily obtained. Note that this has to be done independently for each spin value, contrary to the harmonic calculation. I found that the AF1 state has lower energy than the AF3 states, for spin values up to $S \lesssim 10$. Beyond this value, the AF3 state becomes the ground state selected by quantum fluctuations, as was found in the harmonic approximation. This result is further confirmed by comparison with numerical data obtained by collaborators from the coupled-cluster method.

The spin-wave spectrum is renormalized as well by the interactions. It acquires quantum gaps along the pseudo-Goldstone modes that were present at the harmonic level, and only the true Goldstone modes remain. Expressions for the quantum gaps are derived, as well as for the spin-wave velocities in the two states. The typical linear dispersion for soft modes of antiferromagnets is recovered. Note that the whole renormalization process goes differently for different spin values. More specifically, the effects of interactions become smaller and smaller relatively to the harmonic result, as $S \to \infty$. This is not surprising, as LSWT should be most efficient in the classical limit. Conversely, the effects of magnon-magnon interactions are quite large for small spin values, and the resulting corrections to the ground-state energy, spin reduction and spin-wave spectra are substantial.

Finally, the free energy $\Delta F(T)$ is computed at low-temperatures for the two states. Normal behaviour $\Delta F(T) \sim -T^4$ is recovered for the two states. It appears however, that the AF1 state remains the state selected by thermal fluctuations, as was found in the harmonic approximation. This is directly connected to the different spin-wave velocities found in the spin-wave spectra of the two states. As a result, there is no competition between quantum and thermal fluctuations anymore, at least for reasonable spin length.

The quantum order-by-disorder mechanism in the nearest-neighbor fcc Heisenberg

antiferromagnet is very subtle, as it is greatly affected by the effects of magnon-magnon interactions. Indeed, the ground state selected by quantum fluctuations is different when considering the problem with or without interactions. This qualitative discrepancy between the two results remains true *for all physically relevant values of spin*. This is the result of a combination of several factors. First, the tiny energy difference between the competing states at the harmonic level, which I believe is accidental. This tiny difference is easily overcome by higher-order corrections to the energy. Second, the presence of many pseudo-Goldstone modes in the harmonic spectra, reminiscent of the classical ground-state degeneracy. This causes the harmonic Bogolyubov vacuum somewhat badly-behaved. Indeed, the expected mean value of on-site spin-lowerings in that state is substantial due to these numerous gapless modes. Consequently, the perturbative approach of conventional spin-wave theory is not efficient, as the smallness criterion for the expansion parameter is not met. Effects of interactions in the harmonic Bogolyubov vacuum are non-negligible, which means that it is not a very good approximation to the true quantum ground state that we are looking for.

Nevertheless, it appears that spin-wave theory still provides very convincing results, when including the effects of interactions self-consistently. After self-consistent renormalization of the spectrum, the ΔS is reduced compared to its value in the harmonic approximation. This means both that in the true quantum ground state (to which we necessarily get closer by including higher-order terms), quantum fluctuations are not so strong, and also that the expansion of the square root in the Holstein-Primakoff transformation is necessarily much better justified. Note that the self-consistent loop converges extremely fast, which is very encouraging. This could be explained by the fact that pseudo-Goldstone modes acquire gaps already at the first step of the redefinition of the Bogolyubov transformation due to interactions. These pseudo-Goldstone modes being the main source of trouble in the computation of the mean-field averages, the theory becomes rapidly well-behaved.

6.3 General conclusion

I hope that the present work gives a convincing appreciation of the power of the spin-wave theory for studying quantum order-by-disorder phenomena, even in highly frustrated magnets.

When the classical ground-state degeneracy is very large, results of the perturbative approach have to be taken with a grain of salt. Indeed, the expansion has chances to be badly-behaved, and especially the strength of quantum fluctuations is overestimated. Interactions then might play a determining role in the ground-state selection. This is especially true if two competing ground states are extremely close in energy at the harmonic level, as was illustrated in the fcc antiferromagnet. Nevertheless, effects of higher-order terms can be included self-consistently, and this is not necessarily very complicated. The efficiency of this technique is confirmed by comparison with numerical data. Note however, that this technique only works for collinear states. In-

deed, in non-collinear states, cubic terms are present in the spin-wave Hamiltonian. They induce a renormalization of the spins orientations, which should also be treated self-consistently in a complete theory.

The classical degeneracy is even higher in the kagome and pyrochlore antiferomagnets studied in the first chapter in the context of fractional magnetization plateaus. There should be, however, no concern about this. Indeed, the spin states in the canted phases of their magnetization curves have been already well-defined to be the canted Y and V states. The energy difference to other types of states, coplanar or not, is too large for us to question this result, and there is virtually no chance that interactions alter it. The robustness of this statement is further enhanced by the fact that these are the most symmetric coplanar canted states that can accommodate a collinear configuration at an intermediate field value. Indeed, quantum fluctuations are known to act in favor of coplanar - if not collinear - states. Therefore, the question of the ground state is not really addressed here. What matters is rather the value of the ground-state energy as a function of magnetic field, in order to obtain the magnetization. This might not be very well evaluated in the harmonic approximation, especially for small spin values. At least for large enough spins, however, higher order corrections should not be huge. Therefore, LSWT should remain efficient to study fractional magnetization plateaus in frustrated spin systems with large spins. This is confirmed by comparison of my results with available numerical data on the kagome antiferromagnet.

Appendix

Appendix A

Spin wave theory

In this appendix, I give the main conceptual and analytical steps of a SWT derivation. Let us say we have a given spin Hamiltonian $\mathcal{H}$ that we wish to diagonalize:

$$\hat{\mathcal{H}} = \hat{\mathcal{H}}\left(\mathbf{S}_1, \mathbf{S}_2, \ldots, \mathbf{S}_N\right) \ , \tag{A.1}$$

where N is the total number of spins in the lattice and $\mathbf{S}_i$ is a spin in position $\mathbf{R}_i$. The goal is to find the eigenvalues of this quantum Hamiltonian, in order to determine the ground state of a given system described by it. SWT is a semiclassical analytical approach to approximate the quantum Hamiltonian by a Hamiltonian that can be solved analytically (or numerically but with reasonable computer power) in the thermodynamic limit. In SWT, the assumption is made that the true quantum ground-state spin configuration is not far from a given classical *ordered* ground state of the original Hamiltonian if Eq. (A.1). Quantumness is accounted for as quantum fluctuations (which are presumably small) around this classical ground state: the spin waves.

A.1 Expanded bosonic Hamiltonian

The analytical starting point of the SWT is the Holstein-Primakoff transformation [28]. It is a mapping of the spin operators to bosonic creation and annihilation operators, which allows us to work in second quantization with bosons, of which the behaviour is well understood:

$$\begin{aligned} S_i^+ &= S_i^x + iS_i^y = \sqrt{2S - n_i} \cdot a_i \\ S_i^- &= S_i^x - iS_i^y = a_i^\dagger \cdot \sqrt{2S - n_i} \ , \qquad\qquad n_i = a_i^\dagger a_i \ . \\ S_i^z &= S - n_i \end{aligned} \tag{A.2}$$

In the above, a_i and $a_i^\dagger$ are bosonic annihilation and creation operators, respectively, and n_i is the particle number operator. Using this representation, the number n_i of bosonic particles present on at a given lattice site i is directly equal to the number of times the spin $\mathbf{S}_i$ in this position is lowered from fully polarized position along the

$z-$axis. For that reason, let me refer to these a particles as "local spin-lowerings". The Holstein-Primakoff transformation reproduces exactly the behaviour of original spin operators, meaning that the spin commutation relations are preserved. The Hilbert space of bosons is, however, infinite, whereas the number of times a given spin can be lowered is not. The correct, finite size of the spin Hilbert space would be ensured by a constraint on the boson occupation number:

$$n_i \leq 2S \ .$$

This constraint leads to the so-called *kinematic interactions*, which are neglected in the vast majority of spin-wave studies of the literature. Following this tendency, in my work I also didn't take this constraint into account, assuming the effects of kinematic interactions to be small.

Exactly evaluating the square roots in S_i^+ and S_i^- cannot be done analytically. For that reason, they are expanded in powers of $n_i/2S$:

$$\sqrt{2S - n_i} = \sqrt{2S}\left\{1 - \frac{1}{2}\left(\frac{n_i}{2S}\right) - \frac{1}{8}\left(\frac{n_i}{2S}\right)^2 - \cdots\right\} \ . \tag{A.3}$$

Substituting the above expression into the Holstein-Primakoff transformation of Eq. (A.2), one obtains an expanded expression for the spin lowering and raising operators:

$$S_i^+ \simeq \sqrt{2S}\left[a_i - \frac{1}{4S}a_i^\dagger a_i a_i - \frac{1}{32S^2}a_i^\dagger a_i a_i^\dagger a_i a_i - \ldots\right] \ , \tag{A.4}$$

$$S_i^- \simeq \sqrt{2S}\left[a_i^\dagger - \frac{1}{4S}a_i^\dagger a_i^\dagger a_i - \frac{1}{32S^2}a_i^\dagger a_i^\dagger a_i a_i^\dagger a_i - \ldots\right] \ . \tag{A.5}$$

The above expressions for S_i^+ and S_i^- (as well as the exact expression for S_i^z of Eq. (A.2)) are substituted into the original spin Hamiltonian $\hat{\mathcal{H}}$ of Eq. (A.1). This leads to a new Hamiltonian in expanded form that we call the spin wave (SW) Hamiltonian $\hat{\mathcal{H}}_{SW}$:

$$\hat{\mathcal{H}}_{SW} = \sum_{n=0}^{\infty} \hat{\mathcal{H}}^{(n)} \ ,$$

where $\hat{\mathcal{H}}^{(n)}$ contains only products of n bosonic creation or annihilation operators.

A.1.1 A word on the validity of SW expansion

The point of having such an expansion, is to be able to truncate it at a given desired order, in order to obtain a bosonic Hamiltonian of which we know how to find the eigenvalues. For this truncation to be valid, one needs the higher-order terms beyond the truncation order to be vanishingly small. In other words, the expansion given in

Eq. (A.3) should be well-behaved. This is guaranteed if the expansion parameter is small, that is, if the following condition is satisfied:

$$\frac{n_i}{2S} \ll 1 \ . \tag{A.6}$$

This condition is satisfied for very large S, which is why SWT is usually efficient in describing the behaviour of systems of large spins. From Eq. (A.6) however, it is clear that the validity of a spin-wave derivation not only depends on the spin size S, but also on the n_i parameter, that is, the number of bosonic excitations on a given site. For that reason, if n_i is very large, the SW expansion might not be efficient, *even for large spins*. Oppositely, if n_i is very small, the SW expansion could be very efficient, *even for small spins*.

A.2 Local spin coordinates

Following the validity condition of the SW perturbative treatment given by Eq. (A.6), one needs to construct the Holstein-Primakoff transformation of Eq. (A.2) in such a way, that the number n_i of elementary spin excitations (that is, spin-lowerings from the z-axis) is small. This has to be true for each lattice site. In SWT, the assumption is made that the true quantum ground state is not too far from a classical ground-state configuration. Quantum effects will only appear as small corrections to the spin orientation, spin length, and ground-state energy of the classcial ground state. The classical ground state is, in a way, "dressed" by quantum fluctuations. Thus, in this quantum ground state, it is assumed that n_i is small *if the z axis coincides with the classical orientation of the spin* $\mathbf{S}_i$. For this reason, the SW derivation has best chances to give reliable results when the Holstein-Primakoff transformation is applied to *local* spin coordinates for each spins. Those local spin coordinates are defined such that the local z axis of a given spin $\mathbf{S}_i$ coincides with the orientation and direction of this spin in the classical ground state.

Let us call (x_0, y_0, z_0) the global spin coordinates. In the thesis, I only applied SWT to *coplanar* spin configurations as classical starting points. In a coplanar configuration, all spins belong to the same plane, which for the sake of simplicity, we define as the global x_0z_0 plane. Then the orientation of a given spin $\mathbf{S}_i$ is given by only one angle θ_i with respect to the global z_0-axis. The transformation to local basis is given explicitly below:

$$\begin{aligned} S_i^{x_0} &= \cos\theta_i S_i^x + \sin\theta_i S_i^z \ , \\ S_i^{y_0} &= S_i^y \ , \\ S_i^{z_0} &= \cos\theta_i S_i^z - \sin\theta_i S_i^x \ . \end{aligned} \tag{A.7}$$

This corresponds to a local rotation of the coordinates system about the y_0-axis. Information about the classical ground-state configuration that we started from is thus kept in the angular variables of the rotation in Eq. (A.7).

A.3 Harmonic Hamiltonian in reciprocal space

Linear spin-wave theory (LSWT) consists in truncating the expanded SW Hamiltonian of Eq. (A.6) to the harmonic order, that is, throwing out all terms involving products of more than 2 bosonic operators. This gives:

$$\hat{\mathcal{H}}_{LSW} = \hat{\mathcal{H}}_{SW}^{(0)} + \hat{\mathcal{H}}_{SW}^{(1)} + \hat{\mathcal{H}}_{SW}^{(2)} \ .$$

The Holstein-Primakoff transformation is applied to a classical ground-state configuration, such that $\hat{\mathcal{H}}_{SW}^{(0)}$ is the classical ground-state energy E_{cl}. In the Harmonic approximation, as this classical ground state is a local minimum of the energy, the term linear in bosonic operators $\hat{\mathcal{H}}_{SW}^{(1)}$ vanishes. Then only remains the quadratic terms of $\hat{\mathcal{H}}_{SW}^{(2)}$ as a $1/S$ quantum correction to the ground-state energy.

The Hamiltonian of Eq. (A.1) being a function of all the N spin variables of the lattice, when considering the thermodynamic limit $N \to \infty$, we end up having a bosonic SW Hamiltonian involving sums over an infinite set of position in space. It is more convenient then to work in the reciprocal space (or $\mathbf{k}$-space), such that all relevant information is encoded in the first Brillouin zone, which has finite boundaries. For this reason, one applies a discrete Fourier transformation to the bosonic operators a_i, $a_i^\dagger$, and the SW Hamiltonian will be expressed as a function of $a_\mathbf{k}$, $a_\mathbf{k}^\dagger$. The way this Fourier transformation is made depends on the nature of the lattice and of the classical spin configuration. Indeed, when the lattice is not a Bravais lattice, it is convenient to define a magnetic unit cell containing more than one spin, such that a superlattice of such cells gives back the original lattice. The superlattice is a Bravais lattice. The magnetic unit cell can also be enlarged in relation to the periodicity of the classical spin configuration. For the moment, let us simply distinguish the two situations where we introduce only one bosonic field, or several.

A.3.1 One boson representation

When studying a Bravais lattice with SWT, it is sometimes possible to introduce only one bosonic field, *even with non ferromagnetic arrangements*. Let us say that we attribute a sublattice for each different spin orientations (not necessarily only two, see spiral states). Generally, one would introduce *one bosonic field for each sublattice*. Then the first Brillouin zone is reduced and we have as many magnon modes as we have sublattices.

If the sublattices are symmetry-related (meaning that they have the same surrounding spin orientations in the rotated local basis), then one can introduce only one single flavor for magnons. Then in a sense, the magnetic unit cell is reduced to only one lattice site, and the periodicity of the magnetic structure becomes simply the periodicity of the original Bravais lattice. In such simple situations, the Fourier Transformation is defined as follows:

$$a_i = \frac{1}{\sqrt{N}} \sum_\mathbf{k} a_\mathbf{k} e^{i\mathbf{k}\cdot\mathbf{R}_i} \ . \tag{A.8}$$

Substituting this into the LSW Hamitlonian of Eq. (A.8), one obtains only quadratic contributions of the two following kinds:

- *Normal* terms (particle number is conserved): $a^\dagger_{\mathbf{k}} a_{\mathbf{k}}$,
- *Anomalous* terms (particle number is changed): $a^\dagger_{\mathbf{k}} a^\dagger_{-\mathbf{k}}$ or $a_{-\mathbf{k}} a_{\mathbf{k}}$.

The final LSW Hamiltonian is written in momentum space as follows:

$$\hat{\mathcal{H}}^{(2)} = \sum_{\mathbf{k}} \left\{ A_{\mathbf{k}} a^\dagger_{\mathbf{k}} a_{\mathbf{k}} - \frac{1}{2} B_{\mathbf{k}} \left(a^\dagger_{\mathbf{k}} a^\dagger_{-\mathbf{k}} + a_{-\mathbf{k}} a_{\mathbf{k}} \right) \right\} . \tag{A.9}$$

E_{cl} is of the order of S^2. The coefficients $A_{\mathbf{k}}$ and $B_{\mathbf{k}}$ in front of the normal and anomalous terms are of the order of S, thus they represent a $1/S$ correction to the ground-state energy.

The single magnon representation applies to the fcc Heisenberg AFM with a spiral structure, including the commensurate collinear AF1 structure (see section 4.1.1).

A.3.2 multiple-bosons representation

When all sublattices do not have the same surrounding spin structure in the rotated basis, one has to introduce several bosonic fields, at least one for each different surrounding structure. This is the case for example when the lattice is not a Bravais lattice, like in the kagome and pyrochlore AFMs studied in chapter 2. Indeed, in that case, all the sites of the crystallographic unit cell have different geometrical surrounding. Even in Bravais lattice, it can happen that different sublattices are not symmetry-related and thus one still has to introduce several bosonic fields. It is the case of AF3 state in the fcc lattice, see chapters 3-5 .

The magnetic unit cell contains several lattice sites, one of each sublattice. Sublattices are generally defined such that all spins of a same sublattice have the same orientation in the classical ground-state configuration. Although, as we will see later in the fcc chapter, this is not always the case. The magnetic unit cell is defined as the smallest group of spins of which the classical ground-state configuration is only a repetition of. We denote the different bosonic modes by index $\alpha \in \{a, b, c, \dots\}$. If there are n sublattices, then the lattice is composed of $N_c = N/n$ magnetic unit cells. It is necessary to define as well n sets of N_c bosonic operators. To keep information about the sublattices, a given spin $\mathbf{S}_i$ is identified by both its position $\mathbf{R}_i$ and its sublattice α:

$$\mathbf{S}_i \to \mathbf{S}_{i,\alpha} .$$

Then to each bosonic mode $\alpha \in \{a, b, c\}$ is associated a different set of corresponding N_c bosonic operators a_i, b_i, c_i, and so on:

$$\begin{array}{lll}
S^+_{i,a} = \sqrt{2S - a^\dagger_i a_i}\, a_i & S^+_{i,b} = \sqrt{2S - b^\dagger_i b_i}\, b_i & S^+_{i,c} = \sqrt{2S - c^\dagger_i c_i}\, c_i \\
S^-_{i,a} = a^\dagger_i \sqrt{2S - a^\dagger_i a_i} , & S^-_{i,b} = b^\dagger_i \sqrt{2S - b^\dagger_i b_i} , & S^-_{i,c} = c^\dagger_i \sqrt{2S - c^\dagger_i c_i} , \quad \cdots \\
S^z_{i,a} = S - a^\dagger_i a_i & S^z_{i,b} = S - b^\dagger_i a_b & S^z_{i,c} = S - c^\dagger_i a_c
\end{array}$$

The Fourier transformed is defined similarly as in Eq. (A.8) for each mode:

$$a_i = \frac{1}{\sqrt{N_c}} \sum_{\mathbf{k}} a_{\mathbf{k}} e^{i\mathbf{k}\cdot\mathbf{R}_i} \ , \quad b_i = \frac{1}{\sqrt{N_c}} \sum_{\mathbf{k}} b_{\mathbf{k}} e^{i\mathbf{k}\cdot\mathbf{R}_i} \ , \cdots \tag{A.10}$$

Substituting this into the LSW Hamitlonian of Eq. (A.8), one obtains only quadratic contributions of the four following kinds:

- *Normal* terms between spins of a same mode: $a^\dagger_{\mathbf{k}} a_{\mathbf{k}}$, $b^\dagger_{\mathbf{k}} b_{\mathbf{k}}$, ...
- *Normal* terms between spins of different modes: $a^\dagger_{\mathbf{k}} b_{\mathbf{k}}$, $b^\dagger_{\mathbf{k}} c_{\mathbf{k}}$, ...
- *Anomalous* terms between spins of the same mode: $a^\dagger_{\mathbf{k}} a^\dagger_{\text{-}\mathbf{k}}$ or $a_{\text{-}\mathbf{k}} a_{\mathbf{k}}$, ...
- *Anomalous* terms between spins of different modes: $a^\dagger_{\mathbf{k}} b^\dagger_{\text{-}\mathbf{k}}$ or $a_{\text{-}\mathbf{k}} b_{\mathbf{k}}$, ...

Then it is convenient to write the harmonic SW Hamiltonian in a matrix form:

$$\hat{\mathcal{H}}^{(2)} = \frac{1}{2} \sum_{\mathbf{k}} \left(\hat{X}^\dagger_{\mathbf{k}} H_{\mathbf{k}} \hat{X}_{\mathbf{k}} - \mathrm{Tr}[A_{\mathbf{k}}] \right) \ , \tag{A.11}$$

where $\hat{X}^\dagger_{\mathbf{k}} = \left(a^\dagger_{\mathbf{k}}, b^\dagger_{\mathbf{k}}, ..., a_{\text{-}\mathbf{k}}, b_{\text{-}\mathbf{k}}, ... \right)$ is a row vector containing all the Holstein-Primakoff bosonic operators and $H_{\mathbf{k}}$ is a $(2n) \times (2n)$ matrix with the following block structure:

$$H_{\mathbf{k}} = \begin{pmatrix} A_{\mathbf{k}} & -B_{\mathbf{k}} \\ -C_{\mathbf{k}} & D_{\mathbf{k}} \end{pmatrix} \ .$$

$A_{\mathbf{k}}$, $B_{\mathbf{k}}$, $C_{\mathbf{k}}$ and $D_{\mathbf{k}}$ are $n \times n$ matrices. $A_{\mathbf{k}}$ and $D_{\mathbf{k}}$ contain the coefficients in front of the diagonal terms of the Hamiltonian, while $B_{\mathbf{k}}$ and $C_{\mathbf{k}}$ contain the anomalous terms. In general we have $D_{\mathbf{k}} = A^t_{\text{-}\mathbf{k}} = A_{\mathbf{k}}$ and $C_{\mathbf{k}} = B^\dagger_{\mathbf{k}}$, such that $H_{\mathbf{k}}$ is written as:

$$H_{\mathbf{k}} = \begin{pmatrix} A_{\mathbf{k}} & -B_{\mathbf{k}} \\ -B^\dagger_{\mathbf{k}} & A_{\mathbf{k}} \end{pmatrix} \ . \tag{A.12}$$

The constant term $-\mathrm{Tr}[\mathrm{A}_{\mathbf{k}}]$ in Eq. (A.11) arises from the bosonic commutation relations when rearranging the terms in the Hamiltonian, and consequently has a contribution from half of all the diagonal terms of $H_{\mathbf{k}}$. When there is no sublattice description, $A_{\mathbf{k}}$ and $B_{\mathbf{k}}$ in the matrix representation of Eq. (A.11) are simply scalars, and we recover naturally the form of Eq. (A.9).

A.4 Diagonalization: Bogoliubov transformation

If the anomalous terms $B_{\mathbf{k}}$ are non vanishing in Eq. (A.12), the quadratic bosonic Hamiltonian obtained from the LSW expansion in Eq. (A.11) is not diagonal. This means that the basis of on-site spin-lowering excitations $(a^\dagger_i, b^\dagger_i, c^\dagger_i, \cdots)$ defined in the Holstein-Primakoff transformation is not a good basis to this Hamiltonian. In other words, these excitations are not well-behaved and do not have a definite energy. They

interact with their own vacuum, leading to spontaneous creation or annihilation of pairs of spin-flips of opposite momenta. Due to this, one cannot simply establish the ground state as the vacuum of these spin-lowerings. That also means that the original classical ground state is not a true ground state of the Hamiltonian.

In order to determine the true ground state (up to harmonic approximation), we need to define a proper basis for the quadratic Hamiltonian, in which it is diagonal. Then the ground state becomes indeed the vacuum of such well-behaved particles: the magnons. Those new particles are defined so as to *not* interact with their own vacuum (cancellation of anomalous term). New bosonic excitations $\beta_{\mathbf{k},m}$, $\beta^\dagger_{\mathbf{k},m}$ are thus defined through the Bogolyubov transformation, where $m \in \{1, 2, \cdots, n\}$ refers to the different magnon modes. In the following, we focus on the matrix form of the Hamiltonian, as it is more general [1]. The steps essentially follow [116].

The Bogolyubov transformation is given by:

$$\hat{X}_{\mathbf{k}} = P_{\mathbf{k}} \hat{Y}_{\mathbf{k}} \ , \tag{A.13}$$

where $P_{\mathbf{k}}$ is the (real) change-of-basis matrix. The vector $\hat{Y}_{\mathbf{k}}$ contains the new bosonic particles:

$$\hat{Y}^\dagger_{\mathbf{k}} = \left(\beta^\dagger_{\mathbf{k},1}, \beta^\dagger_{\mathbf{k},2}, ..., \beta_{\text{-}\mathbf{k},1}, \beta_{\text{-}\mathbf{k},2}, ...\right) \ . \tag{A.14}$$

The goal is that this transformation leads to a diagonal harmonic Hamiltonian, that is (see Eq. (A.11)):

$$\hat{X}^\dagger_{\mathbf{k}} H_{\mathbf{k}} \hat{X}_{\mathbf{k}} = \hat{Y}^\dagger_{\mathbf{k}} \Omega_{\mathbf{k}} \hat{Y}_{\mathbf{k}} \ , \tag{A.15}$$

with $\Omega_{\mathbf{k}}$ being a diagonal matrix containing the spin-wave energies. Substituting Eq. (A.13) into the above leads to the following relation:

$$P^\dagger_{\mathbf{k}} H_{\mathbf{k}} P_{\mathbf{k}} = \Omega_{\mathbf{k}} \ . \tag{A.16}$$

If $P_{\mathbf{k}}$ would be unitary, then this would lead to the eignevalue equation corresponding to direct diagonalization of $H_{\mathbf{k}}$. This is, however, not the case here. Indeed, the requirement that the bosonic commutation relations are verified - both for the original particles $(a_{\mathbf{k}}, b_{\mathbf{k}}, \cdots)$ and the eigen-excitations $(\beta_{\mathbf{k},1}, \beta_{\mathbf{k},1}, \cdots)$ - constrains the diagonalization process. The commutation relations are written as follows:

$$\left[\hat{X}_{\mathbf{k}}, \hat{X}^\dagger_{\mathbf{k}}\right] = \hat{X}_{\mathbf{k}} \cdot \hat{X}^\dagger_{\mathbf{k}} - \left(\hat{X}_{\mathbf{k}} \cdot \hat{X}^\dagger_{\mathbf{k}}\right)^t = G \ , \tag{A.17}$$

$$\left[\hat{Y}_{\mathbf{k}}, \hat{Y}^\dagger_{\mathbf{k}}\right] = \hat{Y}_{\mathbf{k}} \cdot \hat{Y}^\dagger_{\mathbf{k}} - \left(\hat{Y}_{\mathbf{k}} \cdot \hat{Y}^\dagger_{\mathbf{k}}\right)^t = G \ , \tag{A.18}$$

where G is defined as:

$$G = \begin{pmatrix} \mathbb{I}_n & 0 \\ 0 & -\mathbb{I}_n \end{pmatrix} \ . \tag{A.19}$$

[1] Note that the Bogolyubov transformation for the single-mode picture is done in chapters 4 and 5.

We substitute Eq. (A.13) into Eq. (A.17). Keeping in mind that $P_{\mathbf{k}}$ is real, from Eq. (A.18) the following relation holds for the change-of-basis matrix:

$$P_{\mathbf{k}} G P_{\mathbf{k}}^{\dagger} = G \ . \tag{A.20}$$

From the property $G^2 = \mathbb{I}_n$, Eq. (A.20) naturally leads to:

$$\left(P_{\mathbf{k}}^{\dagger}\right)^{-1} = G P_{\mathbf{k}} G \ .$$

Multiplying Eq. (A.16) by the above expression, we get:

$$H_{\mathbf{k}} P_{\mathbf{k}} = G P_{\mathbf{k}} G \Omega_{\mathbf{k}} \ . \tag{A.21}$$

We now multiply Eq. (A.21) by G on the left and finally obtain the following eigenvalue problem:

$$\left(G H_{\mathbf{k}}\right) P_{\mathbf{k}} = P_{\mathbf{k}} \left(G \Omega_{\mathbf{k}}\right) \ . \tag{A.22}$$

Indeed, $G\Omega_{\mathbf{k}}$ is still a diagonal matrix. In conclusion, although the original SW matrix $H_{\mathbf{k}}$ cannot be straightforwardly diagonalized as is, one can obtain the diagonal elements of $(G\Omega_{\mathbf{k}})$ by diagonalization of the modified matrix $(GH_{\mathbf{k}})$.

A.4.1 A symmetry-induced simplification

In the situation where $B_{\mathbf{k}}$ is a hermitian matrix, then the block structure of the LSW matrix $H_{\mathbf{k}}$ allows us to reduce the dimension of the eigenvalue problem from $2n$ to n. We have from Eq. (A.12):

$$G H_{\mathbf{k}} = \begin{pmatrix} A_{\mathbf{k}} & -B_{\mathbf{k}} \\ B_{\mathbf{k}} & -A_{\mathbf{k}} \end{pmatrix} \ . \tag{A.23}$$

Take a given eigenvector $W_{\mathbf{k}}$ of $GH_{\mathbf{k}}$ with eigenvalue $\epsilon_{\mathbf{k}}$. Let us define the two smaller vectors $U_{\mathbf{k}}$ and $V_{\mathbf{k}}$ of dimension n such that:

$$W_{\mathbf{k}}^{\dagger} = \left(U_{\mathbf{k}}^{\dagger}, V_{\mathbf{k}}^{\dagger}\right) \ .$$

Then the eigenvalue equation gives two relations for $U_{\mathbf{k}}$ and $V_{\mathbf{k}}$:

$$G H_{\mathbf{k}} W_{\mathbf{k}} = \epsilon_{\mathbf{k}} W_{\mathbf{k}} \Rightarrow \begin{cases} A_{\mathbf{k}} U_{\mathbf{k}} - B_{\mathbf{k}} V_{\mathbf{k}} = \ \epsilon_{\mathbf{k}} U_{\mathbf{k}} \ , \\ B_{\mathbf{k}} U_{\mathbf{k}} - A_{\mathbf{k}} V_{\mathbf{k}} = \ \epsilon_{\mathbf{k}} V_{\mathbf{k}} \ . \end{cases} \tag{A.24}$$

Subtracting and adding the two above equations leads to the following:

$$\left(A_{\mathbf{k}} + B_{\mathbf{k}}\right)\left(U_{\mathbf{k}} - V_{\mathbf{k}}\right) = \epsilon_{\mathbf{k}} \left(U_{\mathbf{k}} + V_{\mathbf{k}}\right) \ , \tag{A.25}$$

$$\left(A_{\mathbf{k}} - B_{\mathbf{k}}\right)\left(U_{\mathbf{k}} + V_{\mathbf{k}}\right) = \epsilon_{\mathbf{k}} \left(U_{\mathbf{k}} - V_{\mathbf{k}}\right) \ . \tag{A.26}$$

We multiply both equations by $\epsilon_{\mathbf{k}}$, which leads to:

$$(A_{\mathbf{k}} + B_{\mathbf{k}})\,\epsilon_{\mathbf{k}}\,(U_{\mathbf{k}} - V_{\mathbf{k}}) = \epsilon_{\mathbf{k}}^2\,(U_{\mathbf{k}} + V_{\mathbf{k}}) \ , \tag{A.27}$$

$$(A_{\mathbf{k}} - B_{\mathbf{k}})\,\epsilon_{\mathbf{k}}\,(U_{\mathbf{k}} + V_{\mathbf{k}}) = \epsilon_{\mathbf{k}}^2\,(U_{\mathbf{k}} - V_{\mathbf{k}}) \ . \tag{A.28}$$

Substituting Eq. (A.25) and Eq. (A.26) back into the left hand-side of Eq. (A.27) and Eq. (A.28), respectively, gives:

$$\Sigma_{\mathbf{k}}\Delta_{\mathbf{k}}\,(U_{\mathbf{k}} + V_{\mathbf{k}}) = \epsilon_{\mathbf{k}}^2\,(U_{\mathbf{k}} + V_{\mathbf{k}}) \ , \tag{A.29}$$

$$\Delta_{\mathbf{k}}\Sigma_{\mathbf{k}}\,(U_{\mathbf{k}} - V_{\mathbf{k}}) = \epsilon_{\mathbf{k}}^2\,(U_{\mathbf{k}} - V_{\mathbf{k}}) \ , \tag{A.30}$$

where we introduced the two $n \times n$ matrices $\Sigma_{\mathbf{k}}$ and $\Delta_{\mathbf{k}}$:

$$\Sigma_{\mathbf{k}} = (A_{\mathbf{k}} + B_{\mathbf{k}}) \ , \tag{A.31}$$

$$\Delta_{\mathbf{k}} = (A_{\mathbf{k}} - B_{\mathbf{k}}) \ . \tag{A.32}$$

The two equations given in Eqs. (A.29, A.30) define two new eigenvalue problems of dimension n. Since they must be verified for any of the $2n$ eigenvalues $\epsilon_{\mathbf{k}}$ of $GH_{\mathbf{k}}$, the diagonal matrix $G\Omega_{\mathbf{k}}$ must be given by:

$$G\Omega_{\mathbf{k}} = \begin{pmatrix} E_{\mathbf{k}} & 0 \\ 0 & \pm E_{\mathbf{k}} \end{pmatrix} \ , \tag{A.33}$$

where $E_{\mathbf{k}}$ is a $n \times n$ diagonal matrix which contains the n positive square roots of the eigenvalues of $\Sigma_{\mathbf{k}}\Delta_{\mathbf{k}}$:

$$E_{\mathbf{k}} = \begin{pmatrix} \epsilon_{1\mathbf{k}} & & \\ 0 & \ddots & 0 \\ & & \epsilon_{n\mathbf{k}} \end{pmatrix} \ . \tag{A.34}$$

One can show that the requirement for linearly independent eigenvectors of $GH_{\mathbf{k}}$ fixes the negative sign in Eq. (A.33). Then we have:

$$\Omega_{\mathbf{k}} = \begin{pmatrix} E_{\mathbf{k}} & 0 \\ 0 & E_{\mathbf{k}} \end{pmatrix} \ . \tag{A.35}$$

To summarise, the energy modes of the quadratic Hamiltonian given by Eq. (A.11) are found by solving the following n-dimensional eigenvalue problem:

$$\boxed{\left|\Delta_{\mathbf{k}}\Sigma_{\mathbf{k}} - \epsilon^2 \mathbb{I}_n\right| = 0} . \tag{A.36}$$

where $\Delta_{\mathbf{k}}$ and $\Sigma_{\mathbf{k}}$ are given by Eqs. (A.31, A.32). The positive square roots of the obtained n eigenvalues give the SW modes $\epsilon_{\mathbf{k},i}$.

In the case where a single-boson representation is allowed, $A_{\mathbf{k}}$ and $B_{\mathbf{k}}$ become simple scalars and the solution of Eq. (A.36) gives the following magnon spectrum (with single mode):

$$\epsilon_{\mathbf{k}} = \sqrt{A_{\mathbf{k}}^2 - B_{\mathbf{k}}^2} \ . \tag{A.37}$$

A.5 Correction to the ground-state energy

The LSW Hamiltonian is given by:

$$\hat{\mathcal{H}}_{LSW} = \hat{\mathcal{H}}^{(0)} + \hat{\mathcal{H}}^{(2)} \ . \tag{A.38}$$

We recall that $\hat{\mathcal{H}}^{(0)}$ is th classical ground-state energy E_{cl}, and from Eq. (A.11) and Eq. (A.15) we have:

$$\hat{\mathcal{H}}^{(2)} = \frac{1}{2}\sum_{\mathbf{k}} \hat{Y}_{\mathbf{k}}^{\dagger}\Omega_{\mathbf{k}}\hat{Y}_{\mathbf{k}} + C \ , \tag{A.39}$$

where C is a constant given generally by:

$$C = -\frac{1}{2}\sum_{\mathbf{k}} \mathrm{Tr}[A_{\mathbf{k}}] = \frac{E_{cl}}{S} \ . \tag{A.40}$$

From Eq. (A.35), we have then:

$$\hat{\mathcal{H}}_{LSW} = E_{cl}\left(1+\frac{1}{S}\right) + \sum_{\mathbf{k},m} \epsilon_{m\mathbf{k}}\left(\beta_{\mathbf{k},m}^{\dagger}\beta_{\mathbf{k},m} + \frac{1}{2}\right) \ . \tag{A.41}$$

The ground state is obviously defined as the vacuum of Bogolyubov particles, such that $\beta_{\mathbf{k},m}^{\dagger}\beta_{\mathbf{k},m} = 0$, for all modes m and all wave-vectors $\mathbf{k}$. We obtain the final ground-state energy, with harmonic quantum corrections:

$$\boxed{E_{gs} = E_{cl}\left(1+\frac{1}{S}\right) + \frac{1}{2}\sum_{\mathbf{k},m}\epsilon_{m\mathbf{k}}} \ . \tag{A.42}$$

We have thus, for the quantum correction ΔE_q:

$$\Delta E_q = E_{gs}^{LSW} - E_{cl} = \frac{1}{2}\sum_{\mathbf{k},m}\epsilon_{m\mathbf{k}} + C \ . \tag{A.43}$$

It corresponds (modulo a constant term) to the zero-point motion of the spin-waves.

A.6 Heisenberg interaction

In this work, we studied the Heisenberg interaction, which involves only scalar products between pairs of spins. Such scalar products are written in terms of the global spin coordinates (x_0, y_0, z_0) as:

$$\mathbf{S}_i \cdot \mathbf{S}_j = S_i^{x_0}S_j^{x_0} + S_i^{y_0}S_j^{y_0} + S_i^{z_0}S_j^{z_0} \ . \tag{A.44}$$

I want to give the contribution of such spin-spin scalar products to the harmonic SW matrix in reciprocal space $H_{\mathbf{k}}$ given by Eqs. (A.11, A.12), in the most general possible terms.

After rotation to the local spin coordinates given by Eq. (A.7) and Holstein-Primakoff transformation, and keeping only terms up to second order (quadratic in bosonic operators), the scalar product of Eq. (A.44) is given by:

$$\begin{aligned}\mathbf{S}_i \cdot \mathbf{S}_j =& S^2 \cos\theta_{ij} \\ &+ \frac{S\sqrt{2S}}{2} \sin\theta_{ij}(a_j + a_j^\dagger - a_i - a_i^\dagger) \\ &+ \frac{S}{2}(1+\cos\theta_{ij})(a_i^\dagger a_j + a_j^\dagger a_i) - \frac{S}{2}(1-\cos\theta_{ij})(a_i a_j + a_i^\dagger a_j^\dagger) \\ &- S\cos\theta_{ij}(a_i^\dagger a_i + a_j^\dagger a_j)\ .\end{aligned} \tag{A.45}$$

The first line of Eq. (A.45) will contribute to the constant, 0-th order term of the expanded SW Hamiltonian $\hat{\mathcal{H}}^{(0)}$. As one can see, it is porportional to S^2. It corresponds to the standard expression of a classical scalar product, such that such terms are easily understood to lead to the classical ground-state energy.

The second line in Eq. (A.45) contains terms involving only one magnon operator, and will contribute to $\hat{\mathcal{H}}^{(1)}$. In collinear configurations, we have $\theta_{ij} = 0$, for any spin pair, such that $\hat{\mathcal{H}}^{(1)}$ identically vanishes. This property is actually true for all the odd orders of the Hamiltonian. For that reason, in collinear arrangements, only even orders of the expansion remain finite, and give rise to energy corrections of increasing power in $1/S$. There is then no renormalization of the spin orientations (angles). This is what allows us to perform the self-consistent treatment of interaction terms in chapter 5, where only collinear states (AF1 and AF3) are compared. More generally, in the harmonic approximation, $\hat{\mathcal{H}}^{(1)}$ always vanishes. This is due to the fact that the classical ground-state configuration is a local minimum of the energy. Consequently, in the following, we will ignore the associated linear terms.

The last two lines are quadratic in bosonic operators and will continute to $\hat{\mathcal{H}}^{(2)}$. Those terms are proportional to S and thus give a $1/S$ correction to the classical energy $E_{cl} \sim S^2$. From Eq. (A.45), it is obvious that when $\theta_{ij} = 0$, no anomalous terms are generated from the scalar product $\mathbf{S}_i \cdot \mathbf{S}_j$. Only interactions between non-parallel spins contribute to the anomalous term $B_{\mathbf{k}}$ in the SW matrix in reciprocal space $H_{\mathbf{k}}$ (see Eq. (A.12)). This is why ferromagnetic states (such as the fully saturated phase in magnetic field) are exact ground states of the Hamiltonian. Indeed, the absence of anomalous terms means that the SW Hamiltonian is already diagonal in the basis of local spin-lowerings. Therefore the true ground state does correspond to the original classical FM ground state with no quantum fluctuations.

A.6.1 Detailed contributions to the spin wave matrix

So far, no information about the sublattices to which the two spins belong (if any) is explicitly written in Eq. (A.45). All information about both position and sublattice is encoded in the i and j subscripts. To see what is the contribution of a given scalar product to the harmonic Hamiltonian in reciprocal space, one needs to apply

a summation in real space. Specifically, the Heisenberg Hamiltonian will give rise to such terms:

$$\sum_{i\in\{i_\alpha\}} \mathbf{S}_{i,\alpha}\cdot\mathbf{S}_{i+\boldsymbol{\delta},\alpha'} \ . \tag{A.46}$$

The index ensemble $\{i_\alpha\}$ corresponds to the set of all lattice cites belonging to the sublattice α. There are N_c such lattice sites for each sublattice. The bond vector $\boldsymbol{\delta}\neq\mathbf{0}$ connects the spin $\mathbf{S}_i$ in position $\mathbf{R}_i$ to another spin in position $\mathbf{R}_i+\boldsymbol{\delta}$, and α' is the corresponding sublattice to which this second spin belongs. No assumption is made about α', in the sense that it can be different or not from α. The above scalar products are expressed in terms of bosonic operators using Eq. (A.45), to which we apply the following changes:

$$\begin{aligned} a_i &\to (a_i, b_i, c_i\cdots) \text{ for } \alpha=(a,b,c,\cdots) \ , \\ a_j &\to (a_{i+\boldsymbol{\delta}}, b_{i+\boldsymbol{\delta}}, c_{i+\boldsymbol{\delta}},\cdots) \text{ for } \alpha'=(a,b,c,\cdots) \ , \\ \cos\theta_{ij} &\to \theta_\alpha(\boldsymbol{\delta}) \ . \end{aligned} \tag{A.47}$$

As previously mentioned, the sublattices are often defined as sets of spins which all have the same classical orientation. In that situation the classical opening angle between two spins (namely θ_{ij} in Eq. (A.45)) only depends on the two sublattices α and α' ad could thus be written as $\theta_{\alpha\alpha'}$. This is, however, not absolutely general. Indeed, the more general way to define sublattices is as sets of spins which all have the same opening angles configurations with their neighbors. Thus, to keep generality as much as possible, I write the opening angle between the two spins of the scalar product of Eq. (A.46) as $\theta_\alpha(\boldsymbol{\delta})$. After applying the changes of Eq. (A.47), we get the following expression for $(\alpha,\alpha')=(a,b)$:

$$\begin{aligned} \mathbf{S}_{i,a}\cdot\mathbf{S}_{i+\boldsymbol{\delta},b} =& S^2\cos\theta_a(\boldsymbol{\delta}) \\ &+\frac{S}{2}\left[1+\cos\theta_a(\boldsymbol{\delta})\right]\left(a_i^\dagger b_{i+\boldsymbol{\delta}}+b_{i+\boldsymbol{\delta}}^\dagger a_i\right) \\ &-\frac{S}{2}\left[1-\cos\theta_a(\boldsymbol{\delta})\right]\left(a_i b_{i+\boldsymbol{\delta}}+a_i^\dagger b_{i+\boldsymbol{\delta}}^\dagger\right) \\ &-S\cos\theta_a(\boldsymbol{\delta})\left(a_i^\dagger a_i+b_{i+\boldsymbol{\delta}}^\dagger b_{i+\boldsymbol{\delta}}\right) \ . \end{aligned} \tag{A.48}$$

Similar expressions are obtained for any pair (α,α') with $\alpha\neq\alpha'$. When we have $\alpha=\alpha'=a$, we obtain:

$$\begin{aligned} \mathbf{S}_{i,a}\cdot\mathbf{S}_{i+\boldsymbol{\delta},a} =& S^2\cos\theta_a(\boldsymbol{\delta}) \\ &+\frac{S}{2}\left[1+\cos\theta_a(\boldsymbol{\delta})\right]\left(a_i^\dagger a_{i+\boldsymbol{\delta}}+a_{i+\boldsymbol{\delta}}^\dagger a_i\right) \\ &-\frac{S}{2}\left[1-\cos\theta_a(\boldsymbol{\delta})\right]\left(a_i a_{i+\boldsymbol{\delta}}+a_i^\dagger a_{i+\boldsymbol{\delta}}^\dagger\right) \\ &-S\cos\theta_a(\boldsymbol{\delta})\left(a_i^\dagger a_i+a_{i+\boldsymbol{\delta}}^\dagger a_{i+\boldsymbol{\delta}}\right) \ . \end{aligned} \tag{A.49}$$

Let us Fourier Transform Eq. (A.48) and Eq. (A.49) using Eq. (A.10), in order to obtain the expression of the scalar product in terms of bosonic operators in reciprocal space $a_{\mathbf{k}}^{(\dagger)}$. We recall the following relation:

$$\sum_{i\in\{i_\alpha\}} e^{i\mathbf{k}\cdot\mathbf{R}_i} = N_c \cdot \delta_{\mathbf{k},\mathbf{0}} \ , \tag{A.50}$$

which allows us to get rid completely of the real-space summation. The constant term (first lines of Eq. (A.48) and Eq. (A.49)) trivially acquires a factor N_c when performing the summation in Eq. (A.46). We focus thus only on the quadratic terms, and we obtain for $(\alpha,\alpha') = (a,b)$:

$$\begin{aligned}\sum_{i\in\{i_a\}} \left(\mathbf{S}_{i,a}\cdot\mathbf{S}_{i+\boldsymbol{\delta},b}\right)^{(2)} = \frac{S}{2}\sum_{\mathbf{k}}\Big\{ &\left[1+\cos\theta_a(\boldsymbol{\delta})\right]\left(a_{\mathbf{k}}^\dagger b_{\mathbf{k}} e^{i\mathbf{k}\cdot\boldsymbol{\delta}} + b_{\mathbf{k}}^\dagger a_{\mathbf{k}} e^{-i\mathbf{k}\cdot\boldsymbol{\delta}}\right) \\ &- \left[1-\cos\theta_a(\boldsymbol{\delta})\right]\left(a_{\text{-}\mathbf{k}} b_{\mathbf{k}} + a_{\mathbf{k}}^\dagger b_{\text{-}\mathbf{k}}^\dagger\right) e^{i\mathbf{k}\cdot\boldsymbol{\delta}} \\ &-2\cos\theta_a(\boldsymbol{\delta})(a_{\mathbf{k}}^\dagger a_{\mathbf{k}} + b_{\mathbf{k}}^\dagger b_{\mathbf{k}})\Big\} \ .\end{aligned} \tag{A.51}$$

In the case where $\alpha' = \alpha = a$, this becomes:

$$\sum_{i\in\{i_a\}} \left(\mathbf{S}_{i,a}\cdot\mathbf{S}_{i+\boldsymbol{\delta},a}\right)^{(2)} = \sum_{\mathbf{k}}\left\{ A_{\mathbf{k}}^{aa}(\boldsymbol{\delta}) a_{\mathbf{k}}^\dagger a_{\mathbf{k}} - \frac{1}{2} B_{\mathbf{k}}^{aa}(\boldsymbol{\delta})\left(a_{\text{-}\mathbf{k}} a_{\mathbf{k}} + a_{\mathbf{k}}^\dagger a_{\text{-}\mathbf{k}}^\dagger\right)\right\} \ . \tag{A.52}$$

where $A_{\mathbf{k}}^{aa}(\boldsymbol{\delta})$ and $B_{\mathbf{k}}^{aa}(\boldsymbol{\delta})$ are given by:

$$\begin{aligned} A_{\mathbf{k}}^{aa}(\boldsymbol{\delta}) =& S\left\{\cos(\mathbf{k}\cdot\boldsymbol{\delta})\left[1+\cos\theta_a(\boldsymbol{\delta})\right] - 2\cos\theta_a(\boldsymbol{\delta})\right\} \ , \\ B_{\mathbf{k}}^{aa}(\boldsymbol{\delta}) =& S\cos(\mathbf{k}\cdot\boldsymbol{\delta})\left[1-\cos\theta_a(\boldsymbol{\delta})\right] \ . \end{aligned} \tag{A.53}$$

When $\alpha' \neq \alpha$, we have for example with $(\alpha,\alpha') = (a,b)$:

$$\begin{aligned}\sum_{i\in\{i_a\}} \left(\mathbf{S}_{i,a}\cdot\mathbf{S}_{i+\boldsymbol{\delta},b}\right)^{(2)} = \frac{1}{2}\sum_{\mathbf{k}}\Big\{ &A_{\mathbf{k}}^{ab}(\boldsymbol{\delta})\left(a_{\mathbf{k}}^\dagger b_{\mathbf{k}} + a_{\text{-}\mathbf{k}} b_{\text{-}\mathbf{k}}^\dagger\right) - B_{\mathbf{k}}^{ab}(\boldsymbol{\delta})\left(a_{\mathbf{k}}^\dagger b_{\text{-}\mathbf{k}}^\dagger + a_{\text{-}\mathbf{k}} b_{\mathbf{k}}\right) + h.c. \\ &+A_{\mathbf{k}}^{aa}(\boldsymbol{\delta})'\left(a_{\mathbf{k}}^\dagger a_{\mathbf{k}} + a_{\text{-}\mathbf{k}} a_{\text{-}\mathbf{k}}^\dagger - 1\right) + A_{\mathbf{k}}^{bb}(\boldsymbol{\delta})'\left(b_{\mathbf{k}}^\dagger b_{\mathbf{k}} + b_{\text{-}\mathbf{k}} b_{\text{-}\mathbf{k}}^\dagger - 1\right)\Big\} \ ,\end{aligned} \tag{A.54}$$

where $A_{\mathbf{k}}^{ab}(\boldsymbol{\delta})$, $B_{\mathbf{k}}^{ab}(\boldsymbol{\delta})$ are given by:

$$\begin{aligned} A_{\mathbf{k}}^{ab}(\boldsymbol{\delta}) =& S\frac{1+\cos\theta_a(\boldsymbol{\delta})}{2} e^{i\mathbf{k}\cdot\boldsymbol{\delta}} \ , \\ B_{\mathbf{k}}^{ab}(\boldsymbol{\delta}) =& S\frac{1-\cos\theta_a(\boldsymbol{\delta})}{2} e^{i\mathbf{k}\cdot\boldsymbol{\delta}} \ . \end{aligned} \tag{A.55}$$

These coefficients are in principle complex, but the sum of such coefficients over the possible $\boldsymbol{\delta}$ vectors linking sublattices α and β might be real. The coefficients $A^{aa}_{\mathbf{k}}(\boldsymbol{\delta})'$ and $A^{bb}_{\mathbf{k}}(\boldsymbol{\delta})'$ are equal and contribute to the diagonal of the normal matrix $A_{\mathbf{k}}$. They are given by:

$$A^{aa}_{\mathbf{k}}(\boldsymbol{\delta})' = A^{bb}_{\mathbf{k}}(\boldsymbol{\delta})' = -S\cos\theta_a(\boldsymbol{\delta})\ . \tag{A.56}$$

The matrix elements of $A_{\mathbf{k}}$ and $B_{\mathbf{k}}$ will thus be given by all these contributions of Eqs. (A.53, A.55, A.56). This will be useful to fill the spin-wave matrix $H_{\mathbf{k}}$.

Appendix B

Mean-field averages values

The present appendix gives the values obtained numerically after self-consistent evaluation of the mean-field averages n, m_{ij} and Δ_{ij} defined in Eq. (5.12), for the AF1 and AF3 states in the nearest-neighbor Haeisenberg model on an fcc lattice.

B.1 Tables

For the AF1 state, expressions for the three mean-field averages n, m and Δ are given by Eq. (5.42). Those expressions are obviously self-consistent in combination with Eqs. (5.32 - 5.33) and Eq. (5.36). We give the numerical values of nm m and Δ for all the spin lengths that were considered in the present work, as well as the quantum correction to the ground state energy ΔE_q, in table B.1:

S	n	m	Δ	$\Delta E_q/(JS)$
1/2	0.140940(1)	0.070658(2)	0.163809(1)	−0.448499(1)
1	0.169642(1)	0.079798(2)	0.184067(2)	−0.459469(1)
3/2	0.186589(2)	0.084692(2)	0.195514(2)	−0.465359(1)
2	0.198397(2)	0.087885(2)	0.203296(2)	−0.469073(1)
5/2	0.207342(6)	0.090186(6)	0.209093(6)	−0.471655(5)
3	0.214474(6)	0.091946(6)	0.213657(6)	−0.473568(5)
7/2	0.220362(6)	0.093349(7)	0.217388(6)	−0.475049(5)
4	0.225347(6)	0.094502(7)	0.220521(6)	−0.476233(5)
5	0.233419(7)	0.096298(7)	0.225545(7)	−0.478018(5)
10	0.256224(8)	0.100885(8)	0.239417(8)	−0.482190(5)
20	0.275359(9)	0.104142(9)	0.250696(9)	−0.484751(5)
100	0.30644(4)	0.10812(4)	0.26828(4)	−0.48727(5)
∞	0.338777(3)	0.109938(2)	0.285365(2)	−0.4880560(8)

Table B.1: Self-consistent mean-field values for the AF1 state.

For the AF3 state, expressions for the four mean-field averages n, m, Δ and $\Delta_{\alpha\alpha}$ are given by Eq. (5.82). Those expressions are to be taken in combination with Eq. (5.57) and Eqs. (5.60 - 5.63). We give the numerical values of n, m, Δ and $\Delta_{\alpha\alpha}$ for all the spin lengths that were considered in the present work, as well as the quantum correction to the ground state energy ΔE_q, in table B.2:

S	n	m	$\Delta_{\alpha\alpha}$	Δ	$\Delta E_q/(JS)$
1/2	0.1297309(7)	0.0578292(7)	0.1612939(9)	0.1411098(7)	−0.4431978(5)
1	0.544883(8)	0.0597221(7)	0.177545(1)	0.1546256(8)	−0.4549419(5)
3/2	0.1696834(9)	0.0598444(7)	0.186873(1)	0.1619486(8)	−0.4615606(5)
2	0.1806216(9)	0.0595168(8)	0.193330(1)	0.1668548(8)	−0.4658707(5)
5/2	0.189135(3)	0.059048(2)	0.198227(4)	0.170489(3)	−0.468941(2)
3	0.196080(3)	0.058539(2)	0.202149(4)	0.173345(3)	−0.471260(2)
7/2	0.201928(3)	0.058028(2)	0.205405(4)	0.175680(3)	−0.473085(2)
4	0.206966(3)	0.057532(2)	0.208179(4)	0.177644(3)	−0.474565(2)
5	0.215307(3)	0.056605(3)	0.212717(4)	0.180803(3)	−0.476832(2)
10	0.240266(4)	0.053144(3)	0.225969(4)	0.189641(3)	−0.482353(2)
20	0.263153(4)	0.049245(3)	0.237853(5)	0.197052(3)	−0.485954(2)
100	0.30569(1)	0.04079(1)	0.25988(2)	0.20934(1)	−0.48978(2)
∞	0.366331(2)	0.0283547(6)	0.294248(2)	0.2232140(6)	−0.4911055(4)

Table B.2: Self-consistent mean-field values for the AF3 state.

The integrals in Eq. (5.42) (AF1 state) and Eq. (5.82) (AF3 state) were evaluated using standard Monte-Carlo integration with $N_{\text{MC}} = 9 \cdot 10^{10}$ random points in the integration volume for $1/2 \leq S \leq 2$, $N_{\text{MC}} = 1 \cdot 10^{10}$ for $5/2 \leq S \leq 20$ and $N_{\text{MC}} = 9 \cdot 10^{8}$ for $S = 100$. The final values for the mean-field averages are taken after convergence of the self-consistent loop. The values for $S = \infty$ were taken from the harmonic approximation, with $N_{\text{MC}} = 1 \cdot 10^{12}$ random points in the integration volume, see Eqs. (4.28 - 4.29) and Eq. (4.31).

The corresponding values for the quantum gaps Δ_1 and Δ_3 can be readily obtained from the above tables, using Eq. (5.95) and Eq. (5.98) for the AF1 and AF3 states, respectively, which we repeat below:

$$\Delta_1 = 8J(\Delta - m) \ , \qquad \Delta_3 = 8J\sqrt{(\Delta_{\alpha\alpha} - m)(\Delta - m)} \ . \tag{B.1}$$

B.2 Curves

In this section, we compare the evolution of various mean-field averages with respect to spin length, for the AF1 and AF3 states. Those are shown on Fig. (B.1), Fig. (B.2) and Fig. (B.3) for n, m and Δ averages, respectively.

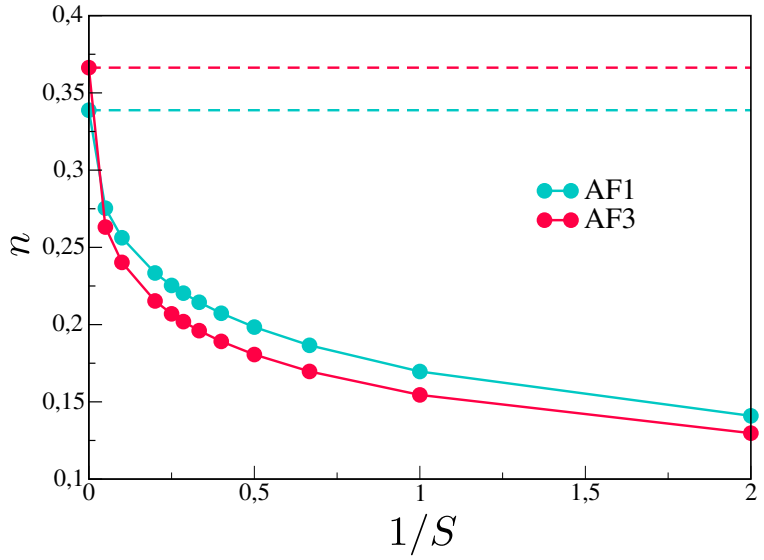

Figure B.1: *Spin reduction n versus inverse spin for the AF1 and AF3 states, after self-consistent renormalization of the vacuum.*

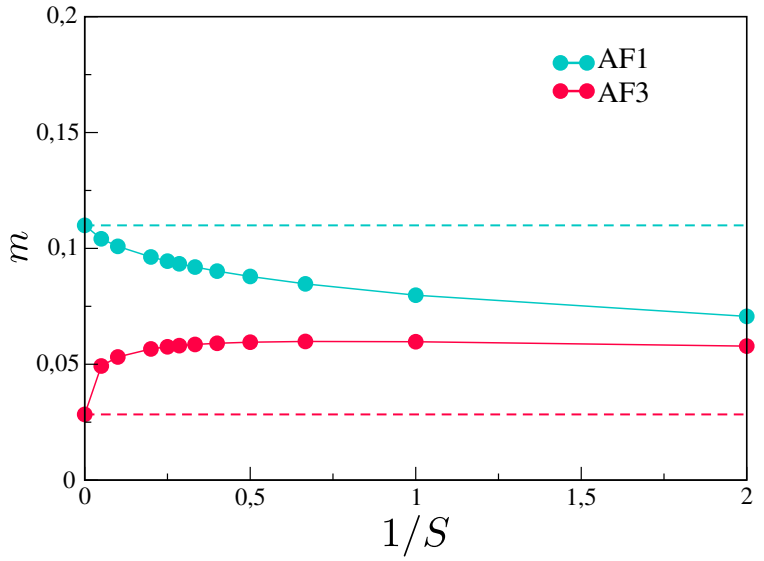

Figure B.2: *Hopping average m versus inverse spin for the AF1 and AF3 states, after self-consistent renormalization of the vacuum.*

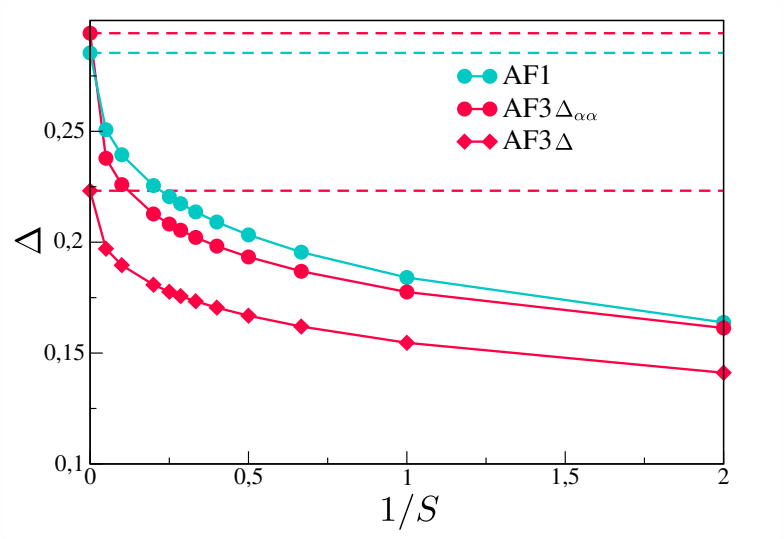

Figure B.3: *Anomalous averages* Δ *versus inverse spin for the AF1 and AF3 states, after self-consistent renormalization of the vacuum.*

Bibliography

[1] C. Lacroix, P. Mendels, and F. Mila. *Introduction to Frustrated Magnetism*. Ed. by C. Lacroix, P. Mendels, and F. Mila. Springer Berlin, 2011.

[2] S. M. Rezende. *Fundamentals of Magnonics*. Springer Cham, 2020. DOI: https://doi.org/10.1007/978-3-030-41317-0.

[3] C. L. Henley. "The "Coulomb Phase" in Frustrated Systems". In: *Annual Review of Condensed Matter Physics* **1** (2010), pp. 179–210. DOI: 10.1146/annurev-conmatphys-070909-104138.

[4] C. Lhuillier and G. Misguich. "Introduction to Quantum Spin Liquids". In: *Introduction to Frustrated Magnetism*. Lacroix, C. and Mendels, P. and Mila, F. Springer Berlin, 2011. Chap. 2, pp. 23–41.

[5] K. Penc and A. M. Läuchli. "Spin Nematic Phases in Quantum Spin Systems". In: *Introduction to Frustrated Magnetism*. Lacroix, C. and Mendels, P. and Mila, F. Springer Berlin, 2011. Chap. 13, pp. 331–362.

[6] L. Savary and L. Balents. "Quantum spin liquids: a review". In: *Reports on Progress in Physics* **80** (Nov. 2016), p. 016502. DOI: 10.1088/0034-4885/80/1/016502.

[7] Y. Zhou, K. Kanoda, and T.-K. Ng. "Quantum spin liquid states". In: *Rev. Mod. Phys.* **89** (Apr. 2017), p. 025003. DOI: 10.1103/RevModPhys.89.025003.

[8] J. Villain et al. "Order as an effect of disorder". In: *J. Phys. (Paris)* **41** (1980), pp. 1263–1272. DOI: https://doi.org/10.1051/jphys:0198000410110126300.

[9] E. F. Shender. "Anti-ferromagnetic garnets with fluctuation-like interacting sublattices". In: *Zh. Eksp. Teor. Fiz.* **83** (1982), pp. 326–337.

[10] Christopher L. Henley. "Ordering due to disorder in a frustrated vector antiferromagnet". In: *Phys. Rev. Lett.* **62** (Apr. 1989), pp. 2056–2059. DOI: 10.1103/PhysRevLett.62.2056.

[11] J. R. Tessman. "Magnetic Anisotropy at 0°K". In: *Phys. Rev.* **96** (Dec. 1954), pp. 1192–1195. DOI: 10.1103/PhysRev.96.1192.

[12] E. Belorizky, R. Casalegno, and P. Fries. "Magnetic stability at 0 K of a simple cubic ferromagnetic array of pseudo-spin S = $\frac{1}{2}$ with anisotropic exchange between nearest neighbours". In: *physica status solidi (b)* **77** (1976), pp. 495–504. DOI: https://doi.org/10.1002/pssb.2220770210.

[13] J. T. Chalker. "Geometrically Frustrated Antiferromagnets: Statistical Mechanics and Dynamics". In: *Introduction to Frustrated Magnetism*. Lacroix, C. and Mendels, P. and Mila, F. Springer Berlin, 2011. Chap. 1, pp. 3–22.

[14] A. V. Chubukov and D. I. Golosov. "Quantum theory of an antiferromagnet on a triangular lattice in a magnetic field". In: *J. Phys.: Condens. Matter* **3** (Jan. 1991), pp. 69–82. DOI: 10.1088/0953-8984/3/1/005.

[15] P. Chandra and B. Doucot. "Possible spin-liquid state at large S for the frustrated square Heisenberg lattice". In: *Phys. Rev. B* **38** (Nov. 1988), pp. 9335–9338. DOI: 10.1103/PhysRevB.38.9335.

[16] A. L. Chernyshev and M. E. Zhitomirsky. "Quantum Selection of Order in an XXZ Antiferromagnet on a Kagome Lattice". In: *Phys. Rev. Lett.* **113** (Dec. 2014), p. 237202. DOI: 10.1103/PhysRevLett.113.237202.

[17] P. Chandra, P. Coleman, and A. I. Larkin. "Ising transition in frustrated Heisenberg models". In: *Phys. Rev. Lett.* **64** (Jan. 1990), pp. 88–91. DOI: 10.1103/PhysRevLett.64.88.

[18] E. Manousakis. "The spin-$\frac{1}{2}$ Heisenberg antiferromagnet on a square lattice and its application to the cuprous oxides". In: *Rev. Mod. Phys.* **63** (Jan. 1991), pp. 1–62. DOI: 10.1103/RevModPhys.63.1.

[19] E. Dagotto and A. Moreo. "Phase diagram of the frustrated spin-1/2 Heisenberg antiferromagnet in 2 dimensions". In: *Phys. Rev. Lett.* **63** (Nov. 1989), pp. 2148–2151. DOI: 10.1103/PhysRevLett.63.2148.

[20] I. G. Gochev. "Theory of the Néel and collinear phases in the J_1-J_2 model of a spin-1/2 square-lattice frustrated antiferromagnet". In: *Phys. Rev. B* **49** (Apr. 1994), pp. 9594–9600. DOI: 10.1103/PhysRevB.49.9594.

[21] S. Morita, R. Kaneko, and M. Imada. "Quantum Spin Liquid in Spin-1/2 J_1-J_2 Heisenberg Model on Square Lattice: Many-Variable Variational Monte Carlo Study Combined with Quantum-Number Projections". In: *J. Phys. Soc. Jpn.* **84** (2015), p. 024720. DOI: 10.7566/JPSJ.84.024720.

[22] M. E. Zhitomirsky and K. Ueda. "Valence-bond crystal phase of a frustrated spin-1/2 square-lattice antiferromagnet". In: *Phys. Rev. B* **54** (Oct. 1996), pp. 9007–9010. DOI: 10.1103/PhysRevB.54.9007.

[23] H.-C. Jiang, H. Yao, and L. Balents. "Spin liquid ground state of the spin-$\frac{1}{2}$ square J_1-J_2 Heisenberg model". In: *Phys. Rev. B* **86** (July 2012), p. 024424. DOI: 10.1103/PhysRevB.86.024424.

[24] V. S. Maryasin and M. E. Zhitomirsky. "Triangular Antiferromagnet with Nonmagnetic Impurities". In: *Phys. Rev. Lett.* **111** (Dec. 2013), p. 247201. DOI: 10.1103/PhysRevLett.111.247201.

[25] R. J. Baxter. *Exactly solved models in statistical mechanics*. Academic press, New York, 1982.

[26] B. S. Shastry and B. Sutherland. "Exact ground state of a quantum mechanical antiferromagnet". In: *Physica B+C* **108** (1981), pp. 1069–1070. ISSN: 0378-4363. DOI: https://doi.org/10.1016/0378-4363(81)90838-X.

[27] A. Kitaev. "Anyons in an exactly solved model and beyond". In: *Annals of Physics* **321** (2006). January Special Issue, pp. 2–111. ISSN: 0003-4916. DOI: https://doi.org/10.1016/j.aop.2005.10.005.

[28] T. Holstein and H. Primakoff. "Field Dependence of the Intrinsic Domain Magnetization of a Ferromagnet". In: *Phys. Rev.* **58** (Dec. 1940), pp. 1098–1113. DOI: 10.1103/PhysRev.58.1098.

[29] M. E. Zhitomirsky and T. Nikuni. "Magnetization curve of a square-lattice Heisenberg antiferromagnet". In: *Phys. Rev. B* **57** (Mar. 1998), pp. 5013–5016. DOI: 10.1103/PhysRevB.57.5013.

[30] S. Nishimoto, N. Shibata, and C. Hotta. "Controlling frustrated liquids and solids with an applied field in a kagome Heisenberg antiferromagnet". In: *Nat. Commun.* **4** (Aug. 2013), p. 2287. DOI: 10.1038/ncomms3287.

[31] M. Takigawa and F. Mila. "Magnetization Plateaus". In: *Introduction to Frustrated Magnetism*. Lacroix, C. and Mendels, P. and Mila, F. Springer Berlin, 2011. Chap. 10, pp. 241–267.

[32] S. Yoshii et al. "High-field magnetization of TmB4". In: *J. Phys.: Conf. Ser.* **51** (Nov. 2006), pp. 59–62. DOI: 10.1088/1742-6596/51/1/011.

[33] F. Iga et al. "Highly anisotropic magnetic phase diagram of a 2-dimensional orthogonal dimer system TmB4". In: *J. Magn. Magn. Mater.* **310** (2007). Proceedings of the 17th International Conference on Magnetism, e443–e445. ISSN: 0304-8853. DOI: https://doi.org/10.1016/j.jmmm.2006.10.476.

[34] K. Siemensmeyer et al. "Fractional Magnetization Plateaus and Magnetic Order in the Shastry-Sutherland Magnet TmB_4". In: *Phys. Rev. Lett.* **101** (Oct. 2008), p. 177201. DOI: 10.1103/PhysRevLett.101.177201.

[35] D. Lançon et al. "Evolution of field-induced metastable phases in the Shastry-Sutherland lattice magnet TmB_4". In: *Phys. Rev. B* **102** (Aug. 2020), p. 060407. DOI: 10.1103/PhysRevB.102.060407.

[36] S. C. Haley et al. "Half-magnetization plateau and the origin of threefold symmetry breaking in an electrically switchable triangular antiferromagnet". In: *Phys. Rev. Research* **2** (Oct. 2020), p. 043020. DOI: 10.1103/PhysRevResearch.2.043020.

[37] M. Oshikawa, M. Yamanaka, and I. Affleck. "Magnetization Plateaus in Spin Chains: "Haldane Gap" for Half-Integer Spins". In: *Phys. Rev. Lett.* **78** (Mar. 1997), pp. 1984–1987. DOI: 10.1103/PhysRevLett.78.1984.

[38] M. E. Zhitomirsky, A. Honecker, and O. A. Petrenko. "Field Induced Ordering in Highly Frustrated Antiferromagnets". In: *Phys. Rev. Lett.* **85** (Oct. 2000), pp. 3269–3272. DOI: 10.1103/PhysRevLett.85.3269.

[39] M. E. Zhitomirsky. "Field-Induced Transitions in a Kagomé Antiferromagnet". In: *Phys. Rev. Lett.* **88** (Jan. 2002), p. 057204. DOI: 10.1103/PhysRevLett.88.057204.

[40] K. Penc, N. Shannon, and H. Shiba. "Half-Magnetization Plateau Stabilized by Structural Distortion in the Antiferromagnetic Heisenberg Model on a Pyrochlore Lattice". In: *Phys. Rev. Lett.* **93** (Nov. 2004), p. 197203. DOI: 10.1103/PhysRevLett.93.197203.

[41] D. C. Cabra et al. "From classical to quantum Kagomé antiferromagnet in a magnetic field". In: *Phys. Rev. B* **65** (Feb. 2002), p. 094418. DOI: 10.1103/PhysRevB.65.094418.

[42] K. Hida. "Magnetization Process of the S=1 and 1/2 Uniform and Distorted Kagomé Heisenberg Antiferromagnets". In: *J. Phys. Soc. Jpn.* **70** (2001), pp. 3673–3677. DOI: 10.1143/JPSJ.70.3673.

[43] A. Honecker, J. Schulenburg, and J. Richter. "Magnetization plateaus in frustrated antiferromagnetic quantum spin models". In: *J. Phys.: Condens. Matter* **16** (Mar. 2004). Highly Frustrated Magnetism 2003 Conference, Inst. Laue-Langevin, Grenoble, FRANCE, AUG 26-30, 2003, S749–S758. DOI: 10.1088/0953-8984/16/11/025.

[44] S. Capponi et al. "Numerical study of magnetization plateaus in the spin-$\frac{1}{2}$ kagome Heisenberg antiferromagnet". In: *Phys. Rev. B* **88** (Oct. 2013), p. 144416. DOI: 10.1103/PhysRevB.88.144416.

[45] T. Coletta, M. E. Zhitomirsky, and F. Mila. "Quantum stabilization of classically unstable plateau structures". In: *Phys. Rev. B* **87** (Feb. 2013), p. 060407. DOI: 10.1103/PhysRevB.87.060407.

[46] T. Coletta et al. "Semiclassical theory of the magnetization process of the triangular lattice Heisenberg model". In: *Phys. Rev. B* **94** (Aug. 2016), p. 075136. DOI: 10.1103/PhysRevB.94.075136.

[47] H. Nakano and T. Sakai. "Magnetization Process of the Spin-S Kagome-Lattice Heisenberg Antiferromagnet". In: *J. Phys. Soc. Jpn.* **84** (2015), p. 063705. DOI: 10.7566/JPSJ.84.063705.

[48] H. Nakano and T. Sakai. "Numerical-Diagonalization Study of Magnetization Process of Frustrated Spin-1/2 Heisenberg Antiferromagnets in Two Dimensions: —Triangular- and Kagome-Lattice Antiferromagnets". In: *J. Phys. Soc. Jpn.* **87** (2018), p. 063706. DOI: 10.7566/JPSJ.87.063706.

[49] J. Schulenburg et al. “Macroscopic Magnetization Jumps due to Independent Magnons in Frustrated Quantum Spin Lattices”. In: *Phys. Rev. Lett.* **88** (Apr. 2002), p. 167207. DOI: 10.1103/PhysRevLett.88.167207.

[50] M. E. Zhitomirsky and H. Tsunetsugu. “Exact low-temperature behavior of a kagomé antiferromagnet at high fields”. In: *Phys. Rev. B* **70** (Sept. 2004), p. 100403. DOI: 10.1103/PhysRevB.70.100403.

[51] J. Richter et al. “Exact eigenstates and macroscopic magnetization jumps in strongly frustrated spin lattices”. In: *J. Phys.: Condens. Matter* **16** (Mar. 2004). Highly Frustrated Magnetism 2003 Conference, Inst Laue Langevin, Grenoble, FRANCE, AUG 26-30, 2003, S779–S784. DOI: 10.1088/0953-8984/16/11/029.

[52] D. C. Cabra et al. “Quantum kagomé antiferromagnet in a magnetic field: Low-lying nonmagnetic excitations versus valence-bond crystal order”. In: *Phys. Rev. B* **71** (Apr. 2005), p. 144420. DOI: 10.1103/PhysRevB.71.144420.

[53] J. T. Chalker, P. C. W. Holdsworth, and E. F. Shender. “Hidden order in a frustrated system: Properties of the Heisenberg Kagomé antiferromagnet”. In: *Phys. Rev. Lett.* **68** (Feb. 1992), pp. 855–858. DOI: 10.1103/PhysRevLett.68.855.

[54] J. N. Reimers. “Absence of long-range order in a three-dimensional geometrically frustrated antiferromagnet”. In: *Phys. Rev. B* **45** (Apr. 1992), pp. 7287–7294. DOI: 10.1103/PhysRevB.45.7287.

[55] R. Moessner and J. T. Chalker. “Properties of a Classical Spin Liquid: The Heisenberg Pyrochlore Antiferromagnet”. In: *Phys. Rev. Lett.* **80** (Mar. 1998), pp. 2929–2932. DOI: 10.1103/PhysRevLett.80.2929.

[56] L. Messio, B. Bernu, and C. Lhuillier. “Kagome Antiferromagnet: A Chiral Topological Spin Liquid?” In: *Phys. Rev. Lett.* **108** (May 2012), p. 207204. DOI: 10.1103/PhysRevLett.108.207204.

[57] B. Canals and C. Lacroix. “Pyrochlore Antiferromagnet: A Three-Dimensional Quantum Spin Liquid”. In: *Phys. Rev. Lett.* **80** (Mar. 1998), pp. 2933–2936. DOI: 10.1103/PhysRevLett.80.2933.

[58] T. Picot et al. “Spin-S kagome quantum antiferromagnets in a field with tensor networks”. In: *Phys. Rev. B* **93** (Feb. 2016), p. 060407. DOI: 10.1103/PhysRevB.93.060407.

[59] J. Schnack et al. “Magnon Crystallization in the Kagome Lattice Antiferromagnet”. In: *Phys. Rev. Lett.* **125** (Sept. 2020), p. 117207. DOI: 10.1103/PhysRevLett.125.117207.

[60] J. Schnack et al. “Independent magnon states on magnetic polytopes”. In: *Eur. Phys. J. B* **24** (2001). DOI: https://doi.org/10.1007/s10051-001-8701-6.

[61] J. Schnack, J. Schulenburg, and J. Richter. "Magnetism of the $N = 42$ kagome lattice antiferromagnet". In: *Phys. Rev. B* 98 (Sept. 2018), p. 094423. DOI: 10.1103/PhysRevB.98.094423.

[62] Y. Okamoto et al. "Magnetization plateaus of the spin-$\frac{1}{2}$ kagome antiferromagnets volborthite and vesignieite". In: *Phys. Rev. B* **83** (May 2011), p. 180407. DOI: 10.1103/PhysRevB.83.180407.

[63] H. Ishikawa et al. "One-Third Magnetization Plateau with a Preceding Novel Phase in Volborthite". In: *Phys. Rev. Lett.* **114** (June 2015), p. 227202. DOI: 10.1103/PhysRevLett.114.227202.

[64] D. Nakamura et al. "Extremely wide $\frac{1}{3}$ magnetic plateau of volborthite $Cu_3V_2O_7(OH)_2 \cdot 2H_2O$ in ultrahigh magnetic fields up to 182 T". In: *Phys. Rev. B* **98** (July 2018), p. 020404. DOI: 10.1103/PhysRevB.98.020404.

[65] R. Shirakami et al. "Two magnetization plateaus in the kagome fluoride $Cs_2LiTi_3F_{12}$". In: *Phys. Rev. B* **100** (Nov. 2019), p. 174401. DOI: 10.1103/PhysRevB.100.174401.

[66] R. Okuma et al. "A series of magnon crystals appearing under ultrahigh magnetic fields in a kagome antiferromagnet". In: *Nat. Commun.* **10** (Mar. 2019), p. 1229. DOI: 10.1038/s41467-019-09063-7.

[67] R. Okuma, D. Nakamura, and S. Takeyama. "Magnetization plateau observed by ultrahigh-field Faraday rotation in the kagome antiferromagnet herbertsmithite". In: *Phys. Rev. B* **102** (Sept. 2020), p. 104429. DOI: 10.1103/PhysRevB.102.104429.

[68] P. W. Anderson. "Ordering and Antiferromagnetism in Ferrites". In: *Phys. Rev.* **102** (May 1956), pp. 1008–1013. DOI: 10.1103/PhysRev.102.1008.

[69] H. Ueda et al. "Successive field-induced transitions in a frustrated antiferromagnet $HgCr_2O_4$". In: *Phys. Rev. B* **73** (Mar. 2006), p. 094415. DOI: 10.1103/PhysRevB.73.094415.

[70] S. Kimura et al. "Evolution of exchange interaction constants across magnetic phase transitions in the chromium spinel oxide $CdCr_2O_4$". In: *Phys. Rev. B* **92** (Oct. 2015), p. 144410. DOI: 10.1103/PhysRevB.92.144410.

[71] N. Shannon et al. "Half-magnetization plateaux in Cr spinels". In: ed. by N Kobayashi, N Toyota, and M Motokawa. Vol. **51**. J. Phys.: Conf. Ser. 60th Yamada Conference on Research in High Magnetic Fields, Sendai, JAPAN, AUG 16-19, 2006. 2006, pp. 31+. DOI: 10.1088/1742-6596/51/1/005.

[72] H. Mitamura et al. "Phase Transitions of a Geometrically Frustrated Spin System CdCr2O4 in Very High Magnetic Fields". In: *J. Phys. Soc. Jpn.* **76** (2007), p. 085001. DOI: 10.1143/JPSJ.76.085001.

[73] E. Kojima et al. "Full-magnetization of geometrically frustrated $CdCr_2O_4$ determined by Faraday rotation measurements at magnetic fields up to 140 T". In: *Phys. Rev. B* **77** (June 2008), p. 212408. DOI: 10.1103/PhysRevB.77.212408.

[74] S. Kimura et al. "Large change in the exchange interactions of $HgCr_2O_4$ under very high magnetic fields". In: *Phys. Rev. B* **83** (June 2011), p. 214401. DOI: 10.1103/PhysRevB.83.214401.

[75] A. Miyata et al. "Magnetic Phases of a Highly Frustrated Magnet, $ZnCr_2O_4$, up to an Ultrahigh Magnetic Field of 600 T". In: *Phys. Rev. Lett.* **107** (Nov. 2011), p. 207203. DOI: 10.1103/PhysRevLett.107.207203.

[76] A. Miyata et al. "Magnetic Phases of ZnCr2O4 Revealed by Magneto-Optical Studies under Ultra-High Magnetic Fields of up to 600 T". In: *J. Phys. Soc. Jpn.* **81** (2012), p. 114701. DOI: 10.1143/JPSJ.81.114701.

[77] A. Miyata, S. Takeyama, and H. Ueda. "Magnetic superfluid state in the frustrated spinel oxide $CdCr_2O_4$ revealed by ultrahigh magnetic fields". In: *Phys. Rev. B* **87** (June 2013), p. 214424. DOI: 10.1103/PhysRevB.87.214424.

[78] A. Miyata, H. Ueda, and S. Takeyama. "Canted 2:1:1 Magnetic Supersolid Phase in a Frustrated Magnet MgCr2O4 as a Small Limit of the Biquadratic Spin Interaction". In: *J. Phys. Soc. Jpn.* **83** (2014), p. 063702. DOI: 10.7566/JPSJ.83.063702.

[79] N. Shannon, K. Penc, and Y. Motome. "Nematic, vector-multipole, and plateau-liquid states in the classical $O(3)$ pyrochlore antiferromagnet with biquadratic interactions in applied magnetic field". In: *Phys. Rev. B* **81** (May 2010), p. 184409. DOI: 10.1103/PhysRevB.81.184409.

[80] Y. Okamoto et al. "Magnetic transitions under ultrahigh magnetic fields of up to 130 T in the breathing pyrochlore antiferromagnet $\mathbf{LiInCr_4O_8}$". In: *Phys. Rev. B* **95** (Apr. 2017), p. 134438. DOI: 10.1103/PhysRevB.95.134438.

[81] M. Gen et al. "Magnetization process of the breathing pyrochlore magnet $CuInCr_4S_8$ in ultrahigh magnetic fields up to 150 T". In: *Phys. Rev. B* **101** (Feb. 2020), p. 054434. DOI: 10.1103/PhysRevB.101.054434.

[82] J. N. Reimers, A. J. Berlinsky, and A.-C. Shi. "Mean-field approach to magnetic ordering in highly frustrated pyrochlores". In: *Phys. Rev. B* **43** (Jan. 1991), pp. 865–878. DOI: 10.1103/PhysRevB.43.865.

[83] R. Moessner and J. T. Chalker. "Low-temperature properties of classical geometrically frustrated antiferromagnets". In: *Phys. Rev. B* **58** (Nov. 1998), pp. 12049–12062. DOI: 10.1103/PhysRevB.58.12049.

[84] S. R. Hassan and R. Moessner. "Semiclassical degeneracies and ordering for highly frustrated magnets in a field". In: *Phys. Rev. B* **73** (Mar. 2006), p. 094443. DOI: 10.1103/PhysRevB.73.094443.

[85] M. E. Zhitomirsky and H. Tsunetsugu. "Lattice gas description of pyrochlore and checkerboard antiferromagnets in a strong magnetic field". In: *Phys. Rev. B* **75** (June 2007), p. 224416. DOI: 10.1103/PhysRevB.75.224416.

[86] A. B. Harris, A. J. Berlinsky, and C. Bruder. "Ordering by quantum fluctuations in a strongly frustrated Heisenberg antiferromagnet". In: *J. Appl. Phys.* **69** (1991), pp. 5200–5202. DOI: 10.1063/1.348098.

[87] H. Nakano and T. Sakai. "Anomalous Behavior of the Magnetization Process of the S = 1/2 Kagome-Lattice Heisenberg Antiferromagnet at One-Third Height of the Saturation". In: *J. Phys. Soc. Jpn.* **83** (2014), p. 104710. DOI: 10.7566/JPSJ.83.104710.

[88] P. W. Anderson. "Generalizations of the Weiss Molecular Field Theory of Antiferromagnetism". In: *Phys. Rev.* **79** (Aug. 1950), pp. 705–710. DOI: 10.1103/PhysRev.79.705.

[89] Ziman J. M. "Antiferromagnetism by the Spin Wave Method III: Application to more Complex Systems". In: *Proc. Phys. Soc. A* **66** (Jan. 1953), pp. 89–94. DOI: 10.1088/0370-1298/66/1/313.

[90] D. Ter Haar, M. E. Lines, and B. Bleaney. "A spin-wave theory of anisotropic antiferromagnetica". In: *Phil. Trans. R. Soc. London A, Mathematical and Physical Sciences* **255** (1962), pp. 1–30. DOI: 10.1098/rsta.1962.0008.

[91] M. E. Lines. "Antiferromagnetism in the face-centred cubic lattice by a spin-wave method". In: *Proc. R. Soc. London A, Mathematical and Physical Sciences* **271** (1963), pp. 105–119. DOI: 10.1098/rspa.1963.0007.

[92] Y. Yamamoto and T. Nagamiya. "Spin Arrangements in Magnetic Compounds of the Rocksalt Crystal Structure". In: *J. Phys. Soc. Jpn.* **32** (1972), pp. 1248–1261. DOI: 10.1143/JPSJ.32.1248.

[93] R. H. Swendsen. "Antiferromagnetic order in cubic crystals". In: *J. Phys. C: Solid State Phys.* **6** (Dec. 1973), pp. 3763–3773. DOI: 10.1088/0022-3719/6/24/032.

[94] M. S. Seehra and T. M. Giebultowicz. "Magnetic structures of fcc systems with nearest-neighbor and next-nearest-neighbor exchange interactions". In: *Phys. Rev. B* **38** (Dec. 1988), pp. 11898–11900. DOI: 10.1103/PhysRevB.38.11898.

[95] M. Matsuura et al. "Classical and quantum spin dynamics in the fcc antiferromagnet NiS_2 with frustration". In: *Phys. Rev. B* **68** (Sept. 2003), p. 094409. DOI: 10.1103/PhysRevB.68.094409.

[96] A. L. Goodwin et al. "MnO spin-wave dispersion curves from neutron powder diffraction". In: *Phys. Rev. B* **75** (Feb. 2007), p. 075423. DOI: 10.1103/PhysRevB.75.075423.

[97] A. M. Balagurov et al. "Magnetostructural phase transitions in NiO and MnO: Neutron diffraction data". In: *JETP LETTERS* **104** (July 2016), pp. 88–93. DOI: 10.1134/S0021364016140071.

[98] A. A. Aczel et al. "Highly anisotropic exchange interactions of $j_{\text{eff}} = \frac{1}{2}$ iridium moments on the fcc lattice in $La_2BIrO_6(B = \text{Mg, Zn})$". In: *Phys. Rev. B* **93** (June 2016), p. 214426. DOI: 10.1103/PhysRevB.93.214426.

[99] T. Chatterji et al. "Magnetic excitations in frustrated fcc type-III antiferromagnet MnS2". In: *J. Phys.: Condens. Matter* **31** (Jan. 2019), p. 125802. DOI: 10.1088/1361-648x/aafaeb.

[100] N. Khan et al. "Cubic symmetry and magnetic frustration on the fcc spin lattice in K_2IrCl_6". In: *Phys. Rev. B* **99** (Apr. 2019), p. 144425. DOI: 10.1103/PhysRevB.99.144425.

[101] A. Revelli et al. "Spin-orbit entangled $j = \frac{1}{2}$ moments in Ba_2CeIrO_6: A frustrated fcc quantum magnet". In: *Phys. Rev. B* **100** (Aug. 2019), p. 085139. DOI: 10.1103/PhysRevB.100.085139.

[102] M. T. Heinilä and A. S. Oja. "Long-range order produced by the interaction between spin waves in classical fcc Heisenberg models". In: *Phys. Rev. B* **48** (Dec. 1993), pp. 16514–16523. DOI: 10.1103/PhysRevB.48.16514.

[103] K. Lefmann and C. Rischel. "Quantum effects in magnetic structures on the fcc lattice". In: *Eur. Phys. J. B* **21** (June 2001), pp. 313–329. DOI: 10.1007/BF01313313.

[104] M. V. Gvozdikova and M. E. Zhitomirsky. "A Monte Carlo study of the first-order transition in a Heisenberg FCC antiferromagnet". In: *JETP LETTERS* **81** (2005), pp. 236–240. DOI: 10.1134/1.1921323.

[105] N.-N. Sun and H.-Y. Wang. "The J1-J2 model on the face-centered-cubic lattices". In: *J. Magn. Magn. Mater.* **454** (2018), pp. 176–184. DOI: 10.1016/j.jmmm.2018.01.076.

[106] D. Kiese et al. *Multiloop functional renormalization group approach to quantum spin systems*. 2021. arXiv: 2011.01269 [cond-mat.str-el].

[107] M. E. Lines. "Green Functions in the Theory of Antiferromagnetism". In: *Phys. Rev.* **135** (Aug. 1964), A1336–A1346. DOI: 10.1103/PhysRev.135.A1336.

[108] T. Oguchi, H. Nishimori, and Y. Taguchi. "The Spin Wave Theory in Antiferromagnetic Heisenberg Model on Face Centered Cubic Lattice". In: *J. Phys. Soc. Jpn.* **54** (1985), pp. 4494–4497. DOI: 10.1143/JPSJ.54.4494.

[109] C. L. Henley. "Ordering by disorder: Ground-state selection in fcc vector antiferromagnets". In: *J. Appl. Phys.* **61** (1987), pp. 3962–3964. DOI: 10.1063/1.338570.

[110] E. Rastelli and A. Tassi. "Competition between thermal and quantum fluctuations in a Heisenberg rhombohedral antiferromagnet". In: *J. Phys. C: Solid State Phys.* **21** (Jan. 1988), pp. L35–L39. DOI: 10.1088/0022-3719/21/2/005.

[111] M. Takahashi. "Modified spin-wave theory of a square-lattice antiferromagnet". In: *Phys. Rev. B* **40** (Aug. 1989), pp. 2494–2501. DOI: 10.1103/PhysRevB.40.2494.

[112] J. G. Rau, P. A. McClarty, and R. Moessner. "Pseudo-Goldstone Gaps and Order-by-Quantum Disorder in Frustrated Magnets". In: *Phys. Rev. Lett.* **121** (Dec. 2018), p. 237201. DOI: 10.1103/PhysRevLett.121.237201.

[113] D. J. J. Farnell, O. Götze, and J. Richter. "Ground-state ordering of the J_1-J_2 model on the simple cubic and body-centered cubic lattices". In: *Phys. Rev. B* **93** (June 2016), p. 235123. DOI: 10.1103/PhysRevB.93.235123.

[114] L. Bergomi and Th. Jolicoeur. "Self-consistent interaction of magnons in a frustrated quantum antiferromagnet". In: *J. Phys. I France* **2** (1992), pp. 371–377. DOI: 10.1051/jp1:1992149.

[115] I. G. Gochev. "Spin-wave expansion of the ground-state energy of the square-lattice Heisenberg antiferromagnet". In: *Phys. Rev. B* **47** (Jan. 1993), pp. 1096–1098. DOI: 10.1103/PhysRevB.47.1096.

[116] J.H.P. Colpa. "Diagonalization of the quadratic boson hamiltonian". In: *Physica A: Statistical Mechanics and its Applications* **93** (1978), pp. 327–353. ISSN: 0378-4371. DOI: https://doi.org/10.1016/0378-4371(78)90160-7.